

Copyright

by

Netzahualc6yotl Arroyo Curr6s

2015

**The Dissertation Committee for Netzahualcóyotl Arroyo Currás certifies that this is
the approved version of the following dissertation:**

**Development of an Alkaline Redox Flow Battery: From Fundamentals
to Benchtop Prototype**

Committee:

Allen J. Bard, Supervisor

Richard M. Crooks

Charles B. Mullins

Michael Rose

Guihua Yu

**Development of an Alkaline Redox Flow Battery: From Fundamentals
to Benchtop Prototype**

by

Netzahualcóyotl Arroyo Currás, B.S.

Dissertation

Presented to the Faculty of the Graduate School of

The University of Texas at Austin

in Partial Fulfillment

of the Requirements

for the Degree of

Doctor of Philosophy

The University of Texas at Austin

May, 2015

Dedication

To Cui and Tabaré, for being my sources of inspiration and contrast in life.

To Maria Luisa and Karen, for their unconditional love.

Acknowledgements

I would like to thank Dr. Allen J. Bard for taking me as a student. I came to Austin with the aspiration to become an electrochemist under his guidance, but Dr. Bard did more than that, he taught me how to be a good scientist overall and an exemplary teacher. His constant demands for better data and harder experiments have pushed my perseverance and creativity to limits I had never explored before. I also thank him for his sincere interest in my professional development and my health; he was supportive of me during all times, good and bad.

I would also like to thank Dr. Richard M. Crooks for his friendship and constant support throughout my Ph.D. program. His interest in my academic progress, his stories, and his recommendations were the perfect complement to my training as a scientist.

I thank Angie Missildine and Bob Villwock for their friendship and constant administrative support. More than once they acted beyond their obligations to help me achieve my goals. I also thank Betsy Hamblen and Penny Kile for their guidance in all academic and administrative matters related to my degree.

Some portions of the work reported here required the expert advice and technical skills of Tim Hooper from the electronics shop, and Mike Ronalter and Adam Kennedy from the glass blowing shop. I thank them for their assistance and friendship.

Finally, I would like to acknowledge the financial support provided in part by the Global Climate and Energy Project (27777240-51978A) and by the Advanced Research Projects Agency (ARPA-E), U.S. Department of Energy (DE-AR0000149) for the development of this work. I hope the concepts presented herein will contribute significantly to the ongoing effort to minimize global warming and to build a fossil-fuel-free energy infrastructure for the future of humankind.

Preface

This dissertation is divided into two parts. The first part presents the development of an alkaline redox flow battery (a-RFB) from the fundamental aspects of its chemistry to the construction of a benchtop prototype. The a-RFB uses concentrated solutions of $\text{NaOH}_{(\text{aq})}$ as the supporting electrolyte. Concentrated base was selected because it is less corrosive to RFB components compared to the ubiquitously used acidic electrolytes. The challenge was to find chemically stable redox couples with sufficiently negative and positive formal potentials to maximize the output voltage of the battery, as well as to produce a battery with high energy density. In this dissertation, an understanding based on chemical equilibrium and thermodynamics is developed to explain the particular difficulty of the challenge, and strategies are presented to overcome it. Chapter 1 presents a description of an a-RFB and introduces thermodynamic and kinetic concepts necessary to understand the complexity of the a-RFB. Chapter 1 also introduces the coordination compounds used in this work and presents data on their electrochemistry.

Chapter 2 provides a discussion on homogeneous kinetics coupled to electron transfer processes, in particular those present in homogeneous reactions associated with the coordination compounds used in the a-RFB. In chapter 2, a method based on scanning electrochemical microscopy (SECM) is proposed as a screening technique to evaluate the chemical stability of redox couples over extended periods of time. The SECM-based technique is particularly useful to detect slow homogeneous kinetics that may be invisible to cyclic voltammetry or other conventional electrochemical methods. This is important because the existence of slow homogeneous kinetics may decrease the charge storage capacity of the a-RFB with time.

Chapter 3 presents structural, electrochemical and spectroscopic characterizations of Fe-TEA, one of the coordination compounds used in the a-RFB. Special attention was given to Fe-TEA because of its importance in the fields of supramolecular inorganic chemistry, synthesis of films with magnetic memory, and electrochemistry. Finally, Chapter 4 presents an a-RFB based on the coordination chemistry of iron and cobalt with amino-alcohol ligands in concentrated base. The Co/Fe a-RFB is the first chemically stable flow battery to achieve 100% coulombic efficiency in over 30 cycles with negligible membrane crossover.

The second part of this dissertation takes the coordination compounds used to store electrical energy in the a-RFB and introduces their application as redox titrants in electrochemical titration experiments carried out in concentrated base. Part 2 provides a brief introduction to the topic of electrochemical titrations, with special focus on coulometric titrations and the surface interrogation mode of SECM (SI-SECM). Chapter 5 describes the use of Fe-TEA in amperometric and potentiometric titrations of molecular oxygen in concentrated base. This work is of extreme importance to the a-RFB because the ferrous form of Fe-TEA reacts rapidly with oxygen to produce hydrogen peroxide, thus decreasing the charging-discharging capacity of the battery. Chapter 6 describes the use of Fe-TEA as an electrochemical titrant for SI-SECM applications in concentrated base. The surface oxidation of Ir polycrystalline electrodes was used as a model to demonstrate the value of Fe-TEA as a titrant in the determination of hydrous oxides of Ir generated at different potentials. Particular attention was given to those oxides that exist at the onset of oxygen evolution. Chapter 7 discusses unanswered questions regarding the Co/Fe a-RFB and its chemistry and presents concluding remarks.

Netz Arroyo

Austin, 2015

Abstract

Development of an Alkaline Redox Flow Battery: From Fundamentals to Benchtop Prototype

Netzahualcóyotl Arroyo Currás, Ph.D.

The University of Texas at Austin, 2015

Supervisor: Allen J. Bard

This work presents the first alkaline redox flow battery (a-RFB) based on the coordination chemistry of cobalt(III/II) and iron(III/II) with amino-alcohol ligands in concentrated $\text{NaOH}_{(\text{aq})}$. The a-RFB was developed by carrying out systematic structural and electrochemical characterizations of various redox-active coordination compounds to find the most suitable candidates for electrochemical energy storage. In the characterization studies, particular attention was given to the redox couple Fe(III/II)-TEA, where TEA = triethanolamine, because of its importance in the fields of supramolecular chemistry, magnetic memory films, and electrochemical energy storage.

The structures of Fe(III)-TEA in the solid state and in alkaline solution are reported for the first time. Moreover, experimental evidence is presented for the existence of an EC reaction in the heterogeneous reduction of Fe(III/II)-TEA in concentrated base. Furthermore, experiments were carried out to study the reactivity of Fe(II)-TEA with O_2 . This is important because O_2 reacts spontaneously with Fe(II)-TEA to produce hydrogen peroxide, decreasing the charging-discharging capacity of the a-RFB. The reduction of

oxygen by Fe(II)-TEA in concentrated base was studied by UV-Vis spectroscopy and coulometric titrations.

Additionally, a new method for the quick identification of redox couples with slow EC reactions, $k_f < 0.1 \text{ s}^{-1}$, is presented. The new method is based on scanning electrochemical microscopy (SECM) and consists of creating a thin-layer cell between the tip and substrate electrode. During analysis of a redox couple, the tip reports a current transient proportional to the decaying concentration of the product of the E reaction, from which an apparent forward rate constant for the C reaction can be determined. This method was designed for the field of RFB research, where the identification of redox couples with no EC reactions is necessary to ensure that a battery can run for thousands of cycles.

Lastly, surface oxidation of polycrystalline Ir ultramicroelectrodes was studied by the surface interrogation mode of SECM (SI-SECM), using Fe(II)-TEA as the titrant. This was done to demonstrate the existence of hydrous oxides of Ir(IV) and Ir(V) prior to the onset of oxygen evolution in concentrated base. Numerical simulations were carried out using commercial software and were used to validate the experimental results reported in this work.

Table of Contents

Symbols	xiv
List of Abbreviations	xvii
List of Tables	xix
List of Figures	xx
PART 1	1
Chapter 1. Electrochemical Energy Storage, and the Chemistry Behind the Alkaline Redox Flow Battery	1
1.1. Introduction	1
1.2. Thermodynamic and Kinetic Considerations	4
Solubility of Transition Metal Ions in 5 M NaOH	4
Relationship Between Formal Potential and Stability Constants	5
Homogeneous Kinetics Coupled to the Electron Transfer Step	8
1.3. Complexes of Fe and Co in 5 M NaOH	9
1.4. Synthesis of Coordination Compounds	13
1.5. Experimental Tuning of Formal Potentials	15
1.6. Viscosities and Densities of Electrolytes.....	17
1.7. Diffusion Coefficients	19
1.8. Electron Transfer Kinetics	21
1.9. Conclusions	26
1.10. References	27
Chapter 2. Use of Scanning Electrochemical Microscopy in the Evaluation of Redox Couples for Flow Battery Applications	30
2.1. Abstract.....	30
2.2. Introduction	30
2.3. Mode of Operation.....	33
2.4. Experimental Section.....	36
Chemicals and Solutions	36

Electrodes and Instrumentation	37
2.5. Numerical Simulations	38
2.6. Results and Discussion	39
Localized Electrolysis.....	42
Evaluation of Redox Couples	44
2.7. Conclusions	48
2.8. References	49
Chapter 3. Structural, Electrochemical and Spectroscopic Characterizations of Fe(III/II)-TEA in Strong Base'	50
3.1. Abstract.....	50
3.2. Introduction	51
3.3. Experimental Section.....	53
Synthesis of [Fe(III)(TEA)(OH)] ⁻ (2).....	53
Synthesis of [(μ-O)(Fe(TEA)) ₂] ⁴⁺ (4).....	54
Synthesis of [(TEA)Fe(III)OFe(II)(TEA)] ⁻ (5).....	55
UV-Vis and Raman Spectroscopy	55
Electrochemical Methods	56
X-ray Crystallography	56
DFT Methods.....	57
3.4. Results and Discussion	57
Crystallography	57
General Electrochemical Analysis.....	58
Raman Spectroscopy	59
Coulometry	61
Cyclic Voltammetry at UMEs	64
Determination of Stability Constants	66
3.5. Conclusions	70
3.6. References	71

Chapter 4. An Alkaline Flow Battery Based on the Coordination Chemistry of Iron and Cobalt	74
4.1. Abstract	74
4.2. Introduction	74
4.3. Methods	76
Synthesis of Coordination Compounds	76
Instrumentation	77
Flow Cell construction and Cycling Analysis	78
4.4. Results	79
Voltammetry	79
Bulk Electrolysis	80
Solubility in 5 M NaOH	82
Charge-Discharge Cycling Performance of the Battery	82
4.5. Discussion	85
Solubility in 5 M NaOH	85
Charge-Discharge Cycling Performance of the Battery	86
4.6. Conclusion	88
4.7. References	88
PART 2	90
Chapter 5. Coulometric Titrations of Molecular Oxygen in Concentrated NaOH	92
5.1. Abstract	92
5.2. Coulometric Titrations	92
5.3. References	102
Chapter 6. Iridium Oxidation as Observed by Surface Interrogation Scanning Electrochemical Microscopy (SI-SECM)	103
6.1. Abstract	103
6.2. Introduction	103
Mode of Operation	106
6.3. Experimental Section	108

Reagents.....	108
Electrodes and SECM Cell.....	109
Instrumentation.....	109
6.4. Results and Discussion.....	111
Coulometry.....	111
Kinetic Data.....	116
6.5. Conclusions.....	121
6.6. References.....	121
Chapter 7. Concluding Remarks.....	124
APPENDIX A	126
7.1. Supporting Information - Chapter 1.....	127
7.2. Supporting Information - Chapter 2.....	137
Dimensions of Electrochemical Cell and Electrodes for e-SECM.....	137
Model for Digital Simulations of e-SECM.....	139
7.3. Supporting Information - Chapter 3.....	142
7.4. Supporting Information - Chapter 4.....	145
Oxidation of Fe(II)-TEA by O ₂	149
7.5. Supporting Information - Chapter 5.....	152
7.6. Supporting Information - Chapter 6.....	153
Fabrication of GC Microelectrodes.....	153
Automation of SI-SECM Experiment.....	154
Interrogation Transient of Hydrogen.....	155
APPENDIX B: OTHER WORKS BY THE SAME AUTHOR	156
REFERENCES	157
VITA	167

Symbols

Symbol	Meaning	Usual Units	Section (First Used)
G	conductance	mS cm ⁻¹	1.1
M	molar	moles L ⁻¹	1.1
e^-	electron		1.2
k_f	forward rate constant	depends on order	1.2
k_b	backward rate constant	depends on order	1.2
$M^{(n)+}$	metal ion with n valence		1.2
$M^{(n-1)+}$	metal ion with $n-1$ valence		1.2
E^0	formal reduction potential	V	1.2
S	solubility	moles L ⁻¹	1.2
t	time	s	1.2
∞	infinite		1.2
k^0	standard rate constant	cm s ⁻¹	1.2
D	diffusion coefficient	cm ² s ⁻¹	1.2
K_{sp}	solubility product		1.2
β	stability constant		1.2
$L^{(l)}$	generic ligand with charge l		1.2
μ	ionic strength, ligand bridge	Moles L ⁻¹	1.2
E^0	standard redox potential	V	1.2
E	measured redox potential	V	1.2
R	gas constant	J K ⁻¹ mol ⁻¹	1.2
T	temperature	K	1.2
n	number of electrons or valency on metal		1.2

l	valency on ligand or		1.2
l	pathlength		1.2
F	Faraday's constant	C mol^{-1}	1.2
γ	activity coefficient		1.2
$[\]$	brackets, concentration	moles L^{-1}	1.2
$p\text{H}$	$-\log [\text{H}^+]$		1.2
EC	reaction: electron transfer step followed by chemical step		1.2
X	unknown chemical species		1.2
λ	dimensionless time parameter		1.3
ρ	resistivity	$\Omega \cdot \text{cm}$	1.4
ρ	density	g/L	1.4
Δ	difference or change		1.4
B	viscometer's constant	L/m	1.6
η	viscosity	cP	1.6
η	electrolysis efficiency		1.7
k	kinetic parameter	cm s^{-1}	1.7
m	mass transfer coefficient	cm s^{-1}	1.7
f	RT/F	V^{-1}	1.7
d	distance	μm	1.7
a	radius of UME	μm	1.7
r_g	radius of insulation sheath	μm	1.7
i_{ss}	steady state current	A	1.7
V	volume	L	2.1
v	scan rate in CV	V s^{-1}	2.1

E_p	peak potential from CV, LSV	V	2.2
k_{mt}	rate of mass transfer	cm s ⁻¹	2.3
p	electrolysis rate	s ⁻¹	2.3
$i_{T,\infty}$	tip current at infinite distance from substrate in SECM	A	2.3
$I_T(L)$	current normalized to i_{ss} in SECM	A	2.3
i_p	peak current in CV, LSV	A	2.4
α	transference number		2.5
E_{in}	initial potential in CV, LSV	V	2.5
R_U	uncompensated resistance	Ω	2.5
C_{dl}	double layer capacitance	μF	2.5
i_{nf}	non Faradaic current	A	2.5
d_{open}	tip-to-substrate distance used in e-SECM	μm	2.6
Q	charge	C	2.6
A	area	cm ²	2.6
χ	mole fraction		5.2

List of Abbreviations

Abbreviation	Meaning	Section References
EES	electrical energy storage	1.1
RFB, RFBs	redox flow battery(ies)	1.1
a-RFB	alkaline RFB	1.1
EDTA	ethylenediaminetetraacetic acid	1.2
Ag/AgCl	KCl-saturated silver-silver chloride reference electrode	1.2
TEA	triethanolamine	1.3
DEA	diethanolamine	1.3
EDEA	N-ethyldiethanolamine	1.3
BYCN	bicine	1.3
TEOH	triethanolmethane	1.3
mTEA	diethanolisopropanolamine	1.3
GC	glassy carbon	1.3
CV	cyclic voltammetry, cyclic voltammogram	1.3
XRD	X-ray diffraction	1.3
DIPSO	3-(N,N-Bis[2-hydroxyethyl]amino)-2-hydroxypropanesulfonic acid	1.5
TiPA	triisopropanolamine	1.5
THEED	N,N,N',N'-Tetrakis(2-hydroxyethyl)ethylenediamine	1.5
BIS-TRIS	2,2-Bis(hydroxymethyl)-2,2',2''-nitrilotriethanol	1.5
OCV	open circuit voltage	1.7
SECM	scanning electrochemical microscopy	1.7

UME	ultramicroelectrode	1.7
LSV	linear sweep voltammetry	1.7
e-SECM	electrolysis mode of SECM	2.3
<i>RG</i>	$RG = rg/a$, UME geometric parameter	2.4
FEA	finite element analysis	2.5
FcMeOH	ferrocene-methanol	2.6
PAP	<i>p</i> -aminophenol	2.6
QI	quinoneimine	2.6
Q	<i>p</i> -benzoquinone	2.6
DFT	density functional theory	3.2
DSA	dimensionally stable anode	6.2
XAS	X-ray absorption spectroscopy	6.2
AIROF	anodically formed iridium oxide films	6.2

List of Tables

Table 1.1. Comparison between experimental and calculated formal redox potentials of ligand – modified couples.....	7
Table 1.2. Approximate time windows accessible for different electroanalytical techniques.....	10
Table 1.3. Standard potentials, formal potentials of [Co(II)/(III)(L)] and [Fe(III)/(II)(L)] in 5 M NaOH.	17
Table 3.1. Numbering of structures used in this chapter.	51
Table 3.2. Comparison of simulated and experimental bond lengths.	61
Table 4.1. Conditions used for the evaluation of battery performance.	83
Table 6.1. Parameters used to simulate the Frumkin isotherms.	115
Table A1. Compendium of Metallic Ions, Ligands and Anions Tested: Mn, Fe, Co.....	127
Table A2. Compendium of Metallic Ions, Ligands and Anions Tested: Sc, Ti, V, Cr.....	136
Table A3. Compendium of Metallic Ions, Ligands and Anions Tested: Ni, Cu, Zn, Sn.....	136
Table A4. Calculated vibrational modes of [Fe(III)(TEA)(OH)] ⁻ and their assigned vibrations.	144

List of Figures

Figure 1.1. Megawatt-hour electrical energy storage plant installed in California by EnerVault in 2014. Courtesy EnerVault.....	2
Figure 1.2. Molecular structures of some of the ligands used in this work.....	11
Figure 1.3. CVs of 10 mM [Co(II)(L)] complexes in 5 M NaOH.....	12
Figure 1.4. CVs of 10 mM [Fe(III)(L)] complexes in 5 M NaOH.	13
Figure 1.5. Molecular structures of the ligands used to tune formal potentials.....	14
Figure 1.6. CVs of 10 mM [Fe(III)(L)] complexes and 10 mM [Co(II)(L)] complexes in 5 M NaOH.	16
Figure 1.7. Viscosities of water, 5 M NaOH _(aq) , 0.5 M [Fe(III)(TEA)] in 5 M NaOH, and 0.5 M [Fe(III)(TEA)] in 5 M NaOH, measured with an Ostwald viscometer.	18
Figure 1.8. Plot of i_{ss} vs. increasing concentrations of [Fe(III)(TEA)] in 5 M NaOH _(aq) , ligand-to-metal ratios of 1:1.	20
Figure 1.9. Schematic diagram of an SECM experiment under positive feedback conditions.	23
Figure 1.10. Determination of k^0 for [Fe(III)(TEA)] reduction to [Fe(II)(TEA)] in 5 M NaOH.....	24
Figure 1.11. Determination of k^0 for [Fe(III)(L)] and [Co(II)(L)] in 5 M NaOH.	25
Figure 1.12. Plot of abundance on Earth's crust vs. price of chloride salt for all first row transition metals.	26

Figure 2.1. Kinetic zone diagram for a first-order EC reaction, calculated with the time parameter for cyclic voltammetry.	32
Figure 2.2. Schematic diagram of the e-SECM set-up.	34
Figure 2.3. Schematic representation of positive feedback mode.	40
Figure 2.4. CVs recorded at the SECM tip and substrate electrodes.	41
Figure 2.5. Bulk electrolysis of 1.2 mM FcMeOH in 0.1 M NaNO ₃ at a GC substrate (2 mm dia.).	42
Figure 2.6. Steady state CVs recorded at a GC tip ($a = 5 \mu\text{m}$) after oxidation of 1.2 mM FcMeOH.	43
Figure 2.7. Experimental e-SECM current transients recorded for the reduction of 1.3 mM FcMeOH ⁺	44
Figure 2.8. CVs of 2 mm diameter glassy carbon electrode, 10 mM [Fe(III)(TEA)], and 10 mM [Co(II)(TEA)] in aqueous 5 M NaOH.	47
Figure 3.1. Solid state structure of the [(Fe(TEA)) ₂ (μ -O)] ²⁻ dinuclear anion.	58
Figure 3.2. CVs of 20 mM Fe(III)-TEA in 5 M NaOH.	59
Figure 3.3. Optimized geometry of [Fe(III)(TEA)(OH)] ⁻ from DFT calculations.	60
Figure 3.4. Current-time curves from 6 consecutive exhaustive electrolyses experiments.	62
Figure 3.5. CVs recorded at a GC tip ($a = 5 \mu\text{m}$) in 3 different solutions.	65
Figure 3.6. Binding isotherms constructed at a constant concentration of ligand, [TEA] = 1 mM.	68
Figure 4.1. Cyclic voltammograms of 20 mM [Fe(TEA)(OH)] ⁻ , and 20 mM [Co(mTEA)(H ₂ O)] in aqueous 5 M NaOH.	79

Figure 4.2. Plots of charge (coulombs) vs. electrolysis time.....	81
Figure 4.3. Plots of number of coulombs vs. half-cycle number extracted from constant-current electrolyses.....	84
Figure 4.4. Charge-discharge cycling curves of the Co/Fe alkaline RFB.	85
Figure 4.5. Plots of efficiency, η , vs. cycle number recorded from the constant-current analysis.	86
Figure 5.1. Electrochemical cells used in this work.	94
Figure 5.2. Current-time curves of solutions containing 7 μ moles of O ₂ in 5 M NaOH recorded with a GC UME ($a = 5 \mu\text{m}$).....	96
Figure 5.3. Coulometric titration of a solution containing 7 μ moles of O ₂ in 5 M NaOH	98
Figure 6.1. Cyclic voltammograms of Ir UMEs ($a = 62.5 \mu\text{m}$) in 2 M NaOH.....	105
Figure 6.2. Description of the surface interrogation technique.	106
Figure 6.3. Cyclic voltammograms at a glassy carbon tip ($a = 50 \mu\text{m}$) in 5 mM Fe(III)-TEA + 2 M NaOH solution, during a titration experiment.	107
Figure 6.4. Plot of charge density vs. E_{subs} constructed from interrogation transients.....	112
Figure 6.5. Interrogation transients obtained in the range $E_{\text{subs}} = -1.00 \text{ V} -$ 0.00 V.	116
Figure 6.6. Numerical fit of experimental voltammograms.	117
Figure 6.7. Interrogation transients obtained after modification of the potential step condition from $t_{\text{step}} = 70 \text{ s}$ to $t_{\text{step}} = 50 \text{ s}$	118

Figure 6.8. Theoretical fit of the interrogation transient obtained after holding the potential of the Ir substrate at $E_{\text{subs}} = 0.25$ V	120
Figure A1. Solid state structure of the anion $[\text{Co(II)(TEA)(H}_2\text{O)}]^-$ determined with crystals grown from 5 M $\text{NaOH}_{(\text{aq})}$	137
Figure A2. Components of the cell set-up.....	138
Figure A3. Calibration of the numerical model of e-SECM with the Cottrell equation.	141
Figure A4. UV-Vis spectra of the various complexes studied in this work.	142
Figure A5. Spectral analysis of 0.5 M $[\text{Fe(TEA)(OH)}]^-$ in 5 M NaOH	143
Figure A6. CV of 250 mM Fe(III)-TEA in 5 M NaOH at a mercury film electrode.....	143
Figure A7. UV-Vis spectra of various solutions.	145
Figure A8. Schematic diagram of the flow cell used in this study.....	145
Figure A9. Preliminary solid state structure of the anion $[\text{Co(II)(mTEA)(H}_2\text{O)}]^-$ determined with crystals grown from 5 M $\text{NaOH}_{(\text{aq})}$	146
Figure A10. Cyclic voltammograms of 20 mM Fe(III)-TEA in 5 M NaOH	147
Figure A11. Cyclic voltammograms of 20 mM Co(II)-mTEA in 5 M NaOH	147
Figure A12. Calibration of electrolysis cell.....	148
Figure A13. Schematic diagram of the optimized flow battery conditions.....	149
Figure A14. UV-Vis spectra of 0.2 M Fe(II)-TEA and Fe(III)-TEA in 5 M NaOH	150
Figure A15. CV of a solution containing 200 μM O_2 in 5 M NaOH	152
Figure A16. Linear sweep voltammogram for GC electrode ($A = 1$ cm^2) in three different solutions.	152

Figure A17. CVs of 100 μm <i>dia.</i> glassy carbon electrode in 2 M NaOH.	154
Figure A18. Screen shots of CHI software “macro command”.	154
Figure A19. Interrogation of hydrogen adsorbed on Ir.	155

PART 1

Chapter 1. Electrochemical Energy Storage, and the Chemistry Behind the Alkaline Redox Flow Battery

1.1. INTRODUCTION

Utility-scale electrical energy storage (EES) is the conversion of electricity from a power grid into different forms of energy, such as chemical energy, that can be stored for later use. This process is important to the utilities industry because it decouples the production of electricity from its consumption by end users,¹ offering flexibility to the model of instantaneous transmission that is currently used.² Different EES technologies are competing to have a share of the global market of energy management,³⁻⁵ a market forecast to reach 300 GW in size over the next 10 to 20 years.^{6,7} This market includes applications like renewable energy integration, contingency services, power reliability, and time-shifting.^{2,9} Among the different EES technologies available for energy management, redox flow batteries (RFBs)¹⁰⁻¹² are considered excellent candidates because they offer durability for large numbers of charge/discharge cycles, high round-trip efficiency, the ability to respond rapidly to changes in load or input, and reasonable capital costs.¹³⁻¹⁵ Figure 1.1A shows a real-life example of a megawatt-hour storage RFB installed in California by EnerVault in 2014.¹⁶ Figure 1.1B presents a schematic diagram of the different components that make a RFB.

A RFB is a type of rechargeable battery in which the chemical species that participate in the electrode reactions are in solution. Such redox couples are stored in independent vessels (beige tanks in Figure 1.1A) that correspond to the two half-cells of the battery, the anolyte and catholyte depicted in Figure 1.1B. The cell is charged with

the input of electrical energy from the grid, while the solutions are pumped through two independent “zero-gap” chambers containing inert electrodes (where the half-cell reactions take place). A physical barrier, such as an ion exchange membrane, separates the two independent chambers. During discharge, electricity is produced as the stored

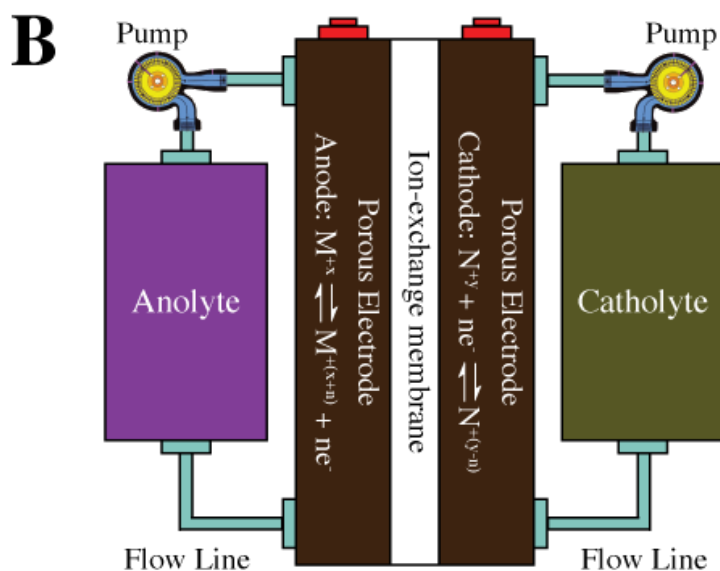


Figure 1.1. **A.** Megawatt-hour electrical energy storage plant installed in California by EnerVault in 2014. Courtesy EnerVault. The red arrow indicates the location of the cell stack. **B.** Schematic diagram of a discharged redox flow battery with a single cell.

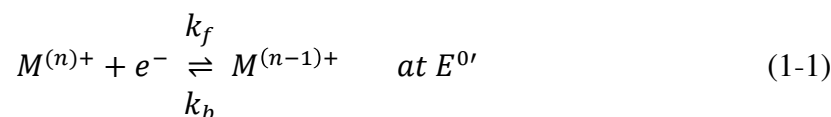
reactants flow back into the cell and react spontaneously at the electrodes. Importantly, the energy storage capacity in a RFB is decoupled from the available power because the energy is related to the electrolyte volume, mass, and concentration (amount of liquid electrolyte), and the power is related to the number of cells included in the battery stack (red arrow in Figure 1.1A) and their current output. This feature is important because it makes the technology easily scalable for a variety of utility-scale grid applications.

State of the art RFBs (*e.g.*, the vanadium RFB) are based on acidic electrolytes.¹⁷ Such technologies often suffer capacity fading due to membrane crossover and the occurrence of undesired secondary reactions during battery cycling (*e.g.*, precipitation, evolution of H₂ and Cl₂ gases).¹³ Acidic electrolytes have a high conductance, $G_{\max} = 825$ mS cm⁻¹ for 3 M H₂SO_{4(aq)},¹⁸ but tend to be corrosive to the cell components, which translates into high operational and maintenance costs.¹⁹ In contrast, alkaline electrolytes such as NaOH have lower conductance, $G_{\max} = 410$ mS cm⁻¹ for 3.7 M NaOH_(aq),¹⁸ but are less corrosive. Alkaline electrolytes employing transition metals generally require the use of coordination compounds as redox species to prevent precipitation of the hydroxides or hydrous oxides. The net charge on these ions can be tailored by ligand selection to minimize membrane crossover with a cation exchange membrane. Moreover, different ligands can be used to tune the electrode potential of the half-cells to optimize the voltage of the battery.²⁰

This work discusses theoretical and experimental aspects relevant to the development of an alkaline RFB (a-RFB), *i.e.* 5 M NaOH_(aq) electrolyte that uses coordination compounds of Fe and Co to store energy. Furthermore, a complete description of the experimental methodology developed to create the a-RFB, from chemical fundamentals to a benchtop prototype, is presented.

1.2. THERMODYNAMIC AND KINETIC CONSIDERATIONS

Any given redox couple intended for use in RFB technology must meet specific thermodynamic and economic criteria. For a couple of the form:

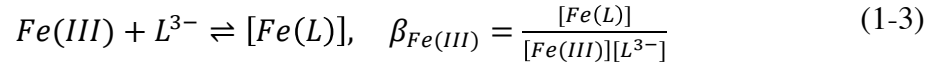
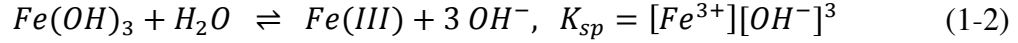


such criteria includes the following six requirements:²⁰ (1) high solubility, S , of both forms of the redox couple: $S_{M^{(n)+}} \approx S_{M^{(n-1)+}} \geq 0.5 \text{ M}$; (2) chemical stability of both $M^{(n)+}$ and $M^{(n-1)+}$ species during generation and storage, for $t \rightarrow \infty$; (3) the formal redox potentials, $E^{0'}$, should be at the extremes of the potential window available in water, approximately 1.23 V; (4) large standard rate constants, $k^0 > 1 \times 10^{-2} \text{ cm s}^{-1}$ (k^0 is the rate when $k_f = k_b$); (5) large diffusion coefficients: $D_{M^{(n)+}} \approx D_{M^{(n-1)+}} > 1 \times 10^{-6} \text{ cm}^2 \text{ s}^{-1}$; and (6) high-value market properties such as low toxicity and cost, and natural abundance.¹³ Finding redox couples based on the coordination chemistry of transition metal ions in 5 M $\text{NaOH}_{(\text{aq})}$ that match these criteria is a challenging endeavor. The following subsections discuss why the problem is intrinsically difficult as well as present thermodynamic approaches to solve it.

Solubility of Transition Metal Ions in 5 M NaOH

Ions of transition metals generally do not dissolve in base but rather precipitate as insoluble hydroxides or hydrous oxides. The molar solubility of a metal ion in base can be estimated from the magnitude of the solubility product, K_{sp} , of its corresponding hydroxide. For example, the solution concentration of Fe(III) calculated from²¹ $K_{\text{sp}} = 6.3 \times 10^{-38}$ of $\text{Fe}(\text{OH})_3$, at $[\text{OH}^-] = 5 \text{ M}$, is $[\text{Fe}(\text{III})] = 5.0 \times 10^{-40} \text{ M}$ (a concentration of Fe(III) below attomolar, or less than one molecule per liter). For a coordination compound to be solvated in strong base at high concentrations, a strong interaction must exist between the metal ion and an organic ligand so that the stability constant of the complex formed, β , is

considerably larger than the K_{sp} of the metal hydroxide ($\beta \gg K_{sp}$). This is expressed analytically for Fe(III) in equations (1-2) – (1-4):



$$[Fe(III)] = \frac{[Fe(L)]}{\beta_{Fe(III)}[L^{3-}]} < \frac{K_{sp}}{[OH^-]^3} \quad (1-4)$$

Equation (1-2) is the solubility product of $Fe(OH)_3$, and equation (1-3) is the complexation equilibrium of Fe(III) with a generic ligand L^{3-} . Equation (1-4) indicates that $\beta_{[Fe(III)(L)]}$ should be large enough so that $[Fe(III)] < K_{sp} / [OH^-]^3$, in the order of $\log \beta_{[Fe(III)(L)]} > 39$ for $[OH^-] = 5 \text{ M}$, $[L^{3-}] = 1 \text{ M}$, and $[Fe(III)(L)] = 1 \text{ M}$. A convenient point of reference for $\log \beta_{[Fe(III)(L)]} > 39$ is the value corresponding to the complex of iron with ethylenediaminetetraacetic acid (EDTA), $[Fe(EDTA)]^-$, one of the strongest stability constants measured in aqueous chemistry for a hexadentate ligand, with a magnitude of $\log \beta_{[Fe(III)(EDTA)]} = 25.1$ at ionic strength $\mu = 0.1$.²² The comparison gives $\beta_{[Fe(III)(L)]} \gg \beta_{[Fe(III)(EDTA)]}$, pointing out the need for ligands with binding affinities for Fe(III) much stronger than EDTA. Ligands with such high affinities do exist, and generally have amines and hydroxyl groups in their structures. The organic ligands identified in this work will be referred to as “amino-alcohols”.

Relationship Between Formal Potential and Stability Constants

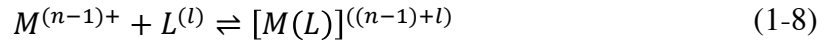
The redox potential of the couple in equation (1-1) is expressed by the Nernst relationship as:

$$E = E^0 - \frac{RT}{nF} \ln \frac{\gamma_{M^{(n-1)+}} [M^{(n-1)+}]}{\gamma_{M^{(n)+}} [M^{(n)+}]} \quad (1-5)$$

where E^0 is the standard redox potential, R is the gas constant, T is the temperature in Kelvin, n is the number of electrons transferred in the reaction, and $\gamma_{M^{(n)+}}$ and $\gamma_{M^{(n-1)+}}$ are the activity coefficients of species $M^{(n)+}$ and $M^{(n-1)+}$, respectively. As established previously, complexation equilibria must exist to solvate $M^{(n)+}$ and $M^{(n-1)+}$ in strong base. The equations describing such complexation equilibria in the presence of a generic ligand L are:



$$\beta_{M^{(n)+}} = \frac{[M(L)]^{(n+l)}}{[M^{(n)+}][L^{(l)}]} \quad (1-7)$$



$$\beta_{M^{(n-1)+}} = \frac{[M(L)]^{((n-1)+l)}}{[M^{(n-1)+}][L^{(l)}]} \quad (1-9)$$

Rearranging relations (1-7) and (1-9) to solve for $[M^{(n)+}]$ and $[M^{(n-1)+}]$, substituting into equation (1-5), and taking $[M(L)]^{(n+l)} = [M(L)]^{((n-1)+l)}$ gives:

$$E^{0'} = E^0 - \frac{RT}{nF} \ln \frac{\gamma_{[M(L)]^{((n-1)+l)}}}{\gamma_{[M(L)]^{(n+l)}}} - \frac{RT}{nF} \ln \frac{\beta_{M^{(n-1)+}}}{\beta_{M^{(n)+}}} \quad (1-10)$$

where $\gamma_{[M(L)]^{(n+l)}}$ and $\gamma_{[M(L)]^{((n-1)+l)}}$ are the activity coefficients of the complexed species, and $\beta_{M^{(n)+}}$ and $\beta_{M^{(n-1)+}}$ are the corresponding stability constants. Equation (1-10) indicates that the formal redox potential of a ligand-modified couple equals the standard potential for

the couple in the absence of complexation, minus a term having the ratio of the activity coefficients, minus a term having the ratio of the stability constants corresponding to the two complexed species involved in the electron transfer reaction. Therefore, from the ratio $\beta_{M(n-1)+} / \beta_{M(n)+}$ one can predict the experimental redox potential of a ligand-modified couple if the magnitude of the stability constant is known, assuming $\gamma_{[M(L)](n+1)} / \gamma_{[M(L)](n-1)+l} = 1$. More importantly, equation (1-10) indicates that the formal potential of a couple can be tuned by careful selection of the ligand to suit particular application needs, such as the case of the alkaline RFB. Table 1.1 shows the application of this principle to the Fe(III) / Fe(II) couple. The formal potential of Fe(III) / Fe(II) is tuned from -1.04 V with triethanolamine to 1.09 V with 5-nitro-o-phenanthroline, as shown in Table 1.1. Further, the calculated and experimental formal potentials are in good agreement, within 0.1 V

Table 1.1. Comparison between experimental, $E^{0'}_{\text{exp.}}$, and calculated, $E^{0'}_{\text{calc.}}$, formal redox potentials of ligand – modified couples.

Ligand, (L)	$\log \beta_{\text{Fe(III)}}$	$\log \beta_{\text{Fe(II)}}$	μ^a	$E^{0'}_{\text{calc.}}, \text{V}^b$	$E^{0'}_{\text{exp.}}, \text{V}^c$	Ref.
(5-nitro-o-phenanthroline) ₃	7.4 ^d	17.4	0.1	1.13	1.09	[22, 20]
(o-phenanthroline)	14	21 ± 1	0.1	0.95	0.84	[22, 20]
(H ₂ O) ₆	-	-	-	-	0.55	[23]
(CN) ₆ ⁶⁻	44 ± 3	35 ± 10	0.1	0.06	0.13	[22, 23]
(EDTA)	25	14 ± 10	0.1	-0.09	-0.11	[22]
(triethanolamine)	31.1 ± 0.3	31.1 ± 0.3	5	-1.07	-1.04	[*]

^a Ionic strength used during measurement of stability constant. *pH* is not reported in this table.

^b Values calculated with the Nernst equation and experimental β 's. Potentials are reported vs. Ag/AgCl.

^c Redox potentials determined by voltammetry.

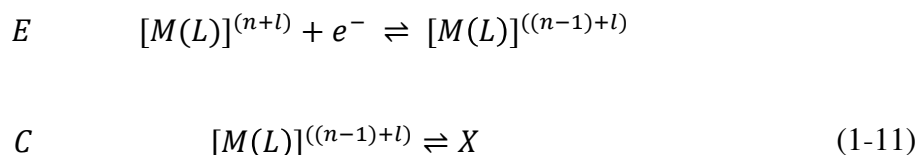
^d Only value available, corresponding to [M(L)], and not [M(L)₃].

* Determined in this work.

error. For the development of an a-RFB, the redox potentials of the selected ligand-modified couples must be at the extremes of the potential window available in 5 M NaOH_(aq), approximately from 0.1 V to -1.2 V vs. Ag/AgCl. The iron complexes reported in Table 1.1 only exist at pH = 0-10, except for the complex with triethanolamine that forms at pH > 14, and cannot be used in an a-RFB. In this study, combinations of 33 ligands, 10 transition metal ions, and 3 anions were screened to find the right couples for the alkaline RFB. Such results are discussed in following sections.

Homogeneous Kinetics Coupled to the Electron Transfer Step

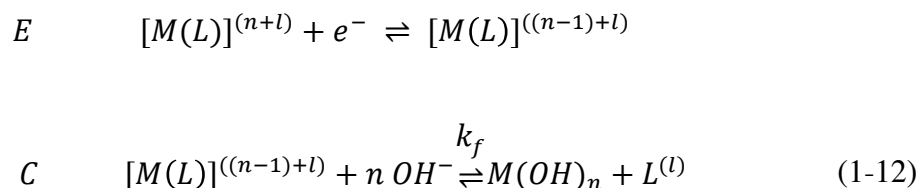
Perhaps the most challenging aspect of developing an a-RFB is to find ligand-supported couples that do not undergo homogeneous reactions after the electron transfer step. In fact, most of the couples evaluated in this work undergo EC reactions. This section reviews the general reaction scheme of EC processes. Using the same notation as in equations (1-6) and (1-8), the reaction scheme of an EC process can be written as follows:²⁴



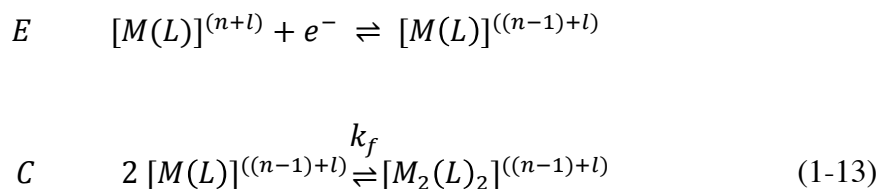
In an EC reaction the product of the electron transfer reaction, $[M(L)]^{((n-1)+l)}$, reacts with the electrolyte, itself, or other chemical species to produce a new species, X, that is not electroactive at potentials where the reduction of $[M(L)]^{(n+l)}$ occurs. In particular, two cases are relevant to this work:

Case 1. The binding constant for $[M(L)]^{((n-1)+l)}$ is significantly smaller than the binding constant for $[M(L)]^{(n+l)}$, $\beta_{M(n-1)+} \ll \beta_{M(n)+}$, therefore the product of

the electron transfer reaction leaves the ligand and reacts with base to precipitate as a hydrous oxide.



Case 2. The product of the electrode process reacts with itself to form a higher-order species (*e.g.*, dimer). The new species may or may not be electroactive at the potential where the first E step occurs.



In both cases, the magnitude of k_f is a measurable parameter that reflects how stable the product of the E step is. Different electroanalytical techniques have specific time ranges that can be accessed to measure k_f . Table 1.2 presents the dimensionless time parameter, λ , that corresponds to different electroanalytical techniques, and time ranges accessible by such techniques. Scanning electrochemical microscopy, steady-state voltammetry, and coulometry were used in this work to evaluate k_f for relevant redox systems.

1.3. COMPLEXES OF FE AND CO IN 5 M NaOH

The search for coordination compounds with the properties described in section 1.2 was initially carried out with a trial and error approach. Tables A1 – A3 in Appendix

A contain a list of selected ligands, transition metal ions, and anions explored in this work.

The ligand triethanolamine (TEA) was found to successfully form soluble complexes of all first row transition metal ions (as well as other transition metals) in $[\text{OH}] = 5 \text{ M}$. The structure of TEA is shown in Figure 1.2. The first reports of TEA being used as a complexing agent in conjunction with polarography date back to 1944 and 1946.^{25, 26} Such manuscripts reported the use of TEA for the polarographic determination of iron and cobalt concentrations in magnetic alloys. Other posterior reports have qualitatively studied the characteristics of the polarographic and voltammetric waves of Fe(III)-TEA as a function of the concentration of different ethanolamines and as a function of pH ,²⁷⁻²⁹ but no previous work has reported the electrochemistry, chemical structures or coordination geometries of the complexes in 5 M NaOH.

Table 1.2. Approximate time windows accessible for different electroanalytical techniques.^a

Technique	Time Parameter, λ	Range	Time Accessible
Rotating disc electrode	$1/\omega$	$\omega = 30 - 1000 \text{ s}^{-1}$	$10^{-3} - 0.03 \text{ s}$
Scanning electrochemical microscopy	d^2/D	$d = 0.01 - 10 \text{ }\mu\text{m}$	$10^{-7} - 0.1 \text{ s}$
Ultramicroelectrode at steady state	r^2/D	$r = 0.1 - 12.5 \text{ }\mu\text{m}$	$10^{-5} - 1 \text{ s}$
Voltammetry	$RT/F\nu$	$\nu = 0.01 - 10^5 \text{ V s}^{-1}$	$10^{-6} - 1 \text{ s}$
Chronoamperometry	τ	$\tau = 10^{-6} - 10 \text{ s}$	$10^{-6} - 10 \text{ s}$
Coulometry	t	$t \geq 100$	$\geq 100 \text{ s}$

^a Table extracted and edited from reference [24].

Definitions: ω , angular frequency; d , distance from substrate; D , diffusion coefficient; r , radius of the electrode; ν , scan rate; τ , time of forward step; and t , electrolysis time.

Here, a systematic study was carried out with Co(II), Fe(III), and different TEA-derived molecules to assess which functional groups in the structure of TEA participate in the coordinative bonding with the two metal ions in 5 M NaOH. Molecular structures of the ligands tested are shown in Figure 1.2. For the case of Co(II), all the ligands formed stable complexes, except for TEOH, when prepared in stoichiometric 1:1 metal-to-ligand ratios. The structures presented in Figure 1.2 help explain why TEOH did not coordinate to Co(II). While DEA, EDEA, TEA, BYCN and mTEA have a central coordinating amine group, TEOH does not. This indicates the importance of nitrogen π -bonding in the complexes formed.

The electrochemistry of the [Co(II)(L)] complexes was studied by cyclic voltammetry (CV). Figure 1.3 presents CVs recorded with a glassy carbon (GC) electrode in 10 mM solutions of the different compounds. The first point to note in Figure 1.3 is the absence of a reverse wave in CVs of the coordination compounds made with DEA and EDEA. This behavior was typically observed in complexes where $\beta_{\text{Co(III)}} \ll \beta_{\text{Co(II)}}$ (Case 1, Section 1.2). After [Co(II)(L)] is oxidized to [Co(III)(L)], the product reacts with base to

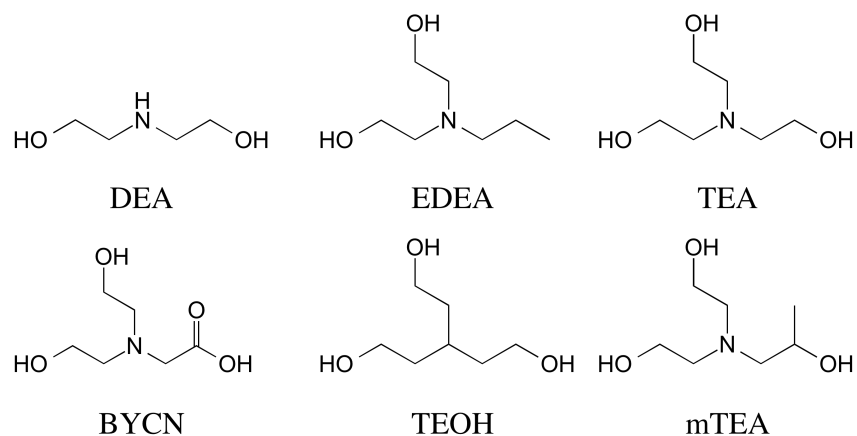


Figure 1.2. Molecular structures of some of the ligands used in this work. DEA: diethanolamine; EDEA: N-ethyldiethanolamine; TEA: triethanolamine; BYCN: bicine; TEOH: triethanolmethane; mTEA: diethanolisopropanolamine.

free the ligand molecule and precipitate as $\text{Co}(\text{OH})_3$. Such a homogeneous ligand-exchange reaction was assessed by exhaustive electrolysis experiments where the appearance of a precipitate was observed at the end of the electrolysis. A second important observation from the CVs shown in Figure 1.3 is the appearance of the reverse wave in complexes made with ligands that contain the TEA backbone in their structure, BYCN and mTEA. This is an indication that the tertiary amine and the three hydroxyls coordinate to $\text{Co}(\text{II})$, therefore TEA, BYCN and mTEA act as tetradentate ligands in 5 M NaOH. This point was later confirmed by X-ray diffraction (XRD) analysis of single crystals of $\text{Co}(\text{II})$ -TEA, with structure $[\text{Co}(\text{II})(\text{TEA})(\text{H}_2\text{O})]^-$, see Figure A1 in Appendix A. Finally, the kinetics of the electron transfer reaction improve when electron donating substituents are present in the TEA backbone, as seen when comparing the CVs of BYCN, TEA and mTEA.

In the case of $\text{Fe}(\text{III})$, only two ligands formed complexes in 5 M NaOH: TEA

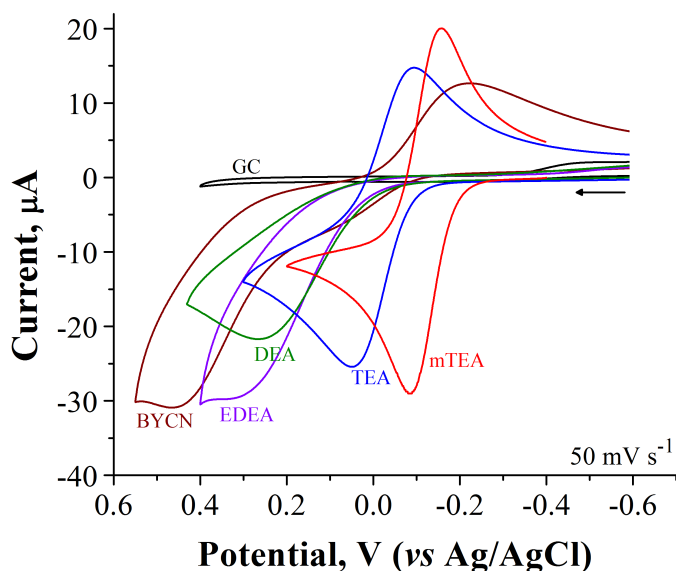


Figure 1.3. CVs of 10 mM $[\text{Co}(\text{II})(\text{L})]$ complexes in 5 M NaOH, recorded at a GC electrode (2 mm dia.). The names of the ligands are written next to the corresponding voltammograms, using the definitions in Figure 1.2. $v = 50 \text{ mV s}^{-1}$, O_2 free solutions. Black arrow shows the direction of the first potential sweep.

and mTEA. Such a result was expected because stronger stability constants are needed to keep Fe(III) solvated in base, since $K_{\text{sp,Fe(III)}} = 10^{-21} \cdot K_{\text{sp,Co(II)}}$. Further, the fact that only TEA and mTEA coordinated to Fe^{3+} indicates that they also act as tetradentate ligands, with strong stability constants presumably due to the chelate effect. This point is demonstrated with experimental evidence in Chapter 3. The CVs of both ligands showed electrochemically reversible redox processes at very similar potentials, shown in Figure 1.4. The general observations made in this section set the basis for the more exhaustive analysis presented in the rest of this chapter and the chapters that follow. The general synthesis for the coordination compounds is described next.

1.4. SYNTHESIS OF COORDINATION COMPOUNDS

All the coordination compounds used in this work were synthesized by the same procedure. Milli-Q water ($\rho \approx 18 \text{ M}\Omega \cdot \text{cm}$) was always used unless noted otherwise.

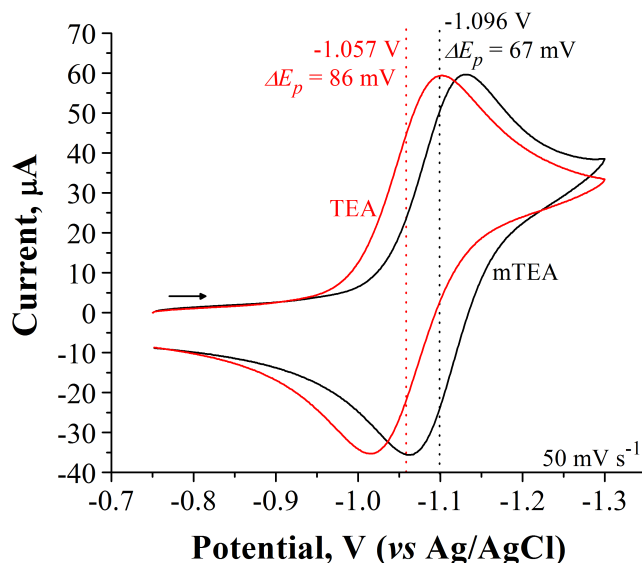


Figure 1.4. CVs of 10 mM $[\text{Fe(III)(L)}]$ complexes in 5 M NaOH, recorded at a GC electrode (2 mm dia.). The names of the ligands are written next to the corresponding voltammograms, using the definitions in Figure 1.2. $v = 50 \text{ mV s}^{-1}$, O_2 free solutions. Black arrow shows the direction of the first potential sweep.

Sodium hydroxide pellets, technical grade, were purchased from Fisher Scientific (Fair Lawn, New Jersey) and used as received. Salts of metal ions and ligands were purchased from different sources as noted within each chapter of this dissertation. A detailed example of the synthesis procedure for a 40.0 mL solution of 50 mM Fe(III)-TEA complex in 5 M NaOH is provided here. Amounts of reagents were scaled as needed for the different concentrations used.

A round bottom flask was filled with deionized water (20.0 mL) and bubbled with argon. After bubbling for 5 min, 2.0×10^{-3} moles of $\text{FeCl}_3 \cdot 6\text{H}_2\text{O}$ were added with stirring. To this solution, 2.0×10^{-3} moles of triethanolamine were added dropwise, also with stirring. In a separate container, NaOH pellets (0.25 moles) were dissolved in 10 mL of deionized water with stirring. After the NaOH dissolved, the container was placed in a water bath to cool at 25° C. This NaOH solution was added dropwise to the M^{n+} + ligand solutions. Over the course of the addition, a gel-like material formed that dissolved back into solution upon addition of all the NaOH. The volume of the solution was adjusted to

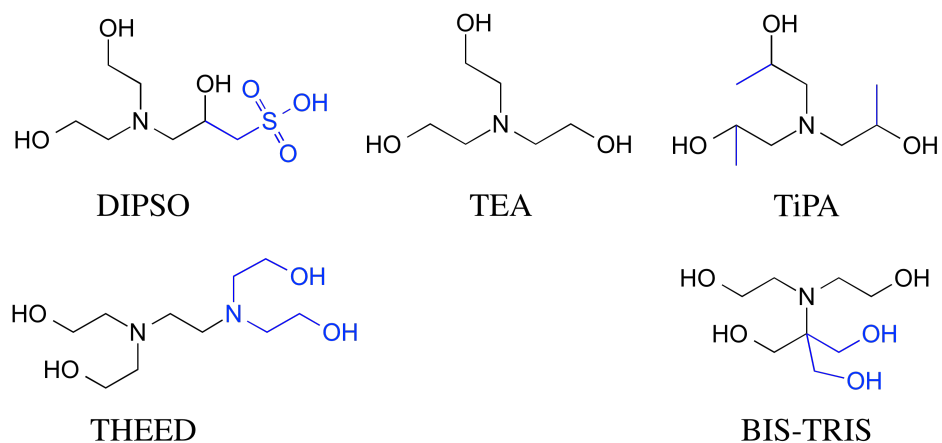


Figure 1.5. Molecular structures of the ligands used to tune formal potentials. TEA: triethanolamine; TiPA: triisopropanolamine; BIS-TRIS: 2,2-Bis(hydroxymethyl)-2,2',2''-nitrilotriethanol; DIPSO: 3-(N,N-Bis[2-hydroxyethyl]amino)-2-hydroxypropanesulfonic acid; THEED: N,N,N',N'-Tetrakis(2-hydroxyethyl)ethylenediamine. Functional groups selected for inductive effects are shown in blue.

40.0 mL upon completion of the synthesis reaction. All reactions yield 95+% product (complexes) as determined by steady state CVs. The ligand-to-metal stoichiometry of all reactions was 1:1; however, some ligands were added in excess to favor the formation of the complexes at high concentrations. Complexes of Co(III) were produced by bulk electrolysis from solutions containing the corresponding complexes of Co(II). Complexes of Fe(II) were prepared from hydrated ferrous salts.

1.5. EXPERIMENTAL TUNING OF FORMAL POTENTIALS

The formal potentials of ligand-modified redox couples are a function of the ratio of the stability constants for the oxidized and reduced forms, as stated in equation (1-10). Further, the discussion in section 1.3 indicates that only ligands containing the TEA backbone are able to keep Co(II) and Fe(III) solvated in 5 M NaOH. Taking those observations into consideration, experiments were carried out to tune the reduction potentials of the metal ions to the extremes of the potential window available in 5 M NaOH_(aq). The ligands explored are shown in Figure 1.5. CVs were recorded in solutions of each coordination compound, and the formal potentials were extracted from the CVs as the average of the anodic and cathodic peak potentials. The CVs corresponding to [Fe(III)(L)], shown in Figure 1.6A, show a clear shift of the formal potential to more negative values when electron donating groups are attached to the TEA backbone, as is the case with TiPA and BIS-TRIS (assuming the coordination geometries are the same). The CV corresponding to DIPSO gave the same formal potential as TEA and is not shown in Figure 1.6A. The ligand THEED presented the most positive formal potential, 100 mV more positive than the one obtained with TEA, but is considered a special case because it can act as a hexadentate ligand; therefore, the inductive effects are not readily predictable when compared to the other ligands. Overall the formal potential of the

couple shifted from -0.95 to -1.11 V, shown in Table 1.3. An important point is that the formal potential of the coordination compound made with BIS-TRIS, -1.11 V, is negative enough that the complex spontaneously catalyzes the homogeneous reduction of water when synthesized with Fe(II). Such a property, although interesting from a fundamental perspective, is not desirable for RFB applications and no further studies were carried out to explore the chemistry of such a reaction. Based on the previous observations, the complexes of Fe(III) with TEA and its methylated derivatives, mTEA and TiPA, were determined to be the best candidates for an alkaline RFB.

In the case of cobalt, the CVs showed only modest shifts in the reduction potentials, going from -0.05 with DIPSO to -0.13 with TiPA, shown in Figure 1.6B and Table 1.3. The complexes formed with BIS-TRIS and THEED presented irreversible electron transfer kinetics and are not shown in Figure 1.6B. The complexes made with the ligands DIPSO and TiPA produced faster electron transfer kinetics than the one made

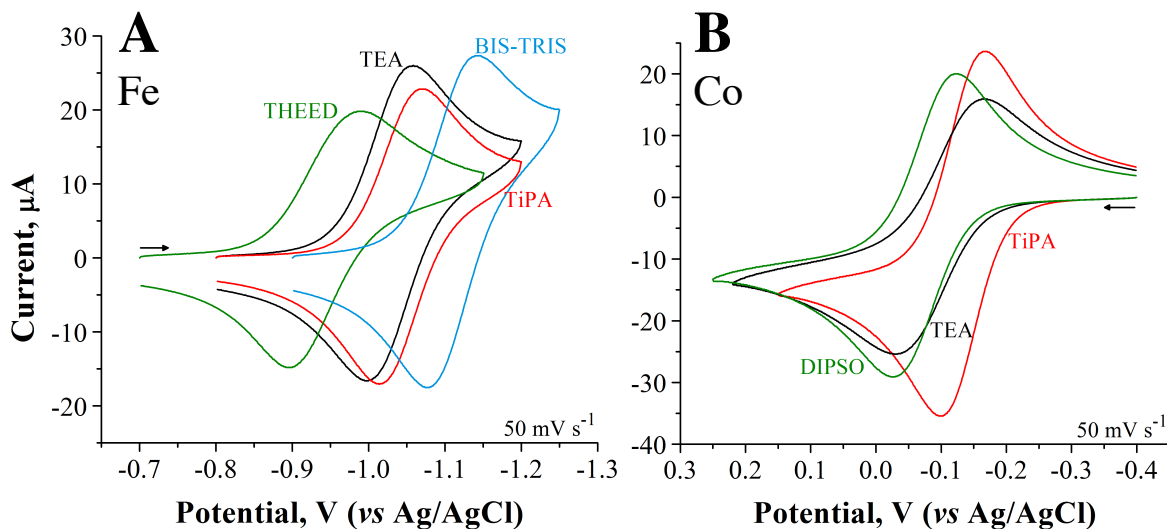


Figure 1.6. **A.** CVs of 10 mM [Fe(III)(L)] complexes in 5 M NaOH. **B.** CVs of 10 mM [Co(II)(L)] complexes in 5 M NaOH. The names of the ligands are written next to the corresponding voltammograms, using the definitions in Figure 1.4. $\nu = 50 \text{ mV s}^{-1}$, O_2 free solutions. Black arrow shows the direction of the first potential sweep. 2 mm dia. GC electrode.

Table 1.3. Standard potentials, formal potentials of [Co(II)/(III)(L)] and [Fe(III)/(II)(L)] in 5 M NaOH, and $\Delta E = E^{0'} - E^0$.

Redox Couple	Ligand	E^0, V^a	$E^{0'}, \text{V}^a$	$\Delta E, \text{V}^a$
Co ²⁺ /Co ³⁺	TiPA ^b	1.70	-0.13	1.83
	TEA		-0.1	1.80
	DIPSO		-0.05	1.75
Fe ³⁺ /Fe ²⁺	BIS-TRIS	0.55	-1.11	1.66
	TiPA		-1.08	1.63
	TEA		-1.05	1.60
	THEED		-0.95	1.50

^a Potentials reported vs. Ag/AgCl. ^b $E^{0'}$ with mTEA is the same as with TiPA.

with TEA, and were therefore selected as the best candidates for the a-RFB.

1.6. VISCOSITIES AND DENSITIES OF ELECTROLYTES

Viscosity is a physicochemical parameter relevant to RFBs because it affects the amount of energy invested in pumping the electrolyte through the cell stack at a certain rate. Therefore, high viscosity of the electrolyte has a negative effect in the overall efficiency of the energy storage process of a RFB. Viscosity is particularly important in this work because several of the ligands discussed herein are viscous liquids at room temperature ($\eta_{\text{H}_2\text{O}} = 1.002 \text{ cP}$ vs. $\eta_{\text{TEA}} = 810 \text{ cP}$ at 20° C).^{30,31} Experiments were carried out to measure the viscosity of 0.5 M solutions of [Co(II)(L)] and [Fe(III)(L)] in 5 M NaOH (ligand-to-metal ratios of 1:1), with an Ostwald³¹ viscometer. The viscometer measures the time it takes a known volume of a solution to flow through a fine capillary between two marks, at constant pressure. The equation to be considered is (1-14):

$$t = B \cdot \frac{\eta}{\rho} \quad (1-14)$$

where t is time, B the viscometer's constant, η the viscosity of the test solution, and ρ the density of the solution. The viscometer's constant was obtained by calibration of the instrument with water at different temperatures. The densities of the different solutions were measured in an analytical balance, by weighting the mass of droplets delivered to the balance, and dividing the mass obtained over the volume dispensed. The densities were: $\rho_{[\text{Fe(III)(TEA)}]} = 1.25 \text{ g L}^{-1}$ and $\rho_{[\text{Co(II)(mTEA)}]} = 1.24 \text{ g L}^{-1}$. In the viscometer, the average time of travel between the two marks for pure water was $t = 15 \text{ min}$, with 10 ms accuracy (an automated optical probe was used for the measurements).

The viscosities of water and solutions of $\text{NaOH}_{(\text{aq})}$ at different temperatures were obtained from references [31] and [32], respectively. The viscosities of the following two

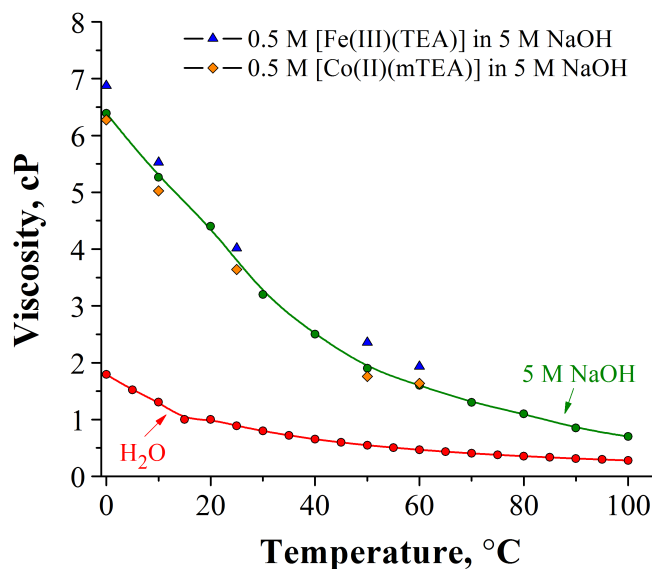


Figure 1.7. Viscosities of water, 5 M $\text{NaOH}_{(\text{aq})}$, 0.5 M $[\text{Fe(III)(TEA)}]$ in 5 M NaOH , and 0.5 M $[\text{Fe(III)(TEA)}]$ in 5 M NaOH , measured with an Ostwald viscometer. Shapes are experimental points, lines are segment unions. The data for H_2O and $\text{NaOH}_{(\text{aq})}$ were extracted from references [31] and [32].

systems were measured in this work: 1) 0.5 M [Co(II)(mTEA)] + 5 M NaOH, and 2) 0.5 M [Fe(III)(TEA)] + 5 M NaOH. Figure 1.7 shows plots of viscosity vs. temperature for the two solutions tested and the reference data. The viscosity of 5 M NaOH (green circles) is four times higher than the viscosity of pure water (red circles) at room temperature. The addition of ligand and metal ions at concentrations as high as 0.5 M did not change the viscosity of the electrolytes significantly with respect to the viscosity of 5 M NaOH_(aq), as shown in Figure 1.7. This result indicated that the viscosities of the catholyte and anolyte are mostly determined by the concentration of NaOH_(aq) used. Importantly, the viscosity of 5 M NaOH_(aq) at 25 °C, 4.5 cP, is similar to the viscosity of 10 M H₂SO₄ at 25 °C, 3.0 cP.³³ Therefore, the use of concentrated NaOH_(aq) as electrolyte in the a-RFB should not increase the amount of energy invested into pumping as compared to the acidic counterparts.

1.7. DIFFUSION COEFFICIENTS

The diffusion coefficients of [Fe(III)(TEA)] and [Co(II)(mTEA)] in 5 M NaOH_(aq) are inversely related to viscosity by the Stokes-Einstein equation.^{34,35} Therefore, D can be used as an electrochemical probe to indirectly observe changes in viscosity as a function of the concentration of [M(L)]. Experiments were carried out to measure changes in the viscosity of the electrolytes as a function of [M(L)] concentration, with particular focus on two cases: 1) The complexes were synthesized at increasing concentrations with ligand-to-metal ratios of 1:2; and 2) The complexes were synthesized at increasing concentrations with [L] = 1 M. Plots of i_{ss} vs. concentration were constructed by measuring the steady-state current in chronoamperometry at an ultramicroelectrode (UME), with $i_{ss} = 4nFDCa$, at the different concentrations C (a is the radius of the UME). In the absence of viscosity effects, the plots of i_{ss} vs. C were expected to present a straight

line with slope $m = 4nFDa$. When viscosity effects were present, D was expected to vary with viscosity in accordance with the Stokes-Einstein relationship, causing the plot of i_{ss} vs. C to deviate from linearity.

The determinations were carried out under mass transfer control. A mercury film UME was used to determine $D_{[\text{Fe(III)TEA}]}$, and a GC UME was used in the determination of $D_{[\text{Co(II)(mTEA)]}$. Figure 1.8 presents plots of i_{ss} vs. C obtained from the different cases

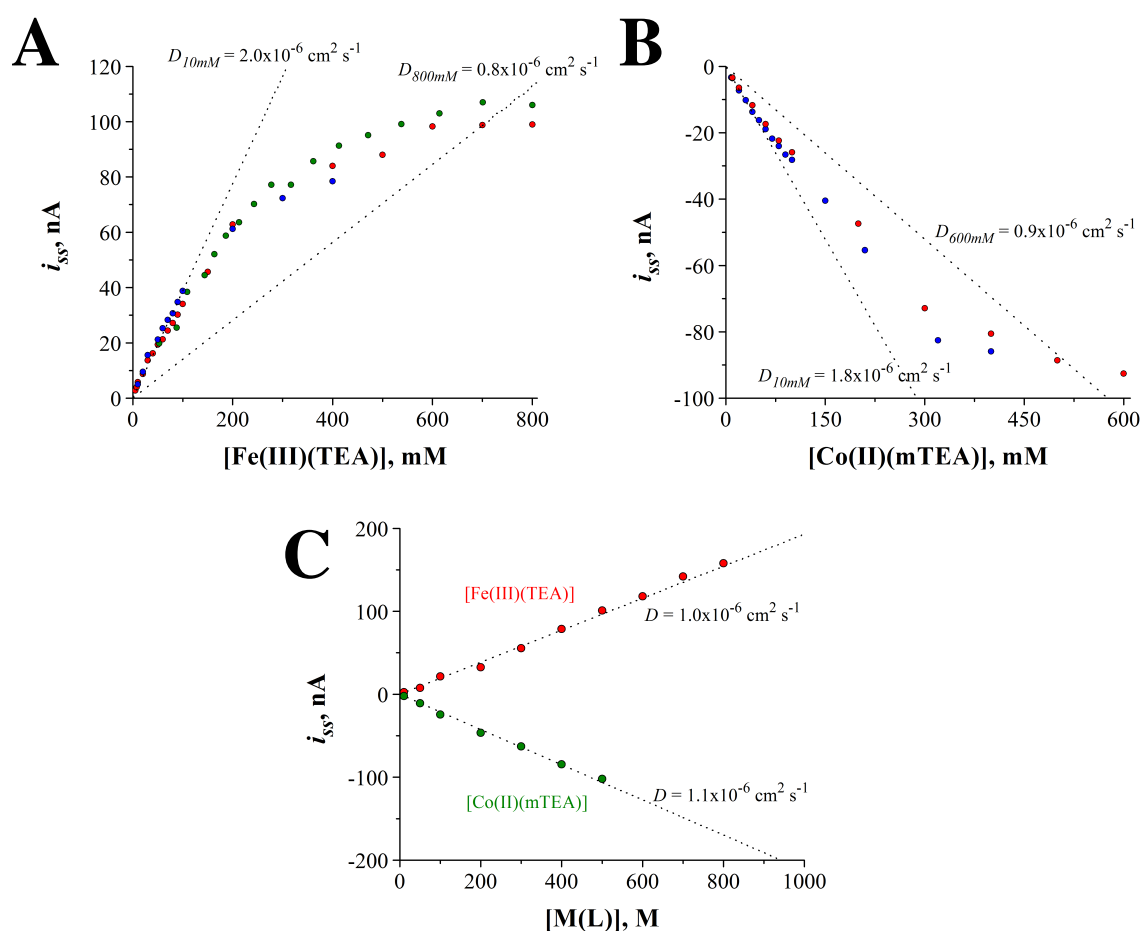


Figure 1.8. **A.** Case a) Plot of i_{ss} vs. increasing concentrations of $[\text{Fe(III)(TEA)}]$ in $5 \text{ M NaOH}_{(\text{aq})}$, ligand-to-metal ratios of 1:1. **B.** Case a) Plot of i_{ss} vs. increasing concentrations of $[\text{Co(II)(TEA)}]$ in $5 \text{ M NaOH}_{(\text{aq})}$, ligand-to-metal ratios of 1:1. Colored circles represent different data sets. **C.** Case b) Plot of i_{ss} vs. increasing concentrations of $[\text{M(L)}]$ in $5 \text{ M NaOH}_{(\text{aq})}$ at a fixed concentration of $[\text{L}] = 1 \text{ M}$.

considered.

In case 1), i_{ss} followed a straight line only at concentrations $[\text{Fe(III)(L)}] < 160$ mM, shown in Figure 1.8A, and $[\text{Co(II)(mTEA)}] < 150$ mM, shown in Figure 1.8B. When the complexes were synthesized at concentrations > 160 mM, the plot of i_{ss} vs. C deviated from linearity because D decreased (*i.e.*, the viscosity increased). To quantify the magnitude of the change in D , the chronoamperometric method³⁶ was used to determine D at the highest and lowest concentrations shown in Figure 1.8A and Figure 1.8B. The chronoamperometric method allows the determination of D disregarding other experimental parameters such as n or C . The values determined were: for $[\text{Fe(III)(TEA)}]$, $D_{10\text{mM}} = 2.0 \times 10^{-6} \text{ cm}^2 \text{ s}^{-1}$ and $D_{800\text{mM}} = 0.8 \times 10^{-6} \text{ cm}^2 \text{ s}^{-1}$; and for $[\text{Co(II)(mTEA)}]$, $D_{10\text{mM}} = 1.8 \times 10^{-6} \text{ cm}^2 \text{ s}^{-1}$ and $D_{600\text{mM}} = 0.9 \times 10^{-6} \text{ cm}^2 \text{ s}^{-1}$. These measurements revealed a dependence of D on the concentration of the ligand, with $D_{600\text{mM}} \approx 0.5 D_{10\text{mM}}$ for both complexes. Such results were expected since the two solutions had different viscosities based on the amount of ligand added.

In case 2) the experiments were repeated with a fixed concentration of ligand, *i.e.* $[\text{TEA}]$ and $[\text{mTEA}] = 1 \text{ M}$. This time, the plots of i_{ss} vs C were straight lines proportional to $D_{(L)}$, shown in Figure 1.8C. The effects that viscosity has on D and i_{ss} are particularly important in voltammetry where mass transport is controlled by diffusion. In a RFB, the mass transfer rate is mainly controlled by hydrodynamic convection and the solution flow rates can be adjusted to minimize the effects that viscosity may have on the current densities passed.

1.8. ELECTRON TRANSFER KINETICS

Electron transfer kinetics have a direct effect on the charging-discharging efficiency of a RFB. As stated in section 1.2, the standard rate constant should be $k^0 >$

$1 \times 10^{-2} \text{ cm s}^{-1}$ for any given redox couple intended for use in RFB applications. This is to ensure that the voltage needed to charge the battery is as close as possible to the open circuit potential (OCV) of the battery at full charge (no overvoltage), so the voltage input during charging equals the voltage output when discharging.

In this work, the standard rate constants of various complexes of Fe(III) and Co(II) with amino-alcohol ligands were measured in 5 M NaOH_(aq) by scanning electrochemical microscopy (SECM)³⁷ and CV at ultramicroelectrodes (UMEs).³⁸ In particular, the electron transfer kinetics corresponding to the complexes selected in section 1.5 were assessed and compared. The determination of k^0 by SECM can be carried out by recording steady state CVs at an SECM tip under positive feedback conditions, as described previously.³⁷ CVs are recorded at various tip-to-substrate distance separations, normalized, and fit to a model based on Butler-Volmer kinetics.^{39, 42} Figure 1.9 presents a step-by-step description of such a procedure.

Figure 1.9A shows a schematic diagram of the SECM feedback experiment. The black trace in Figure 1.9B is an experimental approach curve obtained in 10 mM [Fe(III)(TEA)] + 5 M NaOH that was fit with theory (red circles) to calculate the distance separation between the SECM tip and substrate electrodes. Figure 1.9C presents linear sweep voltammograms (LSV) recorded in the same solution, at different distances from the substrate electrode. Figure 1.9D shows the LSV with the current normalized to the steady state current, i_{ss} , at $E = -1.25 \text{ V vs. Ag/AgCl}$. In Figure 1.9D, a clear deviation from Nernstian behavior is observed at $d = 0.59 \text{ }\mu\text{m}$. The magnitude of k^0 is extracted from the experimental data through the use of equations (1-15) - (1-18):

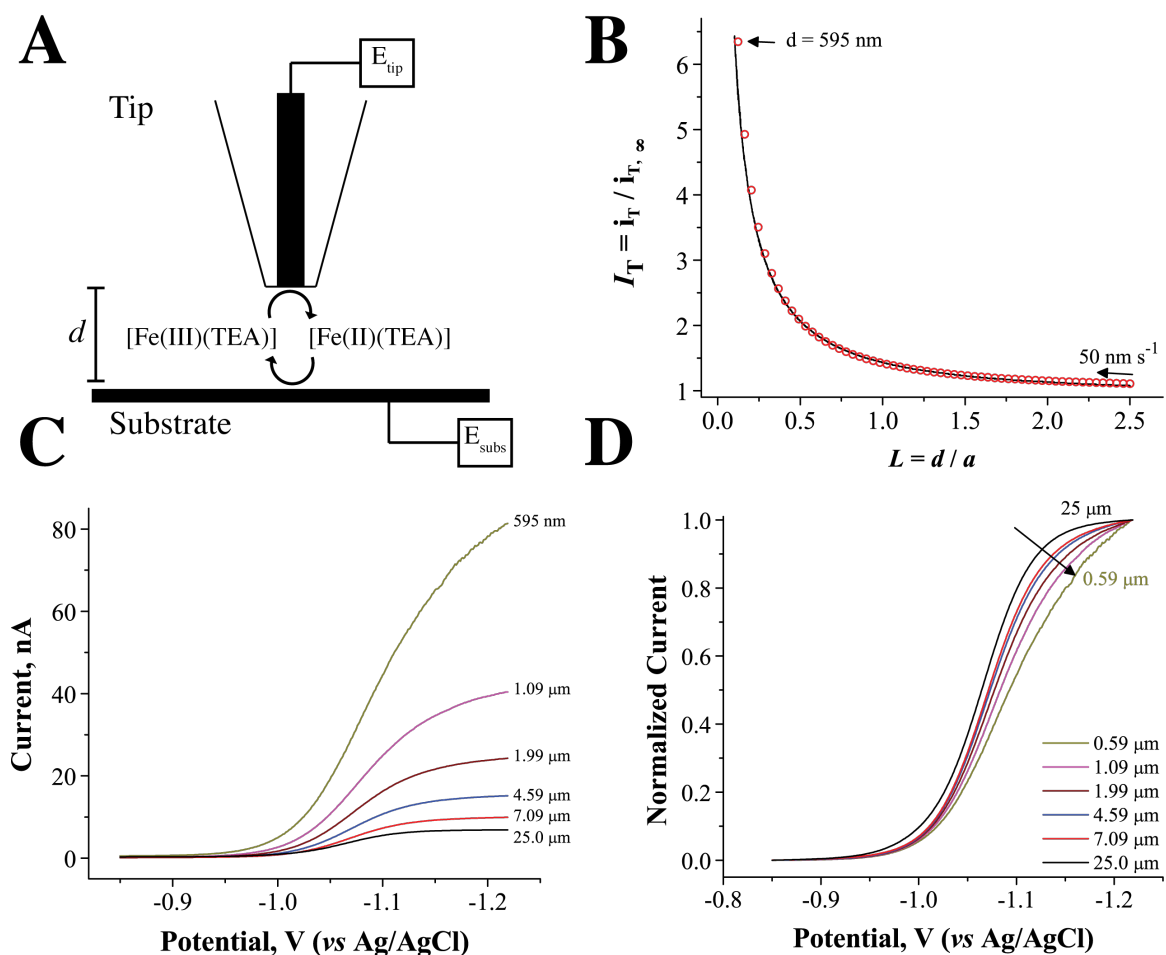


Figure 1.9. **A.** Schematic diagram of an SECM experiment under positive feedback conditions. **B.** Approach curve carried out with a GC UME ($a = 5 \mu\text{m}$) in 10 mM [Fe(III)(TEA)] in 5 M NaOH. The black arrow indicates the direction of the displacement along the z axis, rate = 50 nm s^{-1} . The black trace is the experimental data, red circles are the theoretical fit. **C.** LSV recorded at different distances from the substrate electrode. **D.** Normalized voltammograms to show the effect of electron transfer kinetics. The scan rates are $v = 10 \text{ mV s}^{-1}$.

$$I_T(E, L) = \frac{0.6686 + 0.6973/L + 0.3218e^{-1.744/L}}{\theta + 1/k} \quad (1-15)$$

$$\theta = 1 + \frac{D_{[Fe(III)(TEA)]}}{D_{[Fe(II)(TEA)]}} e^{nf(E-E^{o'})} \quad (1-16)$$

$$k = \frac{k^0 e^{-\alpha nf(E-E^{o'})}}{m_{[Fe(III)(TEA)]}} \quad (1-17)$$

$$m_{[Fe(III)(TEA)]} = \frac{4D_0}{\pi a} (0.6686 + 0.6973/L + 0.3218e^{-1.744/L}) \quad (1-18)$$

where k is the kinetic parameter, m is the mass transfer coefficient, $L = d / a$ is the normalized distance, a is the radius of the UME, and $f = RT/F$. Figure 1.10 presents the fit obtained with equations (1-15) - (1-18) for experimental scans recorded at distances $d = 25 \mu\text{m}$ and $d = 0.59 \mu\text{m}$. The kinetic value obtained is $k^0 = 0.012 \pm 0.007 \text{ cm s}^{-1}$. Such a measurement indicates that the kinetics of electron transfer for [Fe(III)(TEA)] are just above the limit set in section 1.2.

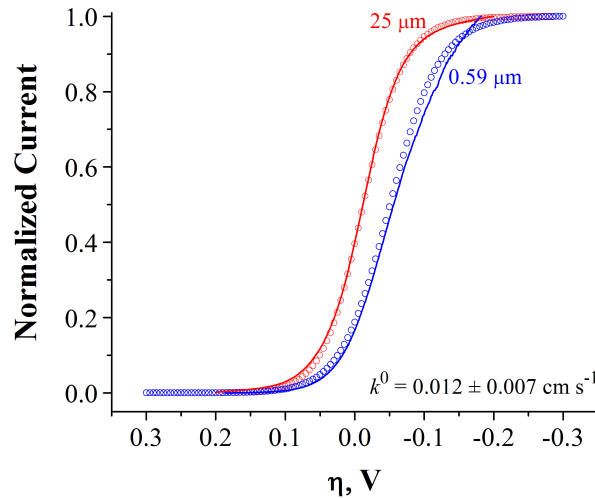


Figure 1.10. Determination of k^0 for [Fe(III)(TEA)] reduction to [Fe(II)(TEA)] in 5 M NaOH. The solution contained 10 mM [Fe(III)(TEA)] in 5 M NaOH. GC UME ($a = 5 \mu\text{m}$), $D = 2.0 \times 10^{-6} \text{ cm}^2 \text{ s}^{-1}$, $\nu = 10 \text{ mV s}^{-1}$. Blue and red traces are the experimental data, circles are the theoretical fits.

Experiments like those described previously were carried out with complexes made with the ligands presented in Figure 1.5, also in 5 M NaOH. This is shown in Figure 1.11. A clear improvement in kinetics was observed when ligands with electron

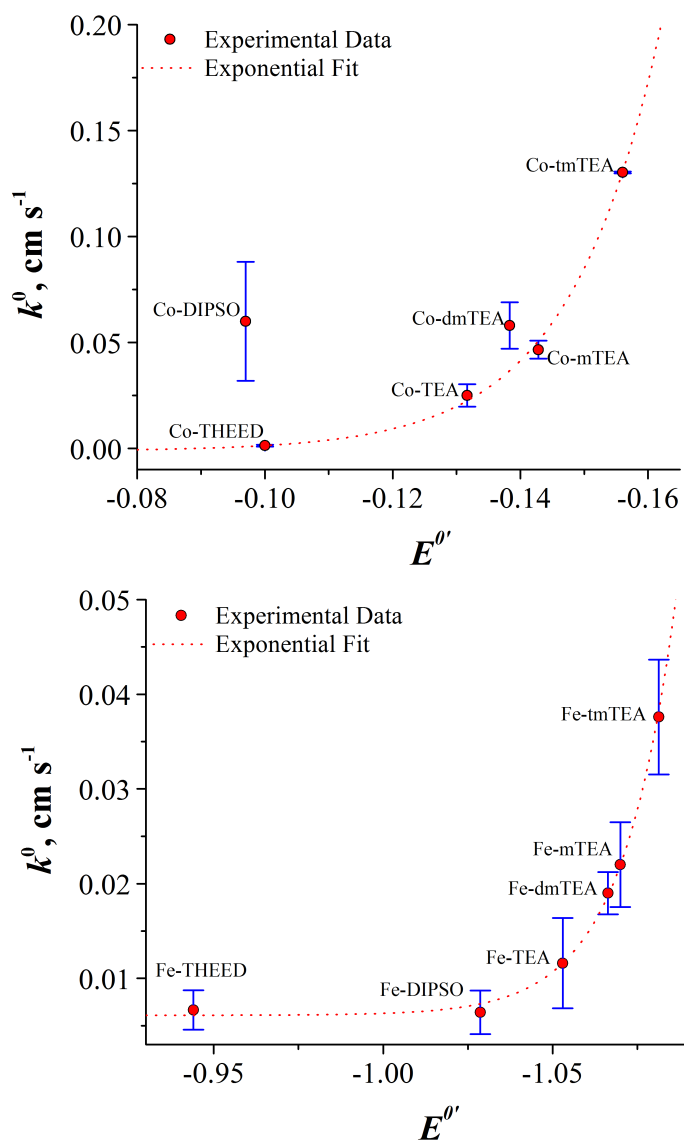


Figure 1.11. Determination of k^0 for $[\text{Fe(III)(L)}]$ and $[\text{Co(II)(L)}]$ in 5 M NaOH. GC UME ($a = 5 \mu\text{m}$), $D = 2.0 \times 10^{-6} \text{ cm}^2 \text{ s}^{-1}$, $\nu = 10 \text{ mV s}^{-1}$. Red circles are experimental data, the dotted lines are exponential fits. Error bars were calculated as the standard deviation from three consecutive measurements of the same rate.

donating groups were used to form complexes of both Co(II) and Fe(III) ions. Further, the complexes of cobalt presented faster transfer kinetics than those of iron. The fit of the experimental data in Figure 1.11 with an exponential function is arbitrary and simply aims to highlight the fast increase of k^0 observed at more negative formal potentials.

1.9. CONCLUSIONS

This chapter was an introduction to the challenges and importance of EES devices, and to RFB technology in general. Further, the idea of developing an alkaline RFB using 5 M NaOH as the electrolyte was presented. Such an idea is attractive because the conductivity of NaOH is the same order of magnitude as that of acidic electrolytes but NaOH is less corrosive to steel and other cell materials, potentially leading to a technology with less maintenance requirements. Moreover, the development of redox couples based on the coordination chemistry of metal ions allows the tuning of certain

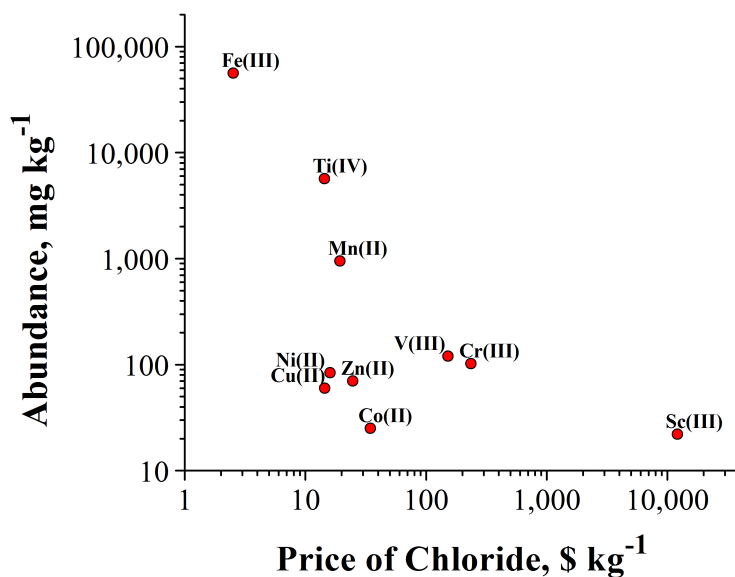


Figure 1.12. Plot of abundance on Earth's crust vs. price of chloride salt for all first row transition metals. Prices were obtained from quotes for bulk amounts of each hydrated salt (ACS grade) from Alfa Aesar.

thermodynamic properties, such as formal potential and surface charge, that could potentially be used to improve the cyclability of the battery. In this work, coordination compounds of iron and cobalt were selected because they can be prepared from inexpensive salts (see Figure 1.12, to the left of V) in a one-pot synthesis. Finally, preliminary experimental data was presented to support the feasibility of constructing an alkaline RFB based on complexes of Co(II) and Fe(III) in 5 M NaOH.

1.10. REFERENCES

- [1] Abraham, S.; *National Transmission Grid Study*, U.S. Department of Energy: Washington, DC: 2003.
- [2] Linden S.; *Energy*, **2006**, *31*, 3446–3457.
- [3] Chen, H.; Cong, T. N.; Yang, W.; Tan, C.; Li, Y.; Ding, Y.; *Prog. Nat. Sci.*, **2009**, *19*, 291-312.
- [4] Mclarnon F. R.; Cairns E. J.; *Ann. Rev. Energy*, **1989**, *14*, 241–271.
- [5] Chatzivasileiadi, A.; Ampatzi, E.; Knocht, I.; *Renew. Sust. Energ. Rev.*, **2013**, *25*, 814-830.
- [6] Eyer, J.; Corey, G.; *Energy Storage for the Electricity Grid: Benefits and Market Potential Assessment Guide*, Sandia National Laboratories, Albuquerque, NM: 2010.
- [7] KEMA, Inc.; *Market Evaluation for Energy Storage in the United States*, Copper Development Association: Fairfax, VA: 2012.
- [8] Baker, J. N.; Collinson, A.; *Power Eng. J.*, **1999**, *6*, 107–112.
- [9] Dobie, W. C.; *Power Eng. J.*, **1998**, *12*, 177–181.
- [10] Giner, J.; Swette, L.; Cahill, A.; *Screening of Redox Couples and Electrode Materials*, CR 134705, NASA-Lewis Research Center, Cleveland, OH: 1976.
- [11] Ciprios, C.; Erslone, W.; Grimes, P. G.; *Redox Bulk Energy Storage System Study*, Vol. I and II, CR 135206, Exxon Research Engineering Co., NASA-Lewis Research Center, Cleveland, OH: 1977.
- [12] Thaller, L. H.; in *Symposium on Load-Leveling*, sponsored by The Electrochemical Society, Atlanta, GA: 1977.

- [13] Wang, W.; Luo, Q.; Li, B.; Wei, X.; Li, L.; Yang, Z.; *Adv. Funct. Mater.*, **2013**, *23*, 970-986.
- [14] Dunn, B.; Kamath, H.; Tarascon, J. M.; *Science*, **2011**, *334*, 928-935.
- [15] Doughty, D. H.; Butler, P. C.; Akhil, A. A.; Clark, N. H.; Boyes, J. D.; *Electrochem. Soc. Interface*, **2010**, *19*, 49-53.
- [16] Enervault. <http://enervault.com/> (accessed Sep 2, 2014).
- [17] Nguyen, T.; Savinell, R. F.; *Interface*, **2010**, *19*, 54-56.
- [18] Rosemount Analytical, *Conductance Data for Commonly Used Chemicals*, Irvine, CA: 2010.
- [19] Kear, G.; Shah, A. A.; Walsh, F. C.; *Int. J. Energy Res.*, **2012**, *36*, 1105-1120.
- [20] Chen, Y. D.; Santhanam, K. S. V., Bard, A. J.; *J. Electrochem. Soc.*, **1981**, *128*, 1460-1467.
- [21] Moore, J. W.; Stanitski, C. L.; Jurs, P. C.; *Chemistry: The Molecular Science*, Cengage Learning, Stamford, 2008, Vol. 2, p. A33-A34.
- [22] Standard Reference Data Program (National Institute of Standards and Technology (U.S.)). *NIST Critically Selected Stability Constants of Metal Complexes Database*; Smith, R. M.; Martell, A. E.; Motekaitis, R. J., Eds.; NIST Standard Reference Database; Version 8.0.; U.S. Dept. of Commerce, Technology Administration, National Institute of Standards and Technology, Standard Reference Data Program: Gaithersburg, MD, 2004.
- [23] Vanysek, P.; *Electrochemical Series, In CRC Handbook of Chemistry and Physics*; CRC Press: Boca Raton, FL, 2013, p. (8-20)-(8-29).
- [24] Bard, A. J.; Faulkner, L. R.; *Electrochemical Methods: Fundamentals and Applications*; Wiley: New York, 2001.
- [25] Wolfson, H.; *Nature*, **1944**, *153*, 375-376.
- [26] Jessop, G.; *Nature*, **1946**, *158*, 59-59.
- [27] Subrahmanya, R. S.; *Proc. Ind. Acad. Sci. A*, **1956**, *43*, 133-147.
- [28] Ibañez, J. G.; Choi, C.; Becker, R. S.; *J. Electrochem. Soc.*, **1987**, *134*, 3083-3089.
- [29] Bechtold, T.; Burtcher, E.; Turcanu, A.; Bobleter, O.; *J. Appl. Electrochem.*, **1997**, *27*, 1021-1028.
- [30] INEOS. Technical Data Sheet: Triethanolamine. <http://www.ineos.com> (accessed Sep 11, 2014).
- [31] Korson, L.; Drost-Hansen, W.; Millero, F. J.; *J. Phys. Chem.*, **1969**, *73*, 34-39.

- [32] Vinnolit. Product Information: Caustic Soda Solution. <http://www.vinnolit.com> (accessed Sep 11, 2014).
- [33] Fasullo, O. T.; Sulfuric Acid: Use and Handling; McGraw-Hill: New York, 1965.
- [34] Einstein, A.; *Ann. der Physik*, **1905**, 322, 560.
- [35] Sutherland, W.; *Phil. Mag.*, **1905**, 9, 781-785.
- [36] Denuault, G.; Mirkin, M. V.; Bard, A. J.; *J. Electroanal. Chem.*, **1991**, 308, 27-38.
- [37] *Scanning Electrochemical Microscopy*; Bard, A. J., Mirkin, M. V., Eds.; Marcel Dekker: New York, 2001.
- [38] Mirkin, M. V.; Bard, A. J.; *Anal. Chem.*, **1992**, 64, 2293-2302.
- [39] Mirkin, M. V.; Bulhões, L. O. S.; Bard, A. J.; *J. Am. Chem. Soc.*, **1993**, 115, 201-204.
- [40] Mirkin, M. V.; Richards, T. C.; Bard, A. J.; *J. Phys. Chem.*, **1993**, 97, 7672-7677.
- [41] Mirkin, M. V.; Bard, A. J.; *Anal. Chem.*, **1993**, 97, 7672-7677.
- [42] Mirkin, M. V.; Bard, A. J.; *J. Electrochem. Soc.*, **1992**, 139, 3535-3539.

Chapter 2. Use of Scanning Electrochemical Microscopy in the Evaluation of Redox Couples for Flow Battery Applications

2.1. ABSTRACT

This chapter introduces a new method based on SECM for the quick identification of redox couples with slow EC reactions, $k < 0.1 \text{ s}^{-1}$. The new method consists on creating a micro-cavity between the tip and substrate electrode where complete, localized electrolysis is achieved in short periods of time ($t \approx 5 \text{ min}$), and with small sample volumes ($V \approx 2 - 5 \text{ }\mu\text{L}$). During analysis of a redox couple, a fast electrolysis experiment is carried out with the substrate for a specific time (E step), while the tip is at open circuit. Then, the potential of the substrate is taken to open circuit, and chronoamperometry is carried out at the tip. The tip reports a current transient proportional to the decaying concentration of the product of the substrate reaction (caused by the C step), from which an apparent forward rate constant can be determined. Further, the current decay recorded at the tip can be probed for extended periods of time to identify reactions with slow kinetics. The method was designed for the field of RFB research, where the identification of chemically stable redox couples is necessary to ensure that a battery can run for thousands of cycles.

2.2. INTRODUCTION

Research efforts on the development of RFBs have increased exponentially in the last 20 years.¹ Of particular interest is the characterization of new redox couples that could extend the cycling life of current RFBs and increase their energy density.²⁻⁴ In this regard, an important challenge is the identification of redox couples with no EC reactions. This is important because EC reactions may dramatically affect the energy

storage capacity of a redox couple by decreasing its concentration in solution. Since RFBs have duty cycles > 10 years, even slow EC reactions, $k \leq 1 \times 10^{-5} \text{ s}^{-1}$, could dramatically affect their performance. EC reactions with slow forward rate constants, on the order of $k \leq 0.1 \text{ s}^{-1}$, are generally out of range for the times accessible by conventional electrochemical techniques (*e.g.*, CV, see Table 1.2). The determination of such slow rates requires the use of time-consuming methods, such as exhaustive bulk electrolysis, typically achieving complete electrolysis in $t > 30 \text{ min}$.⁵ Here, an alternative approach based on SECM⁶ is presented. The new method consists of creating a micro-cavity between the tip and substrate electrodes where complete, localized electrolysis can be achieved in short periods of time ($t \approx 5 \text{ min}$). During analysis of a redox couple, the tip reports a current transient proportional to the decaying concentration of the product of the substrate reaction, from which an apparent forward rate, k_{app} , can be determined. The method was calibrated using *p*-aminophenol (PAP) as a standard for EC reactions,⁷⁻⁹ and ferrocenemethanol (FcMeOH) was used as a reference substance with no coupled kinetics. More importantly, this approach can be used as a quick method to detect EC reactions. This is shown in this chapter for the cases of [Co(TEA)] and [Co(TiPA)] in 5 M NaOH.

The general scheme of an EC reaction is:



where k is the rate of reaction, and X is a species that is not electroactive at the potentials where reaction (2-1) occurs. To measure k from reaction (2-2), an electroanalytical method needs to cover a time range where mass transfer kinetics can be experimentally decoupled from electron transfer kinetics. Such a time range is usually extracted from kinetic zone diagrams.¹⁰ A zone diagram is a plot of the dimensionless time parameter λ (first introduced in Table 1.2) vs. a measurable property of the redox system under study such as the peak potential, E_p in CV. Figure 2.1 presents a zone diagram for an EC reaction using λ from CV (see Table 1.2). The x axis in Figure 2.1 is $\lambda = kRT/vF$, and the y-axis is $F(E_p - E^0)/RT$, where E_p is the peak potential of the forward reaction from CV. The right dashed line in Figure 2.1 shows that $\log \lambda \geq 0.28$ is the lower limit where a kinetic rate can be measured (pure kinetics). Experiments carried out with $-0.95 < \lambda < 0.28$ would inherently present the combination of both mass transfer and electron transfer kinetics, and the rates measured when $\lambda < -0.95$ (left dashed line) would only correspond to mass transfer (pure diffusion). In this example, the slowest k that can be determined by CV is calculated using $v = 0.01 \text{ V s}^{-1}$ (the slowest scan rate generally accessible without

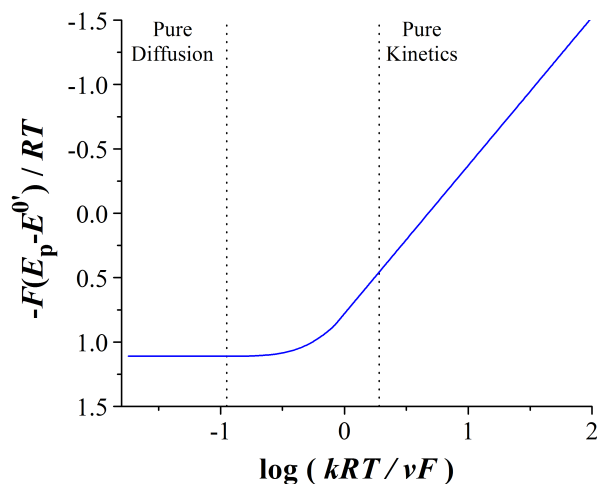


Figure 2.1. Kinetic zone diagram for a first-order EC reaction, calculated with the time parameter for cyclic voltammetry and the peak potential, E_p . The two dashed lines represent the limits of pure diffusion, $\lambda = 0.95$, and pure kinetics, $\lambda = 0.28$.

the effects of natural convection), $\log \lambda = 0.28$, and $n = 1$, and gives $k = 1.0 \pm 0.5 \text{ s}^{-1}$. Therefore, EC reactions with $k < 1.0 \pm 0.5 \text{ s}^{-1}$ would be invisible to a CV experiment. Similar calculations can be carried out to determine the limits of other electroanalytical techniques, such as chronoamperometry, rotating disc electrodes, and conventional SECM.⁵ In fact, the only electrochemical methods that can accurately measure rates below 0.1 s^{-1} are based on bulk electrolysis. Such methods generally are time consuming, typically achieving complete electrolysis in $t > 30 \text{ min}$, except for some special cases previously reported in the literature.¹¹ Thin-layer cells⁵ are an exception to this because they use μL volumes in very narrow gaps ($100 \mu\text{m}$) between two electrodes. Such a configuration is exploited in the present work.

In this chapter, a method that combines the times accessible by bulk electrolysis with UMEs at steady state in an SECM configuration is reported. This approach allowed the sequential sampling of redox couples, and was used for rapid discrimination of couples presenting EC reactions. The goal was to develop an alkaline RFB based on the coordination chemistries of Co and Fe in 5 M NaOH. The redox couples presented in this chapter were actual candidates for the first prototype alkaline RFB.

2.3. MODE OF OPERATION

The new method is called e-SECM, where “e” stands for electrolysis. Figure 2.2 shows a schematic representation of the e-SECM configuration used in this work. In e-SECM, the gap between the tip and substrate electrode is enclosed by a piece of tubing to form a micro-cavity (a thin layer cell), shown in Figure 2.2A. The tip is approached to the substrate under positive feedback conditions⁶ with a dual purpose: first, to partially cover the cavity, as shown in Figure 2.2B; and second, to probe the concentration of redox species over time. When a potential step is applied on the substrate electrode to

carry out a redox reaction under mass-transfer control (while the tip is at open circuit), the diffusion layer growing from the substrate electrode (arrow 1 in Figure 2.2B) is confined between the inner walls of the cavity and local electrolysis is achieved. However, the cavity is not entirely closed to keep conductivity throughout the cell, and a small leak of redox species occurs at all times (arrow 2 in Figure 2.2B). The dimensions of the e-SECM set-up used in this work are provided in Figures 2.2C and 2.2D. Further,

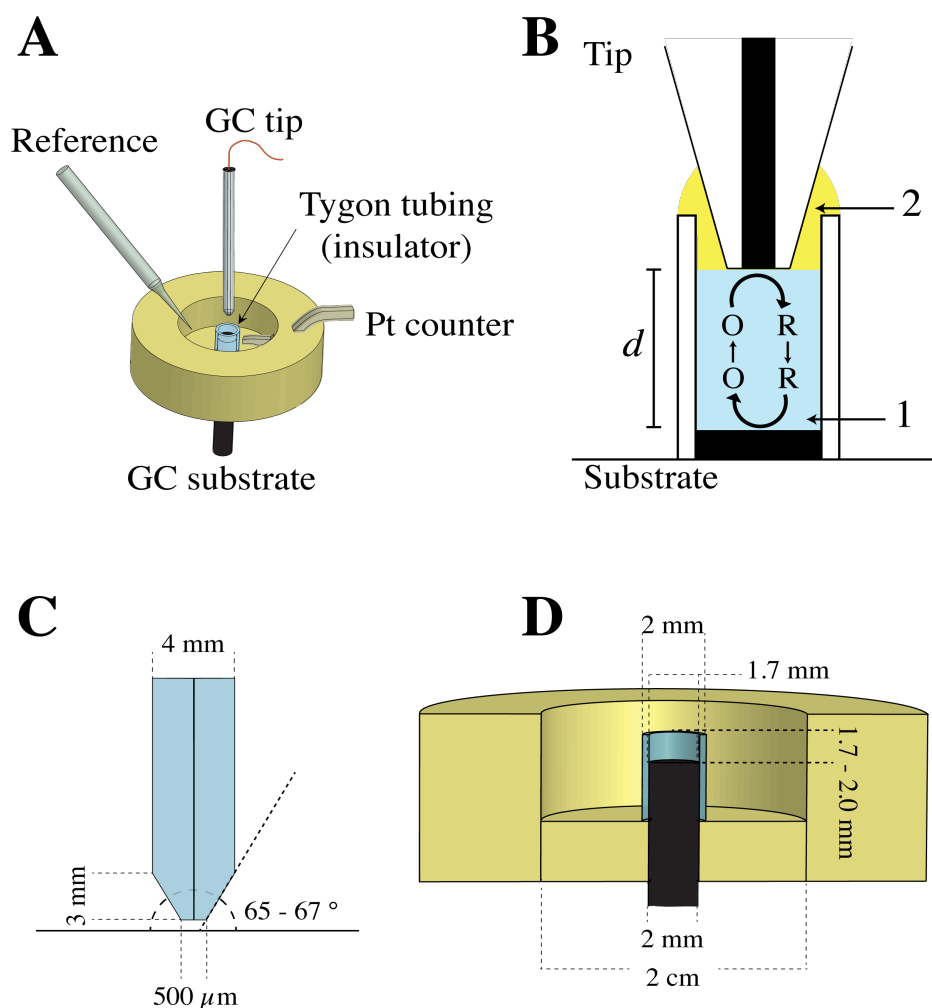


Figure 2.2. **A.** Schematic diagram of the e-SECM set-up. **B.** Cross-section of the e-SECM set-up showing two diffusion regimes indicated by black arrows. **C, D.** Experimental dimensions of the SECM tip and Teflon cell.

pictures of the Teflon cell and electrodes are provided in Figure A2 of Appendix A.

The leak of redox species in e-SECM is a process analogous to the diffusion of molecules through a porous glass frit in a leaking, two-compartment electrolysis cell. When a controlled-potential electrolysis is performed inside the cavity, the concentration of species O decreases exponentially with time as given by equation (2-3):⁵

$$C_O(t) = C_O^* \cdot e^{-pt} \quad (2-3)$$

where C_O^* is the bulk concentration of species O , and $p = m_oAV^{-1}$; m_o is the mass-transfer coefficient, A is the surface area of the electrode, and V the volume of sample solution inside the cavity. However, species O is leaking from the bulk solution into the Tygon cavity (arrow 2 in Figure 2.2B), and the limit $C_O^* \rightarrow 0$ moles (in the cavity) is never achieved. Instead, a constant concentration dictated by the rate of mass transfer of O into the cavity is attained:

$$C_O(t \rightarrow \infty) \propto k_{mt} = m_o A_{or} C_O^* \quad (2-4)$$

where A_{or} is the ring-shaped open area existing between the walls of the Tygon tube and around the SECM tip. The use of Faraday's law, and the addition of equations (2-3) and (2-4) give an expression for the current at the substrate electrode:

$$i(t) = i(0) \cdot e^{-pt} + i(t \rightarrow \infty) \quad (2-5)$$

The magnitude of $i(t \rightarrow \infty)$ in equation (2-5) can be determined experimentally and then subtracted from the current-time curve. The current at the tip electrode is directly proportional to the concentration of R in the micro-cavity:

$$I_T(L) = \frac{i_T(L)}{i_{T,\infty}} \quad (2-6)$$

$$i_{T,\infty} = 4nFDC_R^*a \quad (2-7)$$

$$I_T(L) = A + \frac{B}{L} + C \cdot e^{\left[\frac{D}{L}\right]} \quad (2-8)$$

where $i_T(L)$ is the current recorded at a given distance from the substrate electrode, C_R^* is the concentration of R in the micro-cavity, and a is the radius of the SECM tip. The coefficients in equation (2-8) (A , B , C , D) are kinetic values extracted from feedback theory⁶ and $L = d/a$, the normalized tip-to-substrate distance.

2.4. EXPERIMENTAL SECTION

Chemicals and Solutions

All solutions were prepared in Milli-Q water ($\rho \approx 18 \text{ M}\Omega \cdot \text{cm}$). The following chemicals were used as received: cobalt (II) chloride hexahydrate ($\text{CoCl}_2 \cdot 6 \text{H}_2\text{O}$), sodium nitrate (NaNO_3), iron (III) chloride hexahydrate ($\text{FeCl}_3 \cdot 6 \text{H}_2\text{O}$), and *p*-aminophenol (PAP, 99% purity) from Acros Organics (Belgium); triethanolamine (TEA, $\geq 99\%$), diethanolisopropanolamine (mTEA, 95%), triisopropanolamine (TiPA, 95%), sodium phosphate dibasic anhydrous (Na_2HPO_4), sodium phosphate monobasic anhydrous (NaH_2PO_4), sodium hydroxide (NaOH), and potassium chloride (KCl) from Fisher Scientific (Barrington, IL); ferrocenemethanol (FcMeOH, 97%) from Sigma Aldrich (Russia); and argon gas from Praxair (Danbury, CT).

Preparation of $[\text{Fe}(\text{TEA})(\text{OH})]^-$ and $[\text{Co}(\text{TEA})(\text{H}_2\text{O})]^{2-}$ proceeded as follows: 1×10^{-3} moles of metal ion were dissolved in 20.0 mL of deionized water. Then, 1×10^{-3} moles of TEA were added to the solution with stirring (metal-to-ligand ratio of 1:1). In a separate beaker, 0.5 moles of NaOH were dissolved in deionized water and cooled to room temperature in a water bath. The solution with base was added to the metal + ligand solutions dropwise with stirring, and the volumes were adjusted to 100.0 mL. All

solutions were sonicated for 5 min and passed through Whatman No. 2 filters. 10 mM $[\text{Fe}(\text{TEA})(\text{OH})]^-$ is colorless, whereas 10 mM $[\text{Co}(\text{TEA})(\text{H}_2\text{O})]^{2-}$ is purple. CVs carried out in solutions containing $[\text{Fe}(\text{TEA})(\text{OH})]^-$ and $[\text{Co}(\text{TEA})(\text{H}_2\text{O})]^{2-}$ recorded the following formal potentials: $E_{[\text{Fe}(\text{III/II})(\text{TEA})]}^{0'} = -1.05 \text{ V}$ and $E_{[\text{Co}(\text{III/II})(\text{TEA})]}^{0'} = 0.05 \text{ V}$ vs. Ag/AgCl.

Electrodes and Instrumentation

A GC ultramicroelectrode ($a = 5 \mu\text{m}$) was purchased from Princeton Applied Research (Oak Ridge, TN). All the SECM tips used in this work had $RG = 10$ ($RG = rg/a$), where rg is the radius of the insulation sheath, and a is the radius of the disk electrode. A GC rod (2 mm dia.) was purchased from Alfa Aesar (Ward Hill, MA). The rod was inserted into a piece of Tygon tubing (Tygon R-3603, U.S. Plastic Corporation, Lima, OH) and used as the substrate electrode. All electrodes were polished prior to use with alumina paste (1.0 μm dia. particles) on microcloth pads (Buehler, Lake Bluff, IL), and sonicated for 15 min in deionized water. A Ag/AgCl (saturated KCl) reference electrode was used. A Pt mesh ($A = 1 \text{ cm}^2$, Alfa Aesar) was used as a counter electrode.

SECM measurements were carried out with a CHI920C SECM station and bipotentiostat (CH Instruments, Austin, TX). Pictures and technical specifications of the electrochemical cell employed in this work are provided in section 7.2 and Figure A2 of Appendix A. The SECM cell was designed so that the entrance hole for the SECM tip and the substrate were perfectly aligned, to ensure that both electrodes would stay parallel and centered at all times during experimentation. Since the SECM tip entrance was only 4.1 mm in diameter, and the body of the SECM tip was 4.0 mm in diameter, little room was left for the SECM tip to move away from the center of the Tygon tube; therefore, no alignment procedures were needed prior to experimentation. No problems related to

friction between the SECM tip electrode and the corresponding entrance hole were observed. All solutions were bubbled with argon gas for 15 min. prior to experimentation and kept under a humidified argon blanket.

2.5. NUMERICAL SIMULATIONS

Finite element analysis (FEA) simulations were carried out to validate some experimental results with theory. A complete description of the numerical model is provided in section 7.2 of Appendix A. Briefly, the geometry model was created using COMSOL Multiphysics software. A 2D axial symmetry was employed along with mass transport physics coupled with an appropriate set of boundary conditions. The condition of inward flux of species O and R to the SECM tip electrode was defined according to the Buttlar-Volmer formalism as:

$$-D_O \nabla C_O = -k^0 e^{-\alpha f(E-E^0')} C_O(0, r, t) + k^0 e^{(1-\alpha)f(E-E^0')} C_R(0, r, t) \quad (2-9)$$

$$-D_R \nabla C_R = k^0 e^{-\alpha f(E-E^0')} C_O(0, r, t) - k^0 e^{(1-\alpha)f(E-E^0')} C_R(0, r, t) \quad (2-10)$$

A similar set of equations was used to simulate the flux of species at the SECM substrate. CV experiments were programmed by the use of a Heaviside⁵ step function and equation $E = E_{in} - vt$, where v is the scan rate and t the total time of the voltammetry experiment. Similarly, uncompensated resistance, R_u , and double layer capacitance, C_{dl} , effects were included in the model. The net currents at both tip and substrate electrodes were integrated as the sum of Faradaic and non-Faradaic contributions:

$$i = -2\pi n F D_O \int_{r=0}^{r=a} r \frac{\delta C_O(0, r, t)}{\delta z} dr + i_{nf} \quad (2-11)$$

In the equation above, D_O represents the diffusion coefficient of species O , F is Faraday's constant, n is the number of electrons transferred, and i_{nf} is the non-faradaic contributions from C_{dl} and R_{u} to the final current.

2.6. RESULTS AND DISCUSSION

Figure 2.3 presents a step-by-step depiction of how the e-SECM experiment was carried out. Briefly, the e-SECM experiment started after the tip and substrate electrodes were aligned concentrically. The alignment was carried out manually and away from the cavity. After the alignment was completed, the tip approached the substrate under positive feedback conditions at an approaching rate of 50 nm s^{-1} , as shown in Figure 2.3 A. Figure 2.3B shows an experimental approach curve corresponding to the oxidation of 1.1 mM FcMeOH to FcMeOH^+ ($E^0 = 0.24 \text{ V}$) at a GC tip ($a = 5 \text{ }\mu\text{m}$), with the tip biased at $E_{\text{tip}} = 0.35 \text{ V}$. The potential of the substrate was held at $E_{\text{subs}} = -0.15 \text{ V}$ to carry out the reduction of FcMeOH^+ to FcMeOH . The resulting curve was fit with numerical simulations to calculate the spatial location of the tip with respect to the substrate (red circles).⁶ In Figure 2.3B, the tip was retracted from the end point of the approach curve to $L = 0.25$ (black arrow), corresponding to $d = 1.25 \text{ }\mu\text{m}$ and $I_{\text{T}}(L) = 3.3$.

The tip can approach the substrate until the cavity formed with the tubing is closed, as shown in Figure 2.3C. The point at which the tip started to close the cavity was easily detected by the current readout from the substrate, as shown in Figure 2.3D. The iR drop on the substrate increased considerably as soon as the tip started to block the cavity (due to its larger surface area and current density). Such an iR drop changed the overpotential required to carry out the diffusion-controlled reduction of FcMeOH^+ at the substrate and caused the current to drop, as indicated by the black arrow in Figure 2.3D. Note that the iR drop on the tip was small for most of the approach curve, and the

oxidation reaction continued under diffusion control until the tip was about 50 μm away from closing the cavity.

CV can also be used to evaluate the distance from the substrate where the tip closes the cavity. First, an approach curve was carried out until the current recorded at the

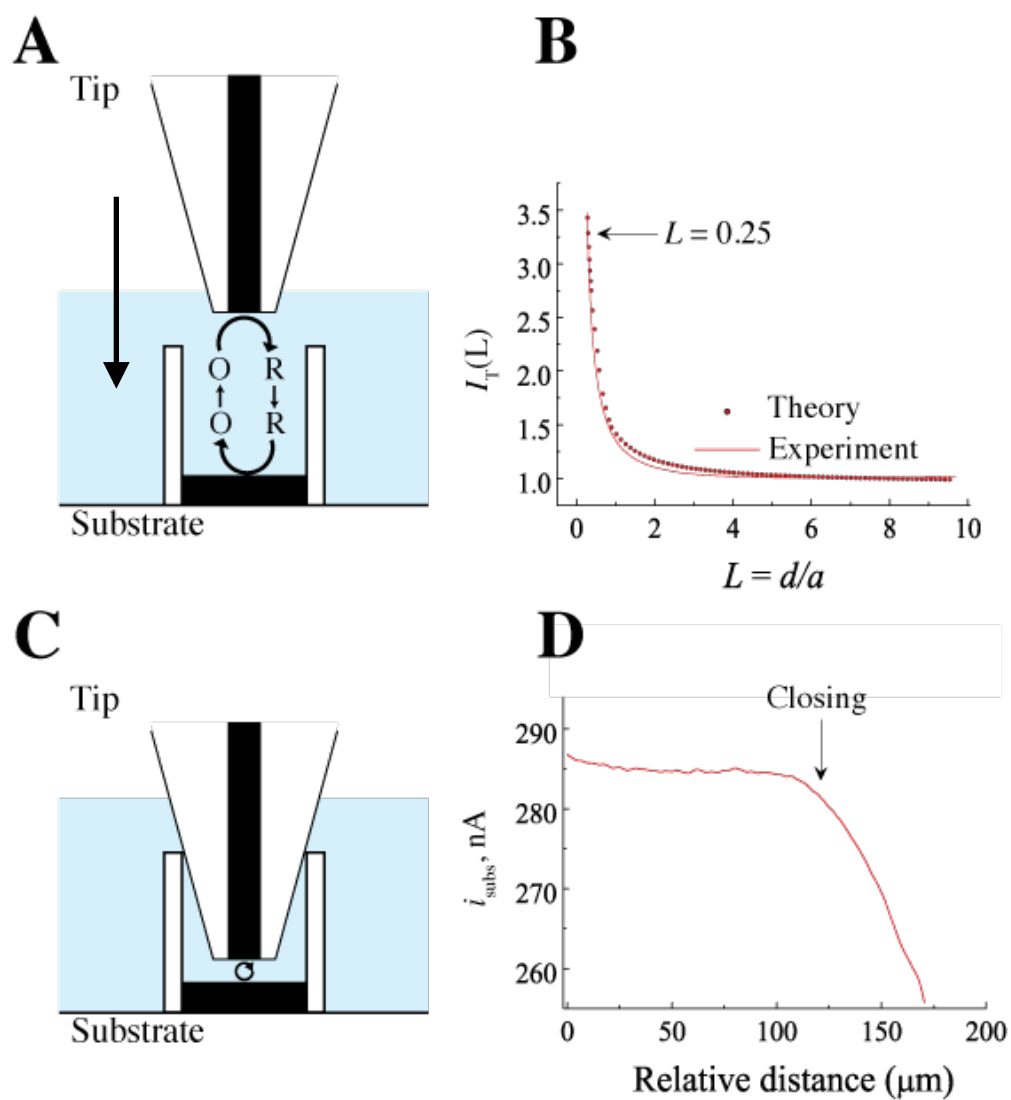


Figure 2.3. **A.** Schematic representation of positive feedback mode. The black arrow shows the direction of the tip while approaching the substrate. **B.** Approach curve carried out in 1.2 mM FcMeOH + 0.1 M NaNO₃ with a GC tip ($a = 5 \mu\text{m}$, at a scanning rate of 50 nm s^{-1}). **C.** Diagram showing the closing of the Tygon cavity. **D.** Current recorded at the substrate during the approach curve in B.

substrate dropped, as shown in Figure 2.3D. Then, CV experiments were carried out at different distances from the point of closure. This was important to characterize the distance where no iR effects were convoluted with the current recorded at the tip. An example of such an evaluation is given in Figures 2.4A and 2.4B for the tip and substrate electrode, respectively.

In Figure 2.4A, CVs from the oxidation of FcMeOH to FcMeOH⁺ carried out at the tip electrode showed pure resistance when the cavity was closed (black trace), and $i_{ss} = 5.2$ nA after the tip was retracted 50 μm away from closure (red trace). Similar results are shown in Figure 2.4B for the GC substrate, with $\Delta E_p = 64$ mV at $d_{\text{open}} = 50$ μm . Currents recorded with the GC substrate at distances shorter than d_{open} presented larger iR drops in the voltamograms. More importantly, by recording CVs at different distances from the substrate, a distance was found where the magnitude of the iR drop at the tip was negligible, and the gap between the tip and the tubing was small enough to minimize

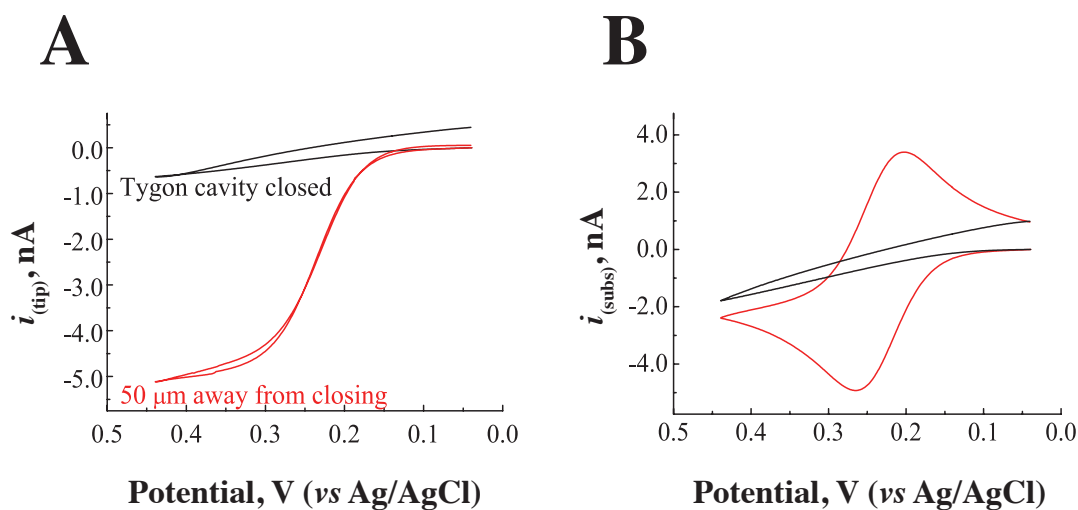


Figure 2.4. CVs recorded at the SECM tip (**A**) and substrate (**B**) electrodes. Black line: resistive CV recorded when the Tygon cavity is closed. Red line: CV recorded when the tip is located 50 μm away from closing the cavity. $v = 10$ mV s^{-1} , $[\text{FcMeOH}] = 1.2$ mM. GC tip ($a = 5$ μm) and substrate (2 mm dia.) electrodes. $\Delta E_p = 64$ mV ($R_u \approx 1.1$ $\text{M}\Omega$).

the extent of species leaking into or out of the cavity. The optimal value of d_{open} depended solely on the geometry of the e-SECM set-up used.

Localized Electrolysis

The bulk electrolysis experiment was carried out at the substrate after the alignment of the electrodes was completed, and the distance d_{open} was known. During electrolysis, the potential of the tip was held at OCV. Examples of electrolysis currents recorded during e-SECM experiments are shown in Figure 2.5 for a solution containing 1.2 mM FcMeOH + 0.1 M NaNO₃. The controlled-potential oxidation of FcMeOH, carried out at $E_{\text{subs}} = 0.35$ V, presented a current that decayed smoothly to background $i(t \rightarrow \infty) = 0.025i_{(0)}$ in $t = 200$ s (see equation (2-5) and black trace in inset from Figure 2.5A), and a plot of $\log(i_{(t)} / i_{(0)})$ vs. t presented a straight line¹² (Figure 2.5A, black trace) after $t = 200$ s. The charge integrated up to $t = 1,000$ s is shown in Figure 2.5B. At $t = 400$

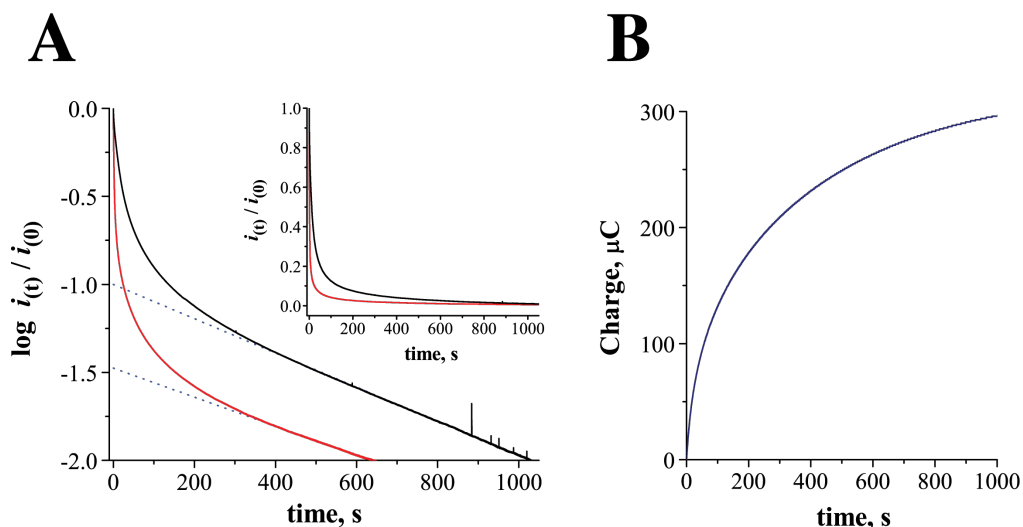


Figure 2.5. Bulk electrolysis of 1.2 mM FcMeOH in 0.1 M NaNO₃ at a GC substrate (2 mm dia.). $V = 2$ μ L. **A.** Plot of $\log(i_{(t)} / i_{(0)})$ vs time made with data from the inset. Inset: Normalized currents recorded during the oxidation of FcMeOH (black trace) at $E_{\text{subs}} = 0.35$ V, and the reduction of FcMeOH⁺ (red trace) at $E_{\text{subs}} = -0.15$ V. $i(t \rightarrow \infty) = 0.025 i_{(0)}$. $\tau = 1000$ s. Dotted lines show linear fits of the data with $p = 8.0 \times 10^{-4}$. **B.** Charge integrated from oxidation of FcMeOH data.

s, an experimental charge of $Q_{\text{exp}} = 231 \mu\text{C}$ was obtained. This value was in agreement with the theoretical charge contained in the cavity, $Q_{\text{exp}} / Q_{\text{theo}} \approx 1.0$ (using $Q_{\text{theo}} = nFVC^*$, where $n = 1$ is the number of electrons, F is Faraday's constant, $V = 2 \mu\text{L}$ is the solution volume, C^* is the initial concentration of FcMeOH, and $Q_{\text{exp}} = 231 \mu\text{C}$). This result was important because it indicated that complete electrolysis is achieved in only 400 s by e-SECM, considerably faster than conventional bulk electrolysis ($t > 30 \text{ min.}$). When the reverse reaction (reduction of FcMeOH⁺ to FcMeOH) was carried out at $E_{\text{subs}} = -0.15 \text{ V}$, the current also decayed to background (red trace in inset) and a plot of $\log(i_{(t)} / i_{(0)})$ vs. t presented a straight line, as shown in Figure 2.5A (red trace). However, a ratio $Q_{\text{exp}} / Q_{\text{theo}} = 0.46$ was obtained at $t = 400 \text{ s}$ in this case. Such a result can be explained by the leak of FcMeOH⁺ diffusing out of the cavity through A_{or} before the electrolysis was carried out.

The progress of electrolysis was monitored over time by recording CVs with the tip. Figure 2.6 presents CVs acquired at $d = 1.25 \mu\text{m}$ for times $t = 0 \text{ s}$ (red), 60 s (green), and 400 s (black). Good agreement was observed between the charge integrated in Figure

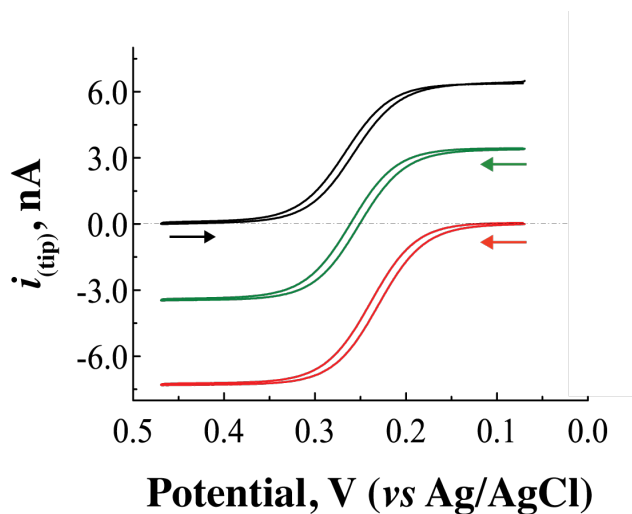


Figure 2.6. Steady state CVs recorded at a GC tip ($a = 5 \mu\text{m}$) after oxidation of 1.2 mM FcMeOH + 0.1 M NaNO₃ in $V = 2 \mu\text{L}$ was carried out at the substrate for $t = 0 \text{ s}$ (red trace), $t = 60 \text{ s}$ (green trace), and $t = 400 \text{ s}$. $d = 1.25 \mu\text{m}$, $v = 10 \text{ mV s}^{-1}$.

2.5B and the expected currents in the steady-state CVs presented in Figure 2.6, when the currents are estimated from an initial concentration of 1.2 mM FcMeOH. The steady state current for voltammograms recorded at distance $d = 1.25 \mu\text{m}$ away from the substrate, and with a GC tip of $a = 5 \mu\text{m}$ is given by equation $i_{ss} = 4nFDC^*aI_T(L) = 5.96 \times 10^{-9} \text{ A}$.

Evaluation of Redox Couples

e-SECM is proposed as a tool for the quick identification of EC reactions. The idea is to carry out the electrolysis of a redox reaction at the substrate, such as the one expressed in equation (2-1), while the tip is at open circuit. The substrate is then turned off, and the tip is used to monitor the concentration of the product of reaction (2-1), confined within the Tygon cavity, over time (by chronoamperometry). In the absence of EC reaction (2-2), the current recorded at the tip should be constant for as long as the concentration of the product R stays constant inside the cavity (R is slowly diffusing out).

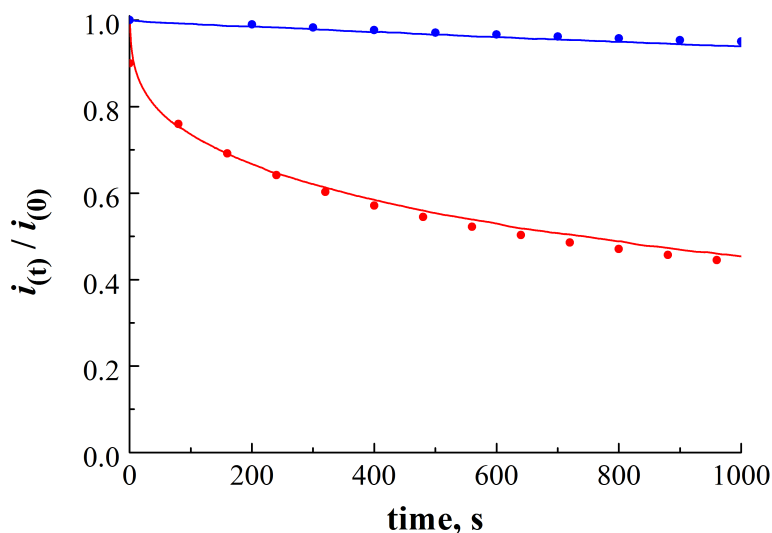
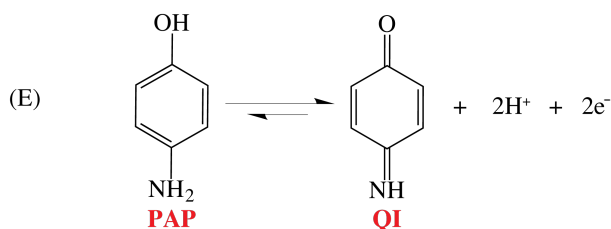


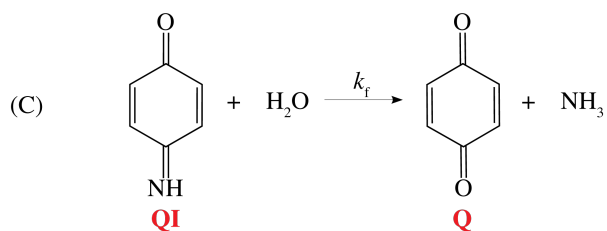
Figure 2.7. Experimental e-SECM current transients recorded for the reduction of 1.3 mM FcMeOH⁺ (blue trace) and 1.3 mM qi (red trace) in 0.1 PBS buffer (pH = 7.00). Electrolysis was carried out with a GC (2 mm dia.) substrate at $E_{\text{subs}} = 0.35 \text{ V}$ for 400 s to generate the electroactive species. Chronoamperograms recorded at a GC tip ($a = 5 \mu\text{m}$) and normalized as $i(t)/i(0)$. Circles are theoretical fits with equation (2-13).

Conversely, in the presence of EC reaction (2-2), the current should decay at a rate proportional to k_f . The technique was validated by first running experiments with a chemically stable couple, FcMeOH/FcMeOH⁺. Figure 2.7 shows the normalized current, $i_{(t)} / i_{(0)}$, recorded with a GC tip ($a = 5 \mu\text{m}$) during the reduction of FcMeOH⁺ for $t = 1000$ s (blue trace). The current in Figure 2.7 was recorded after a potential $E_{\text{subs}} = 0.35$ V was held on the substrate for 400 s. As expected, i_{ss} was essentially constant for 1000 s, showing only a 6% decrease in $i_{(t)} / i_{(0)}$ attributed to FcMeOH⁺ diffusing out of the cavity.

Similar experiments were carried out using the couple *p*-aminophenol (PAP) / quinoneimine (QI) as a standard for EC reactions.⁹ PAP undergoes a two-electron reduction to form the corresponding QI:



However, QI readily undergoes hydrolysis to *p*-benzoquinone (Q):



The reaction is *pH* dependent, and has been studied extensively in the past.⁷ The rate of hydrolysis presents a maximum of $k_f = 0.152 \text{ s}^{-1}$ at $\text{pH} \approx 2.4$.⁷ At $\text{pH} > 2.4$, the rate of hydrolysis decreases (*e.g.*, $k_f = 0.129 \text{ s}^{-1}$ at $\text{pH} = 4.0$).^{8,9}

When QI is generated by e-SECM at $E_{\text{subs}} = 0.35$ V for $t = 1,000$ s, the current transient recorded by the tip after electrolysis presents a steep decay with time, shown by the red trace in Figure 2.7 (40% drop in 300 s). Although the hydrolysis reaction is known to follow first-order kinetics, the transient observed by e-SECM did not present a linear decay with time. Moreover, the normalized current did not follow second order kinetics either. Instead, the normalized current decayed to 75% in the first 50 seconds, and then continued to decay smoothly for the time remaining. Different numerical approximations were tested to fit the behavior observed, and the best fit was obtained with a function of $t^{-1/2}$. Numerical fits of the data were carried out to extract the magnitude of an apparent rate constant k_a from the $t^{-1/2}$ function. The normalized current was multiplied by equation (2-12):

$$f(t) = \frac{1}{1 + \sqrt{k_a t}} \quad (2-12)$$

$$i_{e-SECM} = \frac{i(t)}{i(0)} \cdot \left(\frac{1}{1 + \sqrt{k_a t}} \right) \quad (2-13)$$

Equation (2-12) is a normalized function that gives $f(t) = 1$ at $t = 0$ s, and drops with $t^{-1/2}$ at a rate controlled by k_a . Equation (2-13) was used to fit the experimental transients obtained with FcMeOH^+ and QI, as depicted with circles in Figure 2.7. The rates used in Figure 2.7 were $k_a = 0$ s⁻¹ for FcMeOH^+ , and $k_a = 2.0 \pm 0.2 \times 10^{-2}$ s⁻¹ for QI. More importantly, a clear distinction can be made between the chemically stable couple $\text{FcMeOH} / \text{FcMeOH}^+$, and a couple with EC kinetics, such as PAP / QI .

The value of e-SECM becomes evident when searching for chemically stable couples for RFB applications. The goal was to develop an alkaline RFB in 5 M NaOH, based on a previously identified family of complexes (21 redox couples) with quasireversible electron transfer kinetics on GC electrodes. However, an important limitation in such research was the lack of a quick screening method to ensure that a redox couple could be cycled in a flow cell without actually running the electrolysis experiments. Here, e-SECM measurements carried out on solutions containing the complexes [Fe(III)(TEA)] and [Co(II)(TEA)] in 5 M NaOH are presented, shown in Figure 2.8. CVs recorded from solutions containing 10 mM of each complex are shown in Figure 2.8A. The voltammograms of both complexes show $i_{p,a} / i_{p,c} = 1.0$ at scan rates $10 \text{ mV s}^{-1} \leq \nu \leq 10 \text{ V s}^{-1}$, an indication that fast EC kinetics are not present at this time

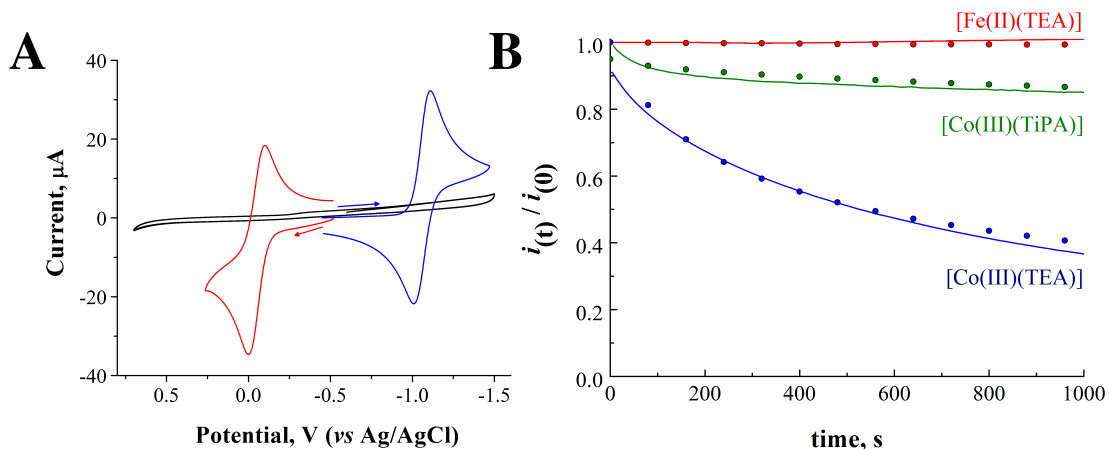


Figure 2.8. **A.** CVs 2 mm diameter glassy carbon electrode (black), 10 mM [Fe(III)(TEA)] (blue), and 10 mM [Co(II)(TEA)] (red) in aqueous 5 M NaOH. The scan rate is $\nu = 50 \text{ mV s}^{-1}$. $\Delta E_{p, \text{Fe-TEA}} = 60 \text{ mV}$, $\Delta E_{p, \text{Co-mTEA}} = 73 \text{ mV}$. $E_{\text{Fe-TEA}}^{0'}$ = -1.05 V and $E_{\text{Co-mTEA}}^{0'}$ = -0.12 V. **B.** Experimental e-SECM current transients recorded for the oxidation of 10 mM [Fe(II)(TEA)] (red trace), and the reduction of 10 mM [Co(III)(TEA)] (blue trace) and 10 mM [Co(III)(TiPA)] (green trace) in 5 M NaOH. Electrolysis was carried out with a GC (2 mm dia.) substrate for 400 s to generate the electroactive species. Chronoamperograms recorded at a GC tip ($a = 5 \text{ }\mu\text{m}$) and normalized as $i(t) / i(0)$. Circles are theoretical fits with equation (2-13).

scale (data not shown). Figure 2.8B shows the e-SECM transients recorded with the same solutions of [Fe(II)(TEA)] (red trace) and [Co(III)(TEA)] (blue trace) in 5 M NaOH. While [Fe(II)(TEA)] shows perfect chemical stability, with only 2% change in current for $t = 1000$ s, [Co(III)(TEA)] showed a 63% decrease in current for the same time. The numerical fits shown with circles in Figure 2.8B correspond to $k_a = 0$ s⁻¹ for [Fe(II)(TEA)] and to $k_a = 3.0 \pm 0.3 \times 10^{-2}$ s⁻¹ for [Co(III)(TEA)]. Clearly, [Co(III)(TEA)] undergoes homogeneous reactions after the electron transfer step. One last experiment was carried out, this time replacing TEA for TiPA to form [Co(III)(TiPA)], as an attempt to improve the chemical stability of the cobalt complex *via* ligand modification (the structure of TiPA is shown in Figure 1.5). The green trace in Figure 2.8B shows the e-SECM transient obtained with such a complex. The normalized current was fit with the numerical approximation to obtain a value of $k_a = 6.0 \pm 0.3 \times 10^{-6}$ s⁻¹, a value approximately four orders of magnitude lower with respect to that of [Co(III)(TEA)].

2.7. CONCLUSIONS

This chapter introduced a new analytical method based on SECM for the quick identification of redox couples with EC kinetics. The new method, called e-SECM, achieves complete, localized electrolysis of a redox couple in short periods of time (2 – 10 times shorter than conventional bulk electrolysis). The tip is used to monitor the chemical stability of a species generated during electrolysis. The validity of the technique was first demonstrated using well-known E and EC systems (FcMeOH and PAP, respectively). Furthermore, e-SECM was used to study three candidate redox couples for RFB applications: [Fe(II/III)(TEA)], [Co(II/III)(TEA)], and [Co(II/III)(TiPA)]. While [Fe(II/III)(TEA)] and [Co(II/III)(TiPA)] showed promising chemical stability for future incorporation into RFBs, [Co(II/III)(TEA)] was chemically unstable. e-SECM offers an

alternative approach to predict the charge-discharge performance of candidate couples without the need of experimental flow cells.

2.8. REFERENCES

- [1] *SciFinder*; Chemical Abstract Service: Columbus, OH, 2014; Year analysis for term: “redox flow battery”, exponential fit carried out in Origin Pro (accessed Jul 24, 2014).
- [2] Wang, W.; Luo, Q.; Li, B.; Wei, X.; Li, L.; Yang, Z.; *Adv. Funct. Mater.*, **2013**, *23*, 970-986.
- [3] Dunn, B. ; Kamath, H. ; Tarascon, J. M.; *Science*, **2011**, *334*, 928-935.
- [4] Yang, Z.; Zhang, J.; Kintner-Meyer, M. C. W.; Lu, X.; Choi, D.; Lemmon, J. P.; Liu, J.; *Chem. Rev.*, **2011**, *111*, 3577-3613.
- [5] Bard, A. J.; Faulkner, L. R.; *Electrochemical Methods: Fundamentals and Applications, Second Edition*; Table 12.1.1, Wiley: New York, 2001.
- [6] Bard, A. J.; Mirkin, M. V. *Scanning Electrochemical Microscopy, Second Edition*; CRC Press: Boca Raton, FL, 2012.
- [7] Hawley, D.; Adams, R. N.; *J. Electroanal. Chem.*, **1965**, *10*, 376-386.
- [8] Malachuk, P. A.; Prater, K. B.; Petrie, G.; Adams, R. N.; *Electroanal. Chem. Interfacial Electrochem.*, **1968**, *16*, 41-46.
- [9] Adams, R. N. *Electrochemistry at solid electrodes*; Monographs in electroanalytical chemistry and electrochemistry; M. Dekker: New York, 1969.
- [10] Andrieux, C. P.; Saveant, J. M.; in *Investigation of Rates and Mechanisms of Reactions*, Part II, 4th ed., C. F. Bernasconi, Ed., Wiley Interscience, New York, 1986, 305-390.
- [11] Bard, A. J.; *Anal. Chem.*, **35**, 1125-1128.
- [12] Santhanam, K. S. V.; Bard, A. J.; *Electroanal. Chem.*, **1970**, *4*, 215-315.

Chapter 3. Structural, Electrochemical and Spectroscopic Characterizations of Fe(III/II)-TEA in Strong Base^{*,†}

3.1. ABSTRACT

We present structural, electrochemical and spectroscopic characterizations of the redox system Fe(III/II)-TEA in 5 M NaOH_(aq). This is important because Fe(III/II)-TEA is a coordination compound of interest in the fields of inorganic supramolecular chemistry, electrodeposition of films with magnetic memory, and electrochemical energy storage. The crystal structure of the Fe(III)-TEA complex was characterized by x-ray diffraction with crystals grown from 5 M NaOH_(aq). In the solid state, Fe(III)-TEA is a dinuclear complex with formula Na₂[(Fe(TEA))₂(μ-O)](H₂O)₆ (**1**, see Table 3.1 for number associations). Raman spectroscopy coupled to DFT calculations were used to determine the structure of Fe(III)-TEA in solution, which indicated a mononuclear complex with formula [Fe(III)(TEA)(OH)]⁻ (**2**). Additionally, electrochemical characterization of Fe(III/II)-TEA carried out by coulometry and CV indicated that the heterogeneous reduction of **2** follows a slow EC reaction scheme, with forward rate constant $k = 2.0 \pm 0.8 \times 10^{-5} \text{ s}^{-1}$, at concentrations > 10 mM. At such concentrations, the reduced form of the complex, [Fe(II)(TEA)(OH)]²⁻ (**3**), undergoes a homogeneous condensation reaction to produce the dinuclear complex [(Fe(TEA))₂(μ-O)]⁴⁻ (**4**). Oxidation of **4** produces a mixed valence compound, [(TEA)Fe(III)OFe(II)(TEA)]³⁻ (**5**), and gives only 1 electron per mole of **4**. This is the first report on the structural characterization of Fe(III)-TEA in alkaline solutions, and the first work to provide

* Arroyo-Currás, N.; Hall, J. W.; Jones, R. A.; Bard, A. J.; *Inorg. Chem.*, (Submitted).

† Justin W. Hall carried out the structural characterization of the complexes using single-crystal XRD. Allen J. Bard and Richard A. Jones were the PIs.

electrochemical evidence for an EC reaction scheme in the heterogeneous reduction of Fe(III)-TEA.

3.2. INTRODUCTION

The coordination chemistry and electrochemistry of Fe(III) with TEA have been studied for 80 years.^{1,2} Coordination compounds of Fe(III/II)-TEA have been used in the electroanalytical determination of iron,^{2,4} the reduction of dyes,⁵⁻⁹ the electrodeposition of films with magnetic memory,¹⁰⁻¹² and in supramolecular chemistry.¹³⁻¹⁶ In addition, Fe(III/II)-TEA in strong base is considered a promising redox couple for flow battery (RFB) applications.^{17,18} TEA is known to act as both a tridentate^{16,19,20} and a tetradentate^{21,22} ligand with Fe(III), depending on the conditions used during the complexation reaction. More importantly, tripodal alkoxide-based ligands, such as TEA, generally form polymetallic clusters with Fe(III) (*e.g.*, ferric wheels) in organic solvents.²³ Ferric wheels of different sizes have been prepared by stabilization of the supramolecular structure of Fe(III)-TEA *via* Li, Na, and Cs ions, and have been studied

Table 3.1. Numbering of structures used in this chapter.

Number	Structure	Phase
1	$\text{Na}_2[(\text{Fe}(\text{TEA}))_2(\mu\text{-O})](\text{H}_2\text{O})_6$	solid
2	$[\text{Fe}(\text{III})(\text{TEA})(\text{OH})]^-$	aqueous
3	$[\text{Fe}(\text{II})(\text{TEA})(\text{OH})]^{2-}$	aqueous
4	$[(\text{Fe}(\text{TEA}))_2(\mu\text{-O})]^{4+}$	aqueous
5	$[(\text{TEA})\text{Fe}(\text{III})\text{OFe}(\text{II})(\text{TEA})]^{3-}$	aqueous

for their properties as single molecule magnets.¹⁴ Several examples of such metallic wheels can be found elsewhere.^{15,24} However, no crystallographic structures have been reported for crystals grown from alkaline aqueous solutions. This is particularly relevant to the field of electrochemical energy storage because the most reversible electrochemistry of Fe(III/II)-TEA is seen at $pH > 12$,^{17,25} which is fortuitous because also in this range the conductivities of strong bases, such as NaOH, reach a maximum.²⁶ There is also a paucity of electrochemical mediators that are strong reductants that can be used in alkaline solutions. CVs of Fe(III)-TEA in 5 M NaOH show an electrochemically reversible heterogeneous electron transfer reaction at a very negative formal potential of $E^0 = -1.05$ V vs. Ag/AgCl^{25,9} (the thermodynamic reduction of water occurs at $E^0 = -1.06$ V vs. Ag/AgCl). This is important in RFB applications because the redox chemistry of Fe(III/II)-TEA is at the limit of the potential window available in strong base; therefore, Fe(III/II)-TEA potentially offers a large output voltage for a battery if coupled to a sufficiently positive redox couple. The utility of Fe(III/II)-TEA in RFBs has already been presented in two patents,^{27,28} which attest to its importance to the field of energy storage applications.

In the present work, we carried out a systematic structural, electrochemical, and spectroscopic characterization of Fe(III/II)-TEA in 5 M NaOH. The solid state structure of Fe(III)-TEA was determined by single-crystal XRD analysis. In addition, Raman measurements were carried out in alkaline solutions containing Fe(III)-TEA to determine the structure of the complex in solution. The Raman spectrum of Fe(III)-TEA was simulated using DFT calculations. The simulated spectrum matched the vibrational modes of the experimental spectrum within ± 20 cm^{-1} . Importantly, the structures determined in this work are in agreement with the typical coordination behavior observed with TEA and Fe(III), and can be considered as fragments of macrocycles or ferric

wheels. Our results demonstrate that a strategy based on using single-crystal XRD analysis, Raman spectroscopy, and DFT calculations is effective to characterize the structure of coordination compounds in solution.

Additionally, electrochemical analysis carried out by CV and coulometry gives strong evidence for an EC reaction scheme at concentrations of **2** > 10 mM (see chapter 4 for experiments with **2** < 10 mM). At such concentrations, the reduced form of the complex, **3**, undergoes a homogeneous condensation reaction to produce the dinuclear complex **4**. Oxidation of **4** produces the mixed valence compound **5** and gives 1 mole of electrons per mole of **4**. The mixed valence compound **5** is chemically stable and can be prepared by oxidation of $[(\text{Fe}(\text{TEA}))_2(\mu\text{-O})]^{4+}$ with O_2 . Electrochemical evidence of the different species is reported. Further, UV-Vis spectroscopy was used to determine the stability constants of $[\text{Fe}(\text{TEA})(\text{OH})]^-$ and $[\text{Fe}(\text{II})(\text{TEA})(\text{OH})]^{2-}$ in 5 M $\text{NaOH}_{(\text{aq})}$. The findings reported in this work led to the development of an alkaline RFB with 100% coulombic efficiency and negligible membrane crossover, reported in Chapter 4.¹⁸

3.3. EXPERIMENTAL SECTION

Synthesis of $[\text{Fe}(\text{III})(\text{TEA})(\text{OH})]^-$ (**2**)

20.0 mL of deionized water ($Q \approx 18 \text{ M}\Omega \cdot \text{cm}$) were added to a round bottom flask and bubbled with argon. After bubbling for 5 min., 0.02 moles of $\text{FeCl}_3 \cdot 6\text{H}_2\text{O}$ from Acros Organics, 99+% (Fair Lawn, NJ) were added with stirring. To this solution, 0.02 moles of TEA from Sigma Aldrich, 98% (St. Louis, MO) were added dropwise with stirring. In a separate container, NaOH pellets (8.0 g) were dissolved in deionized water (10.0 mL) with stirring. After the NaOH dissolved, the container was placed in a water bath to cool to 25° C. This NaOH solution was added dropwise to the Fe(III) + ligand solution. Over the course of the addition, a gel-like material formed that dissolved back into solution

upon addition of all the NaOH. The volume was adjusted to 40.0 mL upon completion of the synthesis reaction, and filtered through Whatman No. 2 paper. The reaction yields > 95% complex, as determined by the plateau current observed in steady state CVs. UV-Vis spectra of solutions containing **2**, **4**, and **5** are shown in Figure A4 of Appendix A. The final solution of **2** is light brown/red, shown in Figure A5A, and has a concentration 0.5 M.

Synthesis of $[(\mu\text{-O})(\text{Fe}(\text{TEA}))_2]^+$ (4**)**

The dinuclear Fe(II)-TEA complex can be synthesized directly with a procedure similar to the one described in the previous paragraph, while keeping the reaction flask under inert atmosphere conditions during and after the synthesis. 20.0 mL of deionized water ($\rho \approx 18 \text{ M}\Omega \cdot \text{cm}$) were added to a round bottom flask and bubbled with argon. After bubbling for 5 min., 0.02 moles of $\text{FeCl}_2 \cdot 4\text{H}_2\text{O}$ from Fisher Scientific (Nazareth, PA) were added with stirring. To this solution, 0.04 moles of TEA were added dropwise with stirring. In a separate container, NaOH pellets (8.0 g) were dissolved in deionized water (10.0 mL) with stirring. After the NaOH dissolved, the container was placed in a water bath to cool at 25° C. This NaOH solution was added dropwise to the Fe(II) + ligand solution. Over the course of the addition, a grey powder formed that dissolved back into solution upon addition of all the NaOH. The volume was adjusted to 40.0 mL upon completion of the synthesis reaction, and filtered through Whatman No. 2 paper. The reaction yields > 95% complex, as determined by the plateau current observed in steady state CVs. The final solution of **4** is light green (Figures A4 and A5B in Appendix) and has a concentration of 0.25 M.

Synthesis of [(TEA)Fe(III)OFe(II)(TEA)]⁻ (**5**)

The mixed valence compound **5** can be synthesized by oxidation of **4** with O₂. The solution of Fe(II)-TEA described above is vigorously bubbled with air for 15 min., while monitoring a color change from light green to dark yellow. The reaction yields > 95% complex, as determined by the plateau current observed in steady state CVs. The final solution of **5** is dark yellow (Figures A4 and A5C in Appendix) and has a concentration 0.25 M.

UV-Vis and Raman Spectroscopy

UV-Vis spectra were acquired with a SEC2000-UV/VIS spectrometer from ALS (Japan), using a quartz cuvette with path length $l = 1$ cm. The determination of stability constants was carried out by the spectrophotometric method.²⁹ Briefly, the complexes **2** and **3** (at concentrations < 5 mM) were prepared under an argon blanket and transferred into a quartz cuvette by pressurized flow injection. The quartz cuvette had a rubber septum through which the solution containing the complexes was injected and/or removed; to prevent oxidation of **3** to **2** by O₂ the solution was never in contact with air. Raman spectra were acquired with a Renishaw inVia microscope system (Hoffman States, IL) having a $\lambda_{\text{ex}} = 514.5$ nm Ar⁺ laser in the backscattering configuration. Liquid samples were placed in a 50 mm diameter crystallizing dish with depth of 1 cm. The beam was focused with a 5× objective lens (short working distance) with a numerical aperture of 0.12, resulting in approximately a 2.6 μm spot diameter under air. Laser irradiation was set to < 3.1 mW power to avoid decomposition of the samples. An acquisition time of 10 s was used for all experiments. Signal-to-noise enhancement was achieved by ensemble averaging. The spectral range between $\nu = 100$ cm⁻¹ to 2,000 cm⁻¹ was considered in this work.

Electrochemical Methods

CV and potential-step experiments were carried out with a CHI660D electrochemistry workstation from CH Instruments (Austin, TX). GC electrodes, 2 mm diameter, and GC UMEs ($a = 5 \mu\text{m}$) were purchased from Princeton Applied Research (Oak Ridge, TN). The electrodes were initially polished with sand paper and then polished on microcloth pads (Buehler, Lake Bluff, IL) with alumina paste of different sizes (1.0 to $0.05 \mu\text{m}$) to ensure a mirror-like finish. Soft polishing with alumina paste was also carried out between measurements. A three-electrode cell configuration was used, with GC as the working electrode, a Ag/AgCl (sat. KCl) reference electrode, and a reticulated carbon mesh ($A = 1 \text{ cm}^2$) as the counter electrode. All potentials in this work are reported *vs.* Ag/AgCl (sat. KCl). For bulk electrolysis, a two-compartment cell with porous glass separators was used.³⁰ The cell was designed to hold a maximum volume of 1 mL in each compartment. Reticulated vitreous carbon from Goodfellow (Corapolis, PA) was used in the electrolysis experiments. High mass transfer rates were achieved by mechanical stirring during electrolysis. All solutions were bubbled thoroughly with argon gas prior to experimentation and were kept under a humidified argon blanket.

X-ray Crystallography

Crystals of $\text{Na}_2[(\text{Fe}(\text{TEA}))_2(\mu\text{-O})](\text{H}_2\text{O})_6$ (**1**) were grown by slow evaporation of the prepared solution in 5 M $\text{NaOH}_{(\text{aq})}$. Diffraction data were collected on a Nonius KappaCCD diffractometer with a graphite monochromator using Mo- $K\alpha$ radiation ($\lambda = 0.71073 \text{ \AA}$) at 153 K. Reflections were collected from omega scans and a multiscan absorption correction was performed using SADABS-2012/1. Structures were solved by direct methods and refined against F^2 by full-matrix least squares using SHELXL-2014/6.³¹ All non-hydrogen atoms were refined anisotropically. All hydrogens were

located from Fourier difference maps and isotropically refined. (CCDC reference number 1029287).

DFT Methods

All calculations were carried out using Gaussian 09W and figures created using GaussView 5. Geometry optimizations and Raman activities were calculated analytically using the B3LYP functional.³² The SDD basis set, using the Stuttgart-Dresden relativistic pseudopotential,³³ was used for iron and the 6-311+g(d,p) basis set for the remaining atoms. Solvation effects were modeled using the conductor-like polarized continuum model (C-PCM).^{34,35} Vibrational frequencies were scaled by 0.9679 to account for anharmonicity.³⁶

3.4. RESULTS AND DISCUSSION

Crystallography

Figure 3.1 shows the solid state structure of Fe(III)-TEA as determined by single crystal X-ray crystallography. The complex crystallizes from 5 M NaOH_(aq) in the C2/c space group with the empirical formula Na₂[(Fe(TEA))₂(μ-O)](H₂O)₆ (**1**). The asymmetric unit consists of one half of a [(Fe(TEA))₂(μ-O)]²⁻ anion and one Na⁺ cation with three waters of crystallization, giving four formula units per cell. The dinuclear iron complex consists of terminal TEA ligands coordinated in the commonly observed κ⁴-N,O,O',O" fashion,^{13,21,22} with a linear oxo bridge between the irons (Figure 3.1A). Each [Fe(TEA)₂(μ-O)]²⁻ ion (Figure 3.1A) is linked to two Na⁺ ions by coordination to oxygen atoms in the TEA ligands (Figure 3.1B). A dinuclear Na₂ unit is formed by two bridging H₂O molecules, and each Na⁺ ion is further coordinated by two terminal H₂O molecules. This arrangement creates 1-D chains which extend along the *a* axis (Figure 3.1C).

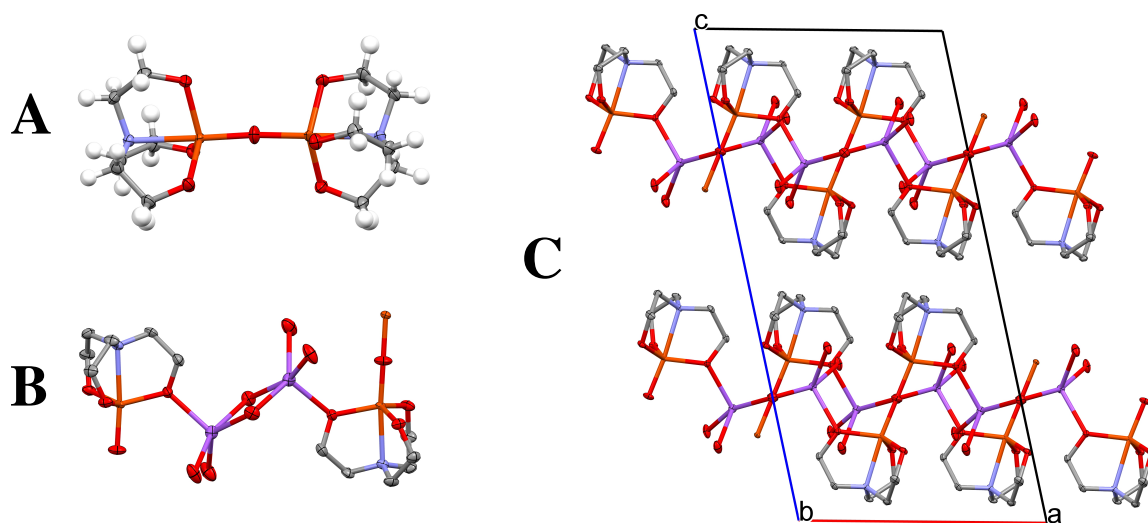
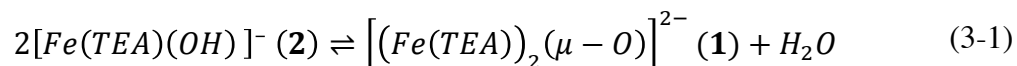


Figure 3.1. Solid state structure of **1** with **A.** the $[(\text{Fe}(\text{TEA}))_2(\mu\text{-O})]^{2-}$ dinuclear anion, **B.** Na to TEA oxygen bonds and **C.** resulting chains along the a-axis. Ellipsoids drawn at the 80% probability level and hydrogens omitted for clarity in parts **B** and **C**. Color code: C atoms are grey, H atoms are white, O atoms are red, N atoms are purple, and Fe atoms are orange.

General Electrochemical Analysis

The structure shown in Figure 3.1A might be expected to present two redox waves in CV due to electronic communication^{37,38} between the two iron centers; *i.e.*, reduction of the first Fe(III) atom to Fe(II) is expected to occur at lower energy than the reduction of the second Fe(III) atom. However, only a single, diffusion controlled wave is seen at $E^0 = -1.05$ V, shown in Figure 3.2A. This result generally indicates the presence of a mononuclear complex. Sweeping the potential of the working electrode to values more negative than -1.25 V causes electrodeposition of iron oxide/hydroxides on GC electrodes. Additionally, no new faradaic processes are seen on mercury electrodes up to -1.60 V, shown in Figure A6 of Appendix A. At potentials more negative than -1.60 V, electrodeposition of iron oxides/hydroxides occurs on mercury as well, also shown in Figure A6.

Given the absence of electrochemical evidence to prove the existence of a dinuclear Fe(III)-TEA species, such as the structure shown in Figure 3.1A, we propose that Fe(III)-TEA exists as a mononuclear complex in solution. The structure shown in Figure 3.1A presumably forms *via* the condensation reaction expressed in equation (3-1) during crystallization:



In order to test this hypothesis, we collected Raman spectra of solutions containing Fe(III)-TEA in 5 M NaOH, and carried out DFT simulations to fit the experimental spectra with calculated vibrations using the structure of the reactant in equation (3-1).

Raman Spectroscopy

Ab initio simulations of the Raman spectrum of Fe(III)-TEA were carried out to provide further evidence for the mononuclear nature of the complex. Figure 3.3A shows

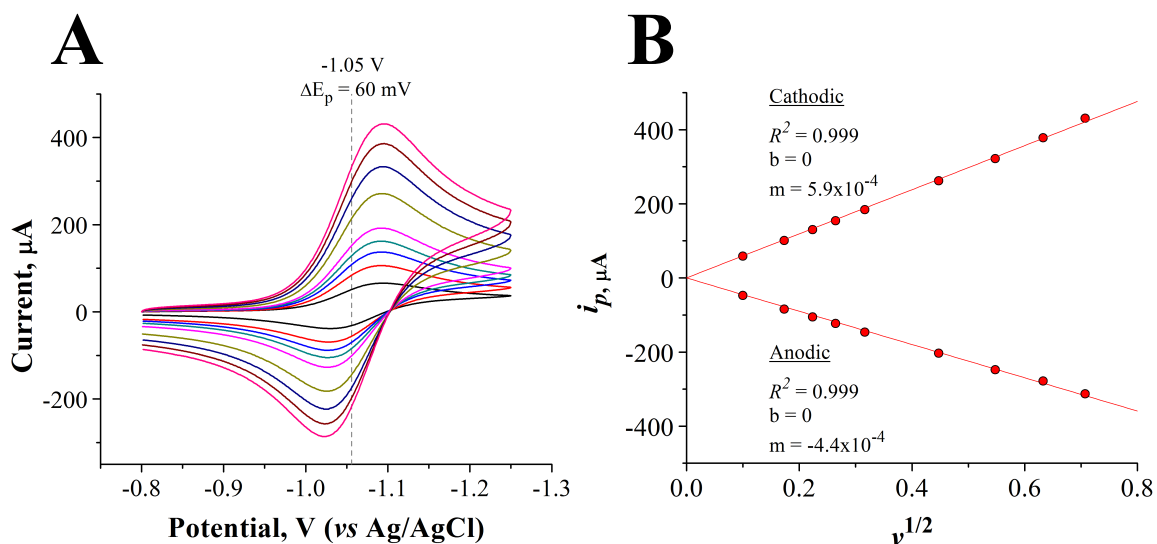


Figure 3.2. **A.** CVs of 20 mM **2** in 5 M NaOH at various scan rates. GC electrode (2 mm dia.). $v = 0.01 - 0.1 \text{ V s}^{-1}$ (from low current to high current). **B.** Linear regression of i_p vs. $v^{1/2}$ for the same solutions.

the optimized structure of **2**. Table 3.2 presents a comparison of metal to ligand bond lengths between values measured in the crystal structure and values obtained by energy minimization. The average Fe-O distance for the TEA ligand is 1.937 Å, which compares favorably with the average of 1.949 Å obtained from the crystal structure. In addition, the distance for the Fe-N bond at 2.387 Å also compares favorably with that in the crystal structure, 2.304 Å.

Figure 3.3B presents a side-by-side comparison between the simulated and experimental Raman spectra. The experimental spectrum contains a moderate intensity peak at $\sim 600\text{ cm}^{-1}$ that can be assigned to the Fe-O-H bending modes obtained from the calculation (Table A4 in Appendix A), indicating the presence of a hydroxyl ligand

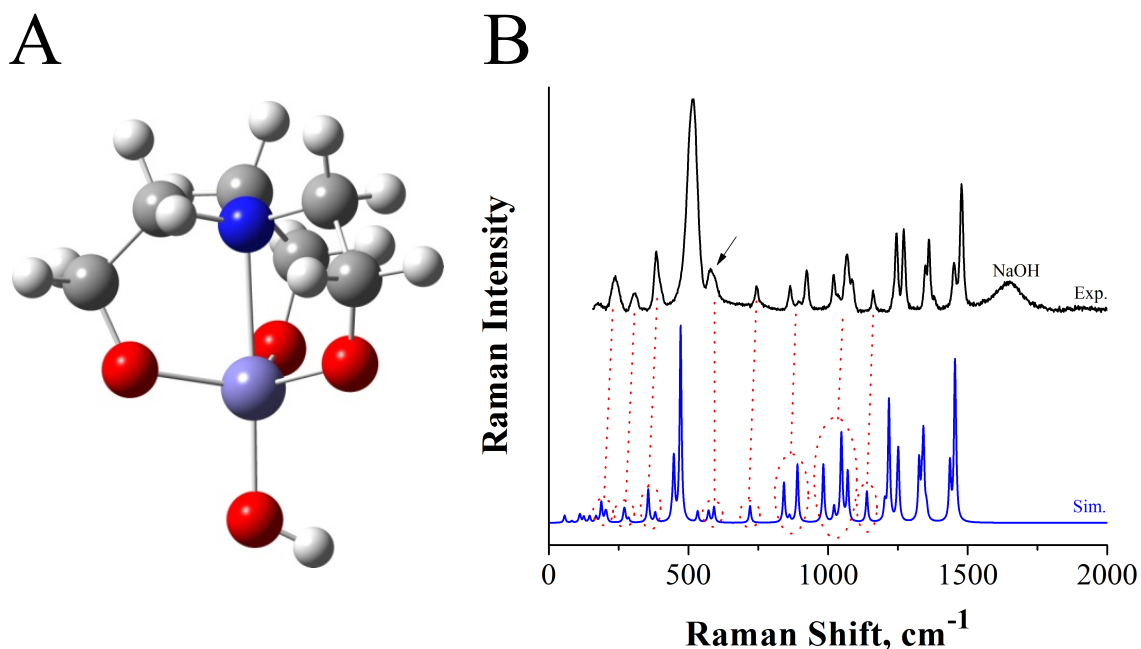


Figure 3.3. **A.** Optimized geometry of **2** from DFT calculations. Color code: C atoms are grey, H atoms are white, O atoms are red, N atoms are blue, and Fe atoms are purple. **B.** Side-by-side comparison of the simulated and experimental Raman spectra of Fe(III)-TEA obtained in solution in the fingerprint region. The black trace is the experiment; the blue trace is the simulation. The dotted red lines indicate the match of lower intensity Raman modes between the two spectra. The black arrow points at an evident -OH bending vibration.

Table 3.2. Comparison of simulated and experimental bond lengths.

Bond	DFT, Å	Crystal, Å	Δ Å
Fe-O ₁	1.932	1.935	0.003
Fe-O ₂	1.939	1.956	0.017
Fe-O ₃	1.940	1.957	0.017
Fe-OH / Fe-(μ -O)	1.935	1.783	0.152
Fe-N	2.387	2.304	0.083

(black arrow in Figure 3.3B). The intense peak observed at ~ 500 cm⁻¹ can be assigned to the Fe-OH stretching vibration, which is higher in energy than expected for the intense Fe-O-Fe stretching vibration in an oxo-bridged dinuclear species.³⁹ Such observations support the existence of a mononuclear [Fe(III)(TEA)(OH)]⁻ rather than the [(Fe(TEA))₂(μ -O)]²⁻ structure shown in Figure 3.1A. A list containing the calculated vibrational modes from Figure 3.3B and their assigned vibrations is presented in Table A4 of Appendix A.

Coulometry

Constant-potential electrolysis of solutions containing **2** at concentrations < 10 mM indicate that the electrochemical reduction of the complex to **3** occurs in a one-electron transfer reaction.¹⁸ Reversal electrolysis, *i.e.*, oxidation of **3** back to **2**, presents 100% coulombic efficiency,¹⁸ see Figure 3.4 as discussed below. However, electrolysis experiments carried out at concentrations > 10 mM reveal a concentration dependent EC

reaction scheme. Figure 3.4 shows consecutive constant-potential electrolysis experiments carried out in 300.0 μL of a solution containing 100 mM **2** in 5 M NaOH.

In Figure 3.4, corresponding forward and reverse electrolysis curves are plotted in the same color. The reduction of **2** to **3**, carried out at $E = -1.25$ V, presented a current that decayed exponentially to background, as shown by the top black trace in Figure 3.4A. The charge integrated from the current-time curve was 2.88 C, shown by the top black circles in Figure 3.4B. Reversal electrolysis carried out at -0.80 V also presented a current that decayed exponentially to background, labeled as “1st ox” in Figure 3.4A, but the charge integrated was only 2.52 C, shown by the bottom black circles in Figure 3.4B. This means that only 87% of the passed electrons were recovered. Subsequent

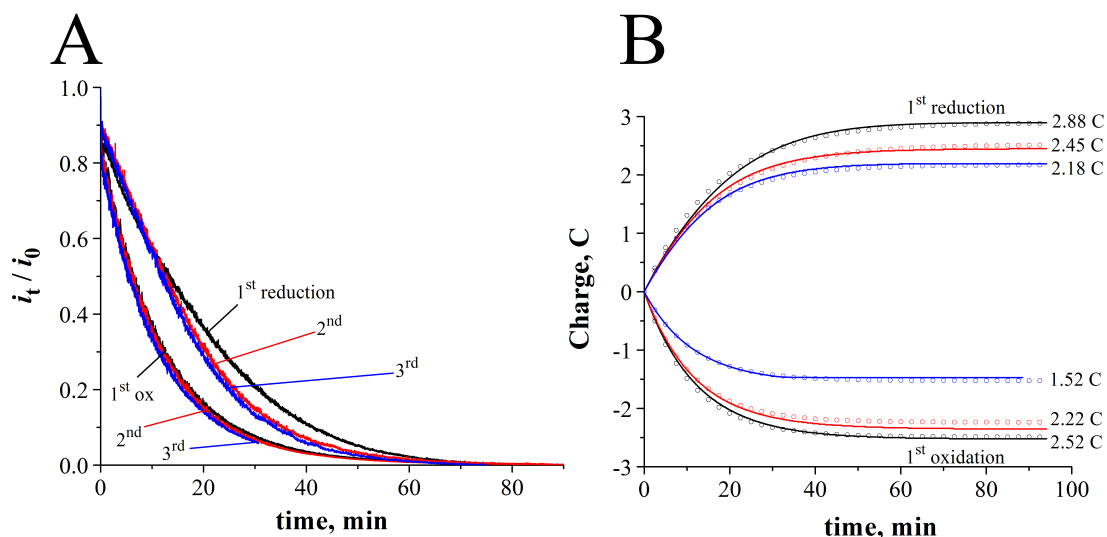


Figure 3.4. **A.** Current-time curves from 6 consecutive exhaustive electrolysis experiments of 300 μL of a solution containing 0.1 M **2** in 5 M NaOH. **B.** Plots of charge (coulombs) vs. electrolysis time constructed from the current-time curves. Circles are experimental data; lines are theoretical fits using equations (2) and (3), as described in Chapter 12 of reference [30]. GC working electrode with $A = 1$ cm^2 . Coefficients $p = m A / V = 1.0 \pm 0.2 \times 10^{-3} \text{ s}^{-1}$ for reductions, and $p = m A / V = 1.2 \pm 0.1 \times 10^{-3} \text{ s}^{-1}$ for oxidations. Reductions were carried out at $E = -1.25$ V vs. Ag/AgCl; oxidations were carried out at $E = -0.80$ V vs. Ag/AgCl. Mechanical stirring was used to speed up mass transfer rates.

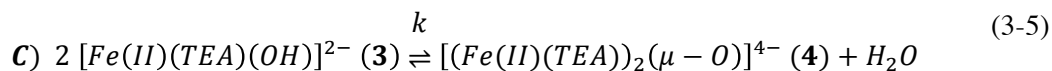
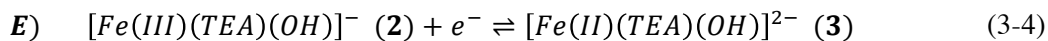
electrolysis carried out with the same solution presented currents that decreased exponentially to background, shown by the remaining red and blue traces in Figure 3.4A. In addition, the charge integrated from those two sequential electrolysis cycles presented coulombic efficiencies of 89% and 70%, respectively (calculated from coulombs in Figure 3.4B). More importantly, the last oxidation reaction (6th experiment) presented an integrated charge of 1.52 C (bottom blue circles in Figure 3.4B), approximately 50% of the number of coulombs integrated from the first experiment, 2.88 C. Electrolysis experiments carried out after the third cycle presented a constant coulombic efficiency of 50%, in agreement with previous observations made by constant-current electrolysis.¹⁸ The charge-time curves obtained from the electrolysis experiments, circles in Figure 3.4B, were fit with equations (3-2) and (3-3) assuming an EC reaction scheme:³⁰

$$Q_f(t) = nFVC_{Fe(III)TEA}^*(0)[1 - \exp(-pt)] \quad (3-2)$$

$$Q_r(t) = \frac{nFVpC_{Fe(II)TEA}^*(t_1)}{(p + k)} [1 - \exp[-(p + k)(-kt_1)]] \quad (3-3)$$

where n is the number of electrons transferred, F is Faraday's constant, $C_{Fe(III)TEA}^*(0)$ is the bulk concentration of **2** at the beginning of the first reduction electrolysis, $C_{Fe(II)TEA}^*(t_1)$ is the bulk concentration of **3** at the beginning of the first oxidation electrolysis, k is the rate constant of the homogeneous EC reaction, and $p = mA/V$, where m is the mass transfer coefficient, A is the area of the electrode, and V is the volume of solution used. The rate of the homogeneous reaction was calculated from the numerical fit of all the charge-time curves presented in Figure 3.4B with equations (3-2) and (3-3), shown by solid lines in the figure. As can be seen, good agreement was obtained between simulated and

experimental data. The rate constant calculated is $k = 2.0 \pm 0.8 \times 10^{-5} \text{ s}^{-1}$. The overall EC scheme can then be expressed as:



We propose that the product of the homogeneous condensation reaction, **4**, is electrochemically active with essentially the same E^0 as Fe(III/II)-TEA. However, oxidation of **4** does not produce 2 moles of **2** but rather the mixed valence compound **5** that is chemically stable in 5 M NaOH. Further evidence for the existence of such mixed valence compound is provided in the next section. The magnitude, $k = 2.0 \pm 0.8 \times 10^{-5} \text{ s}^{-1}$, indicates that the homogeneous condensation reaction of **3** is slower than the experimental time accessible in slow scan rate CVs. Such an observation may explain why the homogeneous reaction was not reported in the past. To the best of our knowledge, this is the first work to report the existence of a homogeneous reaction coupled to the heterogeneous reduction of Fe(III)-TEA in alkaline solutions.

Cyclic Voltammetry at UMEs

Figure 3.5 shows CVs recorded at GC UMEs ($a = 5 \text{ }\mu\text{m}$) from solutions containing the same total concentration of Fe(III) or Fe(II) ions, $C_{Fe} = 0.5 \text{ M}$, but different species in 5 M NaOH_(aq). The black CV in Figure 3.5A corresponds to the reduction of 0.5 M **2** (this solution is light brown, see Figure A5A). The CV presented a quasireversible electron transfer reaction and reached a plateau current of about 100 nA. The electron transfer kinetics for the reduction of **2** were evaluated in triplicate by the method of Mirkin and Bard⁴⁰ from similar CVs, and a value of $k^0 = 1.2 \pm 0.7 \times 10^{-3} \text{ cm s}^{-1}$

was obtained. Such a standard rate constant is smaller than other known couples, *e.g.*, $k^0 = 2 \text{ cm s}^{-1}$ for FcMeOH.⁴¹ The red trace in Figure 3.5A is a CV recorded in a freshly prepared solution of 0.25 M **4** in 5 M NaOH (see light green solution in Figure A5B). The electrode potential is swept positively to carry out the oxidation of **4**, and a plateau current is reached at about -129 nA. The shape of the CV differs from that seen in the black CV, and may suggest two overlapping redox waves with E^0 values separated only by a few tens of mV. The electron transfer kinetics for the oxidation of **4** could not be determined by the method of Mirkin and Bard, but the slope of the CV clearly deviates from Nernstian behavior, indicating a smaller k^0 than the standard rate calculated from the black CV.

Finally, the blue CV shown in Figure 3.5A was recorded after a solution of 0.25 M **4** in 5 M NaOH was vigorously bubbled with air for 15 min. The O₂ present in air was

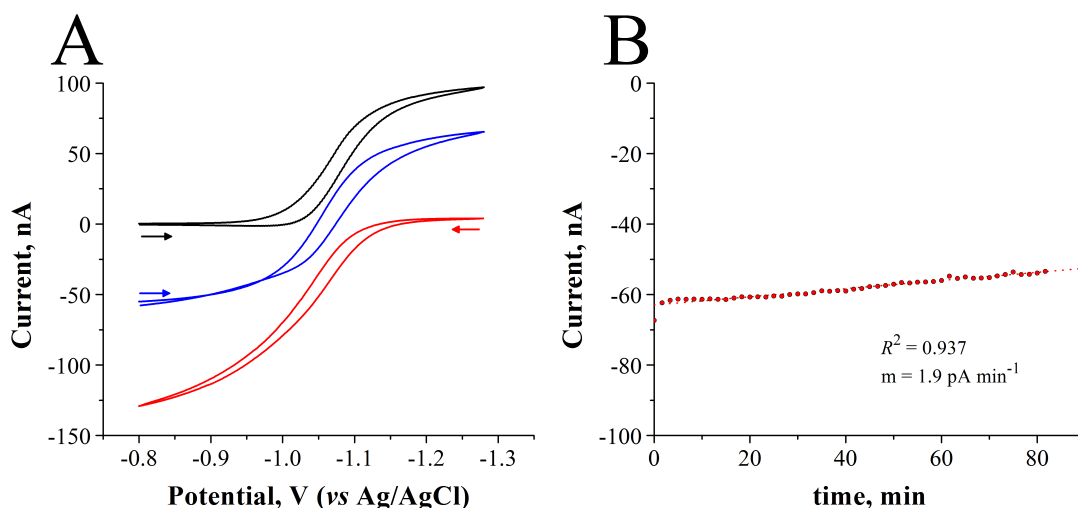


Figure 3.5. **A.** CVs recorded at a GC tip ($a = 5 \mu\text{m}$) in 3 different solutions: black trace is 0.5 M **2** in 5 M NaOH; red trace is 0.25 M **4** in 5 M NaOH; and blue trace is 0.25 M **5** in 5 M NaOH. The blue CV was obtained after vigorously bubbling a solution containing 0.25 M **4** with air for 15 min. $v = 10 \text{ mV s}^{-1}$. **B.** Chronoamperometry recorded in the solution corresponding to the blue trace in Figure 3.5A at $E = -0.80 \text{ V}$. Current sampling is depicted by red dots. The dashed line is a linear fit carried out to extract the change in current over time, with slope $m = 1.9 \text{ pA min}^{-1}$.

reduced to hydrogen peroxide by **4** and produced the mixed valence compound **5** (see dark yellow solution in Figure A5C). As expected, the blue CV in Figure 3.5A shows intermediate behavior between the black and red CVs. More importantly, the cathodic and anodic plateau currents are about 50% of those observed in solutions containing **2** and **4**, respectively. We believe the aforementioned observations are in agreement with the EC reaction scheme proposed in this work. More importantly, the blue CV in Figure 3.5A indicates that **5** is chemically stable in 5 M NaOH. The chemical stability of the mixed valence compound was further investigated by carrying out chronoamperometry in the same solution at $E = 0.80$ V in air, shown in Figure 3.5B. The steady state current recorded at the UME changed only 10 nA in 80 min., at a rate of 1.9 pA min.^{-1} (extracted from a linear fit of the chronoamp, shown by dashed line in Figure 3.5B). The change in current is associated with slow contamination of the electrode surface rather than decomposition of **5**. Treatment of the electrode by mechanical polishing returned the current to the initial steady state value.

Determination of Stability Constants

Experiments were carried out to determine the magnitude of the stability constants, β , of **2** and **3** in 5 M NaOH. Previous works reported β values for structures such as $[\text{Fe(III)}(\text{H}_3\text{TEA})]^{3+}$ at $\text{pH} = 3$ (H_3TEA is the protonated TEA, $\text{pH} < 7.7$), $\log \beta_{\text{Fe(III)TEAH}} = 8.14$,⁴² and $[\text{Fe}(\text{TEA})_2(\text{OH})_4]^-$ at $\text{pH} = 9$, $\log \beta_{\text{Fe(III)(TEA)}_2} = 44.6$.⁴³ However, the experimental results presented herein demonstrate that neither one of such structures exist in 5 M $\text{NaOH}_{(\text{aq})}$. Therefore, experiments were carried out to determine $\beta_{\text{Fe(III)TEA}}$ and $\beta_{\text{Fe(II)TEA}}$. Note that the experimental results presented in this section were obtained at concentrations of each complex < 5 mM, where the EC reaction scheme is not favored. Figure A7 of Appendix A shows typical spectra obtained in the presence and absence of

2 and **3**, at concentrations < 1 mM. When the complexes are present in solution, two broad bands are observed with peak maxima at $\lambda_{\text{max}} = 243$ nm and $\lambda_{\text{max}} = 280$ nm. The spectra obtained from **2** and **3** showed the same absorption bands at concentrations < 1 mM, with molar absorptivities $\epsilon_{\text{Fe}^{3+}} > \epsilon_{\text{Fe}^{2+}}$, as shown in Figure A7. Binding isotherms of absorbance *vs.* concentration of ferric/ferrous ions at a fixed concentration of ligand were constructed by using the maximum absorbance $\lambda_{\text{max}} = 243$ nm, shown in Figure 3.6.

Figure 3.6A shows the binding isotherm constructed with increasing moles of Fe(III) in the presence of 1 mM TEA. The plot shows a straight line with correlation coefficient $R^2 = 0.999$. A flat plateau was reached at $[\text{Fe(III)}]/[\text{TEA}] \approx 0.95$,

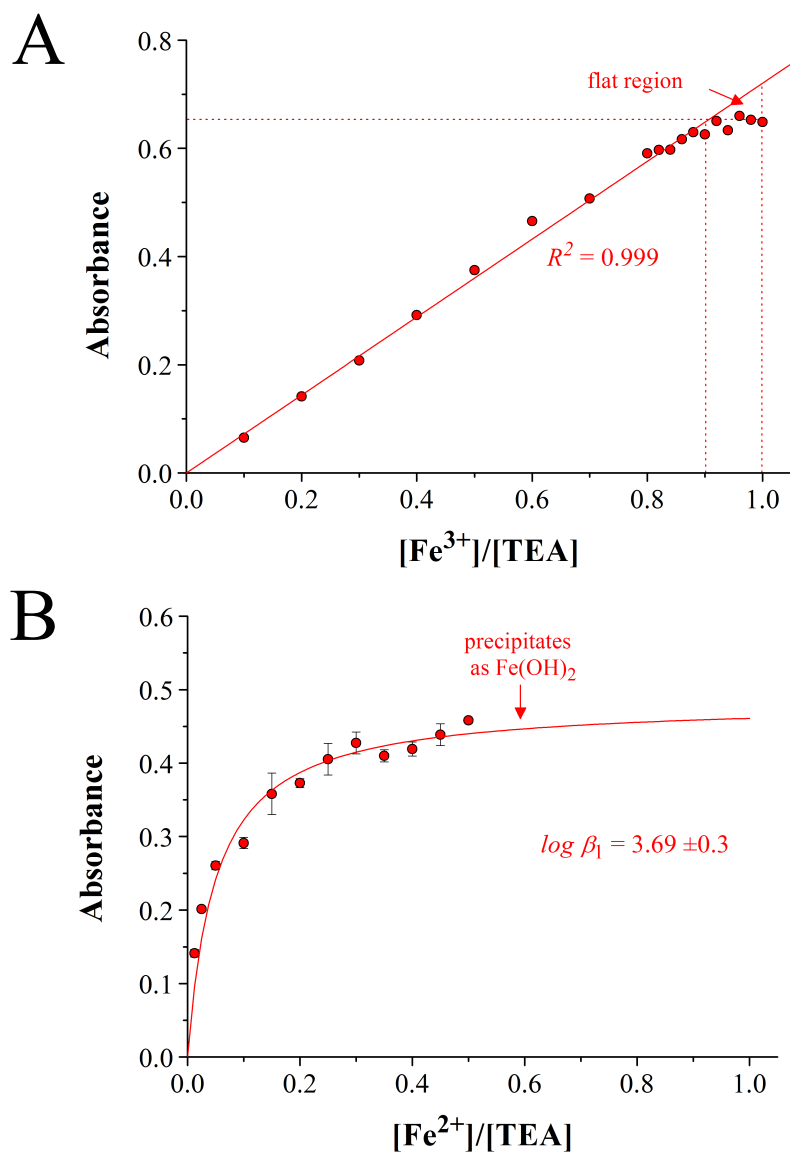


Figure 3.6. Binding isotherms constructed at a constant concentration of ligand, $[\text{TEA}] = 1 \text{ mM}$. A. Isotherm from the complexometric titration of TEA with Fe(III), metal-to-ligand ratio at equivalence point is 1:1. B. Isotherm from the complexometric titration of TEA with Fe(II), metal-to-ligand ratio at equivalence point is 1:2. Absorbance values were recorded using $\lambda = 243 \text{ nm}$. Electrolyte is 5 M NaOH, ionic strength is $\mu = 5.0$.

corresponding to the equivalence point of the complexometric titration. Importantly, the isotherm never deviated from linearity, and indication that $\beta_{\text{Fe(III)TEA}}$ is so large that it cannot be determined by the spectrophotometric method. Since $\beta_{\text{Fe(II)TEA}} \ll \beta_{\text{Fe(III)TEA}}$ we carried out a similar set of experiments to determine $\beta_{\text{Fe(II)TEA}}$. In this case, excess ligand with a metal-to-ligand ratio of 1:2 was used to favor the complexation of Fe(II) with TEA. Figure 3.6B shows the binding isotherm constructed with increasing moles of Fe(II) in the presence of 1 mM TEA. The isotherm was fit with equation (3-6) to extract the stability constant:

$$\frac{A}{l} = \frac{\beta_{\text{Fe(II)TEA}} \varepsilon C_{\text{TEA}} C_{\text{Fe(II)}}}{[\text{OH}^-] + \beta_{\text{Fe(II)TEA}} C_{\text{Fe(II)}}} \quad (3-6)$$

Equation (3-6) was derived from Beer's law and the equilibria equations involved in this system. The stability constant was determined to be $\log \beta_{\text{Fe(II)TEA}} = 3.69 \pm 0.3$. The stability constant $\beta_{\text{Fe(III)TEA}}$ was then calculated from the experimental $E^0_{\text{Fe(III/II)TEA}} = -1.05$ V with the Nernst equation (assuming $[\text{Fe(III)}] = [\text{Fe(II)}]$):

$$E^{0'} = E^0_{\text{Fe(III/II)}} - \frac{RT}{nF} \ln \frac{\beta_{\text{Fe(III)TEA}}}{\beta_{\text{Fe(II)TEA}}} \quad (3-7)$$

where $E^0_{\text{Fe(III/II)}} = 0.57$ V. The magnitude is $\log \beta_{\text{Fe(III)TEA}} = 31.10 \pm 0.3$ at $\mu = 5.0$ M. Such a stability constant is larger than the value corresponding to the complex of iron with ethylenediaminetetraacetic acid (EDTA), $[\text{Fe(EDTA)}]^-$, one of the strongest stability constants measured in aqueous chemistry for a hexadentate ligand, with a magnitude of $\log \beta_{[\text{Fe(EDTA)}]} = 25.1$ at $\mu = 0.1$ M.⁴⁴ We had particular interest in determining the stability constants for the Fe-TEA system because of the relevance of the ferric/ferrous couple in aqueous electrochemistry, with an E^0 that can be tuned by ligand selection from +1.28 V,

using tripyridinetriazine in acidic solutions,⁴⁵ to -1.05 V, using TEA in base, spanning a potential window of 2.3 V and a pH window of 14.7 pH units.

3.5. CONCLUSIONS

This work presented a systematic characterization of the system Fe(III/II)-TEA in 5 M NaOH_(aq) by structural, electrochemical, and spectroscopic analysis. Importantly, we present an approach that suggests the structure of inorganic complexes in solution. The approach uses XRD analysis to determine the structure of a complex in the solid state. Then, Raman spectroscopy is used to analyze the same complex in solution. Finally, DFT analysis is used to predict the Raman spectra of the dissolved species with the structure observed in the solid state. Differences in experimental and simulated spectra indicate different structures in each phase.

The structure of Fe(III)-TEA in the solid state, Na₂[(μ -O)(Fe(TEA))₂](H₂O)₆, determined with crystals grown from 5 M NaOH is reported for the first time. More importantly, the definitive structure of Fe(III)-TEA in alkaline solution, [Fe(III)(TEA)(OH)]⁻, is also reported for the first time. Additionally, electrochemical studies carried out on [Fe(III)(TEA)(OH)]⁻ reveal an EC reaction scheme. [Fe(III)(TEA)(OH)]⁻ is reduced in a one-electron heterogeneous reaction to [Fe(II)(TEA)(OH)]²⁻. At concentrations > 10 mM, the product of the reduction reaction undergoes a homogeneous condensation reaction to form [(μ -O)(Fe(TEA))₂]⁴⁺, the favored dinuclear species. Such species is redox active at the same potentials as [Fe(III)(TEA)(OH)]⁻ and can be oxidized to a mixed valence compound, [(TEA)Fe(III)OFe(II)(TEA)]³⁺, in a reaction that transfers 1 mole of electrons per mole of complex. Such results are particularly relevant to the field of energy storage because Fe(III/II)-TEA is considered a promising candidate for RFB applications.

Finally, the stability constants of $[\text{Fe(III)(TEA)(OH)}]^-$ and $[\text{Fe(II)(TEA)(OH)}]^{2-}$ were determined by UV-Vis spectroscopy and CV from solutions of the complexes at concentrations < 10 mM. $[\text{Fe(III)(TEA)(OH)}]^-$ presents a stability constant of $\log \beta_{\text{Fe(III)TEA}} = 31.10 \pm 0.3$, one of the largest stability constants measured in aqueous chemistry.

3.6. REFERENCES

- [1] Jaffe, E.; *Industria Chimica*, **1934**, *9*, 750-752.
- [2] Wolfson, H.; *Nature*, **1944**, *153*, 375-376.
- [3] Jessop, G.; *Nature*, **1946**, *158*, 59-59.
- [4] Spalenka, M.; *Hutnicke Listy*, **1953**, *8*, 362-363.
- [5] Bechtold, T.; Burtscher, E.; Turcanu, A.; Bobleter, O.; *Text. Res. J.*, **1997**, *67*, 635-642.
- [6] Bechtold, T.; Burtscher, E.; Turcanu, A.; Bobleter, O.; *J. App. Electrochem.*, **1997**, *27*, 1021-1028.
- [7] Bechtold, T.; Turcanu, A.; *J. Electrochem. Soc.*, **2002**, *149*, D7-D14.
- [8] Bechtold, T.; Burtscher, E.; Gmeiner, D.; Bobleter, O.; *J. Electroanal. Chem.*, **1991**, *306*, 169-183.
- [9] Bechtold, T.; Burtscher, E.; Turcanu, A.; Bobleter, O.; *J. Electrochem. Soc.*, **1996**, *143*, 2411-2416.
- [10] Switzer, J. A.; Gudavarthy, R. V.; Kulp, E. A.; Mu, G.; He, Z.; Wessel, A. J.; *J. Am. Chem. Soc.*, **2010**, *132*, 1258-1260.
- [11] Kothari, H. M.; Kulp, E. A.; Limmer, S. J.; Poizot, P.; Bohannan, E. W.; Switzer, J. A.; *J. Mater. Res.*, **2006**, *21*, 293-301.
- [12] Kulp, E. A.; Kothari, H. M.; Limmer, S. J.; Yang, J.; Gudavarthy, R. V.; Bohannan, E. W.; Switzer, J. A.; *Chem. Mater.*, **2009**, *21*, 5022-5031.
- [13] Saalfrank, R. W.; Bernt, I.; Uller, E.; Hampel, F.; *Angew. Chem. Int. Ed. Engl.*, **1997**, *36*, 2482-2485.
- [14] Pilawa, B.; Desquiotz, R.; Kelemen, M. T.; Weickenmeier, M.; Geisselmann, A.; *J. Magn. Magn. Mater.*, **1997**, *177*, 748-749.

- [15] Saalfrank, R. W.; Deutscher, C.; Sperner, S.; Nakajima, T.; Ako, A. M.; Uller, E.; Hampel, F.; Heinemann, F. W.; *Inorg. Chem.*, **2004**, *43*, 4372-4382.
- [16] Murugesu, M.; Abboud, K. A.; Christou, G.; *Dalton Trans.*, **2003**, 4552-4556.
- [17] Wen, Y. H.; Zhang, H. M.; Qian, P.; Zhou, H. T.; Zhao, P.; Yi, B. L.; Yang, Y. S.; *Electrochim. Acta*, **2006**, *51*, 3769-3775.
- [18] Arroyo-Currás, N.; Hall, J.W.; Dick, J.E.; Jones, R. A.; Bard, A.J.; *J. Electrochem. Soc.*, **2015**, *162*, A378-A383.
- [19] Buddhadev, S.; Dotson, R. L.; *J. Inorg. Nucl. Chem.*, **1970**, *32*, 2707-2716.
- [20] Sen, B.; Dotson, R. L.; *J. Inorg. Nucl. Chem.*, **1970**, *32*, 2707-2716.
- [21] Schmidt, S.; Prodius, D.; Novitchi, G.; Mereacre, V.; Kostakis, G. E.; Powell, A. K.; *Chem. Commun.*, **2012**, *48*, 9825-9827.
- [22] Ali, A. E.; *Egypt. J. Chem.*, **2005**, *48*, 121.
- [23] Jones, L. F.; Jensen, P.; Moubaraki, B.; Berry, K. J.; Boas, J. F.; Pilbrow, J. R.; Murray, K. S.; *J. Mater. Chem.*, **2006**, *16*, 2690-2697.
- [24] Fielden, J.; Speldrich, M.; Besson, C.; Korgeler, P.; *Inorg. Chem.*, **2012**, *51*, 2734-2736.
- [25] Ibanez, J. G.; Choi, C.; Becker, R. S.; *J. Electrochem. Soc.*, **1987**, *134*, 3083-3089.
- [26] Rosemount Analytical, *Conductance Data for Commonly Used Chemicals* (Irvine, CA, 2010).
- [27] Wu, X.; He, G.; Gao, Q.; Han, Y.; Zhang, D.; Zhen, D.; Jiang, X.; A full-iron complex flow battery having high open-circuit voltage. CN 103700872 A 20140402, April 2, 2014.
- [28] Zhang, H.; Wen, Y.; Qian, P.; Yi, B.; Fe complex/halogen electrochemical system used for liquid flow electricity storage. CN 101047261 A 20071003, October 7, 2007.
- [29] Connors, K. A.; *Binding Constants: The Measurement of Molecular Complex Stability*, Wiley: New York, 1987.
- [30] Bard, A. J.; Faulkner, L. R.; *Electrochemical Methods: Fundamentals and Applications*; Wiley: New York, 2000.
- [31] Sheldrick, G. M.; *Acta Cryst. A*, **2007**, *64*, 112-122.
- [32] Becke, A. D.; *J. Chem. Phys.*, **1993**, *98*, 5648-5652.
- [33] Dolg, M.; Wedig, U.; Stoll, H.; Preuss, H.; *J. Chem. Phys.*, **1987**, *86*, 866-872.
- [34] Barone, V.; Cossi, M.; *J. Phys. Chem. A* **1998**, *102*, 1995-2001.

- [35] Cossi, M.; Rega, N.; Scalmani, G.; Barone, V. *J. Comp. Chem.* **2003**, *24*, 669-681.
- [36] Andersson, M. P.; Uvdal, P.; *J. Phys. Chem. A*, **2005**, *109*, 2937-2941.
- [37] Robin, M. B.; Day, P.; *Adv. Inorg. Chem. Rad.*, **1968**, *10*, 247-422.
- [38] Day, P.; Hush, N. S.; Clark, J. H.; *Phil. Trans. R. Soc. A*, **2008**, *366*, 5-14.
- [39] Kurtz, D. M.; *Chem. Rev.*, **1990**, *90*, 585-606.
- [40] Mirkin, M. V.; Bard, A. J.; *Anal. Chem.*, **1992**, *64*, 2293-2302.
- [41] Miao, W.; Ding, Z.; Bard, A. J.; *J. Phys. Chem. B*, **2002**, *106*, 1392-1398
- [42] Anderegg, G.; *Inorg. Chim. Acta*, **1986**, *121*, 229-231.
- [43] Kunaszewska, M.; *Roczniki Chemii*, **1973**, *47*, 683-691.
- [44] Standard Reference Data Program (National Institute of Standards and Technology (U.S.)). NIST Critically Selected Stability Constants of Metal Complexes Database; Smith, R. M.; Martell, A. E.; Motekaitis, R. J., Eds.; NIST Standard Reference Database; Version 8.0.; U.S. Dept. of Commerce, Technology Administration, National Institute of Standards and Technology, Standard Reference Data Program: Gaithersburg, MD, 2004.
- [45] Chen, Y. D.; Santhanam, K. S. V., Bard, A. J.; *J. Electrochem. Soc.*, **1981**, *128*, 1460-1467.

Chapter 4. An Alkaline Flow Battery Based on the Coordination Chemistry of Iron and Cobalt^{*,†}

4.1. ABSTRACT

We present the first a-RFB based on the coordination chemistry of cobalt(III/II) with mTEA and iron(III/II) TEA in 5 M NaOH_(aq). The overall redox system has a cell voltage of 0.93 V in the charged state. Importantly, the coordination compounds are negatively charged and have limited transport through the cation exchange membrane (*i.e.*, Nafion), minimizing the extent of redox species crossover during charge-discharge cycling. Fe-TEA is electrochemically reversible and soluble up to 0.8 M, whereas Co-mTEA presents quasireversible electron transfer kinetics and can be solubilized up to 0.7 M. Cyclability was tested with a flow cell at a concentration of 0.5 M up to 30 cycles using a 50 μm thick Nafion membrane, at 30 mA/cm², with minimal crossover (less than 4% of net concentration) or evolution of gases detected.

4.2. INTRODUCTION

RFBs have excellent potential for electrical grid energy storage. However, they have not yet been widely deployed because of problems concerning stability and limited cycle life. In this report we describe the use of coordination compounds of cobalt(III/II) with mTEA (Figure 1.2), and iron(III/II) with TEA (Figure 1.2) in 5 M NaOH_(aq) as a RFB. The flow battery was optimized to achieve stable cycling with 71% average energy efficiency in 30 cycles when passing 30 mA cm⁻², and using a 50 μm -thick Nafion

* Arroyo-Currás, N.; Hall, J. W.; Dick, J. E.; Jones, R. A.; Bard, A. J.; *J. Electrochem. Soc.*, **2015**, *162*, A378-A383.

† Justin W. Hall carried out the structural characterization of the complexes using single crystal XRD. Jeffrey E. Dick assisted in the collection of electrochemical data. Allen J. Bard and Richard A. Jones were the PIs.

membrane as the separator, at a concentration of 0.5 M. Importantly, crossover of the redox species through the membrane was below 4% of the original concentration at the end of the 30th cycle, with no evolution of gases detected during cycling.

We developed this alkaline RFB as an alternative to state-of-the-art RFBs, *e.g.*, the all vanadium RFB, which are based on acidic electrolytes.¹ Acidic RFBs often suffer capacity fading due to membrane crossover and the occurrence of undesired secondary reactions during battery cycling (*e.g.*, precipitation, evolution of H₂ and Cl₂ gases).² Acidic electrolytes have a high conductance, $G_{\max} = 825 \text{ mS cm}^{-1}$ for 3 M H₂SO_{4(aq)},³ but tend to be corrosive to the cell components, which translates into high operational and maintenance costs.⁴ In contrast, alkaline electrolytes, such as NaOH, have lower conductance, $G_{\max} = 410 \text{ mS cm}^{-1}$ for 3.7 M NaOH_(aq),¹⁸ but are less corrosive. Alkaline electrolytes employing transition metals generally require the use of coordination compounds as redox species to prevent precipitation of the hydroxides or hydrous oxides. The net charge on these ions can be tailored by ligand selection to minimize membrane crossover with a cation exchange membrane. Moreover, different ligands can be used to tune the electrode potential of the half-cells to optimize the voltage of the battery.⁵

The formation of chemically stable soluble coordination compounds of cobalt and iron in 5 M NaOH is challenging because of a thermodynamic tendency to form their insoluble hydroxides. For iron(III), with a solubility product, K_{sp} , of the corresponding hydroxide of 10^{-38} , a strong interaction must exist between the Fe(III) ion and an organic ligand, L , so that the stability constant of the complex formed, β , is considerably larger than the K_{sp} of the metal hydroxide, *i.e.* $\beta_{[\text{L}]} \gg K_{\text{sp}, [\text{OH}]}$.³ Thus $\log \beta_{\text{Fe(III)}}$ must be larger than about 39 for $[\text{OH}^-] = 5 \text{ M}$, $[\text{L}] = 1 \text{ M}$, and $[\text{Fe(L)}] = 1 \text{ M}$. We carried out experiments to find coordination compounds that were chemically stable in 5 M NaOH (with $\log \beta \approx 39$), redox active with a very negative E^0 but in the potential window of the

electrolyte, and with fast heterogeneous electron transfer kinetics. This was achieved by coordination of Fe with TEA and of Co with mTEA. In previous reports, complexes of these two metal ions with amino-alcohol ligands, such as TEA, were successfully synthesized in base and used in analytical determinations,⁶⁻⁸ electrodeposition,^{9,10} electrochemical studies,^{11,12} and the reduction of dyes.¹³⁻¹⁵ The Yang group has previously proposed the use of Fe-TEA as the negative redox couple in RFB studies with the Br₂/Br⁻ as the positive couple.¹⁶ However, Br₂ is not stable when it contacts strong base, and it is not possible to maintain and operate a RFB with different pHs on different sides of the ion exchange membrane. Thus, their RFB showed poor coulombic performance. This problem was addressed in the present work by finding a chemically stable, positive redox couple in 5 M NaOH, Co(II/III)-mTEA. This couple is negatively charged and electrochemically quasireversible in 5 M NaOH. The coulombic efficiency of the cell was improved by better understanding the chemistry of Fe(III/II)-TEA, and by using redox couples that present minimal membrane crossover.

4.3. METHODS

Synthesis of Coordination Compounds

A round bottom flask was filled with deionized water (20.0 mL) and bubbled with argon. After bubbling for 5 min., the required mass of FeCl₃·6H₂O, FeCl₂·4H₂O, or CoCl₂ was added with stirring. To this solution, two moles of TEA (with respect to moles of metal ion) were added in the case of Fe(II/III)-TEA, and one mole of mTEA was added in the case of Co(II)-mTEA, with stirring. In a separate container, NaOH pellets (8.0 g) were dissolved in deionized water (10.0 mL). After the NaOH dissolved, the container was placed in a water bath to cool to 25° C. This NaOH solution was added dropwise to the Mⁿ⁺ + ligand solutions. The volumes of all solutions were adjusted to 40.0 mL upon

completion of the synthesis reactions. All reactions yield +95% product (complexes) as determined by the plateau current observed from steady-state voltammograms. The same procedure can be scaled to achieve concentrations up to 0.8 M Fe(III)-TEA (0.2 M higher than previously reported),¹⁶ 0.65 M Fe(II)-TEA, and 0.6 M Co(II)-mTEA. The ligand-to-metal stoichiometry of all reactions is 1:1. TEA was added in excess to favor the formation of the complexes at high concentrations. Synthesis of Co(III)-mTEA (dark green) was carried out by bulk electrolysis from Co(II)-mTEA.

Instrumentation

UV-Vis spectra were acquired with a SEC2000-UV/VIS Spectrometer, using a quartz cuvette with path length $l = 1$ cm. Voltammetry and potential-step experiments were carried out with a CHI660D electrochemistry workstation from CH Instruments (Austin, TX). GC electrodes ($d = 2$ mm) were purchased from Princeton Applied Research (Oak Ridge, TN). The electrodes were initially polished with sand paper, and then on microcloth pads with alumina paste of different sizes (1.0 to 0.05 μm) to ensure a mirror-like finish. Soft polishing with alumina paste was also carried out between measurements. A three-electrode cell configuration was used, with GC as the working electrode, an Ag/AgCl (sat. KCl) reference electrode, and a reticulated carbon mesh ($A = 1$ cm²) as the counter electrode. For bulk electrolysis, a three-compartment cell with porous glass separators was used.¹⁷ Reticulated vitreous carbon was used in the electrolysis experiments. High mass transfer rates were achieved during electrolysis by sonication using a Branson B-220 Ultrasound Cleaner. All solutions were bubbled thoroughly with argon gas before experimentation and kept under a humidified argon blanket.

Flow Cell construction and Cycling Analysis

The flow cell design used in this work was based on a previous report.¹⁸ Briefly, a commercial fuel cell from Fuel Cell Technologies (Albuquerque, NM) was modified to accept a liquid feed at both electrodes, and the surface area of both electrodes was decreased to 3.24 cm², shown in Figure A8. The RFB was assembled in a “zero-gap” configuration. A Nafion-112 membrane (50 μm thick) served as the separator. The high surface area electrodes were 10 AA carbon paper from SGL Technologies GmbH (Germany) with an uncompressed thickness of 380 ± 60 μm and area weight of 85 ± 14 g m⁻². The current collectors were Poco graphite plates with machined serpentine flow channels. Contact to the current collectors was made with nickel-plated copper plates.

Constant-current and current-interrupt experiments were carried out with an Autolab PGSTAT 128N in preliminary tests. Battery cycling studies were carried out with an Arbin BT2000 Battery Cycler in a two-electrode configuration. Charge-discharge curves were recorded galvanostatically, with the battery at an initial state of charge (SoC) of 0%. The SoC was calculated from the total charge collected at constant currents of 70 - 100 mA and Faraday’s law. For example, in a battery containing 50 mM of redox couple (n = 1) in 20 mL of electrolyte, charging from 0% to 100% SoC was achieved in 1,929 s (assuming 100% current efficiency). All cycling measurements were carried out at current densities of 21 - 30 mA/cm². Further, all experiments were carried out at room temperature with no active temperature control.

Magnetic drive pumps from Cole Parmer (Vernon Hills, IL) were used to maintain an electrolyte flow rate of 140 mL min.⁻¹ for Co-mTEA and 200 mL min.⁻¹ for Fe-TEA during cycling. Argon purging in both reservoirs was carried out to minimize spontaneous oxidation of Fe(II)-TEA to Fe(III)-TEA by oxygen during cycling. Norprene[®] tubing was used to connect the pumps to the flow cell and to the storage

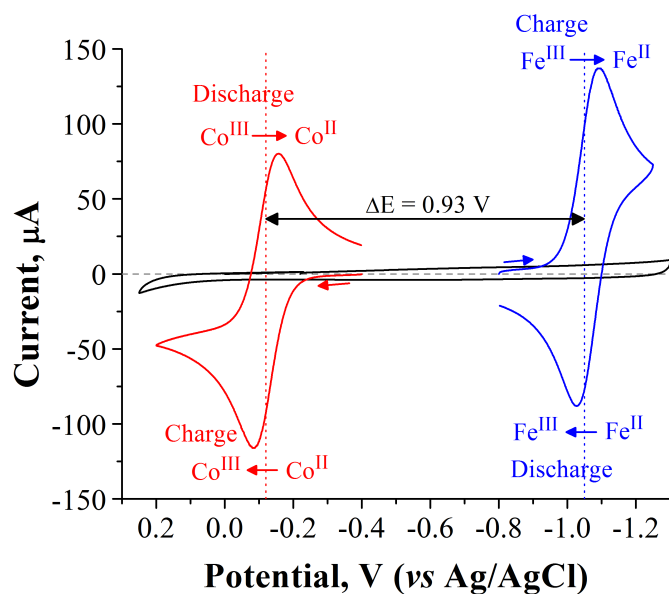


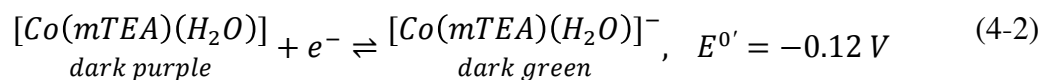
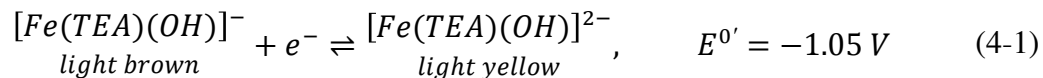
Figure 4.1. Cyclic voltammograms of 2 mm diameter glassy carbon electrode (black), 20 mM $[\text{Fe}(\text{TEA})(\text{OH})]^-$ (blue), and 20 mM $[\text{Co}(\text{mTEA})(\text{H}_2\text{O})]^-$ (red) in aqueous 5 M NaOH. The scan rate is $\nu = 50 \text{ mV s}^{-1}$. The complexes were synthesized using stoichiometric amounts of metal ion and ligand. $\Delta E_{\text{p}_{\text{Fe-TEA}}} = 60 \text{ mV}$, $\Delta E_{\text{p}_{\text{Co-mTEA}}} = 73 \text{ mV}$. $E^{\circ'}_{\text{Fe-TEA}} = -1.05 \text{ V}$ and $E^{\circ'}_{\text{Co-mTEA}} = -0.12 \text{ V}$.

reservoirs. The current-interrupt method³⁰ was used to determine the area specific resistance (ASR) of the cell during cycling, and an $\text{ASR} = 8.3 \Omega \text{ cm}^2$ was obtained.

4.4. RESULTS

Voltammetry

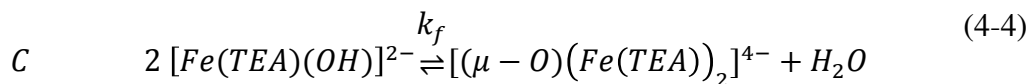
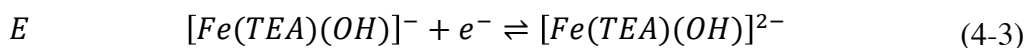
Figure 4.1 shows typical CVs of 20 mM $[\text{Co}(\text{mTEA})(\text{H}_2\text{O})]^-$ (in red) and 20 mM $[\text{Fe}(\text{TEA})(\text{OH})]^-$ (in blue) in 5 M NaOH, recorded at a scan rate $\nu = 50 \text{ mV s}^{-1}$. The reactions corresponding to each redox process are shown in equations (4-1) and (4-2):



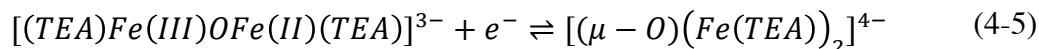
The chemical formula of $[\text{Fe}(\text{TEA})(\text{OH})]^-$ was determined by single-crystal XRD analysis and confirmed by Raman spectrometry coupled to DFT calculations (refer to Chapter 3).¹⁹ The chemical formula of $[\text{Co}(\text{mTEA})(\text{H}_2\text{O})^-]$ is reported from preliminary single-crystal XRD results, shown in Figure A9. Both reactions are diffusion controlled, as determined by plots of i_p vs. $v^{1/2}$ shown in Figures A10 and A11, outer-sphere heterogeneous electron transfer processes. Reaction (4-1) is electrochemically reversible¹⁶ with $\Delta E_p = 60$ mV, whereas reaction (4-2) is quasireversible with $\Delta E_p = 73$ mV.

Bulk Electrolysis

The number of electrons transferred in each reaction was determined by controlled potential coulometry, shown in Figure 4.2. The electrolysis cell was calibrated using FeMeOH as a standard, shown in Figure A12. The reduction of $[\text{Fe}(\text{TEA})(\text{OH})]^-$, reaction (4-1), carried out past the cathodic CV peak at -1.15 V showed $Q_{\text{exp}}/Q_{\text{theo}} = 0.98$ at $t = 700$ s, using $Q_{\text{theo}} = nFVC^*$, where $n = 1$ is the number of electrons, F is Faraday's constant, V is the solution volume, C^* is the initial concentration of analyte, and $Q_{\text{exp}} = 4.51$ C (Figure 4.2A). The current decayed smoothly to the background value and a plot of $\log(i)$ vs. t yielded a straight line (Figure 4.2B).²⁰ Reverse electrolysis carried out at -0.8 V consumed approximately the same number of coulombs as the forward electrolysis (4.89 C). Such results are only valid for concentrations of $[\text{Fe}(\text{TEA})(\text{OH})]^- \leq 10$ mM. At concentrations higher than 10 mM, the reduction of $[\text{Fe}(\text{TEA})(\text{OH})]^-$ follows an EC reaction scheme:¹⁹



where $k_f = 2.0 \pm 0.8 \times 10^{-5} \text{ M}^{-1} \text{ s}^{-1}$. The dinuclear compound produced after the condensation reaction (4-4) is electrochemically active at the same formal potential of $[\text{Fe}(\text{TEA})(\text{OH})]^-$, but only gives one electron back:



The mixed valence compound $[(\text{TEA})\text{Fe}(\text{III})\text{OFe}(\text{II})(\text{TEA})]^{3-}$ is the chemically stable form of the oxidation product of $[(\mu - \text{O})(\text{Fe}(\text{TEA}))_2]^{4-}$ at concentrations $\approx 0.5 \text{ M}$. This indicates that at least 2 moles of Fe(II) per mole of Co(III) must be used in the

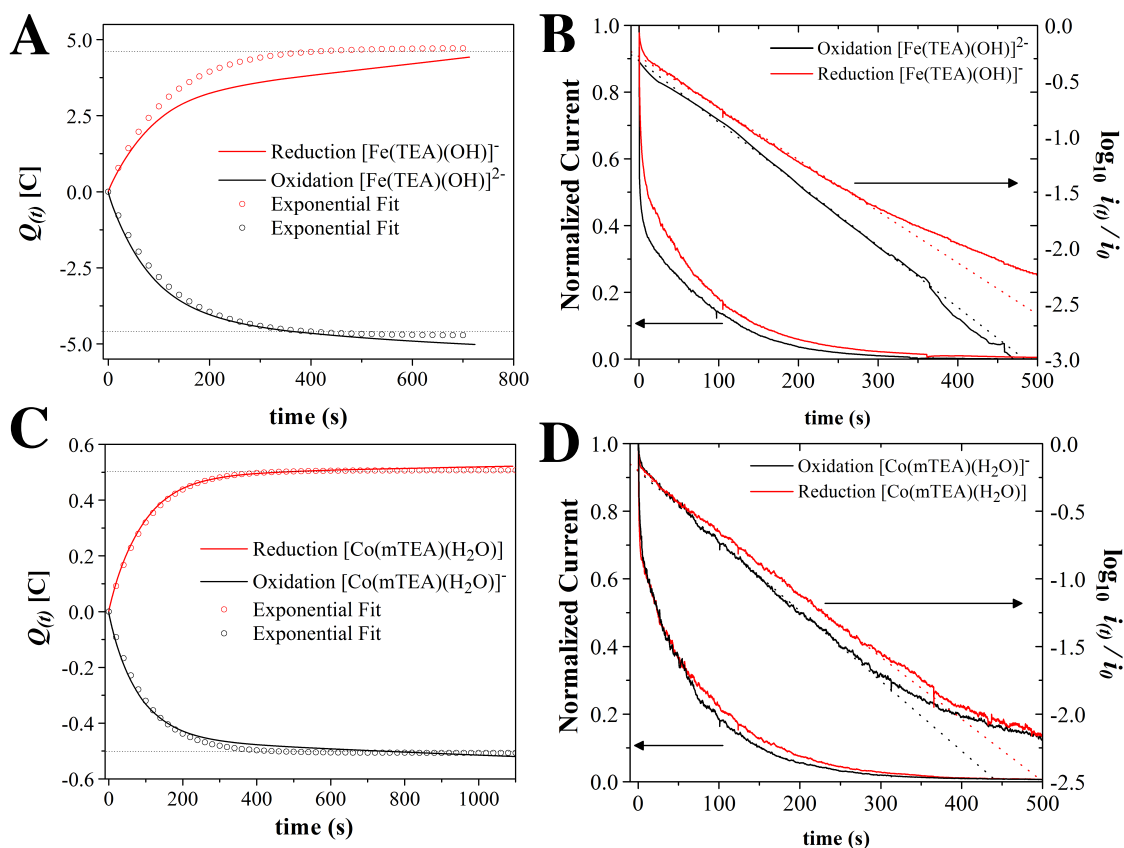


Figure 4.2. **A, C.** Plots of charge (coulombs) vs. electrolysis time constructed from the current-time curves corresponding to 10 mM $[\text{Fe}(\text{TEA})(\text{OH})]^-$ and 1.2 mM $[\text{Co}(\text{mTEA})(\text{H}_2\text{O})]^-$ in aqueous 5 M NaOH. Volume = 4.5 mL. **B, D.** Current-time and $\log_{10}(\text{current})$ -time curves during exhaustive electrolysis of the same solutions at a reticulated vitreous carbon electrode.

battery. Oxidation of $[\text{Co}(\text{mTEA})(\text{H}_2\text{O})]^-$, reaction (4-2), was carried out past the cathodic CV peak at 0.2 V and showed $Q_{\text{exp}}/Q_{\text{theo}} = 1.0$ at $t = 427$ s (Figure 4.2C). The current-time curve also decayed smoothly to background and a plot of $\log(i)$ vs. t yielded a straight line (Figure 4.2D). Reverse electrolysis of the solution at -0.4 V consumed the same number of coulombs as the forward electrolysis (0.52 C). These results confirmed that reactions (4-1) and (4-2) involve the transfer of one mole of electrons per mole of complex.

Solubility in 5 M NaOH

TEA is soluble in 5 M NaOH to ≥ 2.0 M, whereas mTEA was soluble to ≥ 1.5 M. Solutions of $[\text{Fe}(\text{TEA})(\text{OH})]^-$ can be prepared with a stoichiometric metal-to-ligand ratio of 1:1 up to 0.5 M. By adding excess ligand in ratios of 1:1.5 or higher, the solubility can be increased up to 0.8 M. Concentrations of $[(\mu\text{-O})(\text{Fe}(\text{TEA}))_2]^{4+}$ up to 0.325 M can be achieved by maintaining a metal-to-ligand ratio of 1:2 during the synthesis. Solutions of $[\text{Co}(\text{mTEA})(\text{H}_2\text{O})]^-$ can be prepared in a stoichiometric ratio of 1:1 up to 0.5 M. By adding excess ligand in ratios of 1:1.5 or higher, the solubility can be increased up to 0.7 M. Co(III)-mTEA was only prepared by bulk electrolysis from $[\text{Co}(\text{mTEA})(\text{H}_2\text{O})]^-$ and is soluble at the same concentrations.

Charge-Discharge Cycling Performance of the Battery

The performance of the Co/Fe alkaline RFB was initially evaluated at low concentrations by constructing charge-discharge curves from constant-current electrolysis experiments and by analyzing the total charge electrolyzed per half-cycle. Figure 4.3A presents plots of charge vs. half-cycle for the cases (a), (b), and (c) described in Table 4.1.

Table 4.1. Conditions used for the evaluation of battery performance^{a,b}

Case	Volume	Anolyte	Catholyte	Coulombs ^c	Fe/Co
a)	20 mL	50 mM Co(II)-mTEA	50 mM Fe(III)-TEA	96.48 C	1.0
b)	20 mL	50 mM Co(III)-mTEA	50 mM Fe(II)-TEA	96.48 C	1.0
c)	20 mL	50 mM Co(II)-mTEA	50 mM Fe(III)-TEA + 110 mM Fe(II)-TEA	96.48 C	3.2
d)	3 mL Co 6 mL Fe	0.5 M Co(II)-mTEA	0.25 M Fe(III)-TEA + 0.5 M Fe(II)-TEA	144.72 C	3.0

^a SoC = 0 % in all cases.

^b Current density $j_{app} = 21 \text{ mA cm}^{-2}$ in cases (a), (b), and (c). Case (d) used $j_{app} = 30 \text{ mA cm}^{-2}$.

^c Theoretical number of coulombs from moles of limiting reagent.

When stoichiometric amounts of Co(II)-mTEA and Fe(III)-TEA were used as electrolytes in the battery, *i.e.* case (a), we obtained 95.0 C after the initial charging, then the number of coulombs abruptly decayed to 51.5 C in the following discharge (46 % decay), and continued decaying in subsequent half-cycles until a steady number around 35.7 C was attained. Figure 4.3B shows an example of the first charge and first discharge curves obtained in case (a). Case (b) was carried out using equal concentrations of Co(III)-mTEA and Fe(II)-TEA, and achieved $45.4 \pm 15 \text{ C}$ in all half-cycles (47 % of total coulombs). Interestingly, the first discharge gave 55.4 C, approximately the same number of coulombs as the first discharge in case (a). Finally, in case (c), the negative electrolyte was composed of 50 mM Fe(III)-TEA and 110 mM Fe(II)-TEA with 50 mM Co(II)-mTEA. This last experiment with a mole ratio of Fe/Co of 3.2 gave $96 \pm 3 \text{ C}$ in all 25 half-cycles.

Experiments carried out with concentrations 0.5 M of the complexes, case (d) in Table 4.1, are shown in Figure 4.4. The charge-discharge data was collected by cycling from SoC = 0 % to SoC = 100 %. Figure 4.5 shows coulombic and energy efficiencies achieved for every cycle in Figure 4.4. The efficiencies are calculated as follows:

$$\eta_Q = \frac{Q_{discharge}}{Q_{charge}} \cdot 100 \quad (4-6)$$

$$\eta_E = \left(\eta_Q \cdot \frac{\bar{V}_{discharge}}{\bar{V}_{charge}} \right) \cdot 100 = (\eta_Q \cdot \eta_V) \cdot 100 \quad (4-7)$$

where η_Q is coulombic efficiency, Q is charge in coulombs, η_E is energy efficiency, and $\bar{V}_{discharge}$ and \bar{V}_{charge} are the average voltage during discharging and charging, respectively. In Figure 4.5, the initial open circuit voltage (OCV) is 0.7 – 0.9 V. Charging at 30 mA

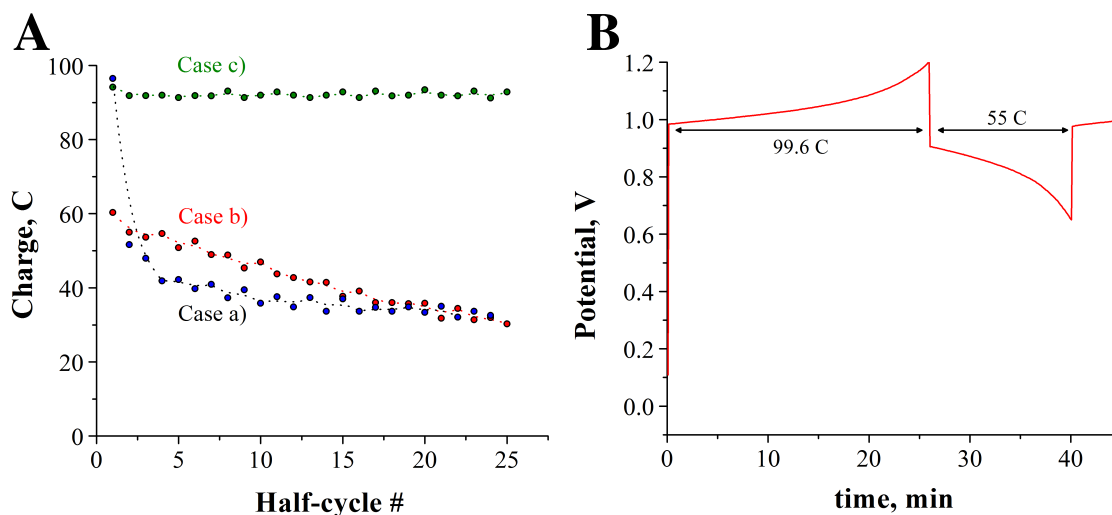


Figure 4.3. **A.** Plots of number of coulombs vs. half-cycle number extracted from constant-current electrolysis of the systems described in Table 4.1. SoC = 0 %. **B.** Example of first charge and first discharge curves obtained in case (a). Catholyte: 20 mL of 50 mM Co(II)-mTEA in 5 M NaOH; Anolyte: 20 mL of 50 mM Fe(III)-TEA in 5 M NaOH; 50 μm thick Nafion membrane; flow rate: 40 mL min^{-1} ; current density: 21 mA cm^{-2} . Initial SoC = 0%.

cm⁻² achieved a full cycle every 42 min., with average coulombic efficiency in any single cycle of $\eta_Q = 99 \%$, at a cut-off cell voltage of 1.25 V. The upper cut-off voltage was not exceeded in order to prevent deposition of magnetite⁹ on the carbon electrodes. The OCV at SoC $\geq 98 \%$ is 0.95 to 1.00 V. The cut-off cell voltage for the discharge was set to 0.40 V. The average energy efficiency in all cycles was $\eta_E = 71 \%$.

4.5. DISCUSSION

Solubility in 5 M NaOH

We start our discussion by indicating that the use of excess ligand during the synthesis of the Fe-TEA and Co-mTEA complexes does not appear to change the coordination chemistry in solution (CV's are identical to 1:1 ratios, see Figures A10 and A11), but it does increase the viscosity of the electrolyte. Moreover, the synthesis of $[\text{Fe}(\text{TEA})(\text{OH})]^-$ consumes OH^- , and TEA will deprotonate ($pK_a = 14.1$)^{21,22} when

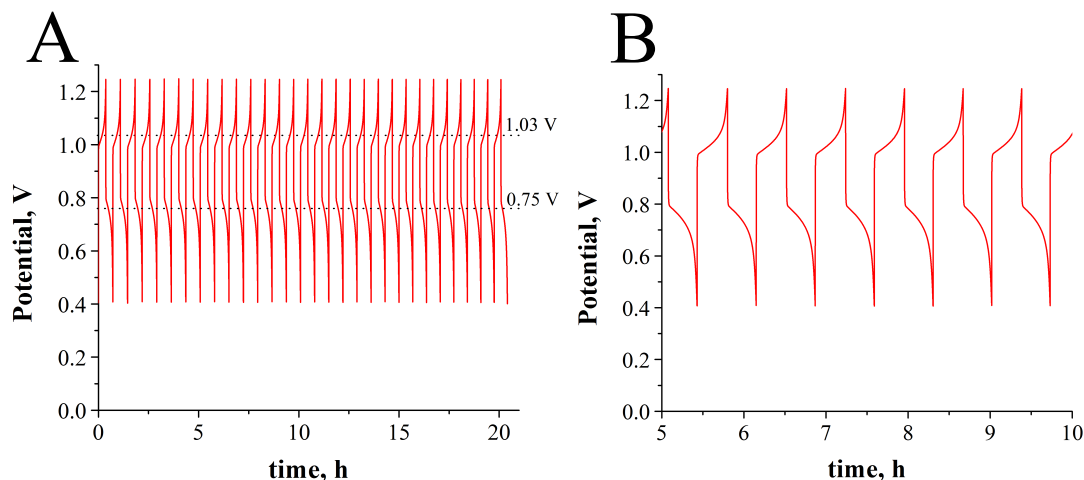


Figure 4.4. **A.** Charge-discharge cycling curves of the Co/Fe alkaline RFB with the following conditions: catholyte: 3 mL of 500 mM Co(II)-mTEA in 5 M NaOH; anolyte: 6 mL of 500 mM Fe(II)-TEA and 250 mM Fe(III)-TEA in 5 M NaOH; 50 μm thick Nafion membrane; flow rate: 140 mL min⁻¹ for Co-mTEA and 200 mL min⁻¹ for Fe-TEA, current density: 30 mA cm⁻². Charging from SoC = 0% to SoC = 100%. **B.** Zoomed-in region of plot A between $t = 5 - 10$ hours.

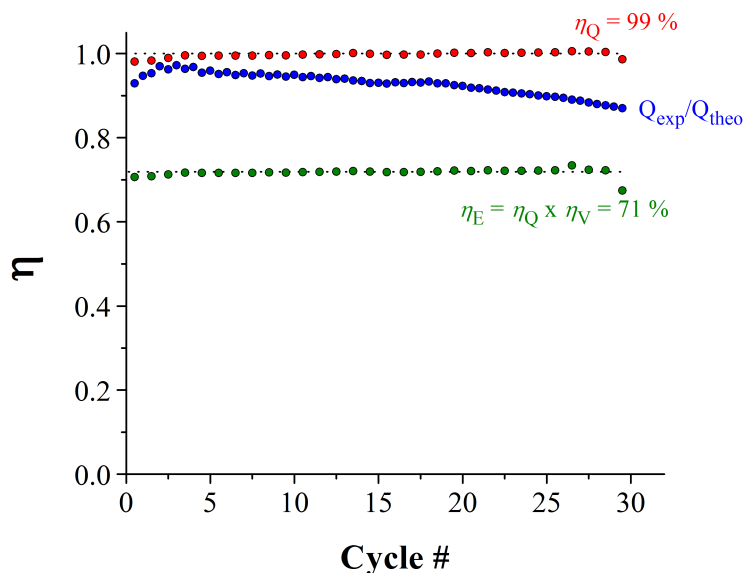
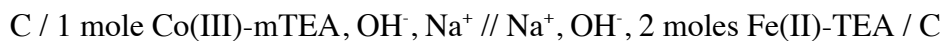


Figure 4.5. Plots of efficiency, η , vs. cycle number recorded from the constant-current analysis in Figure 4.4. Each red point corresponds to coulombic efficiency, η_Q , as calculated from equation (4-6). The green dots correspond to energy efficiency, η_E , calculated from equation (4-7). Blue dots are the ratio of experimental coulombs over theoretical coulombs.

coordinated with iron, further decreasing $[\text{OH}^-]$. Hence, it is important to keep a molar excess of OH^- in solution to prevent the formation of other species that are favored at $\text{pH} < 14$. In the case of $[\text{Fe}(\text{TEA})(\text{OH})]^{2-}$, excess ligand is always needed to favor the complexation of Fe^{2+} with TEA (because $\beta_{\text{Fe(II)}} \ll \beta_{\text{Fe(III)}}$).

Charge-Discharge Cycling Performance of the Battery

Based on the results presented so far, the cell notation for the charged state of the Co/Fe alkaline RFB is:



$$E_{\text{cell}} = 0.93 \text{ V (open circuit)}$$

A schematic representation of the flow battery with these conditions is shown in Figure A13. In the experiments presented in Figure 4.4, the stoichiometric ratios between

the two electrolytes were adjusted on a volume basis, using Co(II)-mTEA as the limiting reagent. We used 0.5 M Co(II)-mTEA in 3 mL as the anolyte. The catholyte was composed of 0.5 M Fe(II)-TEA + 0.25 M Fe(III)-TEA in 6 mL. This was done to start the cycling experiments by charging the battery. When preparing the negative electrolyte, Fe(II)-TEA and Fe(III)-TEA were prepared independently, and then added together to form the final solution. Synthesis of both complexes in the same reaction mixture yields a black precipitate (iron oxides).²³

We have determined that the main source of ohmic drop in our system is the Nafion membrane, due to the poor conductivity of Na^+ from the 5 M NaOH electrolyte. At a constant current density of 30 mA cm^{-2} , the membrane resistance accounts for $iR = 0.2 \text{ V}$ during charge-discharge cycling. Such a resistance limits the overall efficiency of our battery. Importantly, less than 5% crossover was observed at the end of the experiments (after 30 cycles, as determined by CV). To the best of our knowledge, Fe-TEA and Co-mTEA are the first chemistries to present crossover $< 5 \%$ in such a number of cycles. However, a decrease of 10 % in the capacity of the battery was observed after the 30th cycle. The change in capacity over time is attributed to O_2 leaking into the flow lines (see section 7.4 of Appendix A), the 4% crossover, and a net change in the volume of the electrolytes equivalent to $0.04 V_{\text{initial}}$ that diluted the Co-mTEA electrolyte. Different strategies were tested to minimize the oxidation of Fe(II)-TEA by O_2 , and Figures 4.4 and 4.5 show our best operating conditions. The system could be improved by replacing the plastic tubing with other materials (like stainless steel or glass). No precipitation of products or evolution of gases was observed during charge-discharge cycling at the higher concentrations (*i.e.*, $> 10 \text{ mM}$).

4.6. CONCLUSION

We have introduced the first redox flow battery based on the coordination chemistry of iron and cobalt with amino-alcohol ligands in strong base. We selected the redox couples Co(II/III)-mTEA and Fe(II/III)-TEA because they can be prepared from inexpensive salts of transition metal ions and ligands.²⁴ The electrochemistry of the system was characterized by voltammetry, chronoamperometry, and bulk electrolysis. The conditions of the battery were optimized to achieve energy efficiencies of 70 -76 % at current densities of 30 mA cm⁻². More importantly, significant species crossover was not observed in up to 30 charge-discharge cycles, a significant improvement over existing commercial technologies that are known to deactivate due to crossover (*e.g.* vanadium systems,²⁵ and Fe/Cr systems).

4.7. REFERENCES

- [1] Nguyen, T.; Savinell, R. F.; *Interface*, **2010**, *19*, 54-56.
- [2] Wang, W.; Luo, Q.; Li, B.; Wei, X.; Li, L.; Yang, Z.; *Adv. Funct. Mater.*, **2013**, *23*, 970-986.
- [3] Rosemount Analytical, *Conductance Data for Commonly Used Chemicals*, Irvine, CA: 2010.
- [4] Kear, G.; Shah, A. A.; Walsh, F. C.; *Int. J. Energy Res.*, **2012**, *36*, 1105-1120.
- [5] Chen, Y. D.; Santhanam, K. S. V.; Bard, A. J.; *J. Electrochem. Soc.*, **1981**, *128*, 1460-1467.
- [6] Wolfson, H.; *Nature*, **1944**, *153*, 375-376.
- [7] Jessop, G.; *Nature*, **1946**, *158*, 59-59.
- [8] Pribil, R.; Vesly, V.; *Talanta*, **1962**, *9*, 1053-1055.
- [9] Brockman, C. J.; Nowlen, J. P.; *T. Electrochem. Soc.*, **1936**, *69*, 553-556.
- [10] Kothari, H. M.; Kulp, E. A.; Limmer, S. J.; Poizot, P.; Bohannan, E. W.; Switzer, J. A.; *J. Mater. Res.*, **2006**, *21*, 293-301.

- [11] Ibanez, J. G.; Choi, C.; Becker, R. S.; *J. Electrochem. Soc.*, **1987**, *134*, 3083-3089.
- [12] Subrahmanya, R. S.; *Proc. Ind. Acad. Sci. A*, **1956**, *43*, 133-147.
- [13] Bechtold, T.; Turcanu, A.; *J. Electroanal. Chem.*; **2006**, *591*, 118-126.
- [14] Bechtold, T.; Turcanu, A.; *J. Electroanal. Chem.*; **2005**, *580*, 173-178.
- [15] Bechtold, T.; Burtscher, E.; Turcanu, A.; Bobleter, O.; *J. Appl. Electrochem.*, **1997**, *27*, 1021-1028.
- [16] Wen, Y. H.; Zhang, H. M.; Qian, P.; Zhou, H. T.; Zhao, P.; Yi, B. L.; Yang, Y. S.; *Electrochim. Acta*, **2006**, *51*, 3769-3775.
- [17] Bard, A. J.; Faulkner, L. R. *Electrochemical Methods: Fundamentals and Applications*; Wiley: New York, 2000.
- [18] Aaron, D. S.; Liu, Q.; Grim, G. M.; Papandrew, A. B.; Turhan, A.; Zawodzinski, T. A.; Mench, M.M.; *J. Power Sources*, **2012**, *206*, 450-453.
- [19] Arroyo-Currás, N.; Hall, J. W.; Jones, R. A.; Bard, A.J.; Manuscript in preparation.
- [20] Santhanam, K. S. V.; Bard, A. J.; *Electroanal. Chem.*, **1970**, *4*, 215-315.
- [21] Izutsu, K.; *Acid-base dissociation constants in dipolar aprotic solvents*, Blackwell Scientific Publications: Oxford, 1990.
- [22] SciFinder; Chemical Abstracts Service: Columbus, OH; pK_a; CAS 102-71-6; <https://scifinder.cas.org> (accessed November 14, 2013); Calculated using Advanced Chemistry Development (ACD/Labs) Software V11.02 (© 1994-2013 ACD/Labs).
- [23] Massart, R; *IEEE Trans. Mag.*, **1981**, *17*: 1247-1248.
- [24] Alfa Aesar, Quotes in Bulk Prices (1,000 Kg): NaOH, \$13.68; Co(NO₃)₂•6H₂O, \$20.83; Fe(NO₃)₃•9H₂O, \$11.05; TEA, \$11.00; mTEA, \$120.0.
- [25] Kim, S.; Yan, J.; Schwenzer, B.; Zhang, J.; Li, L.; Liu, J.; Yang, Z. G.; Hickner, M. A.; *Electrochem. Comm.*, **2010**, *12*, 1650-1653.

PART 2

The first part of this dissertation, from Chapters 1 to 4, presented the methodology followed to develop an a-RFB. An important portion of that methodology was the characterization of coordination compounds of iron(III/II) and cobalt(III/II) in concentrated base. Particularly, Chapter 3 was dedicated to the structural and electrochemical characterizations of the redox couple Fe(III/II)-TEA. Such a redox couple is of electrochemical interest because it has a very negative reduction potential, $E^0 = -1.05$ V, located at the limit of the thermodynamic reduction of water at $pH \geq 14$ ($E^0 = -1.06$ V). However, Fe(II)-TEA does not spontaneously reduce water. This property makes Fe(II)-TEA a powerful, chemically stable reducing agent in concentrated base.

The second part of this dissertation explores the use of Fe(II)-TEA as a strong reducing agent in electrochemical titrations. Three types of titrations are considered: (1) amperometric (constant-potential), (2) potentiometric (constant-current), and (3) SI-SECM titrations. The latter are a powerful mode of SECM for the interrogation of surface-generated species, such as reaction intermediates, on electrodes. The second part of this dissertation is divided into two chapters. Chapter 5 describes the use of Fe(II)-TEA in amperometric and potentiometric titrations. Particularly, the reduction of O_2 by Fe(II)-TEA in concentrated base was studied. In Chapter 6, the potential-driven surface oxidation of Ir ultramicroelectrodes is investigated by SI-SECM. Special attention was given to the titration of hydrous oxides of Ir that exist prior to the onset of oxygen evolution. In both chapters, the titrant Fe(II)-TEA is generated *in situ* by the electroreduction of Fe(III)-TEA at a GC electrode. Detailed descriptions of the

electrochemical cells used in each chapter and methodology to carry out each type of titration (amperometric, potentiometric, SI-SECM) are presented in Chapters 5 and 6.

Chapter 5. Coulometric Titrations of Molecular Oxygen in Concentrated NaOH

5.1. ABSTRACT

Despite the importance of the oxygen reduction reaction (ORR) in alkaline fuel cells and corrosion science, the reaction mechanism in concentrated $\text{NaOH}_{(\text{aq})}$ remains poorly understood. Our group has previously reported that the number of electrons, n , transferred in the first step of the ORR in solutions of concentrated NaOH changes from $n = 2$ at $[\text{OH}^-] = 1 \text{ M}$ to $n = 1$ at $[\text{OH}^-] \geq 6 \text{ M}$ on Pt ultramicroelectrodes. Here we report on the amperometric and potentiometric titrations of O_2 by Fe(II)-TEA in 5 M NaOH. Fe(II)-TEA is a strong reducing agent with formal potential $E^0 = -1.05 \text{ V vs. Ag/AgCl}$. The reduction of O_2 by Fe(II)-TEA in strong base produces HO_2^- in two steps, each step involving a one-electron transfer reaction. In the first step, O_2 is reduced to superoxide, $\text{O}_2^{\cdot-}$. However, our results indicate that Fe(II)-TEA catalyzes the protonation of $\text{O}_2^{\cdot-}$ to HO_2^{\cdot} . This protonation step can be observed by plotting the first derivative of a titration curve recorded under conditions of non-equilibrium. In the second step, HO_2^{\cdot} reacts with a second Fe(II)-TEA complex to produce the deprotonated peroxide HO_2^- ($pK_a = 11.75$). Importantly, we introduce Fe(II)-TEA as a chemically stable and electrochemically reversible titrant with very negative formal potential in strong base. To the best of our knowledge, this is the first report on the quantitative coulometric titration of O_2 in concentrated NaOH solutions.

5.2. COULOMETRIC TITRATIONS

The oxygen reduction reaction (ORR) is one of the most important electrocatalytic reactions because of its role in electrochemical energy conversion (*e.g.*,

fuel cells), corrosion, and biology.^{1,2} Despite the importance of this reaction and the fact that over 100 years of research have been dedicated to studying it,³ complete understanding of the fundamental mechanism and the intermediates produced during the ORR has not been achieved yet.⁴ This is in part because the ORR mechanism is strongly affected by the physical properties of the solvent and the oxygen bonding strength of the electrocatalyst used to carry out the reaction.⁵ For example, O₂ can be electroreduced to superoxide radical, O₂^{-•}, *via* a one-electron reaction in aprotic solvents, such as acetonitrile;⁶ however, reduction of O₂ in aqueous solutions selectively yields peroxide (two-electron reaction) or water (four-electron reaction) depending on the conditions and the electrocatalyst used.^{7,8,9}

Interestingly, the one-electron reduction of O₂ to O₂^{-•} can be carried out in aqueous solutions by pulse radiolysis.¹⁰ At *pH* < 7, O₂^{-•} decays rapidly (*t*_{1/2} ≈ 1.0 × 10⁻³ s) by reaction with its conjugate acid HO₂[•]. More importantly, at *pH* >> 7 the concentration of HO₂[•] decreases and the lifetime of O₂^{-•} improves (*t*_{1/2} ≈ (1.7 × 10¹ / [O₂^{-•}]) s).^{10,11}

The enhanced chemical stability of O₂^{-•} in alkaline solutions has also been observed in electrochemical studies concerning the ORR on platinum electrodes at *pH* > 12.¹² Our group reported a clear change in the number of electrons, *n*, involved in the first step of the ORR carried out on Pt UMEs with increasing concentrations of OH⁻, from *n* = 2 at [OH⁻] = 1 M to *n* = 1 at [OH⁻] ≥ 6 M.¹³ The aforementioned experimental observations indicate that the one-electron reduction of O₂ to O₂^{-•} is the first thermodynamic step of the ORR in strong base. Surprisingly, there are still very few reports regarding the overall mechanism of the ORR in such a medium.

Here, we report on the amperometric and potentiometric titrations¹⁴ of O₂ using the redox couple Fe(III/II)-TEA as the titrant in 5 M NaOH_(aq). Our titration curves indicate that reduction of O₂ by Fe(II)-TEA occurs in two steps, each step involving a

one-electron transfer reaction, to produce the deprotonated peroxide HO_2^- ($pK_a = 11.75$). Importantly, Fe(II)-TEA catalyzes the protonation reaction from $\text{O}_2^{\cdot-}$ to its conjugate acid HO_2^{\cdot} . If a rapid titration is carried out (*i.e.*, not at equilibrium), the protonation step is observable by plotting the first derivative of the titration curve. To the best of our knowledge this is the first report on the quantitative coulometric titration of O_2 in concentrated $\text{NaOH}_{(\text{aq})}$.

Figure 5.1 shows the electrochemical cells used in this work. For amperometric titrations, a gas-tight glass cell ($V = 35 \text{ mL}$) with a threaded polytetrafluoroethylene (PTFE) cap was used, shown in Figure 5.1A. The PTFE cap had an injection port with a disposable rubber septum. A GC UME (radius $a = 5 \mu\text{m}$) was used as the working electrode, a Ag/AgCl (sat. KCl) was the reference electrode, and a GC rod ($A_l = 1 \text{ cm}^2$) was the counter electrode. A similar cell was used for potentiometric titrations, shown in

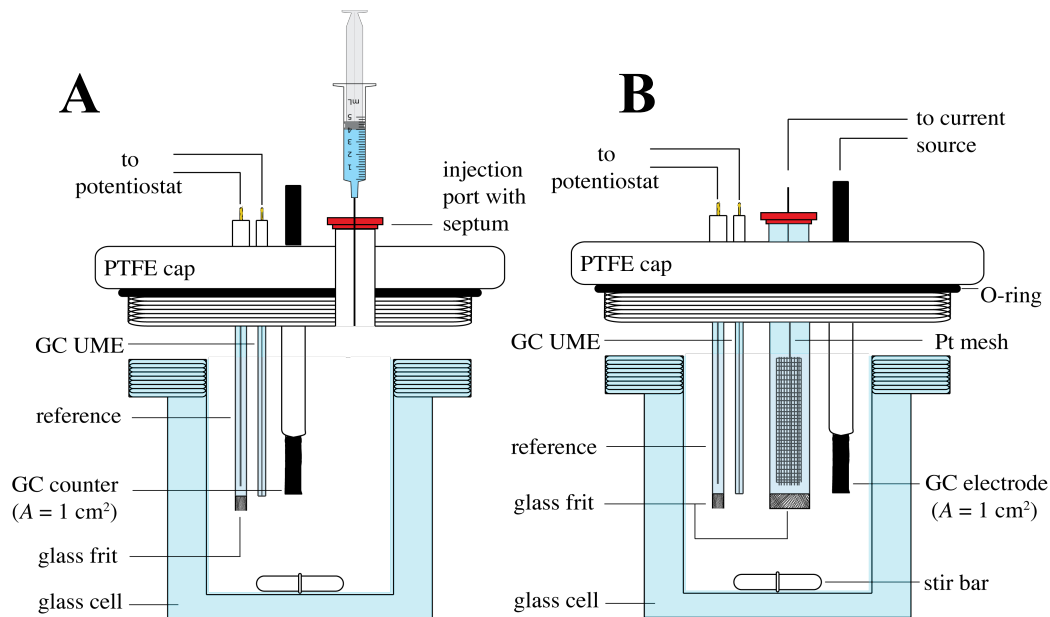


Figure 5.1. Electrochemical cells used in this work. **A.** Cell for amperometric titrations. **B.** Cell for potentiometric titrations. The total volume of solution in the cells was $V = 35 \text{ mL}$.

Figure 5.1B. However, in this case the configuration of the electrodes was different. For potentiometric titrations, the GC UME and the Ag/AgCl reference were connected to a potentiostat and used to probe the OCV of the GC UME *vs.* time. Additionally, a GC electrode ($A_1 = 1 \text{ cm}^2$) and a Pt mesh ($A_2 \gg A_1$) confined in an independent chamber with a glass separator were connected to a current source, shown in Figure 5.1B. The GC electrode was used to generate the titrant. In both types of experiments, aqueous solutions of 5 M NaOH saturated with O_2 were prepared by vigorously bubbling high purity O_2 gas from Praxair (99.9999%, grade 6). Dissolution of O_2 in 5 M NaOH took about 20 min. Once O_2 dissolution was achieved (determined by the highest reduction current observed at a UME), the PTFE caps were screwed to close the cell, making sure that no gas phase was left inside. The concentration of $\text{O}_{2(\text{aq})}$ in 5 M NaOH was 200 μM as determined by coulometric titration. This concentration was lower than values reported elsewhere at the same concentration of $\text{NaOH}_{(\text{aq})}$.^{13,15-18}

We first carried out amperometric titrations to understand the stoichiometry of the homogeneous reaction between O_2 and Fe(II)-TEA in 5 M NaOH. Solutions of Fe(II)-TEA were prepared by procedures described in Chapter 3.¹⁹ Fe(II)-TEA in solution is a dinuclear complex with formula $[(\mu\text{-O})(\text{Fe}(\text{II})(\text{TEA}))_2]^{4+}$ (**1**). Oxidation of **1** gives only one electron and produces the mixed valence compound $[(\text{TEA})\text{Fe}(\text{III})\text{OFe}(\text{II})(\text{TEA})]^{3+}$ (**2**).¹⁹ Henceforth, we will refer to the redox couple **1/2** as Fe(III/II)-TEA (with $n = 1$). A CV of $\text{O}_{2(\text{aq})}$ in 5 M NaOH was carried out to find the potential where the reduction of oxygen occurs under diffusion controlled conditions, shown in Figure A15. The CV showed two redox processes at $E^0 = -0.34 \text{ V}$ ($i_{\text{ss}} = 0.2 \text{ nA}$) and $E^0 = -0.70 \text{ V}$ ($i_{\text{ss}} = 0.39 \text{ nA}$). Based on this information, we decided to carry out amperometric titrations by holding the potential of the GC UME at -1.05 V , where both reactions occur under diffusion control.

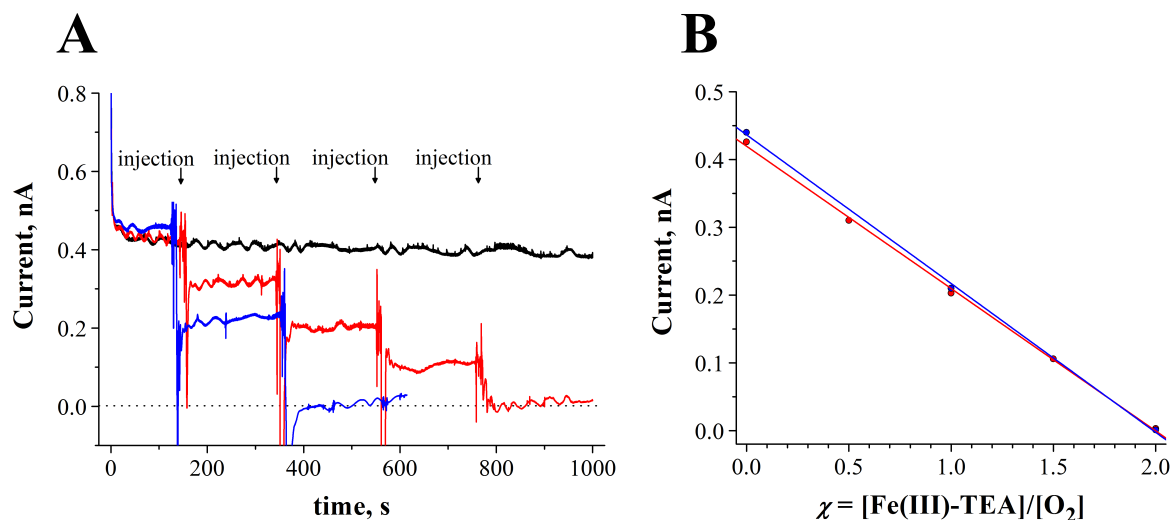
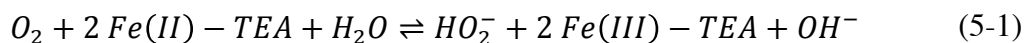


Figure 5.2. **A.** Current-time curves of solutions containing 7 μmoles of O_2 in 5 M NaOH recorded with a GC UME ($a = 5 \mu\text{m}$). The black trace corresponds to the current measured during the reduction of O_2 at -1.05 V . The red trace shows four injections of 3.5 μmoles of Fe(II)-TEA. Each injection was a 35 μL aliquot of 0.1 M Fe(II)-TEA in 5 M NaOH. The blue trace shows two additions of 7 μmoles of Fe(II)-TEA. Each injection was a 70 μL aliquot of 0.1 M Fe(II)-TEA in 5 M NaOH. The cell volume was $V = 35 \text{ mL}$. The dilution factor was neglected. The solutions were stirred at 1500 rpm. **B.** Amperometric titrations of O_2 by Fe(II)-TEA in 5 M NaOH. Blue and red dots correspond to the steady state currents obtained after injection of Fe(II)-TEA from Figure 5.2A. Lines show linear fits of the data. χ is mole fraction.

Figure 5.2 shows the amperometric titrations carried out in this work. In the absence of titrant, the current recorded at the GC UME during chronoamperometry was 0.42 nA, shown by the black trace in Figure 5.2A, in agreement with the plateau current seen in the CV of Figure A15. This current is also shown in Figure 5.2B at $\chi = 0.0$ (blue circle). Mechanical stirring of the solution at 1500 rpm caused fluctuations in the steady state current. The titration of 7 μmoles of $\text{O}_{2(\text{aq})}$ with 7 μmoles of Fe(II)-TEA, corresponding to a mole fraction $\chi = 1.0$, decreased the current to a steady state value of 0.21 nA (50% decrease), shown by the blue trace in Figure 5.2A. This current corresponds to the blue circle shown at $\chi = 1.0$ in Figure 5.2B. A second injection of 7 μmoles of Fe(II)-TEA decreased the current to 0.003 nA, indicating that the equivalence

point was reached at $\chi = 2$. A subsequent injection of 7 μmoles of Fe(II)-TEA gave a negative current of -0.19 nA (not shown) corresponding to the oxidation of Fe(II)-TEA to Fe(III)-TEA) at $E^0 = -1.05$ V. This result confirmed that no reaction between $\text{O}_{2(\text{aq})}$ and Fe(II)-TEA occurred after the equivalence point was reached. A repetition of the experiment was carried out with a fresh solution, this time injecting 3.5 μmoles four times, shown by the red trace in Figure 5.2A and the red circles in Figure 5.2B. As expected, the current decreased by 25% after each injection of Fe(II)-TEA, and the equivalence point was reached at $\chi = 2$. Figure 5.2B presents amperometric titration curves constructed with the red and blue data from Figure 5.2A. Importantly, the two titration curves in Figure 5.2B presented the same slope $m = 0.2$ nA χ^{-1} and an equivalence point of $\chi = 2$. These results indicated that the reduction of $\text{O}_{2(\text{aq})}$ by Fe(II)-TEA involves the transfer of two electrons per molecule of $\text{O}_{2(\text{aq})}$ to produce HO_2^- . This is shown in equation (5-1):



We decided to further investigate reaction (5-1) by potentiometric titration. The coulometric cell shown in Figure 5.1B was filled with 35 mL of a solution containing 0.1 M Fe(III)-TEA + 200 μM O_2 in 5 M $\text{NaOH}_{(\text{aq})}$. The cell was hermetically sealed to ensure that the concentration of $\text{O}_{2(\text{aq})}$ would only be changed by the titration experiment. During the coulometric titration, the OCV of the system was measured at the GC UME vs. the Ag/AgCl reference with a potentiostat. Reduction of Fe(III)-TEA to generate the titrant, Fe(II)-TEA, was carried out on the second GC electrode at a constant-current density of 5.6 mA cm^{-2} in charge steps of $Q = 25$ mC. We waited 30 s between charge steps to allow equilibration of the system. The current efficiency was measured from linear sweep voltammograms of the test solutions as the ratio of the current measured at the GC

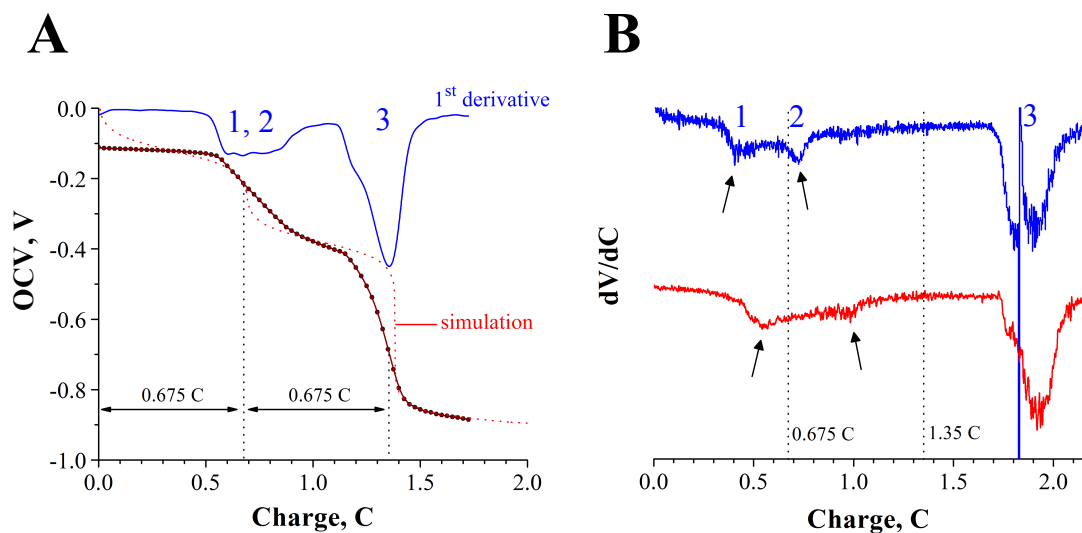


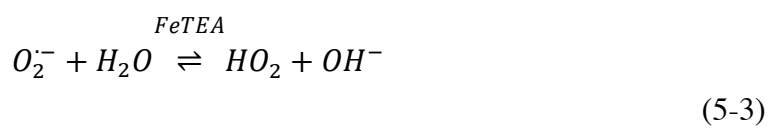
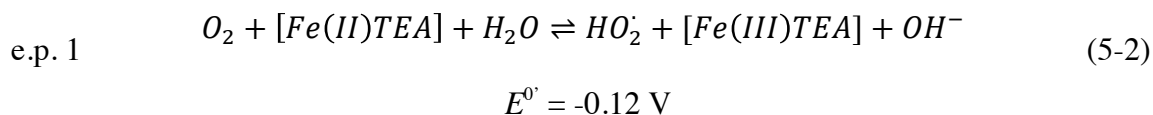
Figure 5.3. **A.** Coulometric titration of a solution containing 7 μmol of O_2 in 5 M NaOH with the titrant Fe(II)-TEA. The OCV was measured with a GC UME ($a = 5 \mu\text{m}$) vs. an Ag/AgCl (sat. KCl) reference. The titrant was generated at a GC electrode ($A = 1 \text{ cm}^2$) passing a constant current density of 5.6 mA cm^{-2} with 96% current efficiency, in charge steps of $Q = 25 \text{ mC}$ every 30 s. The line-crossed circles are the experimental data. The red dotted line was simulated using equations (1) and (3) from the text. The blue trace is the first derivative of the titration curve (data was smoothed by ensemble averaging). **B.** Two plots of first derivative vs. charge corresponding to two independent titration curves carried out under conditions of non-equilibrium. The titrant was generated continuously at the GC electrode by passing a constant current density of 5.6 mA cm^{-2} with 96% current efficiency (data was smoothed by ensemble averaging).

electrode in the absence of titrant and O_2 (Ar atmosphere), over the current measured in the presence of both Fe(III)-TEA and O_2 , shown in Figure A16. The current efficiency was 96% in all experiments. We estimated the number of coulombs needed to complete the titration using Faraday's law as $Q = n C_{\text{O}_2} V F = 1.35 \text{ C}$, where $n = 2$, $C_{\text{O}_2} = 200 \mu\text{M}$, $V = 35 \text{ mL}$, and $F = 96,485 \text{ C mol}^{-1}$.

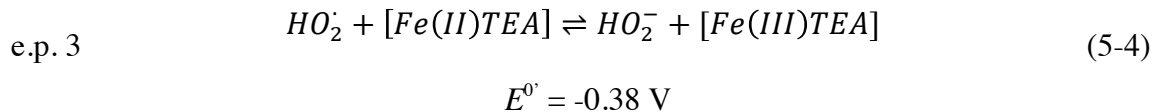
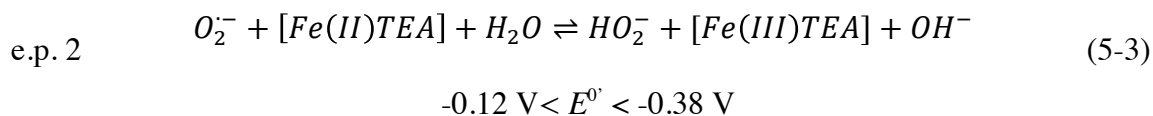
Figure 5.3 shows a typical potentiometric titration curve. The initial OCV of the system was ca. -0.10 V , shown with circles at $Q = 0.0 \text{ C}$ in Figure 5.3A. The magnitude of the OCV was almost constant for about 0.55 C , with average -0.12 V . At $Q \approx 0.68 \text{ C}$,

the OCV decreased to the first equivalence point (*i.e.*, $\chi = 1.0$) with OCP = -0.21 V, shown by the left vertical dotted line in Figure 5.3A. We assigned this first equivalence point to the reduction of O_2 to $O_2^{\cdot-}$. Continuing the titration caused the OCV to decrease until a second plateau was reached at about $Q = 1.0$ with average OCV = -0.38 V. A second equivalence point was reached (*i.e.*, $\chi = 2.0$) at $Q = 1.35$ C with OCP = -0.67 V, shown by the right vertical dotted line in Figure 5.3A. We assigned this second equivalence point to the reduction of HO_2^{\cdot} to HO_2^- . After the second equivalence point was reached, the titration curve dropped to the onset potential corresponding to the half-cell Fe(III/II)-TEA at about -0.91 V. Additionally, the blue line in Figure 5.3A presents a plot of the first derivative of the potentiometric titration curve *vs.* charge. This first derivative shows two curve maxima, one at 0.67 C, matching the predicted charge at $\chi = 1.0$ (labeled 1, 2), and a second at 1.35 C, matching the predicted charge at $\chi = 2.0$ (labeled 3). Importantly, a side-by-side comparison of the two curve maxima provides evidence that the first process is not a sharp peak. In fact, the first maximum is the convolution of two equivalence points occurring at similar charges. We carried out coulometric titrations under conditions of non-equilibrium to separate the equivalence points, shown in Figure 5.3B. This was done by titrating O_2 with Fe(II)-TEA without waiting for the system to equilibrate. The idea was to carry out the titration fast enough to catch the intermediate species responsible for the overlapping. Figure 5.3B shows two experiments carried out in this manner (the black arrows point at the two maxima deconvoluted in each experiment). Under these conditions, three equivalence points were observed, labeled as 1, 2 and 3 in Figure 5.3B, and the charge obtained at $\chi = 2.0$ was $Q = 2.0$ C. The total charge passed at the end of the coulometric titration was larger than the theoretical 1.35 C likely because the forward rate of the homogeneous reduction of O_2 by Fe(II)-TEA was slow, and more coulombs were passed than needed per unit change in

the OCV. Importantly, the equivalence points labeled 1 and 2 in Figure 5.3B always occurred at about $Q > 0.67$ C. We believe Fe(II)-TEA catalyzes the protonation of $O_2^{\cdot-}$ to its conjugate acid HO_2^{\cdot} , otherwise unfavorable in concentrated base ($pK_a = 4.8$)¹⁰. The equilibria involved are expressed in equations (5-3) – (5-4):



$$K = 10^3$$



The standard potential for the couple O_2/HO_2^- is $E^0_{O_2/HO_2^-} = -0.38 \text{ V vs. Ag/AgCl}$.⁹ However, the equilibrium constant K in equation (5-3) pushes the first step in the reduction of O_2 by Fe(II)-TEA to more positive potentials, *i.e.*, -0.12 V . Therefore, the equivalence point reached at approximately $Q = 0.5$ C in Figure 5.3B and labeled as 1 corresponds to equation (5-2). Further, a small fraction of the superoxide produced in (5-2) is not protonated in reaction (5-3) before the second reduction step occurs, producing a second equivalence point in the titration curve, labeled as 2 in Figure 5.3B. Such a reaction is expressed in equation (5-3). The equivalence point labeled as 3 in Figure 5.3B corresponds to the reduction of HO_2^{\cdot} generated in equation (5-3) to HO_2^- . Indirectly, equations (5-2) and (5-3) imply that Fe(II)-TEA undergoes an inner-sphere

electron transfer reaction with O_2 . We intend to carry out Raman and other spectroscopic studies in the future to provide stronger experimental support for equations (5-2) and (5-3).

The equilibria presented in equations (5-2) – (5-5) were used to fit the titration curves obtained in this work. The red dashed line in Figure 5.3A corresponds to the simulation of a titration curve constructed using equations (5-2), (5-3) and (5-5). The value $K = 10^3$ was extracted from numerical fits. A final point to note is that the titration curve shown in Figure 5.3A deviates from Nernstian behavior. This effect is due to mass transfer and electron transfer kinetics and was not taken into account in the simulation of the titration data.

As a conclusion, this chapter described the first amperometric and coulometric titrations of O_2 carried out in concentrated NaOH solutions. Fe(II)-TEA was introduced as a chemically stable and electrochemically reversible titrant with very negative reduction potential. Importantly, the results presented herein indicate that O_2 undergoes a two-step reduction to HO_2^- , each step involving the transfer of one electron. This is important because it confirms previous observations that the ORR undergoes a first one-electron step at $[OH^-] \geq 5 \text{ M}$.⁴ In addition, the experimental set-up described here can quantitatively measure the concentration of dissolved O_2 in solutions where $[OH^-] \geq 1 \text{ M}$. We hope this work on the investigation of the ORR in alkaline solutions will be extended in the future.

Note. The homogeneous reduction of NO_3^- , CO_3^{2-} , and N_2 by Fe(II)-TEA were also attempted in this work. Importantly, titration curves were only obtained with saturated solutions of N_2 in 5 M $NaOH_{(aq)}$. However, the solubility of N_2 in base is $< 100 \mu\text{M}$ and quantification of the products of the reaction could not be achieved.

5.3. REFERENCES

- [1] Adzic, R. In *Electrocatalysis*; Lipkowski, J., Ross, P. N., Eds.; Wiley-VCH: New York, 1998.
- [2] Markovic, N. M.; Ross, P. N. In *Interfacial Electrochemistry: Theory, Experiment, and Applications*; Wieckowski, A., Ed.; Marcel Dekker: New York, 1999; pp 821-841.
- [3] Fischer, F.; Priess, O.; *Ber. Dtsch. Chem. Ges.*, **1913**, *46*, 698-708.
- [4] Liu, B.; Bard, A. J.; *J. Phys. Chem. B*, **2002**, *106*, 12801-12806.
- [5] Sawyer, D. T., Chiericato, G.; Angelis, C. T.; Nanni, E. J.; Tsuchlya, T.; *Anal. Chem.*, **1982**, *54*, 1720-1724.
- [6] Maricle, D. L.; Hodgson, W. G.; *Anal. Chem.*, **1965**, *37*, 1562-1565.
- [7] Shi, C.; Steiger, B.; Yuasa, M.; Anson, F. C.; *Inorg. Chem.*, **1997**, *36*, 4294-4295.
- [8] Song, C.; Zhang, J. In *PEM Fuel Cell Electrocatalysts and Catalyst Layers*; Zhang, J., Ed.; Springer London, 2008; pp. 89-134.
- [9] Sawyer, D. T.; Williams, R. J. P. *Oxygen Chemistry*; Oxford University Press: New York, 1991.
- [10] Bielski, B. H. J.; Cabelli, D. E.; Arudi, R. L.; Ross, A. B.; *J. Phys. Chem. Ref. Data*, **1985**, *14*, 1041-1100.
- [11] Janik, I.; Tripathi, G. N. R.; *J. Chem. Phys.*, **2013**, *139*, (014302-1)-(014302-7).
- [12] Jin, W.; Du, H.; Zheng, S.; Xu, H.; Zhang, Y.; *J. Phys. Chem. B*, **2010**, *114*, 6542-6548.
- [13] Zhang, C.; Fan, F. R. F.; Bard, A. J.; *J. Am. Chem. Soc.*, **2009**, *131*, 177-181.
- [14] Bard, A. J.; Faulkner, L. R.; *Electrochemical Methods: Fundamentals and Applications*; Wiley: New York, 2001.
- [15] Battino, R.; Rettich, T. R.; Tominaga, T.; *J. Phys. Chem. Ref. Data*, **1983**, *12*, 163-178.
- [16] Kierzkowska-Pawlak, H.; Wielgosinsky, G.; *Inz. Chem. Procesowa*, **2001**, *22*, 717-722.
- [17] Tromans, D.; *Hydrometallurgy*, **1998**, *50*, 279-296.
- [18] Tromans, D.; *Ind. Eng. Chem. Res.*; **2000**, *39*, 805-812.
- [19] Arroyo-Currás, N.; Hall, J. W.; Dick, J. E.; Jones, R. A.; Bard, A. J.; *J. Electrochem. Soc.*, **2015**, *162*, A378-A383.

Chapter 6. Iridium Oxidation as Observed by Surface Interrogation Scanning Electrochemical Microscopy (SI-SECM)^{*, †}

6.1. ABSTRACT

The surface interrogation mode of scanning electrochemical microscopy (SI-SECM) was used for the detection and quantification of $-\text{OH}_{(\text{ads})}$ and $-\text{H}_{(\text{ads})}$ species generated at the surface of polycrystalline iridium UMEs in 2 M NaOH. We introduced the redox pair Fe(III/II)-TEA as a reactive, selective, and stable surface interrogation agent at $p\text{H} \geq 12$. Monolayer coverage of $-\text{OH}_{(\text{ads})}$ and $-\text{H}_{(\text{ads})}$ were determined to be $Q_{\theta=1,\text{OH}} = 456 \pm 2.0 \mu\text{C cm}^{-2}$ and $Q_{\theta=1,\text{H}} = 224.2 \pm 0.2 \mu\text{C cm}^{-2}$, respectively. At potentials more positive than $E_{\text{subs}} = 0.20 \text{ V}$, a clear change in the kinetics of chemical reaction between Fe(II)-TEA and the hydrous oxides of Ir was observed. Our kinetic results are interpreted with the aid of a simulated model based on FEA. We present evidence that Ir(IV) and Ir(V) coexist on the surface of Ir during the water oxidation reaction under these conditions.

6.2. INTRODUCTION

The surface interrogation mode of the scanning electrochemical microscope (SI-SECM) is a powerful tool for the study of adsorbed species and intermediates on noble metals.¹ Continuing the results presented in previous reports on Pt and Au,²⁻⁴ we carried out SI-SECM experiments to study the formation of incipient oxides on polycrystalline iridium UMEs in 2 M NaOH. The surface titration was carried out using Fe(II)-TEA as the titrant, starting with an oxide-free Ir(0) surface, and systematically generating the

* Arroyo-Currás, N.; Bard, A.J.; Manuscript in preparation.

† Allen J. Bard was the PI.

incipient oxides over a potential window of 1.8 V. We observed five distinct potential regions in our titration curves corresponding to changes in the oxidation state of iridium between Ir(0)-Ir(V). Additionally, we detected Ir(IV) and Ir(V) oxides coexisting on the surface of the electrode after the onset of O₂ evolution. The introduction of Fe(III/II)-TEA as a chemically stable mediator in strong base extends the applicability of SI-SECM to the titration of oxides at $pH > 12$.

Iridium oxide films are historically important in electrochemistry because of their applications to dimensionally stable anodes (DSA) for water oxidation,^{5,6} their use as pH sensors *in vivo*,^{7,8} and their electrocatalytic activity in the water oxidation reaction.⁹ Surface characterization of iridium oxide films is typically carried out by voltammetry,¹⁰⁻¹² spectroscopy,^{13,14} or by a combination of both.¹⁵ However, such approaches are not ideal for the quantitative study of oxides at or below monolayer coverage, $\theta \leq 1$, for three reasons: 1) They are not sensitive enough;¹⁶ 2) Voltammetry uses the same surface to produce the incipient oxides and to detect them, potentially leading to convoluted results during analysis;¹⁷ and 3) *Ex-situ* techniques, such as XPS, require high vacuum chambers that can induce chemical transformations of the sample.

A recent paper¹⁸ proposes the use of *in-situ* X-ray absorption spectroscopy (XAS) to study the oxidation states assumed by Ir in a thick oxide film during the O₂ evolution reaction. Although powerful, this technique still requires the use of thick oxide films and requires a synchrotron. In contrast, SI-SECM offers several advantages for the study of incipient oxides at $\theta \leq 1$: a) The technique can be used *in-situ*; b) The sample electrode is decoupled from the probe electrode, minimizing unwanted perturbations of the sample during the detection step; c) SI-SECM is sensitive down to 3 - 4 % monolayer coverage;² and d) The time between generation and quantification of adsorbates can be optimized for the detection of short-lived species.¹⁹

The most characteristic feature in voltammograms of anodically-formed iridium oxide films (AIROF) is the quasi-reversible faradaic transition corresponding to Ir(III/IV),¹⁵⁻²¹ at $E^{0'} = -0.40$ V vs. Ag/AgCl in 2 M NaOH, see Figure 6.1. The determination of surface coverage on iridium requires precise control of the potential applied, since thick-oxide growth occurs irreversibly at $E > 1.1$ V in 1 M H₂SO₄;¹⁰ or $E > 0.4$ V in 2 M NaOH. An example of a thick-oxide film grown on an Ir electrode is presented in red in Figure 6.1. Oxygen surface coverage up to $\theta = 1$ was reported in 1.0 M H₂SO₄ to be $\Gamma = 544 \mu\text{C cm}^{-2}$ from galvanostatic curves.²² At potentials more positive than the Ir(III/IV) wave and $\theta = 1$, Ir assumes oxidation states higher than Ir(IV), previously detected by XPS and XAS.^{14,15} It is generally believed that these higher oxidation state Ir oxides are key mediators in the electrocatalysis of water oxidation. Taking this into consideration, we carried out the systematic titration of Ir oxides at coverage $\theta \leq 1$ and $\theta > 1$ by SI-SECM, starting from a clean surface of Ir(0). We

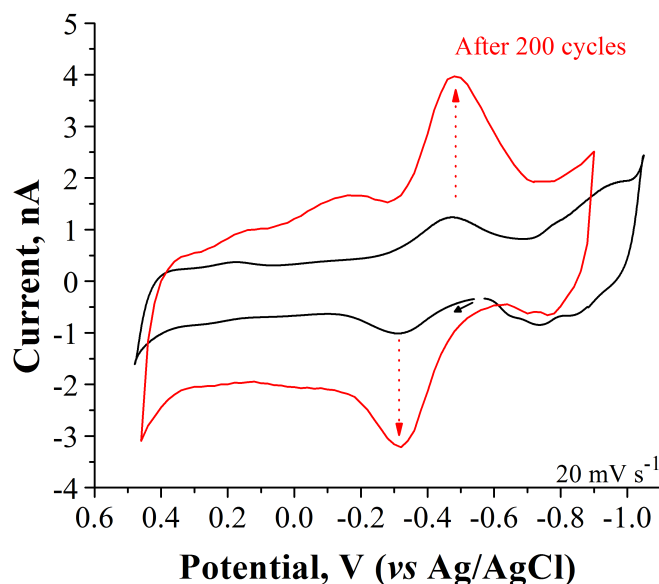


Figure 6.1. Cyclic voltammograms of Ir UMEs ($a = 62.5 \mu\text{m}$) in 2 M NaOH. *Black*: first scan over a clean, mirror-polished surface. *Red*: last scan after the electrode was cycled between -0.85 - 0.48 V 200 times, $v = 20 \text{ mV s}^{-1}$.

focused our efforts on the detection of oxide species with direct involvement in the O_2 evolution reaction. We analyze the coulometry and kinetic data obtained with the aid of numerical simulations based on FEA.

Mode of Operation

Figure 6.2 describes the mode of operation of SI-SECM for the generation and titration of $-OH_{(ads)}$ on Ir. Henceforth, $-OH_{(ads)}$ represents any form of hydrous oxide present on the Ir surface. The substrate is an Ir disk electrode surrounded by glass. The SI-SECM technique is divided in three steps as shown in Figure 6.2. In the first step, a glassy carbon tip is aligned and approached to the Ir substrate, to $d = 1-3 \mu\text{m}$, under positive feedback conditions. In the second step, a potential is applied on the substrate for a characteristic time, t_{step} , to generate hydrous oxides, while the potential on the tip is at OCV. In the third step, the potential of the substrate is taken to OCV and a CV of the

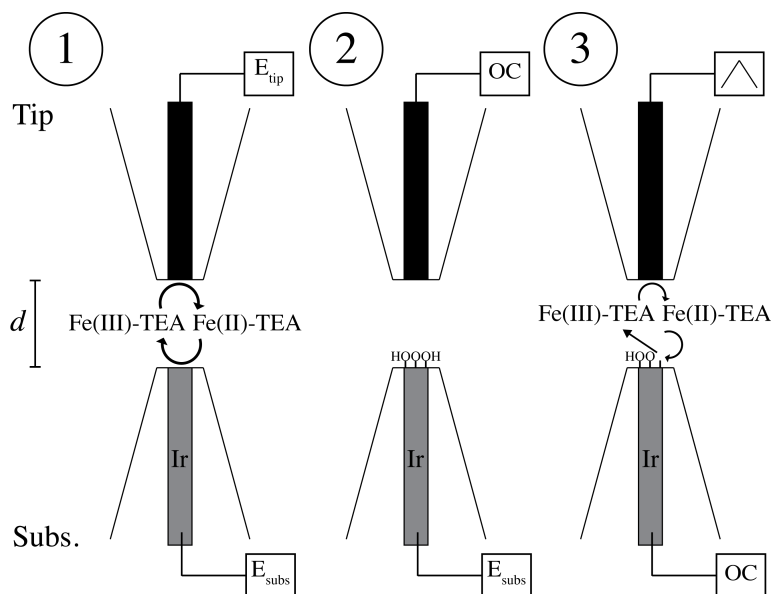


Figure 6.2. Description of the surface interrogation technique for the titration of $-OH_{(ads)}$ on Ir in 2 M NaOH. (1) Aligning and approaching the tip to $d = 1 - 3 \mu\text{m}$ from the substrate. (2) A potential E_{subs} is applied on the substrate while the tip is at OCV: Ir oxides are generated. (3) Titration of Ir oxides takes place by Fe(II)-TEA .

titrant, Fe(III)-TEA, is recorded at the tip. The potential waveform applied to the tip produces the reduced form of the titrant, Fe(II)-TEA, which diffuses toward the substrate and reacts with the hydrous oxides. Such a titration gives a transient positive feedback because Fe(II)-TEA is oxidized back to Fe(III)-TEA by $-OH_{(ads)}$. These reactions are written below:

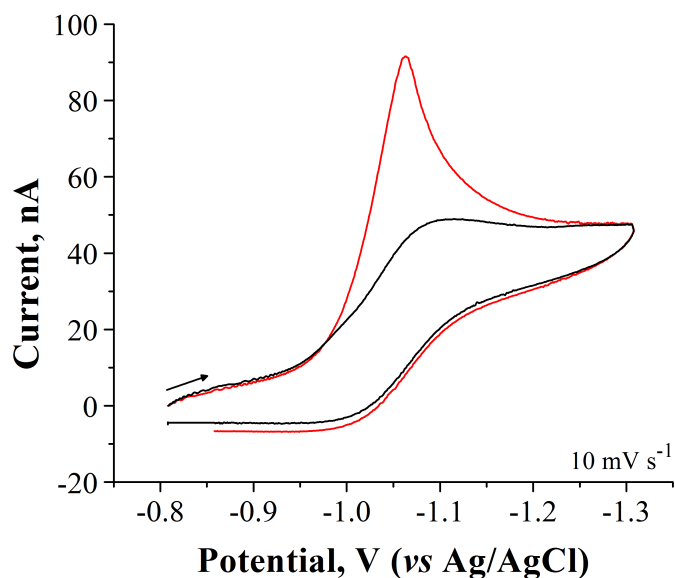
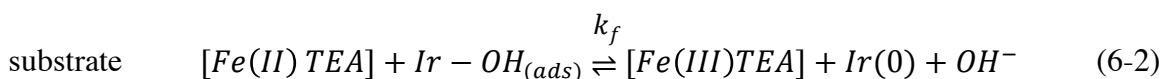
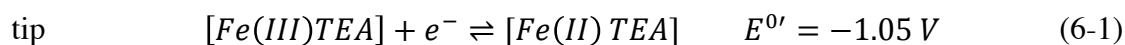


Figure 6.3. Cyclic voltammograms at a glassy carbon tip ($a = 50 \mu\text{m}$) in 5 mM Fe(III)-TEA + 2 M NaOH solution, during a titration experiment, $d = 2.8 \mu\text{m}$. The substrate is an Ir electrode ($a = 62.5 \mu\text{m}$). *Black*: voltammogram recorded in the absence of adsorbed species on the Ir substrate. *Red*: interrogation transient obtained after generation of Ir oxides. The area under the red curve, after subtraction of the black baseline, is divided by the scan rate at the tip, $v = 10 \text{ mV s}^{-1}$, to obtain the coulombs of adsorbates titrated during the experiment.

Equation (6-2) is a generic expression representing the homogeneous electron transfer reaction between Fe(II)-TEA and hydrous oxides $\text{Ir-OH}_{(\text{ads})}$, with rate of reaction k_f . The actual chemical formula of the oxide species produced in the interrogation experiment cannot be determined by SI-SECM.² When all the oxide species have reacted with Fe(II)-TEA, negative feedback behavior is observed, and the substrate electrode returns to its initial state. Figure 6.3 shows a characteristic voltammogram with feedback from the titration of oxides.

6.3. EXPERIMENTAL SECTION

Reagents

All solutions were prepared in 2 M NaOH with Milli-Q water ($\rho \approx 18 \text{ M}\Omega \cdot \text{cm}$). Solutions of FcMeOH 97 % from Sigma Aldrich (Russia) were prepared fresh prior to each experiment and were discarded after 4 h of preparation. The solutions of Fe(III)-TEA were prepared as follows: 20.0 mL of deionized water were poured into a round bottom flask and bubbled with argon. After bubbling for 5 min., 4×10^{-4} moles of $\text{Fe}_2(\text{SO}_4)_3 \cdot 5 \text{H}_2\text{O}$ from Acros Organics (Fair Lawn, NJ) were added with stirring. To this solution, 4.4×10^{-4} moles of TEA 98 % from Sigma Aldrich (St. Louis, MO) were added dropwise with stirring. In a separate container, NaOH pellets (0.08 moles) were dissolved in deionized water (10.0 mL) with stirring. After the NaOH dissolved, the container was placed in a water bath to cool at 25° C. This NaOH solution was added dropwise to the Fe(III) + ligand solutions. The volume was adjusted to 40.0 mL upon completion of the synthesis reaction. The complex produced, $[\text{Fe}(\text{TEA})(\text{OH})]^-$, presents reversible electron transfer kinetics ($\Delta E_p = 60 \text{ mV}$, see Figure A9) and is chemically stable in $[\text{NaOH}] > 1 \text{ M}$. The formal reduction potential is $E^{0'} = -1.05 \text{ V vs. Ag/AgCl}$. No additional supporting

electrolyte was added to the system. The synthesis reaction yields +95 % product as determined by steady-state voltammetry. All chemicals were used as received.

Electrodes and SECM Cell

Iridium wire (99.9%, 125 μm diameter) from Alfa Aesar (Ward Hill, MA) was used to fabricate the substrate electrode by procedures described elsewhere.²³ A 100 μm diameter glassy carbon disk electrode was fabricated according to the procedure described in section 7.6 of Appendix A (see Figure A17). All electrodes were polished prior to use with alumina paste (1 μm diam.) on microcloth pads from Buehler (Lake Bluff, IL), and sonicated for 15 min. in deionized water. Additionally, both substrate and tip electrodes were polished to $RG = 1.1$. All potentials in this work are reported vs. the Ag/AgCl (1.0 M KCl) reference couple. A large surface area Pt mesh (Alfa Aesar) was used as the counter electrode. All solutions used in the electrochemical cell were bubbled with argon gas for 15 min. prior to experimentation and were kept under a humidified argon blanket.

Instrumentation

SECM and other electrochemical measurements were carried out with a CHI920C SECM station bipotentiostat and software from CH Instruments (Austin, TX). CH Instruments software allows the use of macro commands to program instrumental routines. We created a routine to conduct SI-SECM experiments across a potential window of 1.80 V, every 0.01 V, with no intermissions (each instrumental routine ran for approximately 14 h). The program is shown in section 7.6 of Appendix A, Figure A18. The experimental conditions were as follows: the potential of the substrate electrode was stepped at E_{ini} for $t_{\text{step}} = 70$ s, after which it was immediately taken to open circuit. A resting time of $t_r = 2$ s was used between generation and interrogation. Then, CVs were

carried out at the tip electrode over a potential range between -0.85 and -1.30 V at a scan rate of $\nu = 10 \text{ mV s}^{-1}$. The magnitude of the potential step applied on the substrate electrode was changed by $\Delta E_{\text{subs}} = 0.01 \text{ V}$ after each experimental run and the overall sequence was repeated to cover the range between $E_{\text{final}} - E_{\text{ini}} = 1.80 \text{ V}$. All experiments were carried out with +94% collection efficiency. Charge densities were determined from the interrogation transients, by integrating the area under the curve from each titration, then dividing it over both the scan rate used at the tip and the area of the Ir substrate. Additionally, we used numerical simulations to fit our experimental results. The digital model used is described elsewhere.²⁴ Briefly, the reaction $\text{Fe(III)-TEA} + e^- \rightleftharpoons \text{Fe(II)-TEA}$ is considered at the tip, with forward, k_f , and reverse, k_b , rates of reaction defined according to the Butler-Volmer formalism as:

$$k_f = k^0 \exp[-\alpha f(E-E^0)] \quad (6-3)$$

$$k_b = k^0 \exp[(1-\alpha)f(E-E^0)] \quad (6-4)$$

Where the heterogeneous rate constant is $k^0 = 6.3 \times 10^{-2} \text{ cm s}^{-1}$,²⁵ α is the transfer coefficient ($\alpha = 0.5$ in this work), $f = F/RT$, F is Faraday's constant, R is the gas constant, and T is the experimental temperature. The diffusion profile of electroactive species is calculated by solving Fick's second law in Cartesian coordinates for a two-dimensional geometry with axial symmetry. The diffusion coefficient was determined by the chronoamperometric method, $D_{\text{Fe(III)-TEA}} = 2.0 \times 10^{-6} \text{ cm}^2 \text{ s}^{-1}$ (see section 1.8). The net rate of chemical reaction between Fe(II)-TEA and $-\text{OH}_{(\text{ads})}$ at the substrate electrode is defined as:

$$k_{net} = \sum_0^j k_j \Gamma_j C_{Fe(II)-TEA} \quad (6-5)$$

where k_j is the specific rate of chemical reaction between any single oxide of Ir and Fe(II)-TEA, Γ_j represents the surface concentration of $-OH_{(ads)}$ for an iridium oxide with oxidation state Ir^j , and $C_{Fe(II)-TEA}$ is the effective concentration of Fe(II)-TEA reacting with $-OH_{(ads)}$.

6.4. RESULTS AND DISCUSSION

Coulometry

Monolayer coverage of $-OH_{(ads)}$ and $-H_{(ads)}$. Figure 6.4 presents a plot of charge vs. substrate potential with the main results obtained in this work. The first detectable oxide of Ir in 2 M NaOH is seen at about -0.88 V (red circles in Figure 6.4), followed by oxide growth between -0.85 V and -0.47 V. In this potential range, OH^- adsorbs on Ir and the first hydrated oxides are formed.^{26,27} Oxide coverage on the Ir substrate is $\theta < 1.0$. The oxidation state of the atoms on the surface of the electrode is presumably Ir(III).¹⁵ An inflection point is reached at $E_{subs} = -0.40$ V, with $Q_{\theta < 1, OH} = 148 \pm 2.0 \mu C cm^{-2}$. The substrate potential where the inflection point occurs matches with the onset of the Ir(III/IV) wave seen in CVs of Ir UMEs in 2 M NaOH (blue curve in Figure 6.4). At substrate potentials more positive than -0.40 V, two processes occur simultaneously: oxide coverage progressively increases to $\theta \approx 1.0$, and Ir(III) is oxidized to Ir(IV).^{15,28-30} Further, a second inflection point is observed in the titration curve at $E_{subs} = 0.03$ V, with $Q_{\theta=1, OH} = 456 \pm 2.0 \mu C cm^{-2}$. This inflection point corresponds to $\theta = 1.0$. The magnitude of the charge density at the inflection point is $\sim 100 \mu C cm^{-2}$ lower than values previously reported by Dahms and Bockris²² in sulfuric acid ($Q_{\theta=1, OH} = 544 \mu C cm^{-2}$).

In the case of $-\text{H}_{(\text{ads})}$, the first detectable hydrogen atoms adsorbed on Ir are seen at about -0.70 V (green circles in Figure 6.4). The titration was carried out using FcMeOH as the titrant. FcMeOH is not chemically stable in 2 M NaOH over long times. However, we obtained reliable interrogation data within the first two hours after preparation of the solutions (interrogation transients shown in Figure A19). In this case, a Pt UME ($a = 50$ μm) was used as the tip. The reaction can be expressed in general as:

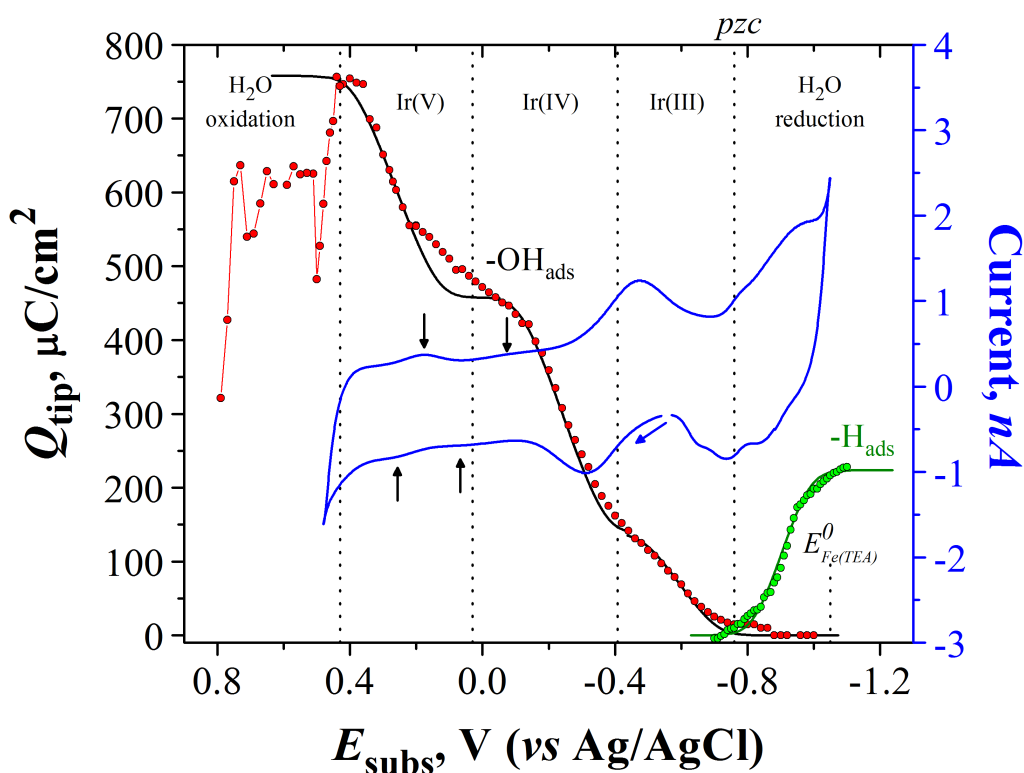
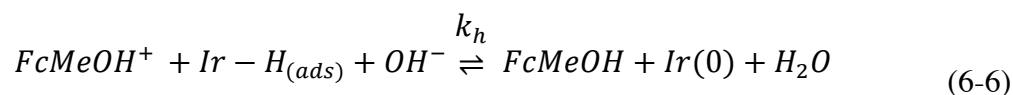


Figure 6.4. Plot of charge density, Q_{tip} , vs. E_{subs} constructed from interrogation transients of $-\text{OH}_{(\text{ads})}$ and $-\text{H}_{(\text{ads})}$ adsorbed on Ir in 2 M NaOH. *Red dots:* $-\text{OH}_{(\text{ads})}$, interrogated with 10 mM Fe(II)-TEA. $\Delta E_{\text{subs}} = 0.01$ V is increased from negative to positive potentials. *Blue dots:* $-\text{H}_{(\text{ads})}$, interrogated with 1 mM FcMeOH⁺. $\Delta E_{\text{subs}} = 0.01$ V is increased from positive to negative potentials. Each dot is one individual SI-SECM measurement. Only a fraction of the data acquired is shown for clarity. *Blue line:* cyclic voltammogram of Ir UME ($a = 50$ μm) in 2 M NaOH, $v = 20$ mV/s. *Black and green lines:* fit of experimental data with Frumkin isotherms, using $g' = -6$ and $g' = -2$, respectively (Table 6.1). *Red line:* trace showing the order in which data was acquired at $\Delta E_{\text{subs}} > 0.44$ V.



At potentials more negative than $E_{\text{subs}} = -0.70$ V, surface coverage increases until a monolayer of $-H_{(ads)}$ is completed, with $Q_{\theta=1,H} = 224.2 \pm 0.2 \mu\text{C cm}^{-2}$. This value is in agreement with previous determinations by Woods³¹ ($Q_{\theta=1,H} = 218 \mu\text{C/cm}^2$).

Potential of zero charge. The surface oxidation of Ir in 2 M NaOH commences at potentials just beyond the hydrogen adsorption region.¹⁰ In fact, $-OH_{(ads)}$ and $-H_{(ads)}$ probably coexist in that region. To characterize the potential range where both adsorbates are simultaneously present on Ir, we carried out titration experiments at substrate potentials close to the potential of zero charge, pzc . In the lower right corner of Figure 6.4, a region is seen where the charge from the titration of $-OH_{(ads)}$ (red circles) overlaps with that obtained from $-H_{(ads)}$ (green circles), at $E_{\text{subs}} \approx -0.78 \pm 0.06$ V. A potential region of about 120 mV exists where both adsorbates are simultaneously present on the surface of Ir. The center of such region is labeled as pzc in Figure 6.4 and matches the substrate potential where a transition between hydrogen adsorption and surface oxidation is seen on the CV of Ir UMEs in 2 M NaOH (blue curve). This overlap region differs from that seen with Pt, where a double layer region separates the initial surface reduction and oxidation processes. The coexistence of $Ir-OH_{(ads)}$ and $Ir-H_{(ads)}$ at low coverages suggests that the adsorbed species are not very mobile on the surface. Additionally, we evaluated the minimum surface concentration of $-OH_{(ads)}$ and $-H_{(ads)}$ detected in our experiments, by averaging the first three data points from the red and green titration curves, and calculating standard deviations. We obtained $Q_{\text{min},H} = 0.93 \pm 0.2 \mu\text{C cm}^{-2}$ for $H_{(ads)}$, and $Q_{\text{min},OH} = 11.4 \pm 2.0 \mu\text{C cm}^{-2}$ for $-OH_{(ads)}$; or 0.01 θ for $H_{(ads)}$ and 0.025 θ for $-OH_{(ads)}$.

Iridium oxides at $\theta > 1.0$. Several waves can be observed in the CVs of Ir in 2 M NaOH_(aq) at $E_{\text{subs}} > 0.03$ V, shown by black arrows in Figure 6.4. Such processes are not evident in the first scan shown in Figure 6.4 (same as the black trace in Figure 6.1), but become obvious after generation of a thick oxide film through constant potential cycling of the iridium electrode, as shown in red in Figure 6.1. The potentials at which those waves are observed in CVs coincide with an increase in charge density detected by SI-SECM. In the range -0.10 V – 0.20 V, the slope of the titration curve presented in Figure 6.4 (red dots) is constant. This indicates that no faradaic process has occurred within the monolayer of oxide. Thus, the wave seen by CV in the same potential region can only be attributed to surface transformation processes: *e.g.*, place exchange, slow oxide growth, dehydration of -OH_(ads) to -O_(ads), etc. However, when $E_{\text{subs}} > 0.20$ V the magnitude of the charge density integrated from SI-SECM transients sharply increases until a third inflection point is reached at $E_{\text{subs}} = 0.44$ V, with magnitude $Q_{\theta>1,0\text{H}} = 757 \pm 2.0 \mu\text{C cm}^{-2}$. From all the data presented so far, the following relationships become evident:

$$\Delta Q_1 = Q_{\theta>1,0\text{H}} - Q_{\theta=1,0\text{H}} = 299 \pm 2.0 \mu\text{C cm}^{-2} \quad (6-7)$$

$$\Delta Q_2 = Q_{\theta=1,0\text{H}} - Q_{\theta<1,0\text{H}} = 310 \pm 2.0 \mu\text{C cm}^{-2} \quad (6-8)$$

$$\Delta Q_1 \approx \Delta Q_2 \quad (6-9)$$

Equations (6-7) through (6-9) clearly indicate that the number of coulombs titrated by SI-SECM in the range 0.40 V – 0.03 V is the same as the number of coulombs obtained in the range -0.40 V – 0.03 V. Thus, the last inflection point (at 0.44 V) must correspond to a new faradaic conversion of Ir(IV) to Ir(V). The existence of Ir(V) oxides prior to the

onset of the water oxidation reaction in acid has been observed by XAS in sulfuric acid elsewhere.¹⁸

The black line in Figure 6.4 is a non-linear fit of the $-\text{OH}_{(\text{ads})}$ titration data with three contiguous Frumkin isotherms.^{32,33} The green line is a non-linear fit of the $-\text{H}_{(\text{ads})}$ data with the Frumkin isotherm. Two adjustable parameters were used to achieve the best fit: 1) an experimental reaction potential, $E^{0'}$, extracted from the data presented in Figure 6.4, and 2) the interaction parameter, g' . The values used as inputs in the Frumkin isotherms are presented in Table 6.1. Interaction parameters $g' = -6$ and $g' = -2$ were used to fit the red and green data sets, respectively. In both cases, the negative magnitude of g' indicate repulsive interactions between the adsorbates.

Iridium oxides after the onset of water oxidation. When potentials more positive than $E_{\text{subs}} = 0.44$ V were applied to the Ir substrate, the SI-SECM titration recorded charge densities that are intermediate between oxides of Ir(IV) and Ir(V). In Figure 6.4,

Table 6.1. Parameters used to simulate the Frumkin isotherms shown in Figure 6.4.

Frumkin isotherm: $\beta_i C_i = \frac{\theta}{1-\theta} e^{-g'\theta}$, where $\beta_i = \gamma_{\pm} \cdot e^{\frac{nF}{RT}(E-E^{0'})}$ and $g' = \frac{2g\Gamma_{\theta=1}}{RT}$				
E_{subs} region	Adsorbate	g'	$E^{0'}$	Charge at Inflexion Point
(-0.40) V – (-0.88) V	$\text{Ir}(\text{OH})_x^{(3-x)}$	-6	-0.58 V	$Q_{\theta < 1, \text{OH}} = 148 \pm 2.0 \mu\text{C cm}^{-2}$
(0.03) V – (-0.40) V	$\text{Ir}(\text{OH})_x^{(3-x)} + \text{Ir}(\text{OH})_y^{(4-y)}$	-6	-0.23 V	$Q_{\theta = 1, \text{OH}} = 456 \pm 2.0 \mu\text{C cm}^{-2}$
(0.44) V – (0.03) V	$\text{Ir}(\text{OH})_y^{(4-y)} + \text{Ir}(\text{OH})_z^{(5-z)}$	-6	-0.26 V	$Q_{\theta > 1, \text{OH}} = 757 \pm 2.0 \mu\text{C cm}^{-2}$
$E_{\text{subs}} > 0.44$ V	H_2O oxidation	-	-	$Q_{> 0.4\text{V}} = 614 \pm 96 \mu\text{C cm}^{-2}$
(-0.70) V – (-1.10) V	$\text{IrH}_n^{(n)}$	-2	-0.90 V	$Q_{\theta = 1, \text{H}} = 224.2 \pm 0.2 \mu\text{C cm}^{-2}$

the charge integrated at $E_{\text{subs}} > 0.44$ V has an average magnitude of $Q_{>0.44\text{V}} = 614 \pm 96 \mu\text{C cm}^{-2}$. Note that the points overlaid with the red trace in Figure 6.4 are at midpoint between the inflection points at $E_{\text{subs}} = 0.44$ V and $E_{\text{subs}} = 0.03$ V. This result presumably indicates that Ir(IV) and Ir(V) oxides coexist at $E_{\text{subs}} > 0.44$ V, and are involved in the catalytic cycle of water oxidation in 2 M NaOH. Such a conclusion is further supported by analysis of the CV transients recorded during the titration experiments and will be discussed further in the following section. The same oxidation states of Ir have been observed by XAS in thick films of AIROFs immersed in acidic solutions during water oxidation.¹⁸

Kinetic Data

Kinetic behavior at $1.0 \geq \theta > 0.0$. Figure 6.5A presents interrogation transients recorded in the range $E_{\text{subs}} = -1.00 - 0.00$ V. The first voltammogram (black line at the bottom) shows pure negative feedback because no $-\text{OH}_{(\text{ads})}$ are generated on the surface of

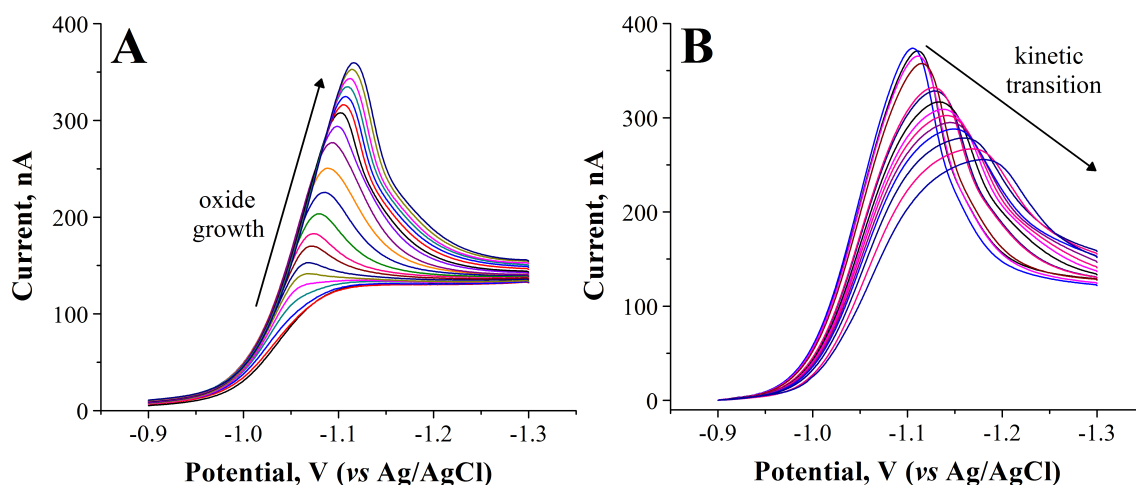


Figure 6.5. **A.** Interrogation transients obtained in the range $E_{\text{subs}} = -1.00$ V – 0.00 V. **B.** Interrogation transients obtained in the range $E_{\text{subs}} = 0.20$ V – 0.61 V. Only a few transients are shown for clarity. In all experiments: $t_{\text{step}} = 70$ s, $t_{\text{rest}} = 2$ s, and $v = 10$ mV s^{-1} . Solution: 10 mM Fe(III)-TEA in 2 M NaOH. GC electrode ($a = 50 \mu\text{m}$).

Ir at $E_{\text{subs}} = -1.00$ V. When E_{subs} is progressively stepped to more positive potentials, an interrogation peak starts to appear as the concentration of $\text{-OH}_{(\text{ads})}$ increases on the surface of Ir. All the interrogation transients recorded in this potential range presented a similar shape, and the peak current progressively increased in magnitude. To better understand such a trend in oxide growth, we carried out numerical simulations and fit our experimental results with transients obtained from the FEA model. The overlap between experimental and simulated results is presented in Figure 6.6 (only a few transients are shown). In the numerical model, the only variable changed was the surface concentration of $\text{-OH}_{(\text{ads})}$, Γ_j in equation (6-5).

Three observations are important from these results: 1) The peak current is a function of the concentration of Ir(III) and Ir(IV) oxides on the surface of Ir; 2) The

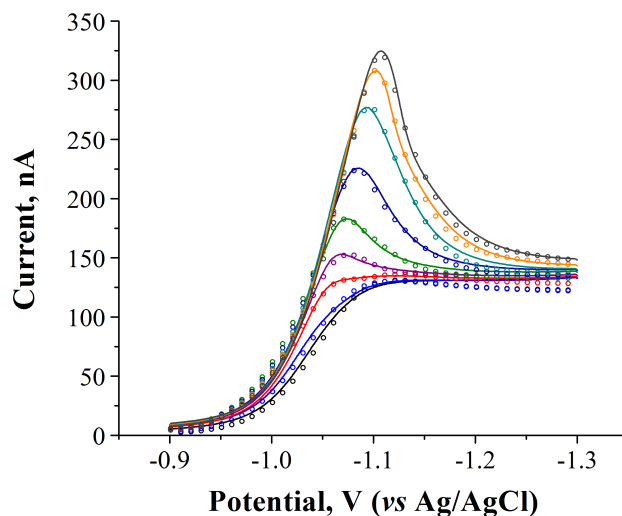


Figure 6.6. Numerical fit of experimental voltammograms from Figure 6.5A with simulated transients. In order of appearance, from bottom to top: -1.00 V (black), -0.90 V (blue), -0.80 V (red), -0.70 V (purple), -0.60 V (green), -0.50 V (navy), -0.40 V (cyan), -0.30 V (orange) and -0.20 V (black); $\nu = 10 \text{ mV s}^{-1}$. The rate constant used to fit the data was $k_{\text{IV,III}} = 40 \pm 5.0 \text{ mM}^{-1} \text{ s}^{-1}$. The subscript in $k_{\text{IV,III}}$ refers to the oxidation states of Ir believed to exist when the titration was carried out, Ir(III) and Ir(IV).

simulated rate constants k_{IV} and k_{III} have the same magnitude, $k_{IV,III} = 40 \pm 5.0 \text{ mM}^{-1} \text{ s}^{-1}$, and are constant over the potential range considered; and 3) The peak potential of the interrogation transient shifts with increasing surface coverage. Such a shift in peak potentials has been discussed in previous reports,^{11,34} in which surface oxidation of metals was studied by voltammetry and is generally attributed to adsorption/desorption kinetics of OH^- and to reorganization processes of the metal surface.

Kinetic behavior at $\theta > 1.0$. The interrogation transients obtained at potentials more positive than $E_{\text{subs}} = 0.20 \text{ V}$ present slower kinetics than those observed at $\theta \leq 1.0$ (Figure 6.5B). To better understand the nature of such changes in kinetic behavior, we modified the potential step condition at the substrate electrode from $t_{\text{step}} = 70 \text{ s}$ to $t_{\text{step}} = 50 \text{ s}$ to change the time-dependence of our SI-SECM titrations. In essence, decreasing the perturbation time, t_{step} , limited the extent of surface reorganization (homogenization) happening before the interrogation of adsorbates. The goal was to detect individual trends

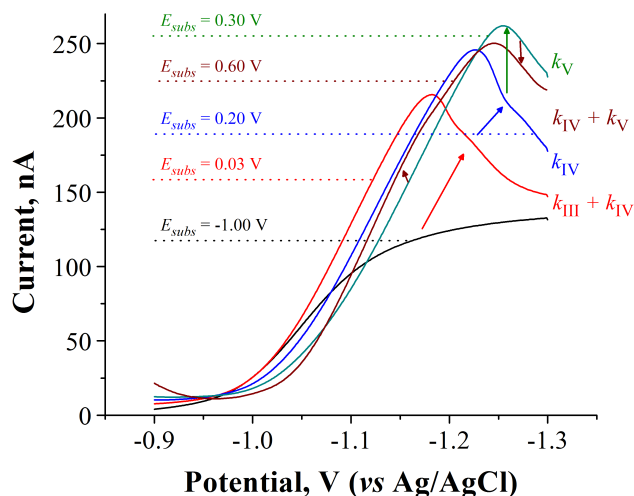


Figure 6.7. Interrogation transients obtained after modification of the potential step condition from $t_{\text{step}} = 70 \text{ s}$ to $t_{\text{step}} = 50 \text{ s}$. Changes in E_{subs} caused shifts in peak potentials and changes in the shape of the interrogation transients. Glassy carbon tip electrode ($a = 50 \mu\text{m}$) and Ir substrate ($a = 65 \mu\text{m}$ diameter); 10 mM Fe(TEA) in 2 M NaOH; $\nu = 10 \text{ mV s}^{-1}$.

of oxide growth at potentials more positive than $E_{\text{subs}} = 0.00$ V. Figure 6.7 shows the transients obtained after modification of t_{step} . In the figure, the first transient, black line, is the negative feedback baseline. The second transient, red line, was obtained after setting $E_{\text{subs}} = 0.03$ V and presents a shape similar to those observed in Figure 6.5A. The rates of reaction corresponding to this transient are k_{III} and k_{IV} as mentioned before. However, at more positive potentials the kinetic regime changes. For instance, the blue line in Figure 6.7 defines the limit in E_{subs} where kinetics are only controlled by rate k_{IV} , with a shift in peak potential of 44 mV more negative (blue arrow) than the red voltammogram. At $E_{\text{subs}} > 0.20$ V, new adsorbates are generated, Ir(V) oxides, and the net rate of reaction between the Ir(IV/V) oxides and Fe(II)-TEA is $k_{\text{IV}} + k_{\text{V}}$. A clear demonstration of this is shown in Figure 6.8, where mathematical fitting of the interrogation transient obtained at $E_{\text{subs}} = 0.25$ V required the addition of a second reaction rate in the FEA model:

$$k_{\text{net}} = k_{\text{V}}\Gamma_{\text{V}}C_{\text{Fe(II)-TEA}} + k_{\text{IV}}\Gamma_{\text{IV}}C_{\text{Fe(II)-TEA}} \quad (6-10)$$

where $k_{\text{IV}} = 40 \pm 5.0 \text{ mM}^{-1} \text{ s}^{-1}$, $k_{\text{V}} = 15 \pm 5.0 \text{ mM}^{-1} \text{ s}^{-1}$, and $\Gamma_{\text{V}} = 0.2 \Gamma_{\text{IV}}$. At $E_{\text{subs}} = 0.30$ V, green line, the contribution of $\Gamma_{\text{V}} > 0.2 \Gamma_{\text{IV}}$ and the peak current potential shifted 30 mV more negative and increased in magnitude. The generation of Ir(V) oxides on the substrate is demonstrated by both coulometry and kinetic results.

Kinetic behavior at $E_{\text{subs}} > 0.44$ V. When the Ir substrate is held at potentials where water oxidation actively occurs, the shape of the interrogation transients show a behavior that is intermediate between Ir(IV) and Ir(V) oxides. This is shown by the dark red voltammogram in Figure 6.7, recorded after $E_{\text{subs}} = 0.60$ V was applied on the Ir substrate. In the figure, the dark red arrows point to a decrease in the peak current obtained from the surface titration, and to a slight improvement in kinetics ($E_{1/2} = 20 \pm 4$ mV more positive, calculated from three repetitions) with respect to the green transient.

The change in kinetics is small, but reproducible. Based on the trends in reactivity observed so far, the change in kinetics at $E_{\text{subs}} = 0.60$ V does not indicate the appearance of a new oxide species (which would have $k < k_V$), but rather the average response of a new distribution of Ir(V) and Ir(IV) oxides on the surface of the substrate. We do not observe this behavior when carrying out the titration with $t_{\text{step}} = 70$ s, possibly because larger amounts of dissolved O_2 are produced and oxidize Fe(II)-TEA (increasing the extent of positive feedback at the tip). When the results from coulometry and the kinetic analysis are evaluated together, it seems reasonable to claim that the water oxidation reaction on iridium oxides in 2 M NaOH follows a similar catalytic cycle to the one observed in acidic solutions:¹⁸

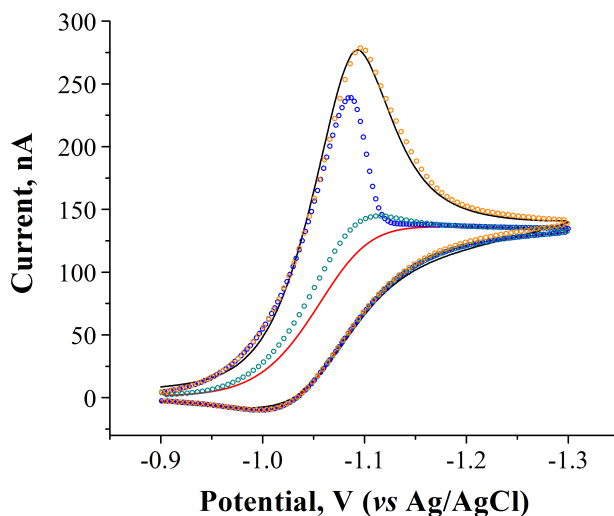
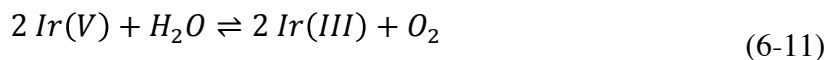


Figure 6.8. Theoretical fit of the interrogation transient obtained after holding the potential of the Ir substrate at $E_{\text{subs}} = 0.25$ V. *Black line*: experimental transient. *Red line*: experimental transient obtained under negative feedback conditions. *Blue dots*: contribution of $k_{\text{IV}}\Gamma_{\text{IV}}$. *Cyan dots*: contribution of $k_{\text{V}}\Gamma_{\text{V}}$. *Orange dots*: $k_{\text{IV}}\Gamma_{\text{IV}} + k_{\text{V}}\Gamma_{\text{V}}$.

where Ir(III) oxides generated from equation (6-11) are immediately converted to Ir(IV) and Ir(V) oxides at potentials $E_{\text{subs}} > 0.44 \text{ V}$.

At substrate potentials $E_{\text{subs}} > 0.60 \text{ V}$, dissolved O_2 accumulates in the gap between the two electrodes, and the SI-SECM titration becomes erratic. Occasionally, we observed formation of O_2 bubbles with consequent loss of electrical contact between the electrodes.

6.5. CONCLUSIONS

SI-SECM was employed to study the surface oxidation of polycrystalline iridium UMEs in 2 M NaOH. In particular, efforts were directed to understanding changes in the oxidation process prior to water oxidation. Several accomplishments are claimed in the present work: Fe(III/II)-TEA was successfully used to carry out SI-SECM detection of $-\text{OH}_{(\text{ads})}$ on Ir in 2 M NaOH; the potential of zero charge of the 2 M NaOH / H_2O / Ir system was characterized by SI-SECM; quantitative determination of the charge density corresponding to one monolayer coverage of $-\text{OH}_{(\text{ads})}$ and $-\text{H}_{(\text{ads})}$ on Ir was performed. Values of $Q_{\theta=1,\text{OH}} = 456 \pm 2.0 \mu\text{C cm}^{-2}$ for $-\text{OH}_{(\text{ads})}$ and $Q_{\theta=1,\text{H}} = 224.2 \pm 0.2 \mu\text{C cm}^{-2}$ for $-\text{H}_{(\text{ads})}$ are reported in this work; quantitative characterization of the main trends in surface oxide formation was achieved; and most importantly, coulometric and kinetic evidence is provided for the coexistence of Ir(IV) and Ir(V) oxide species during the oxygen evolution reaction at $\text{pH} = 14$.

6.6. REFERENCES

- [1] Rodríguez-López, J.; Zoski, C. G.; Bard, A. J., In *Scanning Electrochemical Microscopy*, Second Edition; CRC Press, 2012; pp. 525–568.

- [2] Rodríguez-Lopez, J.; Alpuche-Aviles, M.; Bard, A. J. *J. Am. Chem. Soc.*, **2008**, *130*, 1520-5126.
- [3] Rodríguez-Lopez, J.; *Electroanal. Chem.*, **2012**, *24*, 287-351.
- [4] Rodríguez-López, J.; Minguzzi, A.; Bard, A. J. *J. Phys. Chem. C*, **2010**, *114*, 18645–18655.
- [5] Beer, H. B.; *J. Electrochem. Soc.*, **1980**, *127*, 303C–307C.
- [6] Ardizzone, S.; Trasatti, S.; *Advances in Colloid and Interface Science*, **1996**, *64*, 173–251.
- [7] Papeschi, G.; Bordi, S.; Carlà, M.; Criscione, L.; Ledda, F.; *J. Med. Eng. Technol.*, **1981**, *5*, 86–87.
- [8] Macur, R.; Iridium-iridium oxide electrode for measuring pH of blood and other fluids. US3726777 A, April 10, 1973.
- [9] Buckley, D. N.; Burke, L. D.; *J. Chem. Soc., Faraday Trans. 1*, **1976**, *72*, 2431–2440.
- [10] Mozota, J.; Conway, B. E.; *Electrochim. Acta*, **1983**, *28*, 1-8.
- [11] Stonehart, P.; Kozłowska, H. A.; Conway, B. E.; *Proc. Roy. Soc. A*, **1969**, *310*, 541-563.
- [12] Chen, H.; Trasatti, S.; *J. App. Electrochem.*, **1993**, *23*, 559-566.
- [13] Kotz, R.; Lewerenz, H. J.; Bruesch, P.; Stucki, S.; *J. Electroanal. Chem.*, **1983**, *150*, 209-216.
- [14] Kotz, R.; Neff, H.; Stucki, S.; *J. Electrochem. Soc.*, **1984**, *131*, 72-77.
- [15] Minguzzi, A.; Lugaresi, O.; Locatelli, C.; Rondinini, S.; D’Acapito, F.; Achilli, E.; Ghigna, P.; *Anal. Chem.*, **2013**, *85*, 7009-7013.
- [16] Skoog, D. A.; Holler, F. J.; Crouch, S. R.; *Principles of Instrumental Analysis*, 6 edition., Cengage Learning: Belmont, CA, 2006.
- [17] Stonehart, P.; Kozłowska, H. A.; Conway, B. E.; *Proc. R. Soc. Lond. A*, **1969**, *310*, 541–563.
- [18] Minguzzi, A.; Lugaresi, O.; Achilli, E.; Locatelli, C.; Vertova, A.; Ghigna, P.; Rondinini, S.; *Chem. Sci.*, **2014**, *5*, 3591-3597.
- [19] Park, H. S.; Leonard, K. C.; Bard, A. J.; *J. Phys. Chem. C*, **2013**, *117*, 12093–12102.
- [20] Augustynski, J.; Koudelka, M.; Sanchez, J.; Conway, B. E.; *J. Electroanal. Chem.*, **1984**, *160*, 233-248.
- [21] Vertova, A.; Borgese, L.; Capelletti, G.; Locatelli, C.; Minguzzi, A.; Pezzoni, C.; Rondinini, S.; *J. Appl. Electroche.*, **2008**, *38*, 973-978.

- [22] Dahms, H.; Bockris, J. O'M.; *J. Electrochem. Soc.*, **1964**, *111*, 728-736.
- [23] Bard, A. J.; Mirkin, M. V. *Scanning Electrochemical Microscopy, Second Edition*; 2 edition.; CRC Press: Boca Raton, Fla, 2012.
- [24] Rodriguez-Lopez, J.; Minguzzi, A.; Bard, A. J.; *J. Phys. Chem. C*, **2010**, *114*, 18645-18655.
- [25] Wen, Y. H.; Zhang, H. M.; Qian, P.; Zhou, H. T.; Zhao, P.; Yi, B. L.; Yang, Y. S.; *Electrochim. Acta*, **2005**, *51*, 3769-3775.
- [26] Angerstein-Kozłowska, H.; Conway, B. E.; Mozota, J.; *J. Electroanal. Chem.*, **1979**, *100*, 417-446.
- [27] Jerkiewicz, G.; Vatankhah, G.; Lessard, J.; Soriaga, M. P.; Park, Y., *Electrochim. Acta*, **2004**, *49*, 1451-1459.
- [28] Otten, J. M.; Visscher, W.; *J. Electroanal. Chem.*, **1974**, *55*, 13-21.
- [29] Plichon, V.; Petit, M. A.; *J. Electroanal. Chem.*, **1998**, *444*, 247-252.
- [30] Burke, L. D.; Whelan, D. P.; *J. Electroanal. Chem.*, **1981**, *124*, 333-337.
- [31] Woods, R.; *J. Electroanal. Chem.*, **1974**, *49*, 217-227.
- [32] Delahay, P.; *Double layer and electrode kinetics*; Interscience Publishers, 1965.
- [33] Bard, A. J.; Faulkner, L. R.; *Electrochemical Methods: Fundamentals and Applications*; Wiley: New York, 2001.
- [34] Gileadi, E.; Conway, B. E.; *J. Chem. Phys.*, **1963**, *39*, 3420-3430.

Chapter 7. Concluding Remarks

This dissertation presented the development of the first a-RFB based on the coordination chemistry of Fe(III/II) and Co(III/II) in concentrated $\text{NaOH}_{(\text{aq})}$ solutions. The chemistry of the redox active compounds was characterized by solid-state X-ray analysis, Raman spectroscopy and DFT simulations. The electrochemistry of the system was characterized by voltammetry, chronoamperometry, and bulk electrolysis. The conditions of the a-RFB were optimized to achieve energy efficiencies of 70 -76 % at current densities of 30 mA cm^{-2} . More importantly, significant species crossover was not observed in up to 30 charge-discharge cycles, a significant improvement over existing commercial technologies that are known to deactivate due to crossover.

The importance of this work to stationary scale EES is hard to judge at this stage since the a-RFB discussed and its chemistry have only been tested at a laboratory prototype scale. The challenges of scaling up the technology to kW h^{-1} or MW h^{-1} storage are out of the scope of the present work and require a multidisciplinary team with excellent engineering and chemistry skills. Further, two current limitations of the technology remain to be solved in the future: (1) The energy density of the Co/Fe a-RFB must be increased, from 0.5 M to $> 1 \text{ M}$, for it to be competitive with state-of-the-art RFBs; and (2) Membrane materials, chemically stable in concentrated base and with higher diffusivity of sodium ions than Nafion, must be developed to improve the voltage efficiency of the charging-discharging process. A solution to the first limitation may be found by researching mixed solvent systems (binary systems), where the properties of one solvent could be used to complement those of the second solvent. For example, 5 M NaOH in water has excellent conductivity, but Fe-TEA can only be dissolved to concentrations around 0.6 M. Acetonitrile, however, can dissolve Fe-TEA to

concentrations > 2 M but has poor conductivity. Perhaps a mixture of the two solvents may enhance the energy density of the system by increasing the concentrations of electroactive species without dramatically compromising conductivity. The second limitation requires systematic designing and synthesis of membranes or separators with high and selective permeability to sodium ions.

With respect to the chemistry of the flow battery, unanswered questions still exist regarding the mechanism of electron transfer in Fe(III/II)-TEA. For instance, crystallographic structures of all the different species reported in Chapter 3 have not yet been characterized. The mechanism proposed in Chapter 3 could be further supported or disproven with additional crystallographic information. Moreover, it is intriguing that solutions containing $[(\text{TEA})\text{Fe}(\text{III})\text{OFe}(\text{II})(\text{TEA})]^{3-}$ only present one redox wave in CV. The question of why the second electron cannot be transferred is still unanswered. A possible explanation is that oxidation of $[(\text{TEA})\text{Fe}(\text{III})\text{OFe}(\text{II})(\text{TEA})]^{3-}$ to produce 2 $[\text{Fe}(\text{III})(\text{TEA})(\text{OH})]^-$ requires breaking a bond (since the dinuclear ferric species $[(\text{Fe}(\text{III})(\text{TEA}))_2(\mu\text{-O})]$ were never observed) and thus can only be carried out at potentials more positive than the oxidation of the solvent. However, further experiments and detailed computational simulations are required to support such a hypothesis. Additionally, questions regarding the mechanism of homogeneous reduction of O_2 by Fe(II)-TEA remain unanswered. For example, further experimentation is required to support the catalytic protonation of O_2^- by Fe(II)-TEA, despite $pK_a = 5$ for the conjugate acid.

APPENDIX A

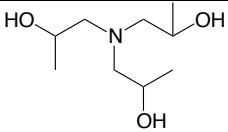
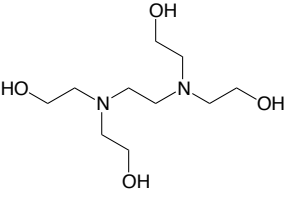
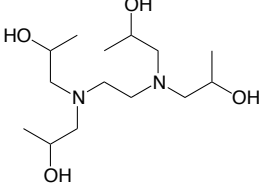
7.1. SUPPORTING INFORMATION - CHAPTER 1

Table A1. Compendium of Metallic Ions, Ligands and Anions Tested: Mn, Fe, Co

#	Ligand Name & Structure	Mn(II) (SO ₄ ²⁻ , Cl ⁻)	Fe(II/III) (SO ₄ ²⁻ , Cl ⁻ , NO ₃ ⁻)	Co(II) (SO ₄ ²⁻ , NO ₃ ⁻)
1	 HO-CH ₂ -CH ₂ -N(CH ₂ -CH ₂ -OH) ₂	✖: disproportionates S, $E_{qr} = -0.470$ V	S, $E_{rev} = -1.05$ V	S, $E_{qr} = -0.10$ V
2	triethanolamine HO-CH ₂ -CH ₂ -N(CH ₂ -CH ₂ -OH) ₃	✖: disproportionates S, $E_{qr} = -0.460$ V	S, $E_{rev} = -1.05$ V	S, $E_{qr} = -0.12$ V
3	2,2'-((2-hydroxypropyl)azanediyl)diethanol HO-CH ₂ -CH(CH ₃)-CH ₂ -N(CH ₂ -CH ₂ -OH) ₂	✖: disproportionates S, $E_{qr} = -0.460$ V	S, $E_{rev} = -1.07$ V	S, $E_{qr} = -0.12$ V
	1,1'-((2-hydroxyethyl)azanediyl)bis(propan-2-ol)			

S: A complex is formed with the ligand in 1 – 5 M NaOH (10 mM), yielding a clear solution with no precipitate. ✖: The metal ion precipitates as an oxide-hydroxide. E: The solution is electrochemically active: $E_{rev} = (\Delta E_p \leq 60$ mV), $E_{qr} = (60$ mV < $\Delta E_p \leq 200$ mV), $E_{irr} = (\Delta E_p > 200$ mV). ☒: No electrochemical activity in potential window of interest. Electrodes: glassy carbon & Au. Reference: Ag/AgCl. Note: the anion contributes significantly to the solubility of the complex: SO₄²⁻ < Cl⁻ < NO₃⁻.

Table A1. (Continued)

#	Ligand Name & Structure	Mn(II) (SO ₄ ²⁻ , Cl ⁻)	Fe(II/III) (SO ₄ ²⁻ , Cl ⁻ , NO ₃ ⁻)	Co(II) (SO ₄ ²⁻ , NO ₃ ⁻)
4	 triisopropanolamine	✖: disproportionates S, $E_{qr} = -0.453$ V	S, $E_{rev} = -1.09$ V	S, $E_{rev} = -0.136$ V
5	 2,2',2''-(ethane-1,2-diylbis(azanetriyl))tetraethanol	✖: disproportionates S, 1 st - $E_{irr} = -0.40$ V 2 nd - $E_{qr} = 0.15$ V	S, $E_{qr} = -0.941$ V	S, E_{irr}
6	 1,1',1'',1'''-(ethane-1,2-diylbis(azanetriyl))tetrakis(propan-2-ol)	✖: disproportionates S, 1 st - $E_{irr} = -0.40$ V 2 nd - $E_{qr} = 0.15$ V	S, $E_{qr} = -0.941$ V	S, E_{irr}

S: A complex is formed with the ligand in 1 – 5 M NaOH (10 mM), yielding a clear solution with no precipitate. ✖: The metal ion precipitates as an oxide-hydroxide. E : The solution is electrochemically active: $E_{rev} = (\Delta E_p \leq 60 \text{ mV})$, $E_{qr} = (60 \text{ mV} < \Delta E_p \leq 200 \text{ mV})$, $E_{irr} = (\Delta E_p > 200 \text{ mV})$. ☒: No electrochemical activity in potential window of interest. Electrodes: glassy carbon & Au. Reference: Ag/AgCl. Note: the anion contributes significantly to the solubility of the complex: SO₄²⁻ < Cl⁻ < NO₃⁻.

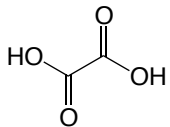
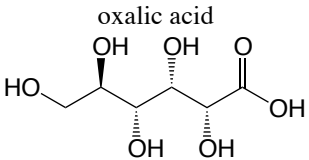
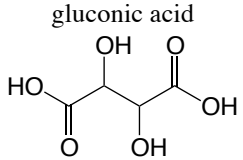
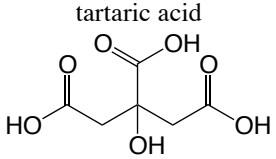
Table A1. (Continued)

#	Ligand Name & Structure	Mn(II) (SO ₄ ²⁻ , Cl ⁻)	Fe(II/III) (SO ₄ ²⁻ , Cl ⁻ , NO ₃ ⁻)	Co(II) (SO ₄ ²⁻ , NO ₃ ⁻)
7	<p>EDTA</p>	✖	✖	S, ☒
8	<p>HEDTA</p>	S, 1 st , 2 nd - $E_{qr} = -0.3$ V	S, $E_{qr} = -1.121$ V	S, ☒

2-(bis(2-hydroxyethyl)amino)-2-(hydroxymethyl)propane-1,3-diol

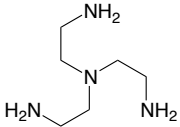
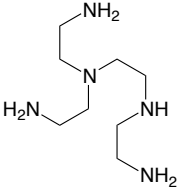
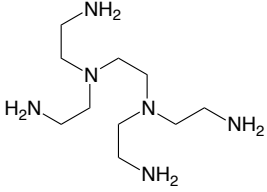
S: A complex is formed with the ligand in 1 – 5 M NaOH (10 mM), yielding a clear solution with no precipitate. ✖: The metal ion precipitates as an oxide-hydroxide. E : The solution is electrochemically active: $E_{rev} = (\Delta E_p \leq 60 \text{ mV})$, $E_{qr} = (60 \text{ mV} < \Delta E_p \leq 200 \text{ mV})$, $E_{irr} = (\Delta E_p > 200 \text{ mV})$. ☒: No electrochemical activity in potential window of interest. Electrodes: glassy carbon & Au. Reference: Ag/AgCl. Note: the anion contributes significantly to the solubility of the complex: $\text{SO}_4^{2-} < \text{Cl}^- < \text{NO}_3^-$.

Table A1. (Continued)

#	Ligand Name & Structure	Mn(II) (SO ₄ ²⁻ , Cl ⁻)	Fe(II/III) (SO ₄ ²⁻ , Cl ⁻ , NO ₃ ⁻)	Co(II) (SO ₄ ²⁻ , NO ₃ ⁻)
10		✖	✖	✖
11	oxalic acid 	S, ☒	S, ☒	S, ☒
12	gluconic acid 	S, ☒	S, ☒	S, ☒
13	tartaric acid 	S, ☒	S, ☒	S, ☒
	citric acid			

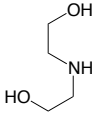
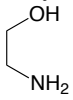
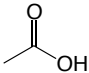
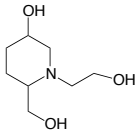
S: A complex is formed with the ligand in 1 – 5 M NaOH (10 mM), yielding a clear solution with no precipitate. ✖: The metal ion precipitates as an oxide-hydroxide. *E*: The solution is electrochemically active: $E_{\text{rev}} = (\Delta E_p \leq 60 \text{ mV})$, $E_{\text{qr}} = (60 \text{ mV} < \Delta E_p \leq 200 \text{ mV})$, $E_{\text{irr}} = (\Delta E_p > 200 \text{ mV})$. ☒: No electrochemical activity in potential window of interest. Electrodes: glassy carbon & Au. Reference: Ag/AgCl. Note: the anion contributes significantly to the solubility of the complex: SO₄²⁻ < Cl⁻ < NO₃⁻.

Table A1. (Continued)

#	Ligand Name & Structure	Mn(II) (SO ₄ ²⁻ , Cl ⁻)	Fe(II/III) (SO ₄ ²⁻ , Cl ⁻ , NO ₃ ⁻)	Co(II) (SO ₄ ²⁻ , NO ₃ ⁻)
14	 N ¹ ,N ¹ -bis(2-aminoethyl)ethane-1,2-diamine	✘	✘	S, E _{irr}
15	 N ¹ ,N ¹ ,N ² -tris(2-aminoethyl)ethane-1,2-diamine	✘	✘	S, E _{irr}
16	 N ¹ ,N ^{1'} -(ethane-1,2-diyl)bis(N ^{1'} -(2-aminoethyl)ethane-1,2-diamine)	✘	✘	S, E _{irr}

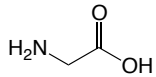
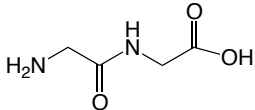
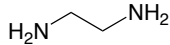
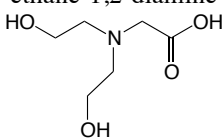
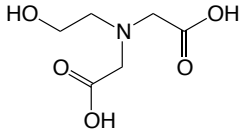
S: A complex is formed with the ligand in 1 – 5 M NaOH (10 mM), yielding a clear solution with no precipitate. ✘: The metal ion precipitates as an oxide-hydroxide. E: The solution is electrochemically active: $E_{rev} = (\Delta E_p \leq 60 \text{ mV})$, $E_{qr} = (60 \text{ mV} < \Delta E_p \leq 200 \text{ mV})$, $E_{irr} = (\Delta E_p > 200 \text{ mV})$. ☒: No electrochemical activity in potential window of interest. Electrodes: glassy carbon & Au. Reference: Ag/AgCl. Note: the anion contributes significantly to the solubility of the complex: SO₄²⁻ < Cl⁻ < NO₃⁻.

Table A1. (Continued)

#	Ligand Name & Structure	Mn(II) (SO ₄ ²⁻ , Cl ⁻)	Fe(II/III) (SO ₄ ²⁻ , Cl ⁻ , NO ₃ ⁻)	Co(II) (SO ₄ ²⁻ , NO ₃ ⁻)
17	 2,2'-azanediyldiethanol	✘	✘	✘
18	 2-aminoethanol	✘	✘	✘
19	 acetic acid	✘	✘	✘
20	 1-(2-hydroxyethyl)-6-(hydroxymethyl)piperidin-3-ol	✘	✘	✘

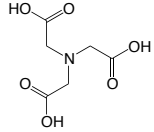
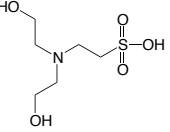
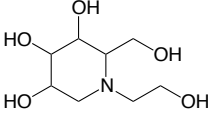
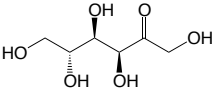
S: A complex is formed with the ligand in 1 – 5 M NaOH (10 mM), yielding a clear solution with no precipitate. ✘: The metal ion precipitates as an oxide-hydroxide. E: The solution is electrochemically active: $E_{rev} = (\Delta E_p \leq 60 \text{ mV})$, $E_{qr} = (60 \text{ mV} < \Delta E_p \leq 200 \text{ mV})$, $E_{irr} = (\Delta E_p > 200 \text{ mV})$. ☒: No electrochemical activity in potential window of interest. Electrodes: glassy carbon & Au. Reference: Ag/AgCl. Note: the anion contributes significantly to the solubility of the complex: $\text{SO}_4^{2-} < \text{Cl}^- < \text{NO}_3^-$.

Table A1. (Continued)

#	Ligand Name & Structure	Mn(II) (SO ₄ ²⁻ , Cl ⁻)	Fe(II/III) (SO ₄ ²⁻ , Cl ⁻ , NO ₃ ⁻)	Co(II) (SO ₄ ²⁻ , NO ₃ ⁻)
21	 glycine	✘	✘	✘
22	 2-(2-aminoacetamido)acetic acid	✘	✘	S, E _{irr}
23	 ethane-1,2-diamine	✘	✘	S, E _{irr}
24	 2-(bis(2-hydroxyethyl)amino)acetic acid	S, E _{irr}	S, E _{rev} = -0.93 V	S, E _{irr}
25	 2,2'-(2-hydroxyethyl)azanediyl)diacetic acid	✘	S, E _{qr} = -0.92 V	S, E _{irr}

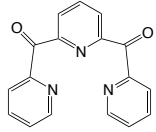
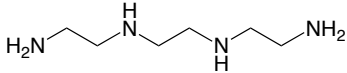
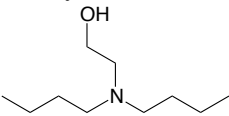
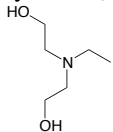
S: A complex is formed with the ligand in 1 – 5 M NaOH (10 mM), yielding a clear solution with no precipitate. ✘: The metal ion precipitates as an oxide-hydroxide. E: The solution is electrochemically active: E_{rev} = ($\Delta E_p \leq 60$ mV), E_{qr} = (60 mV < $\Delta E_p \leq 200$ mV), E_{irr} = ($\Delta E_p > 200$ mV). ☒: No electrochemical activity in potential window of interest. Electrodes: glassy carbon & Au. Reference: Ag/AgCl. Note: the anion contributes significantly to the solubility of the complex: SO₄²⁻ < Cl⁻ < NO₃⁻.

Table A1. (Continued)

#	Ligand Name & Structure	Mn(II) (SO ₄ ²⁻ , Cl ⁻)	Fe(II/III) (SO ₄ ²⁻ , Cl ⁻ , NO ₃ ⁻)	Co(II) (SO ₄ ²⁻ , NO ₃ ⁻)
26	 2,2',2''-nitilotriacetic acid	✖	✖	S, E _{irr}
27	 2-(bis(2-hydroxyethyl)amino)ethanesulfonic acid	S, E _{irr} = -0.450 V	S, E _{qr} = -1.03 V	S, E _{qr} = -0.07 V
28	 1-(2-hydroxyethyl)-2-(hydroxymethyl)piperidine-3,4,5-triol	✖	✖	✖
29	 fructose	S, ☒	S, ☒	S, ☒

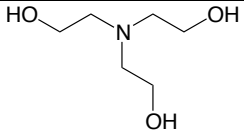
S: A complex is formed with the ligand in 1 – 5 M NaOH (10 mM), yielding a clear solution with no precipitate. ✖: The metal ion precipitates as an oxide-hydroxide. E: The solution is electrochemically active: $E_{rev} = (\Delta E_p \leq 60 \text{ mV})$, $E_{qr} = (60 \text{ mV} < \Delta E_p \leq 200 \text{ mV})$, $E_{irr} = (\Delta E_p > 200 \text{ mV})$. ☒: No electrochemical activity in potential window of interest. Electrodes: glassy carbon & Au. Reference: Ag/AgCl. Note: the anion contributes significantly to the solubility of the complex: SO₄²⁻ < Cl⁻ < NO₃⁻.

Table A1. (Continued)

#	Ligand Name & Structure	Mn(II) (SO ₄ ²⁻ , Cl ⁻)	Fe(II/III) (SO ₄ ²⁻ , Cl ⁻ , NO ₃ ⁻)	Co(II) (SO ₄ ²⁻ , NO ₃ ⁻)
30	 pyridine-2,6-diylbis(pyridin-2-ylmethanone)	✘	✘	✘
31	 triethylenetetramine	✘	✘	S, <i>E</i> _{irr}
32	 2-(dibutylamino)ethanol	✘	✘	S, <i>E</i> _{irr}
33	 2,2'-(ethylazanediyloxy)diethanol	✘	✘	S, <i>E</i> _{irr}

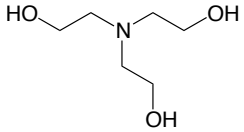
S: A complex is formed with the ligand in 1 – 5 M NaOH (10 mM), yielding a clear solution with no precipitate. ✘: The metal ion precipitates as an oxide-hydroxide. *E*: The solution is electrochemically active: $E_{rev} = (\Delta E_p \leq 60 \text{ mV})$, $E_{qr} = (60 \text{ mV} < \Delta E_p \leq 200 \text{ mV})$, $E_{irr} = (\Delta E_p > 200 \text{ mV})$. ☒: No electrochemical activity in potential window of interest. Electrodes: glassy carbon & Au. Reference: Ag/AgCl. Note: the anion contributes significantly to the solubility of the complex: SO₄²⁻ < Cl⁻ < NO₃⁻.

Table A2. Compendium of Metallic Ions, Ligands and Anions Tested: Sc, Ti, V, Cr

Ligand Name & Structure	ScCl ₃	TiCl ₃	VCl ₃	Cr(NO) ₃
	S, ☒	S, ☒	S, ☒	S, $E_{irr} = 0.40$ V
triethanolamine				

S: A complex is formed with the ligand in 1 – 5 M NaOH (10 mM), yielding a clear solution with no precipitate. ✖: The metal ion precipitates as an oxide-hydroxide. E: The solution is electrochemically active: $E_{rev} = (\Delta E_p \leq 60$ mV), $E_{qr} = (60$ mV < $\Delta E_p \leq 200$ mV), $E_{irr} = (\Delta E_p > 200$ mV). ☒: No electrochemical activity in potential window of interest. Electrodes: glassy carbon & Au. Reference: Ag/AgCl.

Table A3. Compendium of Metallic Ions, Ligands and Anions Tested: Ni, Cu, Zn, Sn

Ligand Name & Structure	NiCl ₂	CuCl ₂	ZnCl ₂	SnCl ₂
	deposits at open circuit potential	deposits at open circuit potential	deposits at open circuit potential	S, E_{irr}
triethanolamine				

S: A complex is formed with the ligand in 1 – 5 M NaOH (10 mM), yielding a clear solution with no precipitate. ✖: The metal ion precipitates as an oxide-hydroxide. E: The solution is electrochemically active: $E_{rev} = (\Delta E_p \leq 60$ mV), $E_{qr} = (60$ mV < $\Delta E_p \leq 200$ mV), $E_{irr} = (\Delta E_p > 200$ mV). ☒: No electrochemical activity in potential window of interest. Electrodes: glassy carbon & Au. Reference: Ag/AgCl.

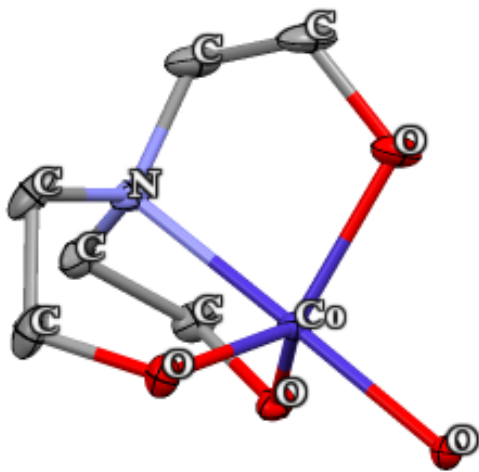


Figure A1. Solid state structure of the anion $[\text{Co}(\text{II})(\text{TEA})(\text{H}_2\text{O})]^-$ determined with crystals grown from 5 M $\text{NaOH}_{(\text{aq})}$. Ellipsoids drawn at the 80% probability level and hydrogens omitted for clarity. A similar structure has been reported elsewhere¹ from crystals grown in the presence of Cl^- ions.

7.2. SUPPORTING INFORMATION - CHAPTER 2

Dimensions of Electrochemical Cell and Electrodes for e-SECM

- The dimensions are provided “as used” in this work.
- The cell is a conventional SECM cell made of Teflon.
- Technical specifications regarding the kind of Tygon tubing employed are provided in section 2.4. All Tygon segments were cut by hand with the aid of a ruler and a stainless steel blade.
- The SECM tip electrode was polished by hand, dimensions are provided as measured under an optical microscope.

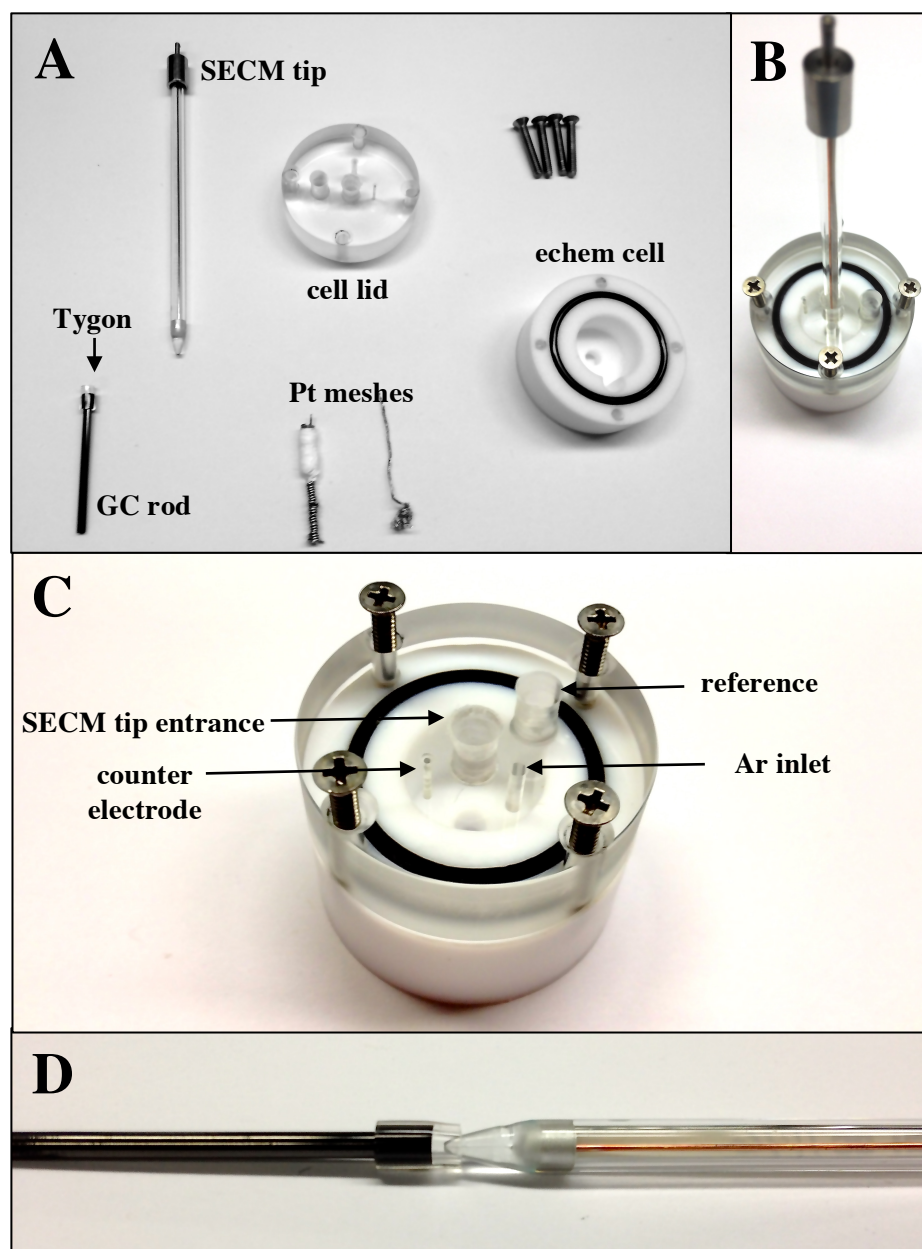
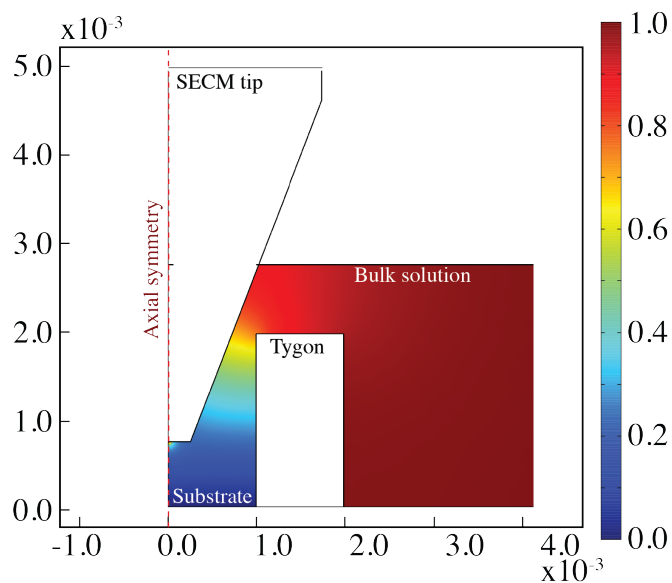


Figure A2. **A.** Components of the cell set-up. **B.** Final configuration of the cell, with SECM tip electrode inserted into SECM tip entrance. This entrance was 4.1 mm in diameter, allowing little space for the tip electrode to move around and keeping it aligned to the center of the Tygon tube. **C.** Top view of experimental cell. **D.** Glassy carbon rod, Tygon tube and SECM tip electrode aligned.

Model for Digital Simulations of e-SECM

COMSOL Multiphysics was used in the present work to model the 2-D axisymmetric geometry shown below:



The model solved for a one-electron transfer reaction with Butler-Volmer kinetics as presented below:



In this equation, the forward and backward rate constants, k_f and k_b , are defined as:

$$k_f = k^0 \cdot e^{\left(-\frac{\alpha F}{RT}(E-E^{0'})\right)} \quad (7-2)$$

$$k_b = k^0 \cdot e^{\left(-\frac{(1-\alpha)F}{RT}(E-E^{0'})\right)} \quad (7-3)$$

where k^0 is the heterogeneous rate of electron transfer, α is the transfer coefficient (assumed to be 0.5 in this model), $E^{0'}$ is the formal redox potential of the redox couple

and E the applied electrode potential. On another hand, diffusion of species O and R in the system was assumed to obey Fick's laws of diffusion with a Laplacian operator adjusted for the geometry of an inlaid disk electrode:

$$\frac{\partial C_O(r, z, t)}{\partial t} = D_O \left[\frac{\partial^2 C_O(r, z, t)}{\partial r^2} + \frac{1}{r} \cdot \frac{\partial C_O(r, z, t)}{\partial r} + \frac{\partial^2 C_O(r, z, t)}{\partial z^2} \right] \quad (7-4)$$

$$\frac{\partial C_R(r, z, t)}{\partial t} = D_O \left[\frac{\partial^2 C_R(r, z, t)}{\partial r^2} + \frac{1}{r} \cdot \frac{\partial C_R(r, z, t)}{\partial r} + \frac{\partial^2 C_R(r, z, t)}{\partial z^2} \right] \quad (7-5)$$

where C_O and C_R are the bulk concentrations of species O and R in solution, D_O and D_R their respective diffusion coefficients, z is the distance normal to the electrode surface and r the radial distance from the center of the disk electrode. The following boundary conditions were used:

- **Initial conditions**

$$D_O = D_R \quad (7-6)$$

$$C_R = C_b - C_O \quad (7-7)$$

with C_b = bulk concentration of analyte

$$C_O = C_b, 0 \leq r \leq a, 0 \leq z \leq z_{max} \quad (7-8)$$

with a = radius of disk electrode and z_{max} = domain limit

$$C_R = 0, 0 \leq r \leq a, 0 \leq z \leq z_{max} \quad (7-9)$$

- **Semi-infinite boundary conditions**

$$\lim_{z \rightarrow \infty} C_O(r, z, t) = C_b \quad (7-10)$$

$$\lim_{z \rightarrow \infty} C_R(r, z, t) = 0 \quad (7-11)$$

- **Semi-infinite boundary conditions**

As given in the main text for both tip and substrate electrodes:

$$-D_O \nabla C_O = -k_f C_O(0, r, t) + k_b C_R(0, r, t) \quad (7-12)$$

$$-D_R \nabla C_R = k_f C_O(0, r, t) - k_b C_R(0, r, t) \quad (7-13)$$

The CV experiment was simulated based on a characteristic time:

$$\tau = \frac{2(E_i - E_f)}{v} \quad (7-14)$$

where E_i is the initial potential and E_f the final potential of a potential sweep and v is the scan rate. The wave function of the CV experiment was simulated as:

$$E = E_i + (E_f - E_i) \frac{2}{\pi} \sin^{-1} \left\{ \sin \left[\frac{\pi v t}{2(E_f - E_i)} \right] \right\} \quad (7-15)$$

$$0 \leq t \leq t_c$$

Similarly, the uncompensated resistance, R_u , and the double-layer capacitance, C_{dl} , were

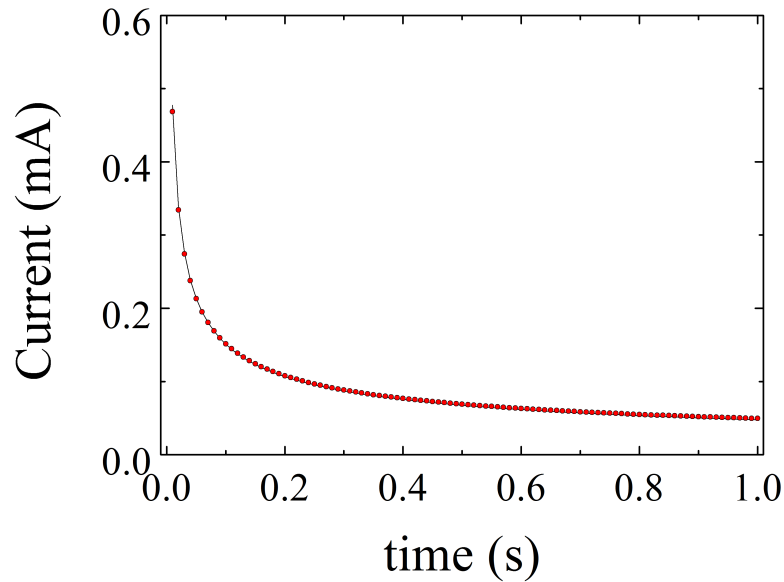


Figure A3. Calibration of the numerical model of e-SECM with the Cottrell equation. The black line is the Cottrell equation, the red circles are the numerical simulation.

inserted into the model as:

$$i_{nF} = vC_{dl} \left[1 - e^{(-t/R_u C_{dl})} \right] \quad (7-16)$$

Finally, the net current at both tip and substrate electrodes was integrated as:

$$i = -2\pi nFD_0 \int_{r=0}^{r=a} r \frac{\delta C_O(0, r, t)}{\delta z} dr + i_{nF} \quad (7-17)$$

The maximum mesh element size (and thus the accuracy of the calculated results) was first calibrated with a potential step, decreasing the size of the elements until the simulated curve fitted the Cottrell equation within 5% error, shown in Figure A2. This was achieved with a mesh size of $m = 0.03 \times a$.

7.3. SUPPORTING INFORMATION - CHAPTER 3

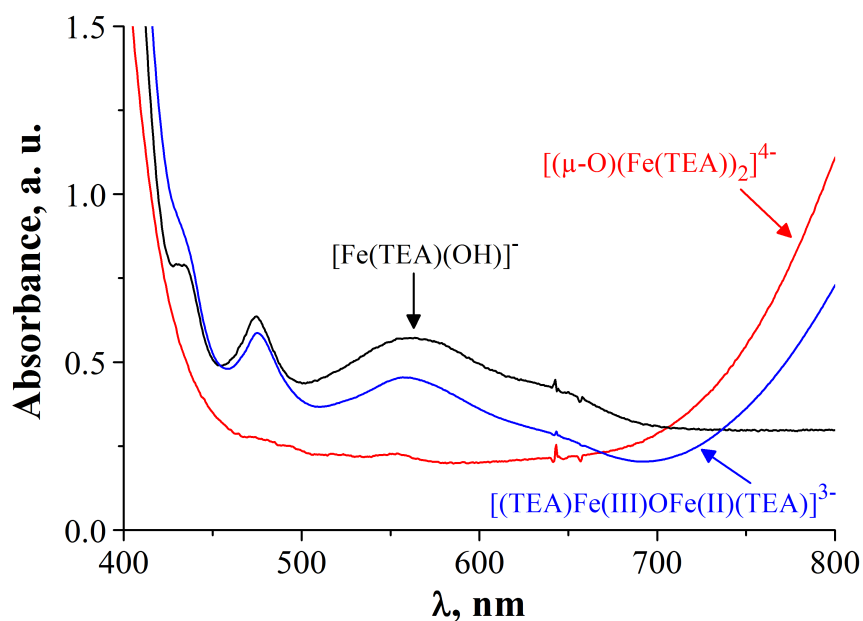


Figure A4. UV-Vis spectra of the various complexes studied in this work. UV-Vis spectra were acquired with a SEC2000-UV/VIS Spectrometer from ALS (Japan), using a quartz cuvette with path length $l = 1$ cm. All solutions are 0.5 M (iron content) in 5 M NaOH.

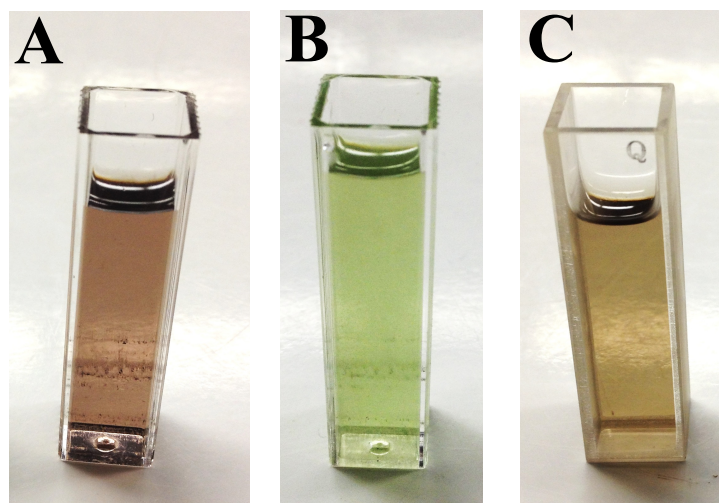


Figure A5. **A.** 0.5 M $[\text{Fe}(\text{TEA})(\text{OH})]^-$ in 5 M NaOH. **B.** 0.25 M $[(\mu\text{-O})(\text{Fe}(\text{TEA}))_2]^{4+}$ in 5 M NaOH. **C.** 0.25 M $[(\text{TEA})\text{Fe}(\text{III})\text{OFe}(\text{II})(\text{TEA})]^{3-}$ in 5 M NaOH.

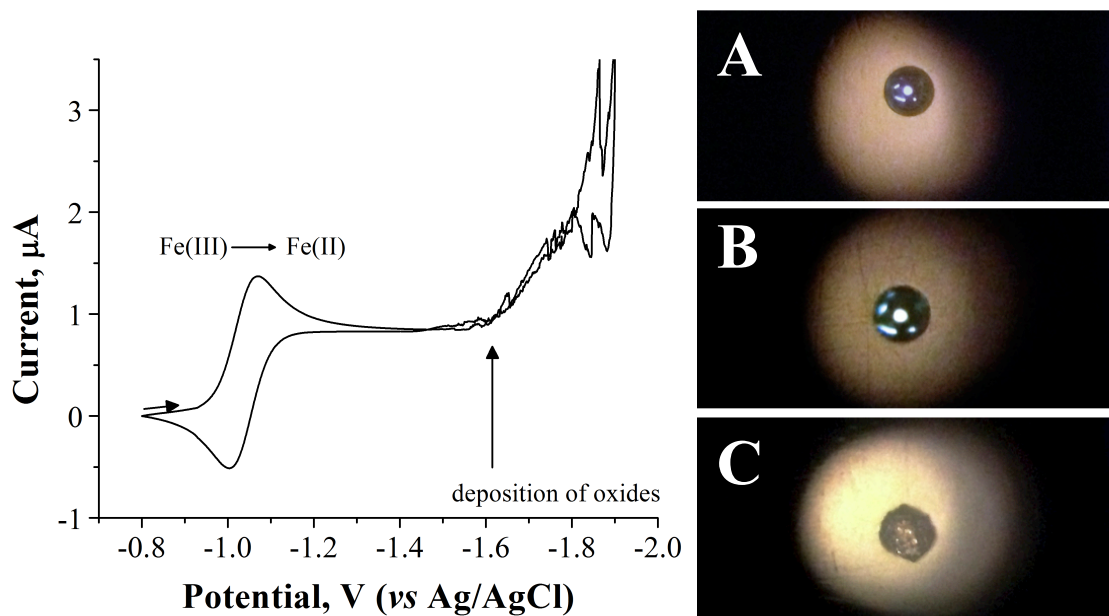


Figure A6. CV of 250 mM Fe(III)-TEA in 5 M NaOH at a mercury film electrode on Au UME ($a = 50 \mu\text{m}$). $v = 50 \text{ mV s}^{-1}$. **A.** Optical image of the mercury film after holding the potential at -1.20 V for 100 s. **B.** After holding the potential at -1.70 V for 100 s. **C.** After holding the potential at -1.90 V for 100 s, clear deposition of iron oxides/hydroxides is observed.

Table A4. Calculated vibrational modes of [Fe(III)(TEA)(OH)]⁻ and their assigned vibrations.

ν (cm ⁻¹)	Assigned Mode	ν (cm ⁻¹)	Assigned Mode	ν (cm ⁻¹)	Assigned Mode
56.82	δ (MOH) twist	570.92	δ (CH ₂) rock, δ (FeOH) scissor	1217.45	δ (CH ₂) twist
82.76	δ (CH ₂) rock, δ (OFeO) scissor	573.08	δ (CH ₂) rock, δ (FeOH) scissor	1247.60	δ (CH ₂) twist
111.00	δ (FeOH) twist, δ (CH ₂) rock, δ (OFeO) scissor	591.63	δ (FeOH) scissor	1250.97	δ (CH ₂) twist
125.09	δ (FeOH) twist, δ (CH ₂) rock, δ (OFeO) scissor	720.52	δ (CH ₂) twist, rock	1251.68	δ (CH ₂) twist
145.72	δ (CH ₂) rock, δ (OFeO) wag, δ (FeOH) scissor	841.41	δ (CH ₂) rock	1326.04	δ (CH ₂) wag
168.91	δ (FeOH) wag	842.00	δ (CH ₂) rock	1326.34	δ (CH ₂) wag
188.05	δ (CH ₂) twist, δ (FeOH) twist, ν (FeO) sym., ν (FeN)	861.73	δ (CH ₂) wag, rock	1336.19	δ (CH ₂) wag
202.82	δ (CH ₂) rock	890.18	δ (CH ₂) twist	1341.92	δ (CH ₂) wag
206.77	δ (CH ₂) rock	890.65	δ (CH ₂) twist	1352.21	δ (CH ₂) wag, twist
268.65	δ (CH ₂) rock	982.82	δ (CH ₂) twist	1352.49	δ (CH ₂) wag, twist
272.00	δ (CH ₂) rock	1021.26	δ (CH ₂) twist, rock, ν (CN) asym., δ (CNC) scissor	1435.59	δ (CH ₂) scissor
285.57	δ (CH ₂) rock	1021.70	δ (CH ₂) twist, rock, ν (CN) asym., δ (CNC) scissor	1435.93	δ (CH ₂) scissor
356.26	ν (FeO) sym., ν (FeN)	1047.01	δ (CH ₂) rock, ν (CO) asym.	1437.36	δ (CH ₂) scissor
381.27	δ (CH ₂) rock	1047.96	δ (CH ₂) rock, ν (CO) asym.	1453.95	δ (CH ₂) scissor
381.81	δ (CH ₂) rock	1049.07	δ (CH ₂) rock, ν (CO) asym.	1454.84	δ (CH ₂) scissor
439.63	δ (CH ₂) twist, ν (FeO) asym.	1069.79	δ (CH ₂) rock, ν (CO) sym.	1458.74	δ (CH ₂) scissor
445.21	δ (CH ₂) twist, ν (FeO) asym.	1138.66	δ (CH ₂) twist, rock		
447.72	δ (CH ₂) twist, ν (FeO) asym., ν (FeN)	1138.95	δ (CH ₂) twist, rock		
472.02	δ (CH ₂) twist, ν (FeO) sym., ν (FeN), ν (Fe-OH), δ (FeOH) scissor	1203.14	δ (CH ₂) twist		
533.55	δ (CH ₂) rock	1217.31	δ (CH ₂) twist		

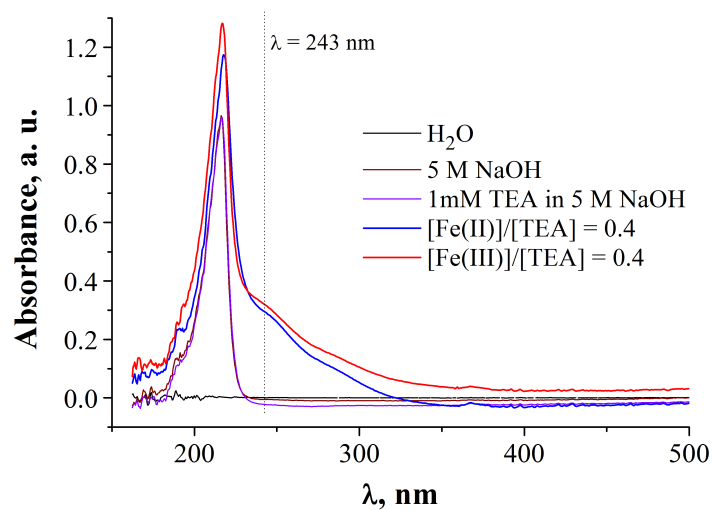


Figure A7. UV-Vis spectra of various solutions as indicated in the figure's legend. The molar absorptivities are $\epsilon_{\text{Fe(II)-TEA}} = 121 \text{ M}^{-1} \text{ cm}^{-1}$ and $\epsilon_{\text{Fe(III)-TEA}} = 125 \text{ M}^{-1} \text{ cm}^{-1}$.

7.4. SUPPORTING INFORMATION - CHAPTER 4

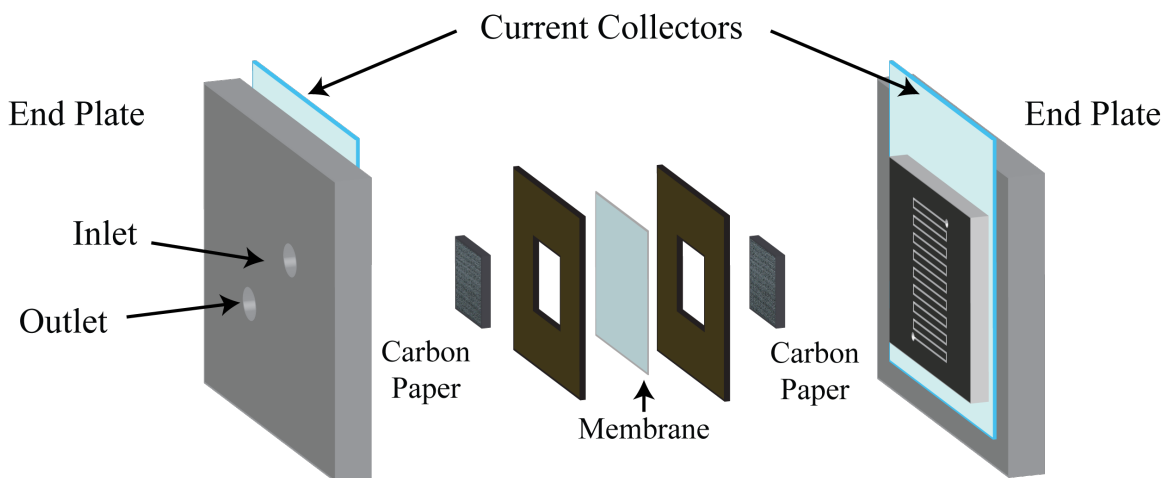


Figure A8. Schematic diagram of the flow cell used in this study.

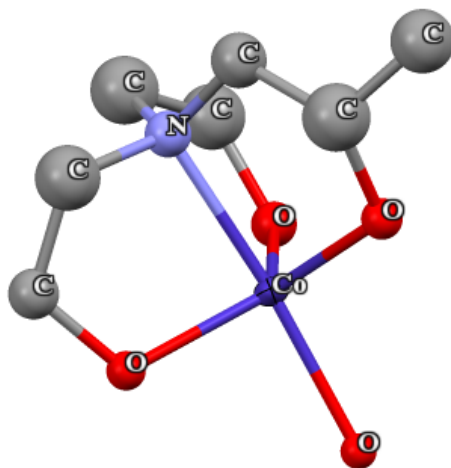


Figure A9. Preliminary solid state structure of the anion $[\text{Co}(\text{II})(\text{mTEA})(\text{H}_2\text{O})]^-$ determined with crystals grown from 5 M $\text{NaOH}_{(\text{aq})}$. Hydrogens are omitted for clarity. Crystals of $\text{Co}(\text{II})\text{-mTEA}$ are twinned, deconvolution of the data was not accomplished when this dissertation was printed.

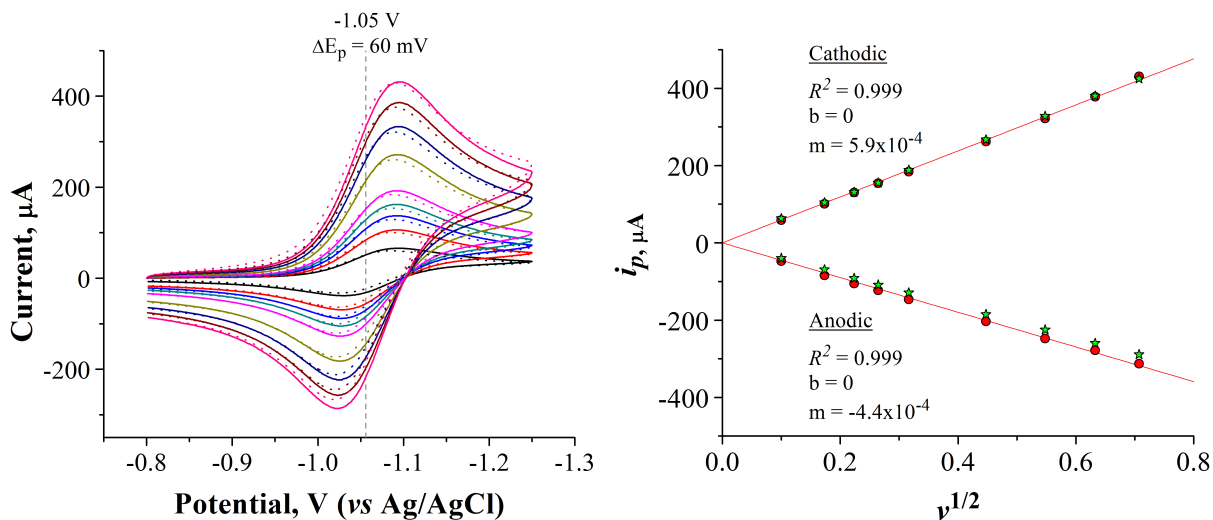


Figure A10. *Left.* Cyclic voltammograms of 20 mM Fe(III)-TEA in 5 M NaOH at various scan rates. Solid lines correspond to metal-to-ligand ratios (MLR) of 1:1, dotted lines to 1:2. Glassy carbon electrode, 2 mm diameter. *Right.* Linear regression of peak current vs. $v^{1/2}$ for the same solutions. Red dots are MLR of 1:1, green stars are MLR of 1:2.

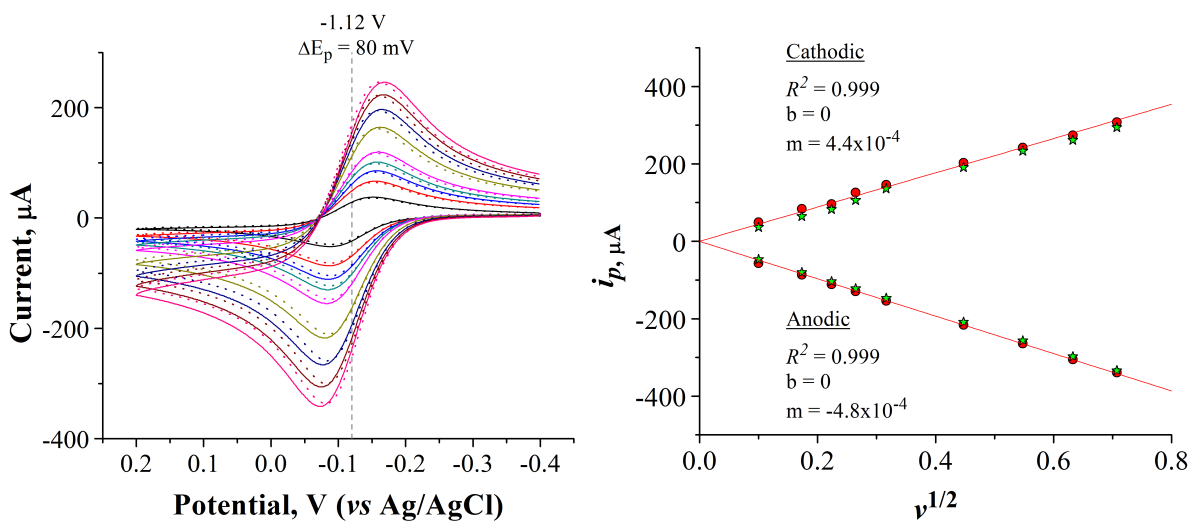


Figure A11. *Left.* Cyclic voltammograms of 20 mM Co^{II}-mTEA in 5 M NaOH at various scan rates. Solid lines correspond to metal-to-ligand ratios (MLR) of 1:1, dotted lines to 1:2. Glassy carbon electrode, 2 mm diameter. *Right.* Linear regression of peak current vs. $v^{1/2}$ for the same solutions. Red dots are MLR of 1:1, green stars are MLR of 1:2.

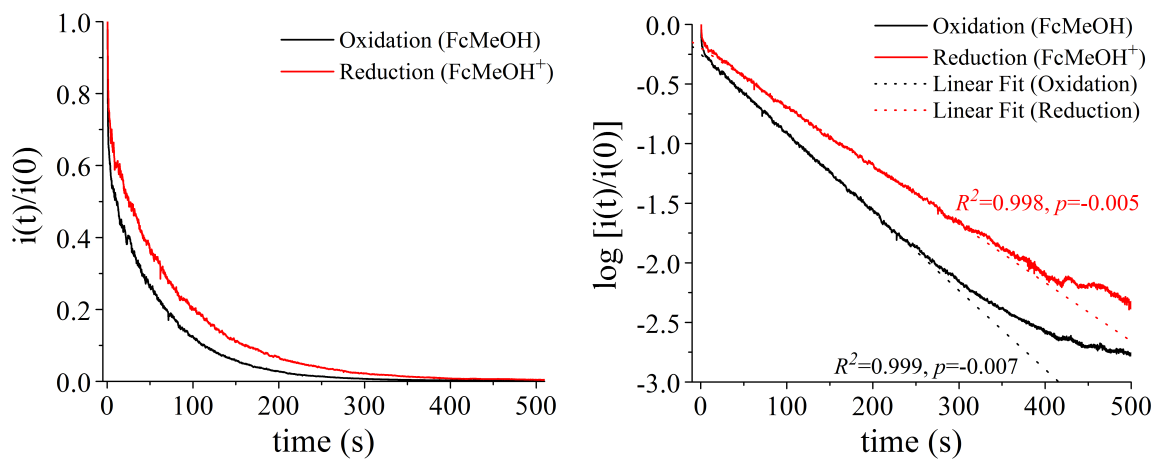
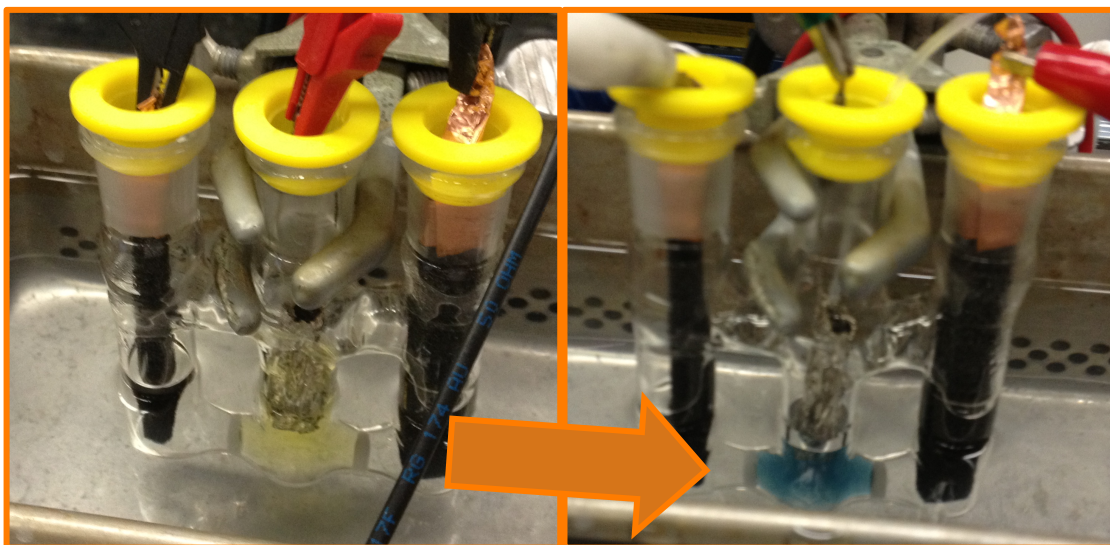


Figure A12. Calibration of electrolysis cell with 2 mM FcMeOH in 0.1 M NaNO₃.

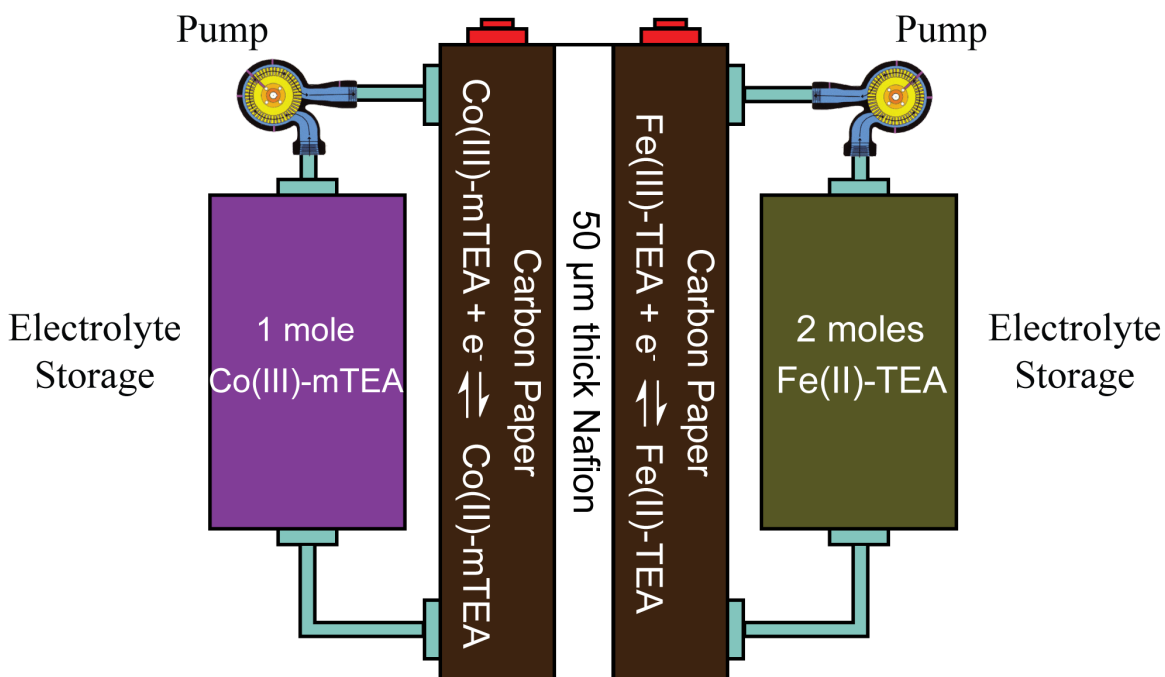


Figure A13. Schematic diagram of the optimized flow battery conditions.

Oxidation of Fe(II)-TEA by O₂

Figure A14 presents typical UV/Vis spectra recorded from solutions of 0.2 M Fe(III)-TEA (black) and 0.2 M Fe(II)-TEA (red), in 5 M NaOH. The images in the inset show the characteristic color of each of these solutions as discussed in Chapter 4. At concentrations > 0.1 M, forbidden electronic transitions appear in the visible range of the spectrum and generate footprint spectra that are unique to each oxidation state of the Fe-TEA complex. When a solution containing only Fe(II)-TEA is exposed to molecular oxygen (*e.g.*, by bubbling O₂), the observed spectrum corresponding to the reduced species (red spectrum in Figure A14) changes into that of the oxidized species (black spectrum). We used the differences between these spectra to determine the rate of oxidation of Fe(II)-TEA in the presence of O₂.

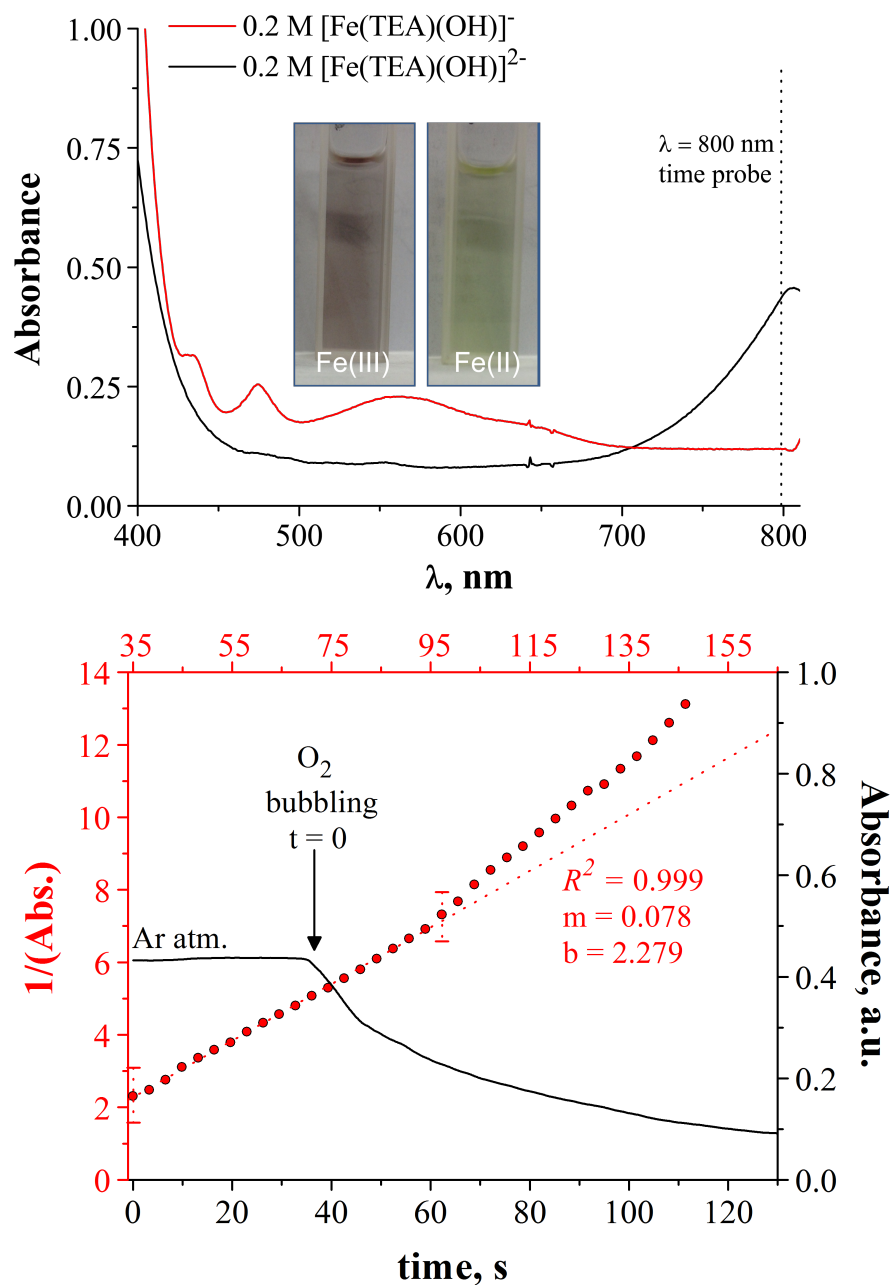


Figure A14. *Top.* UV-Vis spectra of 0.2 M Fe(II)-TEA (black) and Fe(III)-TEA (red) in 5 M NaOH. *Bottom.* Plots of absorbance vs. time (black line) and $1/(abs.)$ vs. time (red dots) for a solution of 0.2 M Fe(II)-TEA in 5 M NaOH during controlled exposure to O₂.

The experiment was carried out as follows: an aliquot of a solution 0.2 M Fe(II)-TEA was transferred into a quartz cuvette by flow injection under argon. A tank

containing pure O₂ was connected to a gas line that ended in a 25G needle, and the needle was inserted into the cuvette through a rubber septum until the tip end was in contact with the bottom of the quartz cuvette. The pressure in the gas regulator was adjusted to 2.5 psi ($P_{\text{O}_2} = 0.170$ atm), and the gas line was closed. Next, a fresh solution of Fe(II)-TEA was injected into the cuvette under argon and absorbance was recorded at $\lambda = 800$ nm for 35 s. Then, the oxygen valve was opened and absorbance was recorded for 100–150 s, Figure A14 (bottom). As shown, exposing the Fe(II)-TEA solution to the O₂ atmosphere generated a decay of the absorbance detected, indicating the spontaneous oxidation of Fe(II)-TEA to Fe(III)-TEA (which has no electronic transitions at $\lambda = 800$ nm). A plot of $1/(\text{abs.})$ vs. t was fit with a straight line, demonstrating second order kinetics with a correlation coefficient of $R^2 = 0.999$. The slope of the straight line was multiplied times the experimental molar absorptivity coefficient $\epsilon = 121 \text{ M}^{-1} \text{ cm}^{-1}$ to calculate the rate of reaction, which was determined to be $k = 9.43 \text{ M}^{-1} \text{ s}^{-1}$. The mathematical fit of $1/(\text{abs.})$ vs. t with second order kinetics is in agreement with previous reports,¹ and $k = 9.43 \text{ M}^{-1} \text{ s}^{-1}$ is expected for the high $p\text{H}^2$ of the system at the partial pressure of oxygen considered. These final results help explain the loss of Fe(II)-TEA seen in the flow battery system, where the contact area of the solution with oxygen-permeable plastic tubing is large, and the gear pumps are not oxygen free.

7.5. SUPPORTING INFORMATION - CHAPTER 5

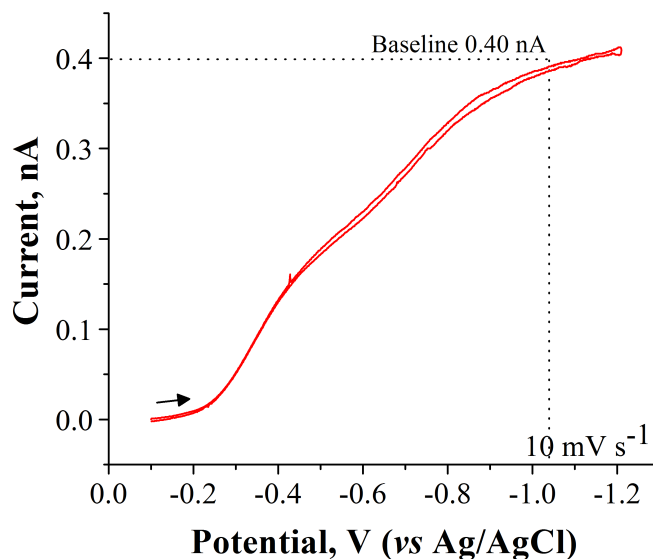


Figure A15. CV of a solution containing 200 μM O_2 in 5 M NaOH. GC UME ($a = 5 \mu\text{m}$). $\nu = 10 \text{ mV s}^{-1}$.

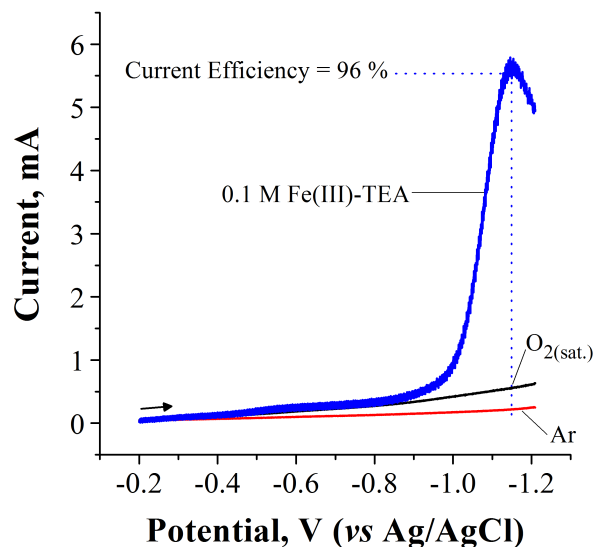


Figure A16. Linear sweep voltammogram for GC electrode ($A = 1 \text{ cm}^2$) in three different solutions: 5 M NaOH under Ar atmosphere (red), 5 M NaOH saturated with O_2 , and 0.1 M Fe(III)-TEA in 5 M NaOH saturated with O_2 . $\nu = 10 \text{ mV s}^{-1}$. $\omega = 1500 \text{ rpm}$.

7.6. SUPPORTING INFORMATION - CHAPTER 6

Fabrication of GC Microelectrodes

A GC rod (1 cm length, 1 mm diameter) was immersed in 4 M KOH solution along with a large graphite counter electrode. D.C. voltage of 5 V was applied between the two electrodes for 20 min. (GC was the anode), after which the GC rod was flipped upside down. The same voltage was applied again for another 20 min. to etch the top end of the rod. This procedure was repeated a few times to produce a final sharp GC needle. The needle was rinsed with water and acetone, and then dried at 120°C for 30 min.

The needle was then inserted into one end of a borosilicate capillary (FHC, 1.5 mm O.D. 0.8 mm I.D.). A copper wire was inserted into the opposite end as a contact wire. Then, Ag Epoxi resin was poured at the gap left between the top of the GC needle and the bottom of the copper wire to make electric contact. The electrode was oven-treated (60 °C) for 3 h. Once polymerization was complete, the exposed end of the GC needle was immersed into a suspension of Clearclad cathodic electrophoretic paint (5:1 ethanol-suspension v/v ratio) along with a Pt wire. D.C. voltage of 30 V was applied for 10 min. to polymerize the cathodic paint on the surface of the GC electrode, after which the electrode was oven-heated at 60 °C for 30 min. This last step was repeated three times.

The coated end of the electrode was covered with epoxy resin to protect the electrophoretic coating from scratches while performing the alignment of the electrodes prior to the SI-SECM experiments. Finally, the electrode was polished with sand paper and alumina suspension.

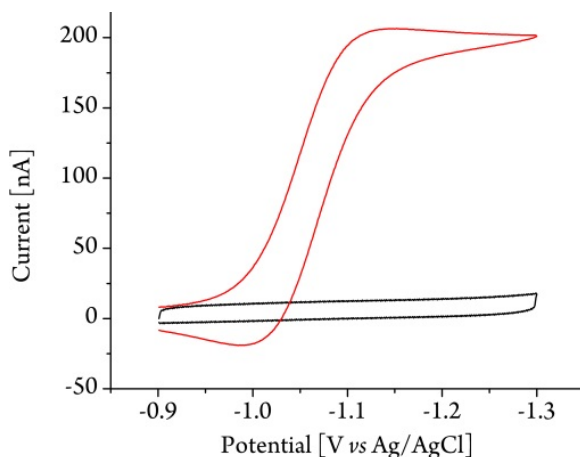


Figure A17. CVs of 100 μm *dia.* glassy carbon electrode in 2 M NaOH, in the absence (black line) and presence (red line) of 10 mM $[\text{Fe}(\text{TEA})(\text{OH})]^+$. $\nu = 20 \text{ mV s}^{-1}$.

Automation of SI-SECM Experiment

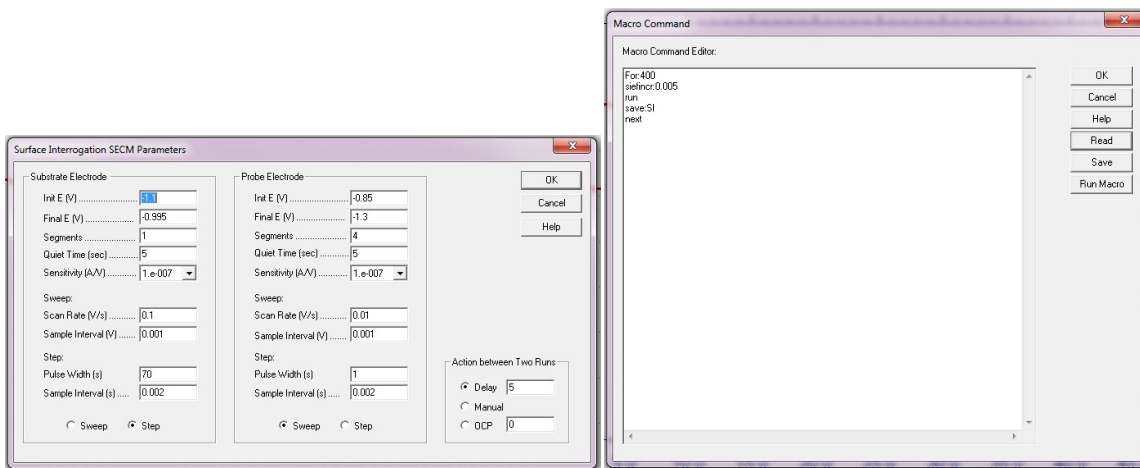


Figure A18. Screen shots of CHI software “macro command”.

Automated program used to perform the SI-SECM experiments. *Left panel:* Experimental conditions. As shown, the program would apply a potential step on the substrate electrode with a magnitude $E_{\text{subs}} = -0.995 \text{ V}$ (*vs.* Ag/AgCl) for 70 seconds, after which a CV experiment would be performed on the SECM tip electrode, sweeping the

potential from -0.85 V to -1.30 V (*vs.* Ag/AgCl) at $\nu = 10 \text{ mV s}^{-1}$ (2 cycles), with a time delay between experiments of $t_r = 5$ seconds (we used a delay of 2 in the experiments). *Right panel:* Macro command that automates the experiment. The program was designed to run the experiment described in the left panel 400 times, with a change in the substrate potential of $\Delta E_{\text{subs}} = 0.005 \text{ V}$ prior to every new SI-SECM experiment. The results would then be saved under label SI, followed by the number of the corresponding experimental run.

Interrogation Transient of Hydrogen

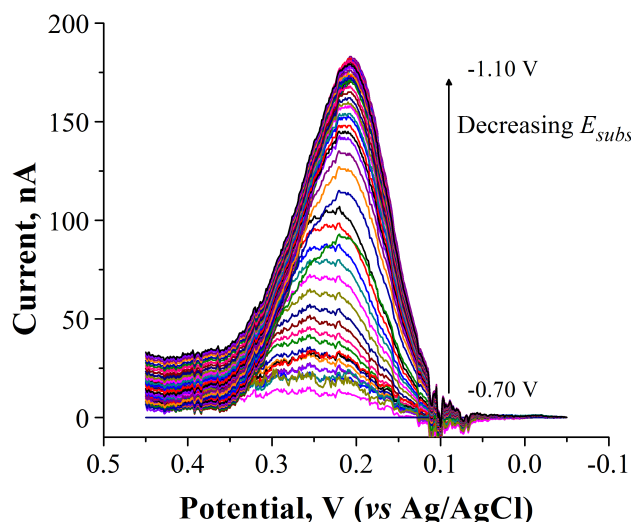


Figure A19. Interrogation of hydrogen adsorbed on Ir with 1 mM FcMeOH⁺ in 2 M NaOH (after baseline subtraction). Pt tip electrode, Ir substrate electrode (both 100 μm diam. $RG \approx 1.1$). E_{subs} was stepped at potentials between -0.70 V and -1.10 V, with $\Delta E_{\text{subs}} = -0.01 \text{ V}$. $\nu = 20 \text{ mV s}^{-1}$.

APPENDIX B: OTHER WORKS BY THE SAME AUTHOR

Storage of Electrical Energy by a Redox Flow Battery Based on Cobalt and Iron Complexes with Amino-Alcohol Ligands in Strongly Alkaline Electrolyte. Arroyo-Currás, N.; Bard, A.J.; *U.S. Patent*. Publication Date: April 2015.

Biodegradable Electroactive Polymers for Electrochemically-Triggered Drug Delivery. Hardy, J.G.; Mouser, D.J.; Arroyo-Currás, N.; Geissler, S.; Chow, J.K.; Nguy, L.; Kim, J.M.; Schmidt, C.E.; *J. Mater. Chem. B*, **2014**, 2, 6809-6822.

Electrochemical Monitoring of TiO₂ Atomic Layer Deposition by Chronoamperometry and Scanning Electrochemical Microscopy. Satpati, A.K.; Arroyo-Currás, N.; Li, J.; Yu, E.T.; Bard, A.J.; *Chem. Mater.*, **2013**, 25, 4165-4172.

Achieving Nanometer Scale Tip-to-Substrate Gaps with Micrometer-Size Ultramicroelectrodes in Scanning Electrochemical Microscopy. Shen, M.; Arroyo-Currás, N.; Bard, A.J.; *Anal. Chem.*, **2011**, 83, 9082-9085.

REFERENCES

Chapter 1

- [1] Abraham, S.; *National Transmission Grid Study*, U.S. Department of Energy: Washington, DC: 2003.
- [2] Linden S.; *Energy*, **2006**, *31*, 3446–3457.
- [3] Chen, H.; Cong, T. N.; Yang, W.; Tan, C.; Li, Y.; Ding, Y.; *Prog. Nat. Sci.*, **2009**, *19*, 291-312.
- [4] Mclarnon F. R.; Cairns E. J.; *Ann. Rev. Energy*, **1989**, *14*, 241–271.
- [5] Chatzivasileiadi, A.; Ampatzi, E.; Knoght, I.; *Renew. Sust. Energ. Rev.*, **2013**, *25*, 814-830.
- [6] Eyer, J.; Corey, G.; *Energy Storage for the Electricity Grid: Benefits and Market Potential Assessment Guide*, Sandia National Laboratories, Albuquerque, NM: 2010.
- [7] KEMA, Inc.; *Market Evaluation for Energy Storage in the United States*, Copper Development Association: Fairfax, VA: 2012.
- [8] Baker, J. N.; Collinson, A.; *Power Eng. J.*, **1999**, *6*, 107–112.
- [9] Dobie, W. C.; *Power Eng. J.*, **1998**, *12*, 177–181.
- [10] Giner, J.; Swette, L.; Cahill, A.; *Screening of Redox Couples and Electrode Materials*, CR 134705, NASA-Lewis Research Center, Cleveland, OH: 1976.
- [11] Ciprios, C.; Erslidne, W.; Grimes, P. G.; *Redox Bulk Energy Storage System Study*, Vol. I and II, CR 135206, Exxon Research Engineering Co., NASA-Lewis Research Center, Cleveland, OH: 1977.
- [12] Thaller, L. H.; in *Symposium on Load-Leveling*, sponsored by The Electrochemical Society, Atlanta, GA: 1977.
- [13] Wang, W.; Luo, Q.; Li, B.; Wei, X.; Li, L.; Yang, Z.; *Adv. Funct. Mater.*, **2013**, *23*, 970-986.
- [14] Dunn, B.; Kamath, H.; Tarascon, J. M.; *Science*, **2011**, *334*, 928-935.
- [15] Doughty, D. H.; Butler, P. C.; Akhil, A. A.; Clark, N. H.; Boyes, J. D.; *Electrochem. Soc. Interface*, **2010**, *19*, 49-53.
- [16] Enervault. <http://enervault.com/> (accessed Sep 2, 2014).
- [17] Nguyen, T.; Savinell, R. F.; *Interface*, **2010**, *19*, 54-56.

- [18] Rosemount Analytical, *Conductance Data for Commonly Used Chemicals*, Irvine, CA: 2010.
- [19] Kear, G.; Shah, A. A.; Walsh, F. C.; *Int. J. Energy Res.*, **2012**, *36*, 1105-1120.
- [20] Chen, Y. D.; Santhanam, K. S. V., Bard, A. J.; *J. Electrochem. Soc.*, **1981**, *128*, 1460-1467.
- [21] Moore, J. W.; Stanitski, C. L.; Jurs, P. C.; *Chemistry: The Molecular Science*, Cengage Learning, Stamford, 2008, Vol. 2, p. A33-A34.
- [22] Standard Reference Data Program (National Institute of Standards and Technology (U.S.)). *NIST Critically Selected Stability Constants of Metal Complexes Database*; Smith, R. M.; Martell, A. E.; Motekaitis, R. J., Eds.; NIST Standard Reference Database; Version 8.0.; U.S. Dept. of Commerce, Technology Administration, National Institute of Standards and Technology, Standard Reference Data Program: Gaithersburg, MD, 2004.
- [23] Vanysek, P.; *Electrochemical Series*, In *CRC Handbook of Chemistry and Physics*; CRC Press: Boca Raton, FL, 2013, p. (8–20)–(8–29).
- [24] Bard, A. J.; Faulkner, L. R.; *Electrochemical Methods: Fundamentals and Applications*; Wiley: New York, 2001.
- [25] Wolfson, H.; *Nature*, **1944**, *153*, 375-376.
- [26] Jessop, G.; *Nature*, **1946**, *158*, 59-59.
- [27] Subrahmanya, R. S.; *Proc. Ind. Acad. Sci. A*, **1956**, *43*, 133-147.
- [28] Ibañez, J. G.; Choi, C.; Becker, R. S.; *J. Electrochem. Soc.*, **1987**, *134*, 3083-3089.
- [29] Bechtold, T.; Burtscher, E.; Turcanu, A.; Bobleter, O.; *J. Appl. Electrochem.*, **1997**, *27*, 1021-1028.
- [30] INEOS. Technical Data Sheet: Triethanolamine. <http://www.ineos.com> (accessed Sep 11, 2014).
- [31] Korson, L.; Drost-Hansen, W.; Millero, F. J.; *J. Phys. Chem.*, **1969**, *73*, 34-39.
- [32] Vinnolit. Product Information: Caustic Soda Solution. <http://www.vinnolit.com> (accessed Sep 11, 2014).
- [33] Fasullo, O. T.; *Sulfuric Acid: Use and Handling*; McGraw-Hill: New York, 1965.
- [34] Einstein, A.; *Ann. der Physik*, **1905**, *322*, 560.
- [35] Sutherland, W.; *Phil. Mag.*, **1905**, *9*, 781-785.
- [36] Denuault, G.; Mirkin, M. V.; Bard, A. J.; *J. Electroanal. Chem.*, **1991**, *308*, 27-38.
- [37] *Scanning Electrochemical Microscopy*; Bard, A. J., Mirkin, M. V., Eds.; Marcel Dekker: New York, 2001.

- [38] Mirkin, M. V.; Bard, A. J.; *Anal. Chem.*, **1992**, *64*, 2293-2302.
- [39] Mirkin, M. V.; Bulhões, L. O. S.; Bard, A. J.; *J. Am. Chem. Soc.*, **1993**, *115*, 201–204.
- [40] Mirkin, M. V.; Richards, T. C.; Bard, A. J.; *J. Phys. Chem.*, **1993**, *97*, 7672–7677.
- [41] Mirkin, M. V.; Bard, A. J.; *Anal. Chem.*, **1993**, *97*, 7672–7677.
- [42] Mirkin, M. V.; Bard, A. J.; *J. Electrochem. Soc.*, **1992**, *139*, 3535–3539.

Chapter 2

- [1] *SciFinder*; Chemical Abstract Service: Columbus, OH, 2014; Year analysis for term: “redox flow battery”, exponential fit carried out in Origin Pro (accessed Jul 24, 2014).
- [2] Wang, W.; Luo, Q.; Li, B.; Wei, X.; Li, L.; Yang, Z.; *Adv. Funct. Mater.*, **2013**, *23*, 970-986.
- [3] Dunn, B. ; Kamath, H. ; Tarascon, J. M.; *Science*, **2011**, *334*, 928-935.
- [4] Yang, Z.; Zhang, J.; Kintner-Meyer, M. C. W.; Lu, X.; Choi, D.; Lemmon, J. P.; Liu, J.; *Chem. Rev.*, **2011**, *111*, 3577-3613.
- [5] Bard, A. J.; Faulkner, L. R.; *Electrochemical Methods: Fundamentals and Applications, Second Edition*; Table 12.1.1, Wiley: New York, 2001.
- [6] Bard, A. J.; Mirkin, M. V. *Scanning Electrochemical Microscopy, Second Edition*; CRC Press: Boca Raton, FL, 2012.
- [7] Hawley, D.; Adams, R. N.; *J. Electroanal. Chem.*, **1965**, *10*, 376-386.
- [8] Malachuk, P. A.; Prater, K. B.; Petrie, G.; Adams, R. N.; *Electroanal. Chem. Interfacial Electrochem.*, **1968**, *16*, 41-46.
- [9] Adams, R. N. *Electrochemistry at solid electrodes*; Monographs in electroanalytical chemistry and electrochemistry; M. Dekker: New York, 1969.
- [10] Andrieux, C. P.; Saveant, J. M.; in *Investigation of Rates and Mechanisms of Reactions*, Part II, 4th ed., C. F. Bernasconi, Ed., Wiley Interscience, New York, 1986, 305-390.
- [11] Bard, A. J.; *Anal. Chem.*, **35**, 1125-1128.
- [12] Santhanam, K. S. V.; Bard, A. J.; *Electroanal. Chem.*, **1970**, *4*, 215-315.

Chapter 3

- [1] Jaffe, E.; *Industria Chimica*, **1934**, *9*, 750-752.
- [2] Wolfson, H.; *Nature*, **1944**, *153*, 375-376.

- [3] Jessop, G.; *Nature*, **1946**, *158*, 59-59.
- [4] Spalenka, M.; *Hutnicke Listy*, **1953**, *8*, 362-363.
- [5] Bechtold, T.; Burtscher, E.; Turcanu, A.; Bobleter, O.; *Text. Res. J.*, **1997**, *67*, 635-642.
- [6] Bechtold, T.; Burtscher, E.; Turcanu, A.; Bobleter, O.; *J. App. Electrochem.*, **1997**, *27*, 1021-1028.
- [7] Bechtold, T.; Turcanu, A.; *J. Electrochem. Soc.*, **2002**, *149*, D7-D14.
- [8] Bechtold, T.; Burtscher, E.; Gmeiner, D.; Bobleter, O.; *J. Electroanal. Chem.*, **1991**, *306*, 169-183.
- [9] Bechtold, T.; Burtscher, E.; Turcanu, A.; Bobleter, O.; *J. Electrochem. Soc.*, **1996**, *143*, 2411-2416.
- [10] Switzer, J. A.; Gudavarthy, R. V.; Kulp, E. A.; Mu, G.; He, Z.; Wessel, A. J.; *J. Am. Chem. Soc.*, **2010**, *132*, 1258-1260.
- [11] Kothari, H. M.; Kulp, E. A.; Limmer, S. J.; Poizot, P.; Bohannan, E. W.; Switzer, J. A.; *J. Mater. Res.*, **2006**, *21*, 293-301.
- [12] Kulp, E. A.; Kothari, H. M.; Limmer, S. J.; Yang, J.; Gudavarthy, R. V.; Bohannan, E. W.; Switzer, J. A.; *Chem. Mater.*, **2009**, *21*, 5022-5031.
- [13] Saalfrank, R. W.; Bernt, I.; Uller, E.; Hampel, F.; *Angew. Chem. Int. Ed. Engl.*, **1997**, *36*, 2482-2485.
- [14] Pilawa, B.; Desquiotz, R.; Kelemen, M. T.; Weickenmeier, M.; Geisselmann, A.; *J. Magn. Magn. Mater.*, **1997**, *177*, 748-749.
- [15] Saalfrank, R. W.; Deutscher, C.; Sperner, S.; Nakajima, T.; Ako, A. M.; Uller, E.; Hampel, F.; Heinemann, F. W.; *Inorg. Chem.*, **2004**, *43*, 4372-4382.
- [16] Murugesu, M.; Abboud, K. A.; Christou, G.; *Dalton Trans.*, **2003**, 4552-4556.
- [17] Wen, Y. H.; Zhang, H. M.; Qian, P.; Zhou, H. T.; Zhao, P.; Yi, B. L.; Yang, Y. S.; *Electrochim. Acta*, **2006**, *51*, 3769-3775.
- [18] Arroyo-Currás, N.; Hall, J.W.; Dick, J.E.; Jones, R. A.; Bard, A.J.; *J. Electrochem. Soc.*, **2015**, *162*, A378-A383.
- [19] Buddhadev, S.; Dotson, R. L.; *J. Inorg. Nucl. Chem.*, **1970**, *32*, 2707-2716.
- [20] Sen, B.; Dotson, R. L.; *J. Inorg. Nucl. Chem.*, **1970**, *32*, 2707-2716.
- [21] Schmidt, S.; Prodius, D.; Novitchi, G.; Mereacre, V.; Kostakis, G. E.; Powell, A. K.; *Chem. Commun.*, **2012**, *48*, 9825-9827.
- [22] Ali, A. E.; *Egypt. J. Chem.*, **2005**, *48*, 121.

- [23] Jones, L. F.; Jensen, P.; Moubaraki, B.; Berry, K. J.; Boas, J. F.; Pilbrow, J. R.; Murray, K. S.; *J. Mater. Chem.*, **2006**, *16*, 2690–2697.
- [24] Fielden, J.; Speldrich, M.; Besson, C.; Korgeler, P.; *Inorg. Chem.*, **2012**, *51*, 2734-2736.
- [25] Ibanez, J. G.; Choi, C.; Becker, R. S.; *J. Electrochem. Soc.*, **1987**, *134*, 3083-3089.
- [26] Rosemount Analytical, *Conductance Data for Commonly Used Chemicals* (Irvine, CA, 2010).
- [27] Wu, X.; He, G.; Gao, Q; Han, Y.; Zhang, D.; Zhen, D.; Jiang, X.; A full-iron complex flow battery having high open-circuit voltage. CN 103700872 A 20140402, April 2, 2014.
- [28] Zhang, H.; Wen, Y.; Qian, P.; Yi, B.; Fe complex/halogen electrochemical system used for liquid flow electricity storage. CN 101047261 A 20071003, October 7, 2007.
- [29] Connors, K. A.; *Binding Constants: The Measurement of Molecular Complex Stability*, Wiley: New York, 1987.
- [30] Bard, A. J.; Faulkner, L. R.; *Electrochemical Methods: Fundamentals and Applications*; Wiley: New York, 2000.
- [31] Sheldrick, G. M.; *Acta Cryst. A*, **2007**, *64*, 112-122.
- [32] Becke, A. D.; *J. Chem. Phys.*, **1993**, *98*, 5648-5652.
- [33] Dolg, M.; Wedig, U.; Stoll, H.; Preuss, H.; *J. Chem. Phys.*, **1987**, *86*, 866-872.
- [34] Barone, V.; Cossi, M.; *J. Phys. Chem. A* **1998**, *102*, 1995-2001.
- [35] Cossi, M.; Rega, N.; Scalmani, G.; Barone, V. *J. Comp. Chem.* **2003**, *24*, 669-681.
- [36] Andersson, M. P.; Uvdal, P.; *J. Phys. Chem. A*, **2005**, *109*, 2937-2941.
- [37] Robin, M. B.; Day, P.; *Adv. Inorg. Chem. Rad.*, **1968**, *10*, 247-422.
- [38] Day, P.; Hush, N. S.; Clark, J. H.; *Phil. Trans. R. Soc. A*, **2008**, *366*, 5-14.
- [39] Kurtz, D. M.; *Chem. Rev.*, **1990**, *90*, 585-606.
- [40] Mirkin, M. V.; Bard, A. J.; *Anal. Chem.*, **1992**, *64*, 2293-2302.
- [41] Miao, W.; Ding, Z.; Bard, A. J.; *J. Phys. Chem. B*, **2002**, *106*, 1392–1398
- [42] Anderegg, G.; *Inorg. Chim. Acta*, **1986**, *121*, 229-231.
- [43] Kunaszewska, M.; *Roczniki Chemii*, **1973**, *47*, 683-691.
- [44] Standard Reference Data Program (National Institute of Standards and Technology (U.S.)). NIST Critically Selected Stability Constants of Metal

Complexes Database; Smith, R. M.; Martell, A. E.; Motekaitis, R. J., Eds.; NIST Standard Reference Database; Version 8.0.; U.S. Dept. of Commerce, Technology Administration, National Institute of Standards and Technology, Standard Reference Data Program: Gaithersburg, MD, 2004.

- [45] Chen, Y. D.; Santhanam, K. S. V., Bard, A. J.; *J. Electrochem. Soc.*, **1981**, *128*, 1460-1467.

Chapter 4

- [1] Nguyen, T.; Savinell, R. F.; *Interface*, **2010**, *19*, 54-56.
- [2] Wang, W.; Luo, Q.; Li, B.; Wei, X.; Li, L.; Yang, Z.; *Adv. Funct. Mater.*, **2013**, *23*, 970-986.
- [3] Rosemount Analytical, *Conductance Data for Commonly Used Chemicals*, Irvine, CA: 2010.
- [4] Kear, G.; Shah, A. A.; Walsh, F. C.; *Int. J. Energy Res.*, **2012**, *36*, 1105-1120.
- [5] Chen, Y. D.; Santhanam, K. S. V.; Bard, A. J.; *J. Electrochem. Soc.*, **1981**, *128*, 1460-1467.
- [6] Wolfson, H.; *Nature*, **1944**, *153*, 375-376.
- [7] Jessop, G.; *Nature*, **1946**, *158*, 59-59.
- [8] Pribil, R.; Vesly, V.; *Talanta*, **1962**, *9*, 1053-1055.
- [9] Brockman, C. J.; Nowlen, J. P.; *T. Electrochem. Soc.*, **1936**, *69*, 553-556.
- [10] Kothari, H. M.; Kulp, E. A.; Limmer, S. J.; Poizot, P.; Bohannan, E. W.; Switzer, J. A.; *J. Mater. Res.*, **2006**, *21*, 293-301.
- [11] Ibanez, J. G.; Choi, C.; Becker, R. S.; *J. Electrochem. Soc.*, **1987**, *134*, 3083-3089.
- [12] Subrahmanya, R. S.; *Proc. Ind. Acad. Sci. A*, **1956**, *43*, 133-147.
- [13] Bechtold, T.; Turcanu, A.; *J. Electroanal. Chem.*; **2006**, *591*, 118-126.
- [14] Bechtold, T.; Turcanu, A.; *J. Electroanal. Chem.*; **2005**, *580*, 173-178.
- [15] Bechtold, T.; Burtscher, E.; Turcanu, A.; Bobleter, O.; *J. Appl. Electrochem.*, **1997**, *27*, 1021-1028.
- [16] Wen, Y. H.; Zhang, H. M.; Qian, P.; Zhou, H. T.; Zhao, P.; Yi, B. L.; Yang, Y. S.; *Electrochim. Acta*, **2006**, *51*, 3769-3775.
- [17] Bard, A. J.; Faulkner, L. R. *Electrochemical Methods: Fundamentals and Applications*; Wiley: New York, 2000.
- [18] Aaron, D. S.; Liu, Q.; Grim, G. M.; Papandrew, A. B.; Turhan, A.; Zawodzinski, T. A.; Mench, M.M.; *J. Power Sources*, **2012**, *206*, 450-453.

- [19] Arroyo-Currás, N.; Hall, J. W.; Jones, R. A.; Bard, A.J.; Manuscript in preparation.
- [20] Santhanam, K. S. V.; Bard, A. J.; *Electroanal. Chem.*, **1970**, *4*, 215-315.
- [21] Izutsu, K.; *Acid-base dissociation constants in dipolar aprotic solvents*, Blackwell Scientific Publications: Oxford, 1990.
- [22] SciFinder; Chemical Abstracts Service: Columbus, OH; pK_a; CAS 102-71-6; <https://scifinder.cas.org> (accessed November 14, 2013); Calculated using Advanced Chemistry Development (ACD/Labs) Software V11.02 (© 1994-2013 ACD/Labs).
- [23] Massart, R; *IEEE Trans. Mag.*, **1981**, *17*: 1247-1248.
- [24] Alfa Aesar, Quotes in Bulk Prices (1,000 Kg): NaOH, \$13.68; Co(NO₃)₂•6H₂O, \$20.83; Fe(NO₃)₃•9H₂O, \$11.05; TEA, \$11.00; mTEA, \$120.0.
- [25] Kim, S.; Yan, J.; Schwenzler, B.; Zhang, J.; Li, L.; Liu, J.; Yang, Z. G.; Hickner, M. A.; *Electrochem. Comm.*, **2010**, *12*, 1650-1653.

Chapter 5

- [1] Adzic, R. In *Electrocatalysis*; Lipkowski, J., Ross, P. N., Eds.; Wiley-VCH: New York, 1998.
- [2] Markovic, N. M.; Ross, P. N. In *Interfacial Electrochemistry: Theory, Experiment, and Applications*; Wieckowski, A., Ed.; Marcel Dekker: New York, 1999; pp 821-841.
- [3] Fischer, F.; Priess, O.; *Ber. Dtsch. Chem. Ges.*, **1913**, *46*, 698-708.
- [4] Liu, B.; Bard, A. J.; *J. Phys. Chem. B*, **2002**, *106*, 12801-12806.
- [5] Sawyer, D. T., Chiericato, G.; Angelis, C. T.; Nanni, E. J.; Tsuchlya, T.; *Anal. Chem.*, **1982**, *54*, 1720-1724.
- [6] Maricle, D. L.; Hodgson, W. G.; *Anal. Chem.*, **1965**, *37*, 1562-1565.
- [7] Shi, C.; Steiger, B.; Yuasa, M.; Anson, F. C.; *Inorg. Chem.*, **1997**, *36*, 4294-4295.
- [8] Song, C.; Zhang, J. In *PEM Fuel Cell Electrocatalysts and Catalyst Layers*; Zhang, J., Ed.; Springer London, 2008; pp. 89-134.
- [9] Sawyer, D. T.; Williams, R. J. P. *Oxygen Chemistry*; Oxford University Press: New York, 1991.
- [10] Bielski, B. H. J.; Cabelli, D. E.; Arudi, R. L.; Ross, A. B.; *J. Phys. Chem. Ref. Data*, **1985**, *14*, 1041-1100.
- [11] Janik, I.; Tripathi, G. N. R.; *J. Chem. Phys.*, **2013**, *139*, (014302-1)–(014302-7).

- [12] Jin, W.; Du, H.; Zheng, S.; Xu, H.; Zhang, Y.; *J. Phys. Chem. B*, **2010**, *114*, 6542–6548.
- [13] Zhang, C.; Fan, F. R. F.; Bard, A. J.; *J. Am. Chem. Soc.*, **2009**, *131*, 177–181.
- [14] Bard, A. J.; Faulkner, L. R.; *Electrochemical Methods: Fundamentals and Applications*; Wiley: New York, 2001.
- [15] Battino, R.; Rettich, T. R.; Tominaga, T.; *J. Phys. Chem. Ref. Data*, **1983**, *12*, 163–178.
- [16] Kierzkowska-Pawlak, H.; Wielgosinsky, G.; *Inz. Chem. Procesowa*, **2001**, *22*, 717–722.
- [17] Tromans, D.; *Hydrometallurgy*, **1998**, *50*, 279–296.
- [18] Tromans, D.; *Ind. Eng. Chem. Res.*; **2000**, *39*, 805–812.
- [19] Arroyo-Currás, N.; Hall, J. W.; Dick, J. E.; Jones, R. A.; Bard, A. J.; *J. Electrochem. Soc.*, **2015**, *162*, A378-A383.

Chapter 6

- [1] Rodríguez-López, J.; Zoski, C. G.; Bard, A. J., In *Scanning Electrochemical Microscopy*, Second Edition; CRC Press, 2012; pp. 525–568.
- [2] Rodríguez-Lopez, J.; Alpuche-Aviles, M.; Bard, A. J. *J. Am. Chem. Soc.*, **2008**, *130*, 1520-5126.
- [3] Rodríguez-Lopez, J.; *Electroanal. Chem.*, **2012**, *24*, 287-351.
- [4] Rodríguez-López, J.; Minguzzi, A.; Bard, A. J. *J. Phys. Chem. C*, **2010**, *114*, 18645–18655.
- [5] Beer, H. B.; *J. Electrochem. Soc.*, **1980**, *127*, 303C–307C.
- [6] Ardizzone, S.; Trasatti, S.; *Advances in Colloid and Interface Science*, **1996**, *64*, 173–251.
- [7] Papeschi, G.; Bordini, S.; Carlà, M.; Criscione, L.; Ledda, F.; *J. Med. Eng. Technol.*, **1981**, *5*, 86–87.
- [8] Macur, R.; Iridium-iridium oxide electrode for measuring pH of blood and other fluids. US3726777 A, April 10, 1973.
- [9] Buckley, D. N.; Burke, L. D.; *J. Chem. Soc., Faraday Trans. 1*, **1976**, *72*, 2431–2440.
- [10] Mozota, J.; Conway, B. E.; *Electrochim. Acta*, **1983**, *28*, 1-8.
- [11] Stonehart, P.; Kozłowska, H. A.; Conway, B. E.; *Proc. Roy. Soc. A*, **1969**, *310*, 541-563.
- [12] Chen, H.; Trasatti, S.; *J. App. Electrochem.*, **1993**, *23*, 559-566.

- [13] Kotz, R.; Lewerenz, H. J.; Bruesch, P.; Stucki, S.; *J. Electroanal. Chem.*, **1983**, *150*, 209-216.
- [14] Kotz, R.; Neff, H.; Stucki, S.; *J. Electrochem. Soc.*, **1984**, *131*, 72-77.
- [15] Minguzzi, A.; Lugaresi, O.; Locatelli, C.; Rondinini, S.; D'Acapito, F.; Achilli, E.; Ghigna, P.; *Anal. Chem.*, **2013**, *85*, 7009-7013.
- [16] Skoog, D. A.; Holler, F. J.; Crouch, S. R.; *Principles of Instrumental Analysis*, 6 edition., Cengage Learning: Belmont, CA, 2006.
- [17] Stonehart, P.; Kozłowska, H. A.; Conway, B. E.; *Proc. R. Soc. Lond. A*, **1969**, *310*, 541-563.
- [18] Minguzzi, A.; Lugaresi, O.; Achilli, E.; Locatelli, C.; Vertova, A.; Ghigna, P.; Rondinini, S.; *Chem. Sci.*, **2014**, *5*, 3591-3597.
- [19] Park, H. S.; Leonard, K. C.; Bard, A. J.; *J. Phys. Chem. C*, **2013**, *117*, 12093-12102.
- [20] Augustynski, J.; Koudelka, M.; Sanchez, J.; Conway, B. E.; *J. Electroanal. Chem.*, **1984**, *160*, 233-248.
- [21] Vertova, A.; Borgese, L.; Capelletti, G.; Locatelli, C.; Minguzzi, A.; Pezzoni, C.; Rondinini, S.; *J. Appl. Electrochem.*, **2008**, *38*, 973-978.
- [22] Dahms, H.; Bockris, J. O'M.; *J. Electrochem. Soc.*, **1964**, *111*, 728-736.
- [23] Bard, A. J.; Mirkin, M. V. *Scanning Electrochemical Microscopy, Second Edition*; 2 edition.; CRC Press: Boca Raton, Fla, 2012.
- [24] Rodriguez-Lopez, J.; Minguzzi, A.; Bard, A. J.; *J. Phys. Chem. C*, **2010**, *114*, 18645-18655.
- [25] Wen, Y. H.; Zhang, H. M.; Qian, P.; Zhou, H. T.; Zhao, P.; Yi, B. L.; Yang, Y. S.; *Electrochim. Acta*, **2005**, *51*, 3769-3775.
- [26] Angerstein-Kozłowska, H.; Conway, B. E.; Mozota, J.; *J. Electroanal. Chem.*, **1979**, *100*, 417-446.
- [27] Jerkiewicz, G.; Vatankhah, G.; Lessard, J.; Soriaga, M. P.; Park, Y., *Electrochim. Acta*, **2004**, *49*, 1451-1459.
- [28] Otten, J. M.; Visscher, W.; *J. Electroanal. Chem.*, **1974**, *55*, 13-21.
- [29] Plichon, V.; Petit, M. A.; *J. Electroanal. Chem.*, **1998**, *444*, 247-252.
- [30] Burke, L. D.; Whelan, D. P.; *J. Electroanal. Chem.*, **1981**, *124*, 333-337.
- [31] Woods, R.; *J. Electroanal. Chem.*, **1974**, *49*, 217-227.
- [32] Delahay, P.; *Double layer and electrode kinetics*; Interscience Publishers, 1965.

- [33] Bard, A. J.; Faulkner, L. R.; *Electrochemical Methods: Fundamentals and Applications*; Wiley: New York, 2001.
- [34] Gileadi, E.; Conway, B. E.; *J. Chem. Phys.*, **1963**, 39, 3420-3430.

Appendix

- [1] Stumm, W.; Lee, G. F.; *Ind. Eng. Chem.*, **1961**, 53, 143-146.
- [2] Morgan, B.; Lahav, O.; *Chemosphere*, **2007**, 68, 2080-2084.

VITA

Netzahualcóyotl Arroyo Currás (Netz Arroyo) was born in Puebla, Mexico. He completed his compulsory education at C.E.N.H.CH. (Puebla) in 2004. He moved to Monterrey to attend college at Tec de Monterrey, from which he obtained his bachelor's degree in Chemistry (Ciencias Químicas) in 2009. While at Tec de Monterrey, he worked in the electrochemistry group of Dr. Marcelo Videa studying the electrochemistry of flavonoids in acetonitrile. He also completed a two year-long program in business and entrepreneurship at Tec de Monterrey (Modalidad Emprendedora), while working on a start-up company he cofounded. Upon graduation and after consolidating his preference for research over financial glory, he quit the start-up and moved to Austin, Texas in 2010 to begin his Ph.D. studies under the supervision of Dr. Allen J. Bard at The University of Texas at Austin. He received the Department of Chemistry Henze Teaching Excellence Award in 2011. He is passionate about basic research and chemical education, and he is committed to the development of knowledge and technologies that improve human life and the environment.

Permanent email address: netz.arroyo@gmail.com

This dissertation was typed by Netzahualcóyotl Arroyo Currás.